Ergodicity breaking in disordered and kinetically constrained quantum many-body systems

by

Pietro Brighi

January, 2023

A thesis submitted to the
Graduate School
of the
Institute of Science and Technology Austria
in partial fulfillment of the requirements
for the degree of
Doctor of Philosophy

Committee in charge:

Zhanybek Alpichshev, Chair
Maksym Serbyn
Robert Seiringer
Marco Schiró

The thesis of Pietro Brighi, titled *Ergodicity breaking in disordered and kinetically constrained quantum many-body systems*, is approved by:

Supervisor: Maksym Serbyn, ISTA, Klosterneuburg, Austria

Signature: _____

Committee Member: Robert Seiringer, ISTA, Klosterneuburg, Austria

Signature: _____

Committee Member: Marco Schiró, Institut de Physique Theorique (IPhT), CEA, Saclay, France

Signature: _____

Defense Chair: Zhanybek Alpichshev, ISTA, Klosterneuburg, Austria

Signature: _____

Signed page is on file

ISTA Thesis, ISSN: 2663-337X

I hereby declare that this thesis is my own work and that it does not contain other people's work without this being so stated; this thesis does not contain my previous work without this being stated, and the bibliography contains all the literature that I used in writing the dissertation.

I declare that this is a true copy of my thesis, including any final revisions, as approved by my thesis committee, and that this thesis has not been submitted for a higher degree to any other university or institution.

I certify that any republication of materials presented in this thesis has been approved by the relevant publishers and co-authors.

Signature: _____

Pietro Brighi
January, 2023

Signed page is on file

Abstract

Nonergodic systems, whose out-of-equilibrium dynamics fail to thermalize, provide a fascinating research direction both for fundamental reasons and for application in state of the art quantum devices. Going beyond the description of statistical mechanics, ergodicity breaking yields a new paradigm in quantum many-body physics, introducing novel phases of matter with no counterpart at equilibrium. In this Thesis, we address different open questions in the field, focusing on disorder-induced many-body localization (MBL) and on weak ergodicity breaking in kinetically constrained models. In particular, we contribute to the debate about transport in kinetically constrained models, studying the effect of $U(1)$ conservation and inversion-symmetry breaking in a family of quantum East models. Using tensor network techniques, we analyze the dynamics of large MBL systems beyond the limit of exact numerical methods. In this setting, we approach the debated topic of the coexistence of localized and thermal eigenstates separated by energy thresholds known as many-body mobility edges. Inspired by recent experiments, our work further investigates the localization of a small bath induced by the coupling to a large localized chain, the so-called MBL proximity effect.

In the first Chapter, we introduce a family of particle-conserving kinetically constrained models, inspired by the quantum East model. The system we study features strong inversion-symmetry breaking, due to the nature of the correlated hopping. We show that these models host so-called quantum Hilbert space fragmentation, consisting of disconnected subsectors in an entangled basis, and further provide an analytical description of this phenomenon. We further probe its effect on dynamics of simple product states, showing revivals in fidelity and local observalbes. The study of dynamics within the largest subsector reveals an anomalous transient superdiffusive behavior crossing over to slow logarithmic dynamics at later times. This work suggests that particle conserving constrained models with inversion-symmetry breaking realize new universality classes of dynamics and invite their further theoretical and experimental studies.

Next, we use kinetic constraints and disorder to design a model with many-body mobility edges in particle density. This feature allows to study the dynamics of localized and thermal states in large systems beyond the limitations of previous studies. The time-evolution shows typical signatures of localization at small densities, replaced by thermal behavior at larger densities. Our results provide evidence in favor of the stability of many-body mobility edges, which was recently challenged by a theoretical argument. To support our findings, we probe the mechanism proposed as a cause of delocalization in many-body localized systems with mobility edges suggesting its ineffectiveness in the model studied.

In the last Chapter of this Thesis, we address the topic of many-body localization proximity effect. We study a model inspired by recent experiments, featuring Anderson localized coupled to a small bath of free hard-core bosons. The interaction among the two particle

species results in non-trivial dynamics, which we probe using tensor network techniques. Our simulations show convincing evidence of many-body localization proximity effect when the bath is composed by a single free particle and interactions are strong. We furthter observe an anomalous entanglement dynamics, which we explain through a phenomenological theory. Finally, we extract highly excited eigenstates of large systems, providing supplementary evidence in favor of our findings.

Acknowledgements

A PhD is a long journey in one's life, and, as most journeys, it is best enjoyed if shared with others. In these few lines, I would like to thank all the wonderful travel companions that I had the luck to have by my side during these years.

First, and foremost, Maksym, who guided me through the fascinating world of nonequilibrium physics and gave me the tools to try and capture its intricacies. Your passion for research and your outstanding physical intuition are a pleasure to witness, and certainly helped me move forward in times when I was disoriented. For all this and for your precious advice on the academic world in general I deeply thank you. I would also like to express my gratitude to Dima Abanin, who has provided fundamental insight in our projects through all the many illuminating discussions we had over these years. Having the chance to work alongside such a brilliant mind was a real honor.

The long office hours spent at ISTA would have been much duller without the presence of many amazing colleagues. I would like to thank Raimel, with whom I shared the good and the difficult times of this PhD. Our conversations about life and science have always provided good laughs as well as food for thought. Similarly, I wish to thank Alex and Marko for teaching me so much about tensor networks, and for sharing with me the pain debugging sometimes can be. Let me also mention all the members, present and past, of our research group, who, in some way or another, have all taught me something through these years. Finally, I would like to thank all the fellow scientists I had the chance to meet at ISTA. Since a complete list would be nearly impossible to write down, I simply express my deep gratitude to each and everyone of you.

Most of the research presented in this thesis has been funded by the European Research Council, under the European Union's Horizon 2020 research and innovation program (Grant Agreement No. 850899). I should also acknowledge the scientific computing facility at ISTA and at the University of Geneva, whose help was fundamental in some of the research presented in this thesis. I acknowledge PRACE for awarding the group access to Joliot-Curie at GENCI@CEA, where the large scale simulations concerning the MBL proximity effect in the finite c-bosons density were performed.

As in life there is more than science, let me thank all the people that have been by my side all these years. In spite of the distance, I always felt the warmth of my family, knowing I had their love to sustain me at all times. Grazie, vi voglio bene. A special thanks goes to Daniela, Annabella, Carlo and Roberto, who followed my research adventures with genuine interest and were always ready to advise me in critical times.

Even if now we see each other much less than I would like to, coming back to my friends in Milan always feels as if I never left. Guido, Bea, Michi and Sergio, you are family to me. I would also like to thank Mario and Romano, real friends whose company I enjoy dearly.

Living abroad may, at times, be difficult. However, if you find such good friends as I had the luck to meet here in Vienna, then you will create a second home. Dario, Lore, Giulia, Bea, Annalisa and Helene: you have made these years in Austria a real blast. I could not hope for a better family away from home.

I want to reserve a last, personal, paragraph to the person that matters the most. To Chicca, then, *'cause even when there is no star in sight, you'll always be my only guiding light.*

About the Author

Pietro Brighi completed his BSc in Physics at the Università degli study di Milano, where he also obtained the MSc with honours. During his undergraduate studies Pietro focused on the theoretical aspects of condensed matter physics, with a particular interest for superconductivity. During a research stay at the Università la Sapienza in Rome he worked on fluctuations of Cooper pairs and how they affect the density of states of two-dimensional disordered superconductors. In September 2018 he joined ISTA for his doctoral studies. After becoming a member of Prof. Serbyn's group, he focused on the dynamical aspects of out-of-equilibrium quantum many-body systems. During his PhD studies, Pietro published his research in high quality international journals and presented it, both in form of posters and talks, in several international conferences.

List of Collaborators and Publications

Prof. Maksym Serbyn: Prof. Serbyn is co-author of all the publications included in this thesis. He contributed in most of the stages of the projects, proposing ideas and approaches to the models studied and discussing the results and the physical interpretation.

Prof. Dmitry A. Abanin: Prof. Abanin was involved in all the publications concerning many-body localization. He offered great input both on the types of models to be studied and on the results coming from numerical simulations.

Dr. Alexios A. Michailidis: Dr. Michailidis was co-author of the many-body localization proximity effect papers. His contribution ranged from discussions about the model, to development of the code for TEBD and DMRG-X and some of the calculations regarding correlation functions. Additionally, he contributed to obtaining the PRACE grant.

Kristina Kirova: Kirova was involved in the Physical Review B paper about MBL proximity effect. Her contribution included the simulation of highly excited eigenstates through DMRG-X algorithm, used in the final Section of the paper.

Dr. Marko Ljubotina: Dr. Ljubotina is co-author of the paper on the quantum East model and of the paper in preparation regarding the clean-disordered bosonic mixture. His insight was valuable in understanding the mechanism behind the quantum Hilbert space fragmentation and in general in discussions about the model. He also contributed to obtaining the PRACE grant.

1. **Brighi P.**, Abanin D. A., Serbyn M. "Stability of mobility edges in disordered interacting systems," Phys. Rev. B **102** 060202(R) (2020)

2. **Brighi P.**, Michailidis A. A., Abanin D. A., Serbyn M. "Propagation of many-body localization in an Anderson insulator," Phys. Rev. B (Letters) **105** L220203 (2022)

3. **Brighi P.**, Michailidis A. A., Kirova K., Abanin D. A., Serbyn, M. "Localization of a mobile impurity interacting with an Anderson insulator," Phys. Rev. B **105** 224208 (2022)

4. **Brighi P.**, Ljubotina M. and Serbyn M. "Hilbert space fragmentation and slow dynamics in particle conserving quantum East models," arXiv:2210.15607 (2022)

5. **Brighi P.**, Ljubotina M., Abanin D. A., and Serbyn M. " Many-body localization proximity effect in two-species bosonic Hubbard model." In preparation, 2023

Table of Contents

List of Figures

CHAPTER 1

Introduction

Understanding the behavior of complex systems formed by a large number of components is a ubiquitous, yet extremely complicated, problem in the natural sciences. As an example, the microscopic description of the dynamics of the particles making up a cloud of gas requires tracking the trajectories of a humongous amount of degrees of freedom and is, a priori, a terribly demanding task. The intuition that the relevant macroscopic quantities describing the thermodynamic state of the gas are independent of the individual motion of the single constituent represented a groundbreaking turning point in physics. The ergodic hypothesis further formalizes this concept, stating that generic systems relax to equilibrium as their dynamics equally explore the available phase space on long times. Based on the ergodic hypothesis, the instantaneous motion of the particles looses relevance to the statistical description of the system, through a specific thermodynamic ensemble ρ defining the set of physically allowed states and their probability. The central object of statistical mechanics is then the *partition function* $\mathcal{Z} = \mathrm{tr}[\rho]$, establishing relations between the microscopic world and the macroscopic thermodynamic quantities.

This description, however, is effective for systems at thermal equilibrium. As it will be shown in this introduction, a surmise similar to the ergodic hypothesis exists in isolated quantum many-body systems, the so-called eigenstate thermalization hypothesis (ETH) [1, 2]. However, there exist systems whose dynamics escape the fate of thermalization and where the long time saturation is dependent on the microscopic details of the initial condition, and not only to the macroscopic thermodynamic conditions. These systems can be realized in state of the art experiments, thus raising the relevant question of understanding their behavior. In this work, we focus on the description of the out-of-equilibrium dynamics of models that present examples of anomalous thermalization or that fail to thermalize whatsoever.

In this introduction we provide a brief survey of the main results in the field of out-of-equilbrium quantum many-body physics in recent years and of the essential methods used in the remaining Chapters. First, we describe some of the main experimental platforms where the dynamics of out-of-equilibrium quantum systems can be probed and sketch different paradigmatic behaviors expected in non-equilibrium quantum dynamics in Section 1.1. We then highlight the main features of thermalizing and ergodicity-breaking systems in Sections 1.1.1 and 1.1.2 respectively. In Section 1.2 we give a short introduction to some of the methods used throughout this work, with particular attention to tensor network techniques. Next, we highlight the contributions of the author to the field in

Section 1.3. Finally, in the last Section 1.4 we discuss relevant challenges and open questions.

1.1 Dynamics of systems far from equilibrium

The last decades have seen the emergence of exceptional new experimental setups allowing the direct study of non-equilibrium phenomena, thus pushing forward the field of quantum many-body physics. As these experiments can effectively recreate the environment experienced by electrons in real materials, we will generically refer to them as *artificial matter*. A major advantage of artificial matter is that it allows a great degree of control on the parameters of the system, thus providing an excellent ground to test theories. This is in contrast to more traditional condensed matter experiments, where changing the Hamiltonian describing the system is often very complicated, or even impossible. Another great advantage of artificial matter is the built-in possibility to probe non-equilibrium dynamics, a task much harder in solid state physics, where going beyond the linear response regime requires extremely powerful, yet non-destructive, excitations of the system.

Of particular relevance for this work are those platforms that can reproduce a d-dimensional system ($d = 1, 2, 3$) embedded in an artificial lattice, where all phononic excitations are inherently removed. Realizing artificial lattices that serve as experimental platforms for non-equilibrium quantum matter relies on the ability of creating a confining potential for the individual constituents of the system. This can be achieved by optical lattices and laser traps, where the properties of light-matter interaction allow the creation of a controllable geometric potential pattern. To this category belong experiments with ultracold neutral atoms [3, 4, 5, 6], trapped ions [7, 8, 9] and atoms excited to Rydberg levels [10, 11, 12]. While the first typically interact via on-site potentials of the Hubbard type, trapped ions and Rydberg arrays inherently implement long-range interactions. A different setup corresponds to superconducting circuits [13, 14, 15], where the lattice geometry can be implemented via circuit lithography, thus allowing a great degree of control. These platforms then use anharmonic potentials to implement an effective two-level system, which can represent a spin degree of freedom. All these platforms are currently studied and their performances pushed forward in the quest for a reliable quantum computer [16].

Non-equilibrium dynamics in these experimental setups is usually probed through the

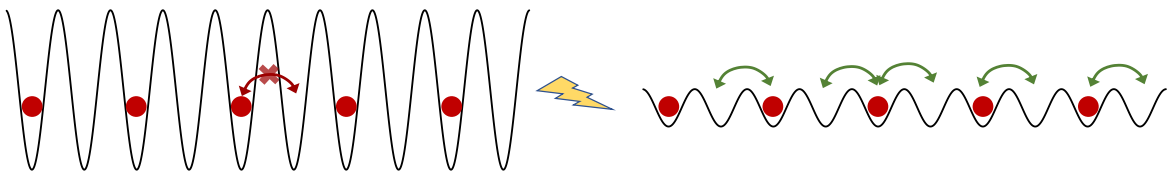

Figure 1.1: Pictorial representation of a quantum quench protocol. The state is initialized in a *deep* lattice, where the tunnelling amplitude is too small to allow the particles to leave their position. Upon a global quench, the lattice depth is reduced and the resulting state is far from equilibrium, enabling particles dynamics.

so-called quench protocol. In this setting, the system is initialized in the ground state of a given Hamiltonian, whose parameters are then suddenly changed, as shown pictorially in Figure 1.1. Upon the fast variation of the parameters the system typically finds itself in a configuration very far from thermal equilibrium, and its dynamics are described by effects beyond linear response theory. The fate of these *isolated* systems driven out of equilibrium then poses new fundamental questions and requires a change of perspective from the conventional statistical mechanics approach. One of the most relevant questions in this setting is if a system prepared in a highly excited state reaches thermal equilibrium or not, and the investigation of how such equilibration takes place.

A natural expectation for a thermalizing quantum many-body system, is that the long time behavior of local observables coincides to the thermal average obtained in the correct statistical ensemble. Thus, one of the central objects in the study of out-of-equilibrium dynamics is the time-evolution of local observables. In systems of bosons and fermions, they typically correspond to particle densities $\hat{n}_i = \hat{c}_i^\dagger \hat{c}_i$, where the operators $\hat{c}_i^\dagger$ ($\hat{c}_i$) creates (annihilates) a particle on site i. In spin systems, instead, these can be represented by the local magnetizations $\hat{S}_i^\alpha = \frac{\hbar}{2}\sigma_i^\alpha$, where σ_i^α is any of the three Pauli matrices. Other relevant quantities are the correlation functions relative to these local observables, which can be used to measure the transport properties of the system. Finally, we highlight the importance in this field of concepts from quantum information. Among these, the most widely used is the entanglement entropy among two sub-systems A and B. Entanglement is obtained by first taking the reduced density matrix corresponding to one of the two sub-systems, $\rho_A = \mathrm{tr}_B \left|\psi\right\rangle \left\langle\psi\right|$, and then calculating its von Neumann entropy

$$S_A = -\operatorname{tr} \rho_A \log \rho_A. \tag{1.1}$$

The entanglement entropy plays a central role in the field of non-equilibrium quantum dynamics, as it probes the amount of quantum correlations between the two sub-systems and provides a basis independent measure that has distinct behavior for thermalizing and nonergodic systems.

As we mentioned above, thermalization is expected to manifest as a relaxation to the correct thermal ensemble in the long-time behavior of the system. In absence of coupling with an external bath, however, an isolated system has to act as its own heat bath. Determining how this happens, then, requires a deeper investigation of the mechanisms leading to thermalization in isolated quantum systems. In the next Subsection, we present the main theoretical result in this direction, describing its assumptions and its consequences.

1.1.1 The eigenstate thermalization hypothesis

In classical isolated systems, thermalization is understood in terms of the ergodic hypothesis [17, 18], stating that dynamics lead the system to explore all the available phase space in an equal manner and to spend in every region time intervals proportional to its volume. As a consequence, late time averages of macroscopic observables correspond to averages over the available phase space, hence to the thermal value expected in the microcanonical ensemble describing systems that do not exchange energy nor particles with the environment. However, ergodicity only implies thermalization in a *weak* sense [18], as it concerns late time *averages*. A stronger condition for thermalization would require that time-evolution leads, at late times, to instantaneous agreement at almost all times of the time-evolved observables and the corresponding thermal average.

In this direction, a stronger condition for thermalization, although less rigorous, relies on the concept of *typicality*. Intuitively, *typical* configurations in the phase space are likely to have macroscopic observables in agreement with the thermal average, at least to leading order. Hence, the condition for thermalization in this setup is that any initial configuration, no matter how atypical, does eventually evolve to typical configurations. This is the case in *chaotic* systems, where time-evolution eventually leads the system through every configuration in the phase space. As typical states are the most probable, chaotic dynamics inevitably yields thermalization.

The question of how to translate these classical concepts to the quantum realm is still open, and represents an active area of research. The definition of chaos in classical models relies on the concept of trajectories, which does not have an analogue in the quantum language. Furthermore, the Schrödinger equation preserves the overlap of wave-functions evolved with the same Hamiltonian, thus the core idea of classical chaos that trajectories initially close in phase space become exponentially distant upon time evolution does not hold in the quantum setup.

Nevertheless, a commonly accepted definition of quantum chaos exists, and is based on the spectral statistics of the Hamiltonian. The main idea comes from the work of Wigner [19, 20] and Dyson [21] on the spectra of atomic nuclei. They noticed that a statistical description of the energy levels of complex quantum many-body systems may be a convenient way to avoid the intricacies required to obtain an exact prediction. The next fundamental step corresponds to realizing that in a generic basis and within a small energy shell the Hamiltonian is essentially a random matrix. Thanks to this intuition, the study the spectral properties of complex Hamiltonians can be reduced to the analysis of random matrices satisfying the same symmetries. The probability distribution, $P(s)$, of the differences among adjacent energy levels, $s_i = \varepsilon_i - \varepsilon_{i+1}$, in the sorted spectrum can be calculated for 2×2 matrices, resulting in the celebrated Wigner surmise, that provides an excellent approximation for the level statistics of large random matrices. The particular ensemble from which the random matrix distribution is obtained depends on the details of the physical system, and for time-reversal symmetric Hamiltonians it corresponds to the Gaussian Orthogonal Ensemble (GOE), $P(s) = \frac{\pi}{2} s e^{-\frac{\pi}{4}s^2}$.

The connection between quantum chaotic Hamiltonians and random matrices was only established in the 1980s, when Bohigas, Giannoni and Schmit conjectured that the level statistics of systems with chaotic classical counterpart is given by random matrix theory [22]. A consequence of this conjecture is that typical eigenstates of chaotic Hamiltonians are similar to random vectors in the Hilbert space [23]. This of course excludes very special eigenstates, such as the ground state, that have to fulfil very strict conditions. This concept is central in the construction of the eigenstate thermalization hypothesis (ETH) [1, 2, 24], where it is employed to formally connect chaotic Hamiltonians with thermalizing systems.

Let us state ETH in its more common form of an Ansatz for the matrix element of local operators [24]. Let $\hat{O}$ be a local operator representing a physical observable and $\{|E_m\rangle\}$ be the basis of eigenstates of a chaotic Hamiltonian. The eigenstates thermalization hypothesis then states that

$$\langle E_m | \hat{O} | E_n \rangle = O_{mn} = \mathcal{O}(\overline{E})\delta_{mn} + e^{-S(\overline{E})/2} f_O(\overline{E}, \omega) R_{mn}, \tag{1.2}$$

where $\overline{E} = (E_m + E_n)/2$, $\omega = E_m - E_n$ and $S(E)$ is the thermodynamic entropy corresponding to energy E, defined as the von Neumann entropy of the thermal density matrix

ρ, $S(E) = -\operatorname{tr}[\rho \log \rho]$. Crucially, the diagonal term corresponds to the microcanonical value at the temperature corresponding to energy $\overline{E}$, $\mathcal{O}(\overline{E}) = \operatorname{tr}\left[\rho_{\mathrm{mc}}\hat{O}\right]/\mathcal{Z}$, with $\mathcal{Z}$ the microcanonical partition function. The off-diagonal term is characterized by an exponential decay in system size due to the thermodynamic entropy, by the zero mean and unit variance Gaussian random variable R_{mn} and by an observable-dependent function $f_O(\overline{E}, \omega)$. A fundamental feature of ETH, that distinguishes it from the prediction of random matrix theory, is that it takes into account the *physical* nature of the eigenstates, thus introducing the dependence on energy of the matrix elements, which is essential for an accurate description.

We now use the statement (1.2) to show how it implies thermalization. The long time average of the observable $\hat{O}$ is given by

$$\overline{O} = \lim_{T\to\infty} \frac{1}{T} \int_0^T dt \, \langle\psi(t)| \, \hat{O} \, |\psi(t)\rangle = \sum_m |C_m|^2 O_{mm}, \tag{1.3}$$

where we used the decomposition of the initial state over eigenstates $|\psi_0\rangle = \sum_m C_m \, |E_m\rangle$ and the fact that in the absence of degeneracies only the diagonal term survives in the infinite time limit. Now, upon the reasonable assumption that the initial state has overlap with eigenstates only within a narrow energy shell, the outcome of the time evolution will then coincide with the thermal average given by the microcanonical ensemble in the same energy shell [2, 24]. Through ETH one can also obtain the temporal fluctuations of $\hat{O}$, i.e. the average distance of the instantaneous value from the diagonal ensemble Eq. (1.3), and show that they decay exponentially with system size. As a consequence, the eigenstate thermalization hypothesis provides a condition for *strong* thermalization.

The eigenstate thermalization hypothesis is supposed to hold when the eigenstates of the Hamiltonian are essentially random vectors in the Hilbert space, as it is conjectured to be the case for *chaotic* systems whose level statistics satisfies the Wigner surmise. Bridging the gap between quantum chaos and thermalization, ETH predicts that time-evolution eventually leads to thermal equilibrium in chaotic systems. This implies that physical observables loose *memory* of the initial state, and are determined mainly by the conservation laws encoded in the Hamiltonian.

An additional property of ergodic systems that can be directly obtained from the statement of ETH concerns the entanglement entropy of eigenstates. Let us consider the expectation value of an observable inside a small subsystem A over a thermal eigenstate $|E_m\rangle$, i.e. such that it satisfies (1.2). The expectation value can be obtained through the reduced density matrix $\rho_A = \operatorname{tr}_B |E_m\rangle \langle E_m|$ and it has to correspond to the thermal average. Hence, the reduced density matrix ρ_A is thermal, and its von Neumann entropy is extensive. The von Neumann entropy of the reduced density matrix, however, is by definition (1.1) the entanglement entropy of the eigenstate $|E_m\rangle$. Therefore, ETH implies that thermal eigenstates have entanglement entropy satisfying *volume law*, $S_A \propto \mathrm{Vol}(A)$, increasing with the volume of subregion A (if this region is much smaller than remainder of the system).

As we showed, the connection between ergodicity, chaos, and thermalization provides a powerful Ansatz for the behavior of the eigenstates of thermal Hamiltonians, which was extensively tested numerically [18]. Nevertheless, not all classical models are chaotic, and a natural question in the quantum setting is whether thermalization is the only possible outcome of dynamics. The next section and the remainder of this Thesis are dedicated to investigating situations where thermalization breaks down.

1.1.2 Breakdown of thermalization

As sketched in the previous Section, quantum dynamics in ergodic many-body systems erases the information about the initial state, except for the conservation laws that ultimately define the thermal ensemble entering equation (1.2). However, there exist different universality classes of dynamics, where the initial state influences the outcome of time evolution. It is the case of systems that avoid thermalization via *ergodicity breaking*.

The eigenstate thermalization hypothesis strongly depends on the absence of features of highly excited eigenstates. ETH is essentially a generalization of random matrix theory that takes into account the few global conservation laws present in physical Hamiltonians. While typical quantum many-body systems only have a few conservation laws (energy, particle number etc.), whenever the number of integrals of motion becomes large the eigenstates have too much *structure* to be resemblant of random vectors, and ETH is inapplicable. A different scenario, intermediate between thermalization and strong ergodicity breaking, has recently been discovered [25], called *weak* ergodicity breaking [26].

Weak ergodicity breaking, scars and Hilbert space fragmentation

In systems that feature weak ergodicity breaking, a vanishing fraction of eigenstates present anomalous features, such as a low entanglement entropy, when compared with other eigenstates in their energy surroundings. This suggests the non-thermal nature of these eigenstates as they deviate from the expected volume-law entanglement, within an otherwise fully thermal spectrum. The overwhelming amount of thermal eigenstates would naïvely suggest that the few non-thermal eigenstates, referred to as quantum many-body scars [25, 27, 28, 29, 30, 31], may have little or no effect on dynamics. As it turns out, scars actually significantly influence the dynamics, unexpectedly showing dynamical signatures in the time evolution of simple product states [10, 31].

This property implies that systems presenting weak ergodicity breaking feature typical characteristics of both thermal and non-thermal models. On one hand, average properties generally have thermal nature, due to the overall negligible number of scarred eigenstates. On the other hand, dynamics show a strong state-dependence, typical of non-thermal systems, as states with high overlap with the scarred eigenstates show anomalous behaviors.

Paradigmatic examples of weak ergodicity breaking are given by kinetically constrained models. Initially introduced to describe the behavior of classical glasses [32], kinetically constrained models are characterized by constraints on the kinematic terms, which make them effectively interacting. As an example, we report the Hamiltonian of the celebrated PXP model, obtained as the Schriffer-Wolff transformation [33] of the Hamiltonian governing strongly interacting Rydberg atoms [28] $\hat{H}_{\mathrm{PXP}} = \sum_i \hat{\mathcal{P}}_{i-1}\sigma_i^x\hat{\mathcal{P}}_{i+1}$. In this case, the constraint corresponds to the two projectors on the down spin state, $\hat{\mathcal{P}}_i$, effectively making the model interacting. Kinetically constrained models are characterized by the dynamical disconnection of different sectors of the Hilbert space, the so-called Hilbert space fragmentation [34, 35, 36, 37]. This is due to the emergence of conserved quantities, which effectively reduce the Hamiltonian in block-diagonal form.

Fragmentation can be distinguished in two types, depending on the basis it takes place in [36]. If fragmentation happens in a product state basis, then it is said to be *classical*. In the example above of the PXP Hamiltonian, the configuration where all Rydberg atoms are in the ground state $|\circ\rangle$ is dynamically disconnected from any state containing a pair of neighboring excited states $|\bullet\rangle$, hence $|\cdots\circ\circ\circ\ldots\rangle \not\leftrightarrow |\cdots\circ\bullet\bullet\ldots\rangle$. On the other

hand, if fragmentation takes place in an *entangled* basis then it is called *quantum Hilbert space fragmentation*. Different constraints give rise to different types of fragmentation. If all emerging sectors have $O(1)$ dimension, then thermalization breaks down due to the impossible relaxation to thermal equilibrium in such effectively small systems [38, 39]. When instead some sectors have dimension scaling as the global Hilbert space, one typically observes thermalization within said subsectors. However, even thermalizing subsectors might present anomalous features [40, 41], as described in Section 2.

While the emergence of classical Hilbert space fragmentation is rather well understood and studied, its quantum version still requires a deeper investigation. General mechanisms yielding quantum Hilbert space fragmentations are in fact not completely understood, with very few examples available in the literature [36, 40, 42].

Strong ergodicity breaking and many-body localization

A more dramatic way of avoiding thermalization, where *all* states are non-thermal and dynamics retains local information about the initial state indefinitely in time is strong ergodicity breaking. As mentioned above, it happens whenever an *extensive* number of integrals of motion emerges in the system. A class of systems showing this feature are integrable models [43, 44]. In integrable models, in fact, there is an extensive set of conserved *rapidities* and the system thermalizes to the so-called Generalized Gibbs Ensemble (GGE) [45, 46, 47]. However, integrable models are very sensitive to perturbations, and as such represent fine tuned, zero measure, set in the parameter space where thermalization fails.

Disordered systems, instead, provide a robust way of strong ergodicity breaking, stable to perturbations. Already in the seminal work by Anderson [48] the absence of transport was posed as a possible obstacle to thermal equilibrium. The single particle eigenstates are exponentially localized around each lattice site, hence if localization is stable in presence of interaction it provides a perfect ground to study the absence of thermalization. The first works providing evidence for the perturbative stability of localization to interactions were given in the early 2000s [49, 50]. Ever since, the resulting *many-body localization* (MBL) has attracted significant interest for its peculiar dynamical and spectral properties. Several theoretical [51, 52, 53, 54, 55, 56, 57, 58, 59, 60, 61, 62, 63, 64, 65] and experimental [66, 67, 68, 69, 70, 71, 72] work has thoroughly investigated the main features of MBL, providing evidence for its existence in many different models. Additionally, a number of excellent reviews provide a good survey of the phenomenology of MBL and of open questions [73, 74, 75]. As a paradigmatic example, we write down one of the most commonly used models for the study of many-body localization: the disordered XXZ chain

$$\hat{H} = \frac{J}{2}\sum_i (\sigma_i^+\sigma_{i+1}^- + \text{H.c.}) + \Delta\sum_i \sigma_i^z\sigma_{i+1}^z + \sum_i h_i\sigma_i^z, \tag{1.4}$$

where the random magnetic field $h_i \in [-W, W]$ is uniformly distributed in the range W, setting the disorder strength. It is commonly believed that at strong enough disorder $W > W_c$ the system enters the MBL phase [59, 76, 77, 78].

Inside the many-body localized phase, the breakdown of thermalization is explained in terms of the emergence of quasi-local integrals of motion, also known as LIOMs or l-bits [56, 57, 58]. These are dressed versions of the local degrees of freedom, obtained

through a unitary rotation $\hat{\mathcal{U}}$

$$\hat{\tau}_i^\alpha = \hat{\mathcal{U}}\, \sigma_i^\alpha\, \hat{\mathcal{U}}^\dagger \tag{1.5}$$

which also brings the Hamiltonian in diagonal form. As opposed to ergodic Hamiltonians, where diagonalization implies highly non-local rotations, in the MBL case $\hat{\mathcal{U}}$ can be written as a product over unitary operators of increasing support (2-sites, 3-sites, ...), whose action vanishes exponentially as the distance from site i increases $||\mathbb{I} - \hat{U}_{i,i+1,\dots i+n}||_F < e^{-n/\xi}$, where $||\cdot||_F$ is the Frobenius norm and ξ is commonly interpreted as the localization length. The resulting operators $\hat{\tau}_i^z$ are then integrals of motion, and they keep the local structure of the original degrees of freedom, since the transformation $\hat{\mathcal{U}}$ has exponentially vanishing effect away from i. The Hamiltonian in the diagonal form reads

$$\hat{H}_{\text{MBL}} = \sum_i h_i \hat{\tau}_i^z + \sum_{i,j} J_{ij} \hat{\tau}_i^z \hat{\tau}_j^z + \sum_{i,j,k} J_{ijk} \hat{\tau}_i^z \hat{\tau}_j^z \hat{\tau}_k^z + \dots, \tag{1.6}$$

where each coupling constant decays exponentially as the largest distance among the LIOMs involved in the n-th term $J_{i_1 i_2 \dots i_n} \approx \exp(-\max_{n,m} |i_m - i_n|/\kappa)$.

The Hamiltonian written in this way and the emergence of the quasi-local integrals of motion has dramatic consequences which can directly explain many features of the phenomenology of MBL. First, as in the LIOMs basis the Hamiltonian is diagonal, each eigenstate is fully determined by a LIOMs-string $\{\tau_i^z\}$ and the main energy contribution comes from the random potential h_i. Hence, to obtain two similar energies one typically needs to reshuffle many τ^zs in the two strings defining the eigenstates, thus explaining the observed Poissonian level statistics and absence of level repulsion [51, 53]. Additionally, the exponentially vanishing overlap of far away LIOMs implies that correlations are short-ranged in MBL eigenstates. As a consequence, upon splitting the system in two halves, only the LIOMs in the vicinity of the bipartite cut retain information about the other subsystem and can contribute to entanglement entropy, thus explaining the area-law entanglement typical of many-body localized eigenstates [56, 79].

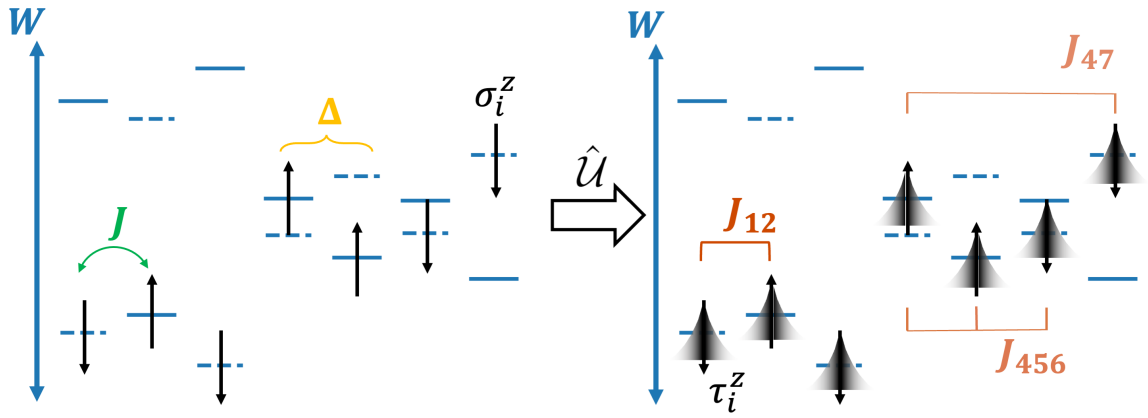

Figure 1.2: Cartoon picture of the disordered XXZ chain and its transformation to the MBL Hamiltonian. Before the transformation the spins can flip with amplitude $J/2$ and interact locally with coupling strength Δ. After the transformation the LIOMs are quasi-local, with exponential tails, and interact through the $2, 3 \dots n$-body terms $J_{i_1 \dots i_n}$.

Besides these *spectral* properties of MBL, which can be probed through exact diagonalization on small systems and used as evidence for the existence of the MBL phase, the localized nature of the Hamiltonian (1.6) has consequences also on the dynamics. As the

integrals of motion have a large overlap with the local degrees of freedom, one expects the time-evolution from a product state to retain memory of the local information for indefinitely long times. This intuition can be probed, both numerically and experimentally, through the so-called imbalance $I(t)$, an observable that quantifies how *far* the time-evolved state is from the initial state [66]. Typically, the system is initialized in a density wave pattern, such that all odd sites are occupied and all even are empty, then the imbalance is defined as

$$I(t) = \frac{N_o(t) - N_e(t)}{N_o(t) + N_e(t)}, \quad \hat{N}_o = \sum_{i \text{ odd}} \hat{n}_i, \quad \hat{N}_e = \sum_{i \text{ even}} \hat{n}_i. \tag{1.7}$$

A saturating imbalance to a finite value, then, indicates absence of thermalization.

A second dynamical probe of MBL, which is a hallmark of this phase, is the logarithmic growth of entanglement entropy [55, 68, 80]. Again this characteristic property can be understood in terms of the Hamiltonian (1.6) through the following thought experiment [55, 57]. Let us initialize the system in a product state in the LIOMs basis, the state will then acquire entanglement due to the interaction among different integrals of motion. This interaction can be viewed as an effective field $\tilde{h}_{i,i+x}$ representing the coupling with LIOMs within a distance x from site i. The time evolution then will yield a precession of the LIOM at site i governed by $e^{-\imath \tilde{h}_{i,i+x} t}$, and this will become relevant for entanglement at a time $t(x)$ where the phase is of order one. As the effective field depends on the interaction strengths, and these decay exponentially away from i, one can write $\tilde{h}_{i,i+x} \sim J_0 e^{-x/\xi'}$. Hence the condition for two LIOMs to be correlated by the time-evolution, $\tilde{h}_{i,i+x} t(x) \sim 1$, yields

$$x_{\text{corr}}(t) = \xi' \log(J_0 t), \quad S(t) \propto \xi' \log(J_0 t). \tag{1.8}$$

We notice that, besides the fundamental logarithmic growth of entanglement, this construction also predicts saturation of entanglement from a quench to a value proportional to the system size. The entanglement entropy in a quench then presents volume-law, as opposed to eigenstates, albeit saturation is approached in an extremely slow fashion.

In spite of the good understanding of the MBL phenomenology reached thanks to the description sketched above, there are still numerous open questions in the field. Most of the theoretical and numerical work is limited to one dimension, where the stability of the sequence of local rotations diagonalizing the Hamiltonian is proved to the mathematical level of rigour under mild and physically reasonable assumptions [60]. In higher dimensions, instability of MBL has been conjectured due to the so-called *avalanche scenario* [62]. In this picture, a rare region of weak disorder, whose presence is almost certain in the thermodynamic limit, becomes locally ergodic. As a consequence, it delocalizes neighboring degrees of freedom, increasing its size and its *thermalizing* effect. While in one dimension this mechanism can be stopped if disorder is strong enough, in 2d the avalanche scenario would predict that the geometry of the system leads to an unbounded growth of the ergodic region, eventually delocalizing the whole chain. This conjecture is however not proven, and the fate of MBL in two dimensions remains an open question. Few numerical simulations have shown that indeed localization might be harder to obtain in 2-dimensional systems [81], detecting a larger critical disorder as the width of a quasi-one-dimensional chain is increased. However, the stability of MBL in 2d is still a debated topic, with experimental work showing signatures of localization in 2-dimensional lattices [82, 83], in contrast with the predictions of the avalanche scenario.

Another discussed topic is the existence of many-body mobility edges. A mobility edge is an energy value separating localized from delocalized parts of the spectrum [84], and its

presence implies that thermal and MBL eigenstates can coexist in the same Hamiltonian. An argument similar to the avalanche scenario was used in Ref. [85] to suggest the absence of many-body localization in presence of a mobility edge, while earlier studies had predicted its existence [50] and confirmed numerically the coexistence of localized and thermal regions of the spectrum [59]. Section 3 deals with this open question, presenting the results of our work [86] which shows stability of many-body mobility edges in particle density.

Similarly unclear is the fate of a many-body localized system coupled to a small thermal bath. One outcome of such coupling is the possibility of localizing the bath through the interaction with the many-body localized degrees of freedom, a phenomenon proposed in Ref. [61] and named many-body localization proximity effect. Several attempts have focused on the fate of the localized system coupled with the bath [87, 88], using different approaches and showing different results depending on the way the bath is modelled. Inspired by the experimental work of Refs. [70, 72], Chapter 4 investigates the dynamical properties of a small bath, showing evidence of many-body localization proximity effect [65, 89] at strong disorder and coupling, for a system of Anderson localized particles interacting with a small bath including a single degree of freedom.

Finally, recent years have seen an active debate about the finite size effects influencing the study of many-body localization [90, 91, 92, 93, 94]. Numerical results on small systems have suggested a possible drifting of the critical disorder with system size, yielding an infinite critical disorder in the thermodynamic limit. This is however in contrast with the mathematical proof of John Imbrie [60], and with established experimental evidence in systems beyond the reach of exact numerical simulations [66, 68]. This debate is very hard to settle, due to the limited system sizes available to exact numerics and to the absence of reliable analytic schemes beyond phenomenological renormalization group techniques [63]. The significant influence of finite size effects then demands an effort in finding new numerical methods, able to study large systems.

1.2 State of the art numerical methods for the study of large many-body systems

The improvement of technological resources together with the advance in numerical techniques have led in the last decades to an increased understanding of out-of-equilibrium physics. Oftentimes however, as discussed at the end of the last section, a correct interpretation of the numerical simulations requires to overcome finite size effects and extrapolate results to the thermodynamic limit. Due to the exponential increase of the Hilbert space with system size, this task represents one of the biggest challenges in modern quantum many-body physics and requires finding numerical methods capable of pushing forward the investigation of large systems. Therefore, the development of new techniques is an active field of research in quantum many-body physics.

1.2.1 Exact diagonalization and related methods for the study of states and time-evolution

We can roughly split the existent numerical methods into those which focus on finding (parts of) the eigenstates, and those which target the time-evolution. One method,

however, gives access to both simultaneously: exact diagonalization (ED). As the name suggests, ED numerically diagonalizes the Hamiltonian, returning the whole spectrum $\{|E_m\rangle, E_m\}$, which allows the study of dynamics of any initial state $|\psi_0\rangle$

$$|\psi_0\rangle = \sum_m \langle E_m|\psi_0\rangle |E_m\rangle \quad \Rightarrow |\psi(t)\rangle = e^{-\imath \hat{H} t}|\psi_0\rangle = \sum_\alpha \langle E_m|\psi_0\rangle e^{-\imath E_m t}|E_m\rangle . \tag{1.9}$$

Exact diagonalization however is limited by the size of the Hamiltonian, whose growth quickly makes the problem intractable due to the exponential increase in system size of the Hilbert space.

Going beyond this limitation then requires some additional effort, often guided by the knowledge of the physical system under investigation. One can take advantage of the sparse nature of local Hamiltonians and keep only the relevant information. In Hamiltonians with strictly local interactions, each basis state is typically connected through the Hamiltonian to $\sim O(L)$ other states, thus the amount of information that needs to be stored scales as $\sim O(L2^L)$ as opposed to 2^{2L} required for the full Hamiltonian, reducing drastically the memory requirements. One can then use iterative algorithms, such as the Arnoldi or Lanczos methods, to obtain extremal eigenvalues and eigenvectors of the Hamiltonian. However, in non-equilibrium settings highly excited eigenstates are often the target and in the middle of the spectrum the above mentioned methods become more challenging due to the exponentially small level spacing. Typical workarounds consist in spectral transformations that *move* the relevant part of the spectrum to the edges, such that iterative algorithms can be used. One way of obtaining this result is through the so-called *shift-invert* transformation [59, 95]

$$\hat{G} = (\hat{H} - \sigma \mathbb{I})^{-1} \tag{1.10}$$

where eigenvalues of the Hamiltonian close to the target energy σ are moved to the edges of the spectrum of $\hat{G}$. Additionally, the spacing among energy levels gets increased, thus improving the performance of iterative algorithms. An alternative way recently proposed, the polynomially filtered exact diagonalization (POLFED), uses an expansion of the spectrum in Chebyshev polynomials, which also proved efficient in obtaining internal eigenstates [96, 97]. The main bottleneck in this methods is still given by the size of the matrices involved, which limits the applicability to system sizes $L \lesssim 30$.

In the direction of time-evolution similar methods rely on Krylov subspace techniques, used also by the Arnoldi and Lanczos algorithms. Their application to dynamics basically consists in writing the time-evolution operator $\hat{U}(t) = \exp\left(-\imath \hat{H} t\right)$ in a Krylov subspace of dimension m

$$\mathcal{K}_m = \{|v_0\rangle, \hat{H}|v_0\rangle, \hat{H}^2|v_0\rangle, \ldots, \hat{H}^{m-1}|v_0\rangle\}, \tag{1.11}$$

related to a given state $|v_0\rangle \in \mathcal{H}$, and where $m \ll \mathcal{D}$ with $\mathcal{D}$ the dimension of the Hilbert space $\mathcal{H}$. Then one defines the Hamiltonian restricted to the Krylov subspace $\hat{H}_m = \hat{H}|_{\mathcal{K}_m}$ and use it to construct the time-evolution operator $\hat{U}_m$ [98]. The matrix vector multiplication $|\psi(t+\delta t)\rangle = \hat{U}(\delta t)|\psi(t)\rangle$, demanding due to the dense nature of $\hat{U}$, is then replaced by the much cheaper operation $|\psi(t+\delta t)\rangle \approx \hat{V}_m^\dagger \hat{U}_m(\delta t)\hat{V}_m|\psi(t)\rangle$, where the matrix $\hat{V}_m$ embeds the state in the Krylov subspace and $\hat{V}_m^\dagger$ brings it back to the full Hilbert space. This powerful method is limited by the memory requirements on the Hamiltonian similarly to the ones used to obtain the spectrum, thus limiting the investigation to system sizes up to $L \lesssim 30$.

1.2.2 Matrix product states approach to eigenstates and dynamics

The methods described above are relatively general, as they rely only on the sparseness of the Hamiltonian. However, over the last decades, an alternative approach which takes into account some additional physical intuition has proved to be extremely efficient: tensor network techniques. The main intuition is that the whole Hilbert space contains an amount of information which is irrelevant for most of the physical observables. This information is naturally encoded in the entanglement properties of the states, with the entanglement entropy and entanglement spectrum determining whether a state is *compressible*, i.e. if it can be represented in a more compact way without loosing relevant physical information. An efficient way of retaining in the wavefunction only the significant information, then, can result in a dramatic decrease of the computational costs. Tensor network methods deal exactly with this issue, using the concept of entanglement, as defined at the beginning of this chapter, to determine how to approximate the description of quantum states in an efficient, yet accurate, way.

The efficient compression of the significant information shows its best results in one dimension, where it takes the name of *matrix product states* (MPS) [99, 100, 101, 102]. Analogous generalizations to 2-d (*projected entangled pair states*-PEPS) also exist [103, 104, 105, 106], although they are currently far less efficient. We will then focus on one dimensional MPS. A one dimensional wavefunction $|\psi\rangle$ can be decomposed over a local product states basis $\{|\sigma_i\rangle\}_{i=1,\dots,L}$, where each local degree of freedom σ_i can take up to p values ($p = 2$ for spin-1/2 systems). In this basis the state reads

$$|\psi\rangle = \sum_{\{\sigma\}} C_{\sigma_1,\sigma_2,\dots,\sigma_L} |\sigma_1\sigma_2\dots\sigma_L\rangle \,. \tag{1.12}$$

The p^L coefficients C can be interpreted as a rank-L tensor, where each index can take up to p values. To obtain the compressed MPS form, one then performs a series of singular value decompositions (SVD) on the tensor C, transforming it in a product of local tensors. We illustrate for clarity the first two steps of this process. In the first step, the indices $(\sigma_2, \dots, \sigma_L)$ are grouped together transforming C in a rectangular matrix of dimension

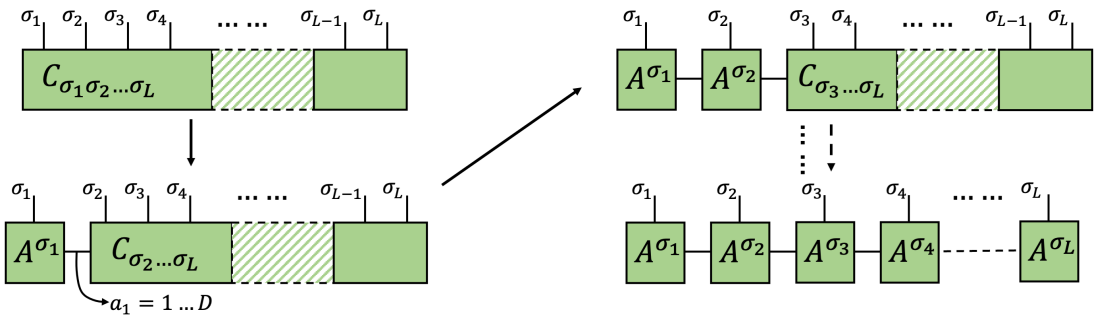

Figure 1.3: Diagrammatic representation of the series of transformations bringing the wavefunction in MPS form. Each rectangle corresponds to a tensor, whose rank is determined by the number of *legs* sticking out of it. Legs connecting different tensors represent contracted indices, as for instance the bond indices $a_1 \dots a_L$.

$p \times p^{L-1}$ on which an SVD is performed

$$C_{\sigma_1,(\sigma_2,\ldots,\sigma_L)} = \sum_{a_1=1}^{\min(\mathcal{D}_1,\mathcal{D}_{2\ldots L})} U_{\sigma_1,a1} S_{a1,a1} V^{\dagger}_{a1,(\sigma_2,\ldots,\sigma_L)} = \sum_{a_1=1}^{\min(\mathcal{D}_1,\mathcal{D}_{2\ldots L})} U_{\sigma_1,a1} C_{a1\sigma_2,(\sigma_3,\ldots\sigma_L)}, \tag{1.13}$$

where $\mathcal{D}_1, \mathcal{D}_{2,\ldots,L}$ are the Hilbert space dimensions of the two subsystems, and in the last equality we multiplied the matrices S and $V^{\dagger}$ and reshaped them in a matrix of dimensions (p^2, p^{L-2}). After renaming the matrix $U_{\sigma_1,a1} = A^{\sigma_1}$, we proceed with the second step

$$C_{a1\sigma_2,(\sigma_3,\ldots,\sigma_L)} = \sum_{a_2=1}^{\min(\mathcal{D}_2,\mathcal{D}_{3\ldots L})} U_{a1\sigma_2,a2} S_{a2,a2} V^{\dagger}_{a2,(\sigma_3,\ldots,\sigma_L)} = \sum_{a_2=1}^{\min(\mathcal{D}_2,\mathcal{D}_{3\ldots L})} U_{a1\sigma_2,a2} C_{a2\sigma_3,(\sigma_4,\ldots\sigma_L)}, \tag{1.14}$$

and again we rename the rank-3 tensor $U_{a1\sigma_2,a2} = A^{\sigma_2}_{a_1,a_2}$. It is clear then, that repeating this operation until the opposite boundary we can write the state as

$$|\psi\rangle = \sum_{\{\sigma\}} \sum_{a1,\ldots,a_{L-1}} A^{\sigma_1}_{a_1} A^{\sigma_2}_{a1,a2} \ldots A^{\sigma_{L-1}}_{L-2,L-1} A^{\sigma_L}_{a_{L-1}} |\sigma_1 \ldots \sigma_L\rangle . \tag{1.15}$$

So far, this description is exact, and as such it does not provide any advantage with respect to the initial representation of the state (1.12). The key point here is that the auxiliary dimension introduced, the *bond dimension* D related to the values the indices a_n can take, can be limited to a maximal cutoff $\chi \ll \mathcal{D}$. This can be justified whenever the *singular values*, i.e. the diagonal entries of the matrix S_{a_n,a_n}, decay fast enough, such that truncating the matrix to a given bond dimension has very little effect on the state. Thanks to this insightful observation, the global complexity of the wavefunction can be reduced from p^L to a much more manageable pLD^2, i.e. *polynomial* in system size. This great gain in efficiency comes at a cost, namely the limitation on the amount of entanglement one can represent with such a wavefunction. It can be shown that the entanglement entropy of the bipartite cut i is given exactly by the Shannon entropy of the squared singular values of the matrix S_{a_i,a_i} resulting from the SVD at site i

$$S = -\sum S^2_{a_i,a_i} \log\left(S^2_{a_i,a_i}\right). \tag{1.16}$$

Hence, for a matrix of bond dimension D, one obtains $S \leq \log(D)$, which in turn implies that the bond dimension required to describe a system depends exponentially on its entanglement entropy.

The MPS representation of the wavefunction can be used, similarly to exact diagonalization, to obtain both eigenstates and time-evolution. Its limitation is not the system size, however, as the scaling of the complexity is only linear in L, but rather the bond dimension, which limits the efficient and accurate MPS description to quantum states whose entanglement corresponds to a treatable D. Nevertheless, this is still a very powerful ansatz, as many physically relevant states happen to have area-law entanglement, as it is the case for ground states of gapped local Hamiltonians [107] or for the eigenstates of MBL Hamiltonians (see Section 1.1.2). A typical approach to obtain ground states in MPS form is to use the celebrated density matrix renormalization group (DMRG) algorithm [108] applied to matrix product states representations of the wavefunction [109]. The Hamiltonian is minimized locally, taking into account only two physical degrees of freedom at a time, and keeping the remainder of the system as a left and right *environment*. After each local energy minimization, the MPS form is restored through an SVD and the left and

right environments updated. The algorithm then consists of *sweeps* through the chain from left to right and vice versa until convergence is reached. The key to the success of DMRG applied to MPS Ansätze is that it allows studying system sizes well beyond the limits of the methods described above, thanks to the linear scaling in system size of the complexity. Additionally, if the system is translationally invariant, the infinite DMRG algorithm can be applied, thus allowing the study of ground state properties directly in the thermodynamic limit. When highly excited eigenstates of the Hamiltonian are also weakly entangled, the DMRG method can be applied to transformations of the Hamiltonian, such as the shift-invert defined above. This eigensolver for highly excited eigenstates, called DMRG-X [110, 111, 112], is particularly useful in many-body localized Hamiltonians, where it can provide spectral properties deep in the MBL phase. The drawback, however, is that the DMRG-X algorithm cannot be applied through the phase transition, as approaching the critical disorder eigenstates' entanglement starts growing with system size.

Besides their use in determining area-law entangled eigenstates, matrix product states can be used to simulate the time-evolution of the system, as long as the entanglement generated is low. Again, MBL provides a good ground for application of MPS methods, as the logarithmic growth of entanglement implies an algebraic growth in time of the bond dimension, thus allowing the study of dynamics on relevant timescales. We identify two main algorithms for the dynamics of matrix product states, the time-dependent variational principle (TDVP) [113] and the time-evolving block decimation (TEBD) [114]. The latter, in particular, is the method of choice in the works presented in this thesis.

The time-dependent variational principle *projects* the dynamics onto a manifold of fixed bond dimension χ, where it solves the time-dependent Schrödinger equation. As such, the time-evolution is exactly unitary, and preserves the norm and all conserved quantities, as opposed to TEBD. Additionally, it can be directly used to study the dynamics of long-range Hamiltonians. Nevertheless, the projection of the dynamics introduces a weakly controllable source of error, thus requiring running several bond dimensions until convergence is reached.

The time-evolving block decimation is best suited for short range Hamiltonians, where the action of the time-evolution operator can be split into different sets of *gates* whose elements are commuting with one another. The continuous time-evolution is then approximated via a Suzuki-Trotter decomposition [115] of n-th order with time-step δt. The resulting local gates are applied to the MPS, and after each application the MPS form is restored through a singular value decomposition. To obtain accurate results, one needs to employ a higher order decomposition, as the error scales as δt^n, which in turn requires an increasing number of local gates applications, reducing the efficiency. However, as long as the time-step is small enough and the truncation error arising from the discarded singular values in the SVD are controlled, TEBD provides a quasi-exact method for the time-evolution.

1.3 Author's contributions

As outlined above, there are numerous open questions in the field of nonergodic quantum many-body systems. In this Thesis, we present original research results obtained on several interrelated topics. In particular, in the first part of the thesis we focus on kinetically constrained systems, investigating the nature of fragmentation and its effects on dynamics. Next, in Chapter 3, we study the interplay of constraints and disorder, using the resulting

system to analyze the many-body mobility edge. Finally, in Chapter 4, we present our results concerning the interplay of localized and thermal degrees of freedom, showing evidence for the MBL proximity effect in large systems and studying its stability.

1.3.1 Kinetically constrained models

The first Chapter is based on the results of Ref. [40]. There, we introduce a class of particle-conserving kinetically constrained models, characterized by inversion-symmetry breaking constraints. We analyze the structure of the Hilbert space, observing the expected *classical* fragmentation. A careful inspection of the largest subsector of the Hilbert space however reveals the presence of *quantum* Hilbert space fragmentation, a phenomenon far less understood and observed only in few models [36, 42].

We present an analytical construction of the states yielding quantum Hilbert space fragmentation, where the combination of $U(1)$ symmetry and chiral constraints plays a crucial role. We conjecture that the interplay of these symmetries provides a generic way of realizing quantum fragmentation. The further investigation of the system's dynamics reveals signatures of quantum fragmentation in the time-evolution of local observables in quenches from simple product states.

Studying transport within the largest subsector of the classically fragmented Hilbert space we observe transient superdiffusive transport followed by a slow, logarithmic, behavior, that we intuitively understand from the structure of the Hamiltonian representing the allowed transitions. Finally, implementing the same constraint in a classical cellular automaton we find signatures of ballistic dynamics on short timescales, before the logarithmic spreading of density arises at later times.

1.3.2 Many-body mobility edges

In Chapter 3 we present the results obtained in [86], where we dealt with the problem of stability of many-body mobility edges in disordered interacting systems. As mentioned in Section 1.1.2, the coexistence of thermal and localized eigenstates in the spectrum was conjectured to destabilize many-body localization [85]. In this work, we introduce a model of hard-core bosons where the interaction is mediated by a correlated hopping. The model is designed in such a way that the interplay of the free and constrained hopping, and of the disorder, leads to a many-body mobility edge in particle density.

The mobility edge in particle density allows a much easier and deterministic access to localized and thermal parts of the spectrum, a property we take advantage of directly simulating the time-evolution of states belonging to different sectors of the spectrum. In particular, we use both Krylov time-evolution and tensor network techniques to study the dynamics generated by the constrained Hamiltonian. Our results show stable coexistence of localization within the MBL part of the spectrum, together with thermalizing eigenstates at higher particle densities. Additionally, we probe the mechanism proposed in Ref. [85] as a source of delocalization, showing evidence of absence of the predicted motion of locally ergodic regions in our model.

1.3.3 Many-body localization proximity effect

The concluding part of this Thesis, Chapter 4, is dedicated to [65, 89], where we study many-body localization proximity effect [61], inspired by recent experimental work [70, 72].

A key difference between our work and related previous literature [61, 87, 88] consists in the fact that we probe both the stability of MBL and the eventual localization of the small bath, whereas earlier work mainly focused on properties of the system as a whole, detecting localization or thermalization of the mixture of bath and localized particles. To achieve this goal, we introduce a model with two species of hard-core bosons, of which one is Anderson localized and the second one is free. Our model can be viewed as a fermionic Hubbard model, where disorder affects only one spin direction and spin is conserved. We then analyze the fate of the system once the interaction among the two species is turned-on.

We first study the system in a mean field approximation, resulting in localization of the bath. Building on this, we obtain an analytical criterion for the stability of localization to the most relevant two-body processes induced by the interaction. This result suggests stability of proximity effect at strong coupling strengths. We then numerically study this particular case, first with an approximate method and later with quasi-exact time-evolving block decimation [114]. While the approximate method shows signatures of thermalization, tensor networks simulation show instead convincing evidence of the MBL proximity effect, on system sizes well beyond the ones achievable with exact diagonalization. Additionally, we observe a characteristic inhomogeneous entanglement growth, which we explain through a phenomenological theory. We finally obtain highly excited eigenstates through the DMRG-X algorithm [110, 111, 112] and find clear signatures of localization of the bath together with strong dependence of the entanglement entropy on the localization center of the free particle. Effectively probing the infinite time regime, the study of eigenstates provide complementary evidence for the findings presented in the analysis of dynamics.

Lowering interaction strength, we observe signatures of delocalization of the bath using extremely large systems $L \approx 200 \div 2000$ sites. Investigating the dynamical behavior of the bath, we report a crossover from localization at strong coupling, to subdiffusion at intermediate values and finally diffusion as the interaction strength is decreased further. Interestingly, the delocalization of the bath affects also the Anderson localized particles, although on extremely long timescales, whose investigation remains beyond our current capabilities.

Finally, we study the behavior of the system as the density of particles composing the bath is changed. At large density close to half filling we observe delocalization of both types of particles, characterized by diffusive transport observed in the dynamics of density matrices close to infinite temperature. As the coupling is reduced, and the localized phase is approached, a subdiffusive behavior arises in the transport of the disordered particles. Further reducing the density of particles in the bath shows an enhancement of localization, which is eventually restored at very low densities.

1.4 Outlook

The results presented in this thesis and summarized above investigate various aspects of ergodicity breaking in quantum many-body physics. In particular, we demonstrated the existence of many-body mobility edges in large system [86], providing evidence in favor of the stability of MBL in presence of mobility edges [59, 71, 85]. Additionally, we thoroughly investigated the topic of many-body localization proximity effect [61], presenting the first results beyond the limits of exact diagonalization [65, 89]. Although not directly related, our results on localization in extremely large systems also provide evidence suggesting

the stability of MBL in the thermodynamic limit. Our work then contributes also to the understanding of finite size effects in the many-body localized phase and of the fate of localization as $L \to \infty$ [90, 92, 93, 94].

Regarding the rich field of kinetically constrained models, our work [40] poses new intriguing questions regarding the existence of new transport universality classes related to different types of constraints, a topic also addressed in [41, 116]. Furthermore, the observation of quantum fragmentation in our model and our analytical understanding of it providing interesting insight in the description of this phenomenon.

Throughout this work, we mainly focus on the investigation of isolated systems described by time-independent Hamiltonians. Beyond this paradigm, however, a large amount of fascinating phenomena have recently been discovered. In periodically driven Floquet systems, whenever the energy absorption can be suppressed, novel phases can arise with no counterpart in the Hamiltonian scenario. A particular example is provided by the time-crystal, recently realized in simulations and experiments [14, 117] thanks to an underlying MBL phase. A similar new phase is the anomalous Floquet insulator [118], where the localized phase yields an insulating bulk coexisting with extended wavefunctions on the boundaries. These examples highlight how the combination of ergodicity breaking and periodic driving can lead to the emergence of novel phases of matter with no counterpart in the time-independent setup. A particularly exciting direction may be the study of phenomena enabled by *weak* ergodicity breaking and Floquet driving in the setting of kinetically constrained models, where one can expect state-dependent dynamical behaviors and possibly different phases.

In a similar direction, recent studies have explored the behavior of systems coupled with the external environment, and in particular subject to measurements. This line of research has established a new type of phase transition, which affects the entanglement properties of the system [119, 120, 121]. This setup can be further explored in search of new physics arising due to the effects of the interaction with the external world. Furthermore, on a more applied side, several proposals have suggested to use this setup to *navigate* through the Hilbert space [122], a direction with potential application in experiments, where preparing complex states is a hard task.

Finally, despite great advance in numerical techniques, accessing large system sizes still remains one of the main obstacles in settling many debated topics, such as the significant finite system size effects affecting MBL. In this context, the ever increasing effort of the community in developing better quantum devices keeps making more real the promise of reliable quantum computing in the not-too-far future [9, 10, 16, 123]. The development of quantum computing requires a deeper understanding of the laws governing the behavior of qubits in these setups, which are often not ideal and affected by noise and other effects of the coupling with the environment. As a consequence, the study of non-equilibrium quantum many-body physics in its general sense, including open systems and time-dependent Hamiltonians, is a fundamental step for the advancement of fundamental and technological purposes.

CHAPTER 2

Hilbert space fragmentation and slow dynamics in particle-conserving quantum East models

In this Chapter, we investigate the effect of kinetic constraints on the dynamics of many-body quantum systems. We introduce a pure kinetically constrained model, where the Hamiltonian only contains correlated hopping terms. We analyze the spectrum of the Hamiltonian, observing both classical and quantum Hilbert space fragmentation. Next, we show dynamical signatures of quantum Hilbert space fragmentation in the time-evolution of simple product states. Finally, we present the anomalous transport properties of the domain wall initial state in this model, namely a transient superdiffusive dynamics followed by logarithmic behavior. This Section is based on

Brighi P., Ljubotina M. and Serbyn M. "Hilbert space fragmentation and slow dynamics in particle conserving quantum East models," arXiv:2210.15607 (2022)

2.1 Introduction

In recent years, kinetically constrained models, originally introduced to describe classical glasses [32, 124, 125], have received considerable attention in the context of non-equilibrium quantum dynamics [116, 126, 127, 128, 129]. In analogy with their classical counterparts, they are characterized by unusual dynamical properties, including slow transport [116, 130, 131, 132, 133, 134], localization [35, 64, 135] and fractonic excitations [136, 137]. Additionally, in the quantum realm, other interesting phenomena have been observed, such as Hilbert space fragmentation [34, 35, 37, 42, 138, 139, 140, 141] and quantum many-body scars [25, 29, 142, 143, 144].

Among the many possible types of constraints, one can distinguish models that are inversion symmetric from those that break inversion symmetry. Among the latter models, the so-called quantum East model [129, 135, 145, 146, 147, 148] where spin dynamics of a given site is facilitated by the presence of a particular spin configuration *on the left* represents one of the most studied examples. The quantum East model has been shown to host a localization-delocalization transition in its ground state [135], which allows the approximate construction of excited eigenstates in matrix product state form. Transport

in particle-conserving analogues of the East model was recently investigated through the analysis of the dynamics of infinite-temperature correlations, revealing subdiffusive behavior. A similar result has also been observed in spin-1 projector Hamiltonians [149].

The interplay of particle conservation and kinetic constraints that break inversion symmetry opens several interesting avenues for further research. First, the phenomenon of so-called Hilbert space fragmentation that is known to occur in constrained models and is characterized by the emergence of exponentially many disconnected subsectors of the Hilbert space is expected to be modified. The additional $U(1)$ symmetry is expected to influence Hilbert space fragmentation beyond the picture presented in previously studied models [129, 135, 145]. Second, the presence of a conserved charge allows the study of transport [116, 133, 134]. While transport without restriction to a particular sector of fragmented Hilbert space results in slow subdiffusive dynamics [116, 133], a recent work [41] demonstrated that a restriction to a particular sector of fragmented Hilbert space can give rise to superdiffusion. This motivates the study of transport in the particle conserving East model restricted to a particular sector of the Hilbert space.

In this work, we investigate a generalized East model, consisting of hard-core bosons with constrained hopping. The constraint prevent hopping in the absence of bosons on a few preceding sites *to the left*. The chiral nature of such facilitated hopping strongly breaks inversion symmetry, akin to the conventional East model, additionally featuring the conservation of the total number of bosons. Our results show that combining charge conservation and the breaking of inversion symmetry yield new interesting transport phenomena. Specifically, we characterize the proposed generalized East model using its eigenstate properties and dynamics. The detailed study of the eigenstates reveals so-called quantum Hilbert space fragmentation, so far reported only in a few other models [36, 42]. The quantum fragmentation we observe in our model leads to the existence of eigenstates that have zero entanglement along one or several bipartite cuts. The number of these low entanglement eigenstates increases exponentially with system size. We find that these unusual eigenstates can be constructed recursively, relying on special eigenstates existing in small chains that are determined analytically. Thus the particle-conserving East model provides an example of *recursive quantum* Hibert space fragmentation.

The study of dynamics of the particle-conserving East model reveals that weakly entangled eigenstates existing in the spectrum can be probed by quenches from simple product states. In addition, the dynamics from a domain wall initial state reveals two distinct transport regimes. At short times dynamics is superdiffusive, whereas at longer times the constraint leads to a logarithmically slow spreading. We recover the logarithmically slow dynamics within a classically simulable cellular automaton that has the same features as the Hamiltonian model. In contrast, the early time dynamical exponent differs between the quantum Hamiltonian dynamics and the cellular automaton. Additionally, the transport properties show signatures of dependence on the density of particles in the leftmost part of the chain of the initial state. These unusual results call for a more detailed exploration and better understanding of the reported superdiffusive dynamics and its stability in the thermodynamic limit. This invites the systematic study of such models using large scale numerical methods and development of a hydrodynamic description of transport in such systems.

The remainder of the paper is organized as follows. In Section 2.2 we introduce the Hamiltonian of the particle-conserving East model and explain the effect of the constraint. We then investigate the nature of the Hilbert space fragmentation and of the eigenstates

in Section 2.3. In Section 2.4 we investigate the dynamical properties of the system, showing similarities in the long-time behavior among the quantum dynamics and the classical cellular automaton. Finally, in Section 2.5, we conclude by presenting a summary of our work and proposing possible future directions.

2.2 Family of particle-conserving East models

We introduce a family of particle conserving Hamiltonians inspired by the kinetically constrained East model in one dimension. The East model, studied both in the classical [32, 148] and quantum [135, 145, 147] cases, features a constraint that strongly violates inversion symmetry: a given spin is able to flip only if its *left* neighbor is in the up (↑) state. A natural implementation of such a constrained kinematic term in the particle-conserving case is a hopping process *facilitated* by the presence of other particles on the left. The simplest example of such a model is provided by the following Hamiltonian operating on a chain of hard-core bosons,

$$\hat{H}_{r=1} = \sum_{i=2}^{L-1} \hat{n}_{i-1}\left(\hat{c}_i^\dagger \hat{c}_{i+1} + \hat{c}_{i+1}^\dagger \hat{c}_i\right), \tag{2.1}$$

where the operator $\hat{n}_i = \hat{c}_i^\dagger \hat{c}_i$ is a projector onto the occupied state of site i. We assume open boundary conditions here and throughout this work, and typically initialize, without loss of generality, the first site as being occupied by a frozen particle. All sites to the left of the leftmost particle, in fact, cannot be occupied, hence they are not relevant to the behavior of the system.

The Hamiltonian (2.1) implements hopping facilitated by the *nearest neighbor* particle on the left, hence we refer to it as the range-1, $r = 1$, particle conserving East model. A natural extension of this model would be hopping facilitated by the nearest *or* next nearest neighbor, which reads:

$$\hat{H}_2 = \sum_{i=2}^{L-1} (\hat{n}_{i-2} + \hat{n}_{i-1} - \hat{n}_{i-2}\hat{n}_{i-1})(\hat{c}_i^\dagger \hat{c}_{i+1} + \text{H.c.}), \tag{2.2}$$

where we treat the operator $\hat{n}_{i=0} = 0$ as being identically zero. Note, that in this Hamiltonian we use the same hopping strength irrespective if the facilitating particle is located on the nearest neighbor or next nearest neighbor site, however this condition may be relaxed. Examples of range-1, $\hat{H}_1$, and range-2, $\hat{H}_2$, particle conserving East models can be further generalized to arbitrary range r as

$$\hat{H}_r = \sum_{i=r+1}^{L-1} \hat{\mathcal{K}}_{i,r}\left(\hat{c}_{i+1}^\dagger \hat{c}_i + \text{H.c.}\right), \tag{2.3}$$

$$\hat{\mathcal{K}}_{i,r} = \sum_{\ell=1}^{r} t_\ell \hat{\mathcal{P}}_{i,\ell} \tag{2.4}$$

where the operator $\hat{\mathcal{K}}_{i,r}$ implements a range-r constraint using projectors on the configurations with $\hat{n}_{i-\ell} = 1$ and the region $[i-\ell+1, i-1]$ empty, $\hat{\mathcal{P}}_{i,\ell} = \hat{n}_{i-\ell}\prod_{j=i-\ell+1}^{i-1}(1-\hat{n}_j)$. The coefficients t_ℓ correspond to the amplitude of the hopping facilitated by the particle located ℓ-sites on the left. The Hamiltonian $\hat{H}_2$ in Eq. (2.2) corresponds to the particular case when all $t_\ell = 1$.

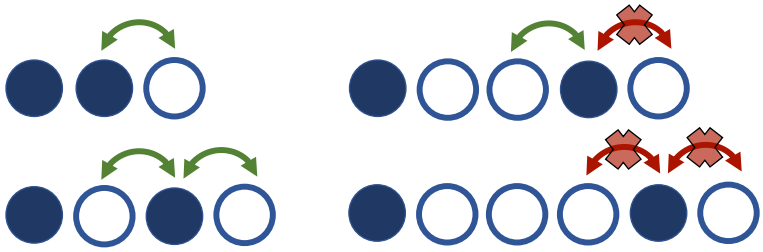

Figure 2.1: Illustration of constrained hopping in the range-2 particle conserving East model.

Models with similar facilitated hopping terms were considered in the literature earlier. In particular a pair hopping $\bullet\bullet\circ \leftrightarrow \circ\bullet\bullet$ was introduced in [85] and later used in [86] to probe many-body mobility edges, and shown to be integrable in Ref. [141]. In [150] a similar constrained hopping term was shown to arise from the Jordan-Wigner transformation of a next nearest neighbor XY spin chain. Another constrained model recently studied is the so-called *folded* XXZ [37, 64], where the $\Delta \to \infty$ limit of the XXZ chain is considered, leading to integrable dynamics [139, 140]. The key difference in our work, compared to the previous literature, consists of having a chiral kinetic term, whereas in the mentioned works symmetric constraints are considered.

Hamiltonians $\hat{H}_r$ for all values of r feature $U(1)$ symmetry related to the conservation of total boson number, justifying the name of particle-conserving East models. In this work we mostly focus on the case of $r = 2$ with homogeneous hopping parameters $t_\ell = 1$, as written in Eq. (2.2). We discuss the generality of our results with respect to the choice of hopping strengths and range of constraint in Appendices A.4 and A.6. A major feature of this family of models is Hilbert space fragmentation, which is known to affect spectral and dynamical properties. As such we begin our investigation by looking into the nature of Hilbert space fragmentation in these models in Section 2.3, where we highlight the generality of our results, by formulating them for a general range r and show examples for $r = 2$.

2.3 Hilbert space fragmentation and eigenstates

In this Section we focus on the phenomenon of Hilbert space fragmentation in the particle-conserving East models introduced above. First, we discuss the block structure of the Hamiltonian in the product state basis — known as a classical Hilbert space fragmentation — and define the largest connected component of the Hilbert space. Next, in Sec. 2.3.2 we discuss the emerging disconnected components of the Hilbert space that are not manifest in the product state basis, leading to quantum Hilbert space fragmentation.

2.3.1 Classical Hilbert space fragmentation

Due to the $U(1)$ symmetry of the Hamiltonian (2.3), the global Hilbert space is divided in blocks labeled by the different number of bosons N_p with dimension given by the binomial coefficient $\mathcal{C}^L_{N_p}$. Within each given sector of total particle number N_p, the constrained hopping causes further fragmentation of the Hilbert space in extensively many subspaces. First, the leftmost boson in the system is always frozen. Hence, as we discussed in Section 2.2, we choose the first site to be always occupied, which may be viewed as a

boundary condition. In addition, a boson may also be frozen if the number of particles to its left is too small. An example configuration is given by the product state $|\bullet\circ\circ\circ\bullet\bullet\circ\circ\rangle$ for the $r=2$ model, where $\circ$ corresponds to an empty site and $\bullet$ is a site occupied by one boson. Here the second boson cannot move since the previous two sites are empty and cannot be occupied.

In view of this additional fragmentation, we focus on the largest classically connected sector of the Hilbert space with a fixed number of particles, N_p. This sector can be constructed starting from a particular initial state $|\mathrm{DW}\rangle$, where all particles are located at the left boundary,

$$|\mathrm{DW}\rangle = |\underbrace{\bullet\bullet\bullet\cdots\bullet}_{N_p}\underbrace{\circ\circ\circ\cdots\circ}_{L-N_p}\rangle. \tag{2.5}$$

Starting from this initial state the constraint will limit the spreading of particles, that can reach at most

$$L_r^*(N_p) = (r+1)N_p - r \tag{2.6}$$

sites, corresponding to the most diluted state, $|\bullet\circ\circ\bullet\circ\circ\bullet\circ\circ\bullet\ldots\rangle$ for $r=2$. Thus, in what follows we use the system size $L = L_r^*$ uniquely defined by the number of particles and the range of the constraint in Eq. (2.6).

The fragmentation of the Hilbert space discussed above may be attributed to a set of emergent conserved quantities in the model in addition to the total particle number, $\hat{N}_{\mathrm{tot}} = \sum_i \hat{n}_i$. The first class of conserved operators responsible for the freezing of the leftmost particle is written as

$$\hat{N}_{\ell_0} = \ell_0\Big[\prod_{i<\ell_0}(1-\hat{n}_i)\Big]\hat{n}_{\ell_0}. \tag{2.7}$$

Since projectors in this operator are complementary to the projectors in the Hamiltonian, this satisfies the property $\hat{N}_{\ell_0}\hat{H}_r = \hat{H}_r\hat{N}_{\ell_0} = 0$, hence trivially having a zero commutator. This conservation law induces further fragmentation of the Hilbert space into $L - N_p$ sectors labeled by the position of the leftmost boson.

The second class of operators yields a further fragmentation within each sector with fixed position of the leftmost particle. Bearing in mind that the leftmost compact cluster of $\tilde{N}$ particles cannot expand farther than $\tilde{L} = L_r^*(\tilde{N})$, one can realize that if $r+1$ sites or more are left empty to the right of $\tilde{L}$ then the chain is dynamically separated into two independent regions. The $\tilde{N}$ particles on the left cannot spread to the right side $i \geq \tilde{L}+r$ as well as the leftmost particle on the right cannot move to the left as the constraint is never fulfilled. The simplest example of such configuration is given by $|\bullet\circ\circ\bullet\circ\circ\circ\bullet\ldots\rangle$ for $r=2$, $\tilde{N}=2$ and $\tilde{L}=4$. Crucially, the position $\tilde{j} > \tilde{L}+r$ of the first occupied site on the right can be chosen arbitrarily, as long as it satisfies the global constraints of the system. Formally, then, one can define a family of conserved quantities given by the projector $\hat{\mathcal{P}}_{\tilde{N}}$ on configurations with $\tilde{N}$ particles in the leftmost $\tilde{L}$ sites followed by a sufficiently large empty region, and, finally, an occupied site $\tilde{j}$

$$\hat{O}_{\tilde{N}}^{\tilde{j}} = \hat{\mathcal{P}}_{\tilde{N},\tilde{i}}\Big[\prod_{k=\tilde{L}+1}^{\tilde{j}-1}(1-\hat{n}_k)\Big]\hat{n}_{\tilde{j}}. \tag{2.8}$$

The freedom in the choice of $\tilde{j}$ yields $r(N_p-\tilde{N}-1)$ different sectors for a fixed $\tilde{N}$. Hence, the number of fragmented sectors is given by

$$\sum_{\tilde{N}=1}^{N_p-1} r(N_p-\tilde{N}-1) = \Big[\frac{1}{2}(N_p^2-3N_p)+1\Big] \propto N_p^2. \tag{2.9}$$

We notice that additional levels of fragmentation can emerge whenever the right part can be further decomposed in a similar way to the one discussed above. This corresponds to composing two different $\hat{O}^{\tilde{j}}_{\tilde{N}}$ where the second is shifted by $\tilde{j}$ sites. Every time that happens, additional subsectors appear for some of the sectors identified by the operator $\hat{O}^{\tilde{j}}_{\tilde{N}}$. As the number of additional levels of fragmentation increases proportionally to N_p, each adding subsectors to the previous level, one finally obtains that the asymptotic behavior of the global number of classically fragmented subsectors has to be $O(\exp(N_p))$. The exponential increase of the number of disconnected subsectors was verified numerically, thus properly identifying a case of Hilbert space fragmentation. Finally, we notice that in our case, the operators defined in Eq. (2.8) do not commute with each of the individual terms of the Hamiltonian, as in the definition of Ref. [36]. Nevertheless, they define an algebra of conserved quantities whose size grows exponentially with system size.

2.3.2 Recursive quantum Hilbert space fragmentation

Due to the fragmentation of the Hilbert space in the computational basis discussed above, we focus on the largest sector of the Hilbert space as defined in the previous section. In Appendix A.1 we show that the statistic of the level spacing for the Hamiltonian $\hat{H}_2$ within this block follows the Wigner-Dyson surmise, confirming that we resolved all symmetries of this model and naïvely suggesting an overall thermalizing (chaotic) character of eigenstates [18].

To further check the character of eigenstates, we consider their entanglement entropy. We divide the system into two parts, A containing sites $1, \ldots, i$, $A = [1, i]$ and its complement denoted as $B = [i+1, L]$. The entanglement entropy of the eigenstate $|E_\alpha\rangle$ for such bipartition is obtained as the von Neumann entropy of the reduced density matrix $\rho_i = \mathrm{tr}_B \, |E_\alpha\rangle \langle E_\alpha|$

$$S_i = -\,\mathrm{tr}\Big[\rho_i \ln \rho_i\Big]. \tag{2.10}$$

In thermal systems entanglement of highly excited eigenstates is expected to follow volume

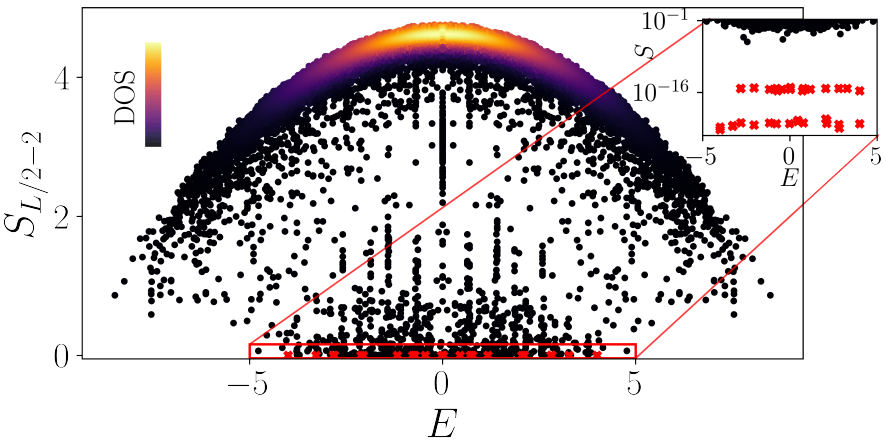

Figure 2.2: Entanglement entropy of eigenstates along the bipartite cut at the site 8 for $N_p = 8$ and $L = 22$. The color intensity corresponds to the density of dots, revealing that the majority of the eigenstates have nearly thermal entanglement. However, a large number of eigenstates has entanglement much lower than the thermal value. Among these, the red dots correspond to entanglement being zero up to numerical precision (inset).

law scaling, increasing linearly with i for $i \ll L$, and reaching maximal value for $i = L/2$. However, our numerical study of the entanglement entropy shows strong deviations from these expectations, in particular revealing a significant number of eigenstates with extremely low, and even exactly zero, entanglement, a feature typical of quantum many-body scars [25, 26, 27, 28, 29, 30, 142, 151, 152, 153].

Figure 2.2 illustrates such anomalous behavior of eigenstate entanglement for a chain of $L = 22$ sites. For the bipartite cut shown, $A = [1, 8]$, most of the eigenstates have increasing entanglement as their energy approaches zero, where the density of states is maximal, in agreement with thermalization. Nevertheless, a significant number of eigenstates features much lower values of entanglement, and the red box and inset in Fig. 2.2 highlight the presence of eigenstates with zero entanglement (up to numerical precision). We explain this as a result of an additional fragmentation of the Hilbert space caused by the interplay of the constraint and boson number conservation.

Eigenstates with zero entanglement, denoted as $|E_{S=0}\rangle$, are separable and can be written as a product state of the wave function in the region A and in its complement B. To this end, we choose the wave function $\left|\psi_m^\ell\right\rangle$ of the separable state $|E_{S=0}\rangle$ in the region A as an eigenstate of the Hamiltonian $\hat{H}_r$ restricted to the Hilbert space of m particles in ℓ sites. The state $\left|\psi_m^\ell\right\rangle$ has to satisfy the additional condition $\left\langle\psi_m^\ell\right| \hat{n}_\ell \left|\psi_m^\ell\right\rangle = 0$, i.e. that the last site of the region is empty. Provided such state exists, we construct the separable eigenstate $|E_{S=0}\rangle$ as

$$|E_{S=0}\rangle = \left|\psi_m^\ell\right\rangle \otimes \underbrace{|\circ\, \circ \cdots \circ\rangle}_{q} \otimes |\psi_R\rangle\,, \tag{2.11}$$

where $|\psi_R\rangle$ is an eigenstate of the Hamiltonian restricted to $L - \ell - q$ sites and $N_p - m$ particles. Inserting an empty region of $q \geq r$ sites separating the support of $\left|\psi_m^\ell\right\rangle$ and $|\psi_R\rangle$ ensures that the two states are disconnected. Note that q is upper bounded by the requirement that the resulting state belongs to the largest classically fragmented sector. It is easy to check that the state $|E_{S=0}\rangle$ is an eigenstate of the full Hamiltonian. Indeed, thanks to the empty region q the particles in A cannot influence those in B and the two eigenstates of the restricted Hamiltonian combine into an eigenstate of the full system.

Similarly to the case of classical fragmentation discussed in Eq. (2.8), one can define a family of operators that commute with the Hamiltonian and label the different sectors arising due to quantum fragmentation

$$\hat{O}^q_{\psi_m^\ell} = \hat{\mathcal{P}}_{\psi_m^\ell}\Big[\prod_{k=\ell+1}^{\ell+q+1}(1-\hat{n}_k)\Big]\hat{n}_{\ell+q+2}, \tag{2.12}$$

where $\hat{\mathcal{P}}_{\psi_m^\ell}$ is the projector onto the eigenvalue of the restricted Hamiltonian $\left|\psi_m^\ell\right\rangle$.

The construction of $|E_{S=0}\rangle$ relies on the existence of eigenstates $\left|\psi_m^\ell\right\rangle$ with vanishing density on the last site. This is a non-trivial requirement that *a priory* is not expected to be satisfied. However, we observe that such eigenstates can be found within the degenerate subspace of eigenstates with zero energy, see Appendix A.3. If $\left|\psi_m^\ell\right\rangle$ is an eigenstate with zero energy, the energy of eigenstate $|E_{S=0}\rangle$ is determined only by the energy of the $|\psi_R\rangle$. The existence of $\left|\psi_m^\ell\right\rangle$ relies on two conditions which have to hold simultaneously: $\ell > m + r$ and $(r+1)m - r \geq \ell$. These are satisfied only for $m \geq 3$ particles, thus resulting in a minimal size of the left region $\ell_{\min} = 6$ for $r = 2$. While there is no guarantee that

states $\left|\psi_m^\ell\right\rangle$ exist for generic (m,ℓ), we have an explicit analytic construction for the smallest state $|\psi_3^6\rangle$ for $(m,\ell)=(3,6)$

$$\left|\psi_3^6\right\rangle = \frac{1}{\sqrt{2}}\Big[\,|\bullet\bullet\circ\circ\bullet\circ\rangle - |\bullet\circ\bullet\bullet\circ\circ\rangle\Big], \tag{2.13}$$

similarly we report solutions up to $(m,\ell)=(7,18)$ in Appendix A.3. Furthermore, for each (m,ℓ) satisfying the condition, one can easily verify that stacking multiple $|\psi_m^\ell\rangle$ separated by at least r empty sites generates another state fulfilling the same condition. This recursive construction of the left states in Eq. (2.11), together with the explicit example Eq. (2.13), guarantees the existence of an infinite number of $\left|\psi_m^\ell\right\rangle$, in the thermodynamic limit. We further notice that a similar decomposition can be applied to the right eigesntates, $|\psi_R\rangle$ in a recursive fashion.

The construction of the eigenstates described above suggests that combining two operators $\hat{O}_{\psi_m^\ell}$, one shifted by $\ell+q$ sites, yields a new operator commuting with the full Hamiltonian and labeling a different fragmented subsector. Since there exist at least two different $\left|\psi_m^\ell\right\rangle$, one can combine them in various ways always obtaining new sectors. Due to this property, the size of the algebra of operators $\hat{O}_{\psi_m^\ell}$ scales as the total number of such combinations, which increases exponentially with system size in the thermodynamic limit. We observe that the operators defined in Eq. (2.12) do not commute with each individual term of the Hamiltonian, as required by the definition of Ref. [36]. However, they still give rise to a block-diagonal Hamiltonian in the *entangled* basis resulting from the product of the eigenestates of the restricted Hamiltonian on the left with product states on the remainder of the system, thus presenting a genuine case of quantum Hilbert space fragmentation. The recursive nature of the construction of constrained eigenstates might indicate the existence of a more general structure, possibly common to models featuring both particle conservation and chiral constraints. Hence, the formal definition of such *recursive* Hilbert space fragmentation presents an interesting direction for future work.

Let us explore the consequence of the existence of the special eigenstates defined in Eq. (2.11). Given the special character of the wave function $\left|\psi_m^\ell\right\rangle$, we expect that states $|E_{S=0}\rangle$ have a similar pattern of local observables in the first ℓ sites. An example of such behavior is shown in Figure 2.3(a), which reveals that all four states $|E_{S=0}\rangle$ that have zero entanglement across at least one bipartite cut in the $L=13$ chain for $r=2$ feature the same density expectation values, $\langle\hat{n}_i\rangle_\alpha = \langle E_\alpha|\,\hat{n}_i\,|E_\alpha\rangle$, in the first $\ell=6$ sites. Starting from the site number $i=9$, the density profile has different values on different eigenstates, corresponding to different wave functions $|\psi_R\rangle$ in Eq. (2.11).

The number of eigenstates with zero entanglement grows exponentially with system size. Even for the case of a fixed $\left|\psi_m^\ell\right\rangle$, the right restricted eigenstate $|\psi_R\rangle$ is not subject to any additional constraints, hence the number of possible choices of $|\psi_R\rangle$ grows as the dimension of the Hilbert space of N_p-m particles on $L-\ell-r$ sites, that is, at fixed m, asymptotically exponential in N_p. In the general case where (m,ℓ) are allowed to change, new $|E_{S=0}\rangle$ states will appear, with zero entanglement entropy at different bipartite cuts, according to the size of the left region. Finally, the recursive nature of the fragmentation discussed above is expected to give eigenstates with zero entropy across two or more distinct cuts which are separated by a non-vanishing entanglement region. These states are observed in numerical simulations starting from $N_p=7$ and $L=19$.

To illustrate the counting of eigenstates with zero entropy at a cut separating subregion $A=[1,i]$ from the rest of the system, we denote their number as $\mathcal{N}_S(i)$. For $i<5$, this

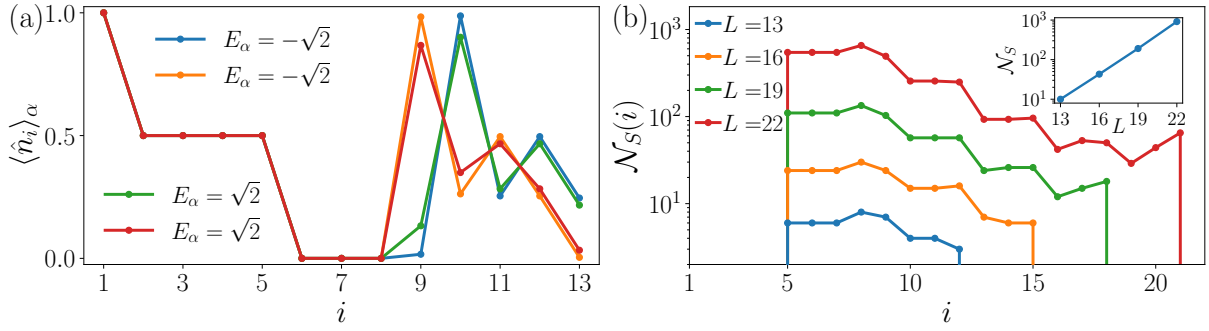

Figure 2.3: (a): The density profile of the zero-entanglement eigenstates for $L = 13$ shows a common pattern, due to their special structure (2.11). The first sites correspond to the zero mode of the Hamiltonian restricted to 3 particles in 6 sites $|\psi_3^6\rangle$, followed by 2 empty sites. The right subregion can then be any of the 6 eigenstate of H for 2 particles in 4 sites, with energy $\pm\sqrt{2}$, 0. We notice that eigenstates with the same $|\psi_R\rangle$ but a different number of empty sites separating it from $\left|\psi_m^\ell\right\rangle$ are degenerate and can be mixed by the numerical eigensolver, as is the case in the density profiles shown here. (b): The number of zero entanglement entropy eigenstates $\mathcal{N}_S(i)$ depends on the boundary of the subregion $A = [1, i]$. In particular, in the interval $i \in [5, 9]$ the number of zero-entanglement eigenstates is exponentially larger compared to more extended left subregions. At larger i recursively fragmented eigenstates contribute to $\mathcal{N}_S(i)$ for $L \geq 13$. The total number of zero-entanglement eigenstates, $\mathcal{N}_S$, grows exponentially in L, as shown in the inset. Note that $\mathcal{N}_S \neq \sum_i \mathcal{N}_S(i)$, as some eigenstates have zero entanglement across multiple bipartite cuts.

number is zero $\mathcal{N}_S(i) = 0$, as explained in the construction of these states. For $i \geq 5$ we observe a large $\mathcal{N}_S(i)$, exponentially increasing with system size. However, at larger i, the available configurations that can support states of the form Eq. (2.11) decrease and $\mathcal{N}_S(i)$ drops and eventually vanishes. As N_p and system size increase, left states $\left|\psi_m^\ell\right\rangle$ with a larger support ℓ are allowed thus increasing the range of sites where $\mathcal{N}_S(i) > 0$. This is also due to recursive fragmentation which can appear starting from $N_p = 5$ and $L = 13$. Carefully counting all *distinct* eigenstates $|E_{S=0}\rangle$ we confirm that their total number $\mathcal{N}_S$ grows exponentially with system size in the inset of Fig. 2.3(b)

2.4 Dynamics

After discussing recursive quantum Hilbert space fragmentation in the particle-conserving East model, we proceed with the study of the dynamics. First, in Section 2.4.1 we consider the dynamical signatures of Hilbert space fragmentation. Afterwards, in Section 2.4.2 we discuss the phenomenology of particle spreading starting from a domain wall state and illustrate how this can be connected to the structure of the Hilbert space. Finally, we compare the quantum dynamics to that of a classical cellular automaton in Section 2.4.3.

2.4.1 Dynamical signatures of quantum Hilbert space fragmentation

The zero-entanglement eigenstates $|E_{S=0}\rangle$ identified in Eq. (2.11) span a subsector of the Hilbert space which is dynamically disconnected from the rest. In this subspace

the Hamiltonian has non-trivial action only in the right component of the state, and eigenstates can be written as product states across the particular cut. Below we discuss signatures of such fragmentation in dynamics launched from weakly entangled initial states.

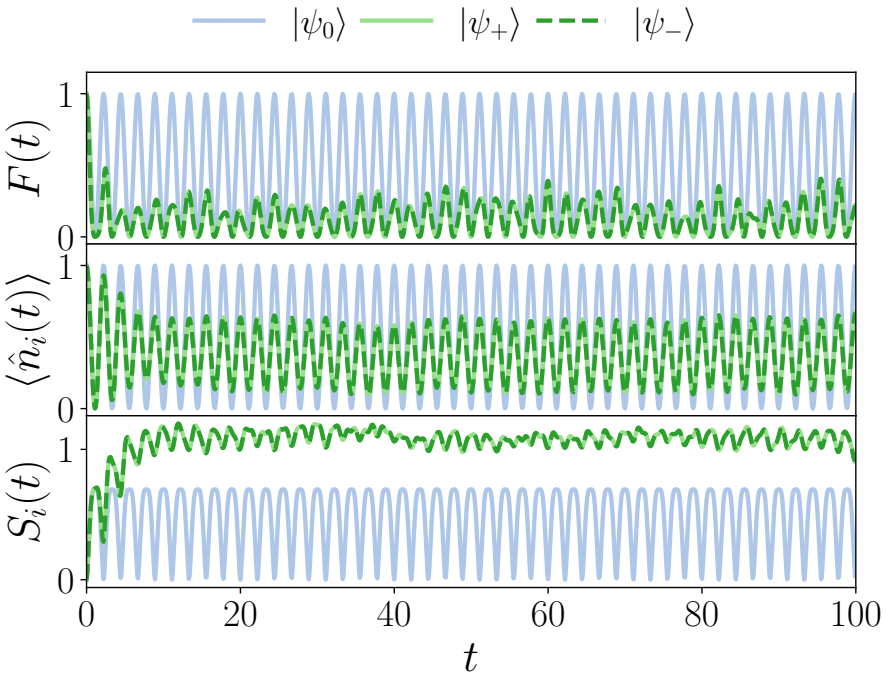

Figure 2.4: The signatures of quantum Hilbert space fragmentation can be observed for initial states that have a large overlap with zero-entanglement eigenstates $|E_{S=0}\rangle$. The fidelity $F(t) = |\langle\psi_0|\,\psi(t)\rangle|^2$ shows periodic revivals for all three initial states; choosing an eigenstate on the left portion of the chain results in perfect revivals (blue curve). Entanglement entropy across the cut $i = 11$ in the middle of the right region R and density on the same site show oscillations with identical frequency.

As an illustrative example, we show in Figure 2.4 the time evolution of a state of the form defined in Eq. (2.11) for $L = 13$. To obtain non-trivial dynamics, we replace the eigenstate $|\psi_R\rangle$ with a product state. In particular, we choose the initial state as

$$|\psi_0\rangle = \frac{|\bullet\bullet\circ\circ\bullet\circ\rangle - |\bullet\circ\bullet\bullet\circ\circ\rangle}{\sqrt{2}} \otimes |\circ\circ\rangle \otimes |\bullet\circ\bullet\circ\circ\rangle\,, \tag{2.14}$$

and consider the time-evolved state $|\psi_0(t)\rangle = e^{-it\hat{H}_2}\,|\psi_0\rangle$. The action of the full Hamiltonian does not affect the left part of the state and the Hamiltonian acting on the last five sites in the chain $R = [9, 13]$ is a simple 3×3 matrix

$$\hat{H}_R = \begin{pmatrix} 0 & 1 & 0 \\ 1 & 0 & 1 \\ 0 & 1 & 0 \end{pmatrix}. \tag{2.15}$$

in the $\{|\bullet\bullet\circ\circ\circ\rangle\,, |\bullet\circ\bullet\circ\circ\rangle\,, |\bullet\circ\circ\bullet\circ\rangle\}$ basis. Diagonalizing this matrix, we write the time-evolved state $|\psi_0(t)\rangle$ as

$$\begin{aligned} |\psi(t)\rangle = \left|\psi_m^\ell\right\rangle \otimes |00\rangle \otimes \Big[&\cos\left(\sqrt{2}t\right) |\bullet\circ\bullet\circ\circ\rangle \\ &- \sin\left(\sqrt{2}t\right) \frac{|\bullet\bullet\circ\circ\circ\rangle + |\bullet\circ\circ\bullet\circ\rangle}{\sqrt{2}} \Big], \end{aligned} \tag{2.16}$$

hence the fidelity reads $F(t) = |\langle\psi_0|\,\psi(t)\rangle|^2 = \cos^2(\sqrt{2}t)$. As the time-evolution in Eq. (2.16) involves only three different product states, it produces perfect revivals with period $T = \pi/\sqrt{2}$. This periodicity also affects observables, such as the density in the region R, and the entanglement entropy.

This periodic dynamics also appears in the two product states $|\psi_+\rangle = |\bullet\bullet\circ\circ\bullet\circ\circ\circ\bullet\circ\bullet\circ\circ\rangle$ and $|\psi_-\rangle = |\bullet\circ\bullet\bullet\circ\circ\circ\circ\bullet\circ\bullet\circ\circ\rangle$ that are contained in Eq. (2.14). These states indeed show revivals of the fidelity with the same period T, although the peaks are more suppressed. This is not surprising, as these states have only part of their weight in the disconnected subspace.

In Figure 2.4 we show the results of the dynamics of the state $|\psi_0\rangle$, Eq. (2.14), together with the two product states generating the superposition, $|\psi_\pm\rangle$. In addition to fidelity, we also show the density and entanglement dynamics of sites i within the right region R. As expected, the fidelity shows revivals with period $T = \pi/\sqrt{2}$, and similar oscillations are also observed in local operators and entanglement. While the initial state $|\psi_0\rangle$ defined in Eq. (2.14) presents perfect revivals with $F(T) = 1$, the product states $|\psi_\pm\rangle$ does not display perfect fidelity revivals show larger entanglement. We note, that since the two product states $|\psi_\pm\rangle$ together form a state $\left|\psi_m^\ell\right\rangle$ their dynamics in the region R is not affected by the choice of the left configuration, and all considered quantities for theses two initial states have identical dynamics.

2.4.2 Phenomenology of dynamics from the $|\mathrm{DW}\rangle$ initial state

After exploring the dynamics resulting from quantum Hilbert space fragmentation, we now turn to the dynamics in the remainder of the constrained Hilbert space focusing on the domain wall state (2.5). The domain wall state does not have any overlap with zero entanglement eigenstates except for possibly states with zero entanglement on the last cut. It is also characterized by a vanishing expectation value of the Hamiltonian, corresponding to zero energy density, where the density of states is maximal. Hence, thermalization implies that time evolution from the domain wall leads to the steady

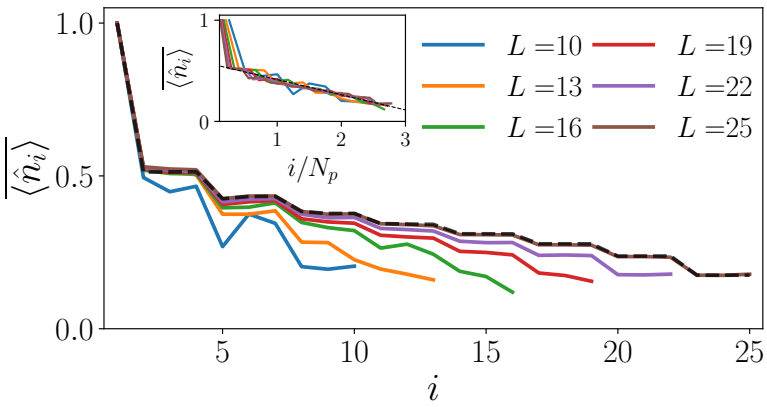

Figure 2.5: The constrained character of the model leads to a non-uniform stationary density profile for the domain wall initial state. This coincides with the infinite-temperature prediction on large systems, as highlighted by the dashed line corresponding to $\mathrm{tr}[\hat{n}_i]/\,\mathrm{tr}[\mathbb{1}]$ for $L = 25$, where $\mathrm{tr}\left[\hat{O}\right] = \sum_j \hat{O}_{jj}$. Rescaling the x-axis by the number of particles N_p, we obtain a good collapse of the data, as shown in the inset. The particle density follows a linear decrease $\overline{\langle\hat{n}_i\rangle} \approx \overline{\langle\hat{n}_2\rangle} - c(i-2)/N_p$, with $c \approx 0.15$.

state where all observables agree with their infinite-temperature expectation value. To check this property we focus on the expectation value of the particle density operators throughout the chain.

Figure 2.5 shows the infinite time average of the particle density, $\overline{\langle \hat{n}_i \rangle}$ obtained through the diagonal ensemble

$$\overline{\langle \hat{n}_i \rangle} = \sum_{\alpha} |\langle \mathrm{DW}| E_\alpha \rangle|^2 \langle E_\alpha| \hat{n}_i |E_\alpha\rangle \,, \tag{2.17}$$

where the sum runs over all eigenstates α. This calculation is performed for $L \leq 22$, where the full set of eigenstates can be obtained through exact diagonalization. For larger systems, the infinite time average value of $\overline{\langle \hat{n}_i \rangle}$ is approximated as the average of the density in the time-window $t \in [6.9 \times 10^3, 10^4]$. We observe that the density profile agrees well with the infinite-temperature prediction. See Appendix A.1 for details of the calculation.

The infinite-temperature prediction for the density profile does not result in a homogeneous density due to the constraint. The number of allowed configurations with non-zero density in the last sites is indeed limited by the constraint, and results in a lower density in the rightmost parts of the chain. In addition, the profile has a step-like shape that is related to the range-2 constraint in the model. In the inset of Fig. 2.5 we show that the density profiles collapse onto each other when plotted as a function of i/N_p. This suggests the heuristic expression for the density profile $\overline{\langle \hat{n}_i \rangle} \approx \overline{\langle \hat{n}_2 \rangle} - c(i-2)/N_p$ where $c \approx 0.15$ is a positive constant.

Although the saturation profile of the density is consistent with thermalization, below we demonstrate that *relaxation* to the steady state density profile is anomalous. The time-evolution of the density $\langle \hat{n}_i(t) \rangle = \langle \psi(t)| \hat{n}_i |\psi(t)\rangle$ is shown in Figure 2.6 for $L = 28$ sites up to times $t \approx 10^4$. The data demonstrates that the relaxation of density qualitatively depends on the location within the chain. In the left part of the chain with $i \leq 2N_p$, the spreading of the density front is fast, and saturation is reached quickly on timescales of

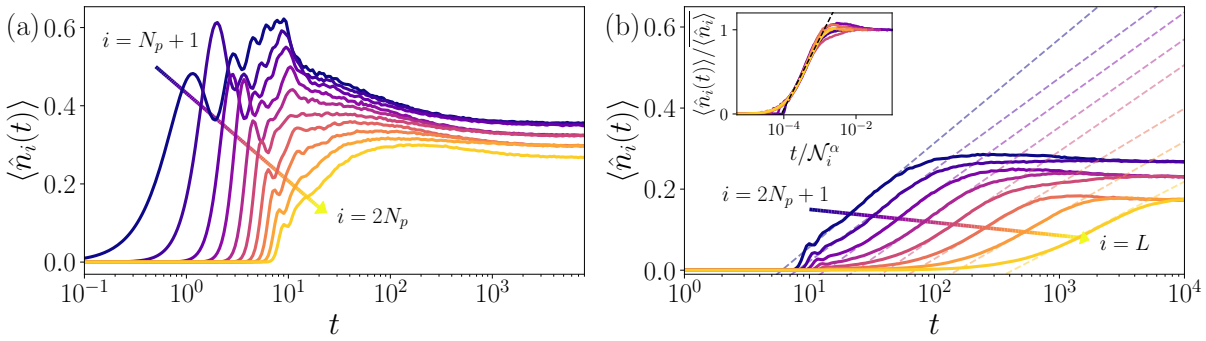

Figure 2.6: The approach to saturation in the density dynamics is very different depending on the region within the chain. (a) In the first $2N_p$ sites of the chain a fast relaxation takes place due to the weak role of the constraint in dense regions. (b) For the right part of the chain, $i > 2N_p$ anomalously slow logarithmic dynamics arise. The inset shows the data collapse upon rescaling the density axis by the long time average and the time axis by the number of states within each *leg* of the graph $\mathcal{N}_i$ to the power $\alpha \approx 1.15$, as discussed in more detail at the end of this section. The data shown here are for a system of $L = 28$ sites with $N_p = 10$ bosons.

$O(10)$, as shown in Fig. 2.6(a). This can be attributed to the fact that the constraint is not effective at large densities. In contrast, in the rightmost part of the chain, $i > 2N_p$ the constraint dramatically affects the spreading of particles resulting in the logarithmically slow dynamics in Fig. 2.6(b).

To further characterize the anomalous dynamics, we study the transport of the particle density on short time-scales for larger systems up to $L = 37$ sites. For the systems with $L > 28$ we use a fourth-order Runge-Kutta algorithm with a time-step as small as $\delta t = 10^{-3}$. This allows us to reliably study the short-time behavior with sufficient accuracy down to $\delta t^4 = 10^{-12}$. We consider the dynamics of he particle flow across the domain wall

$$\delta n(t) = \sum_{i \leq N_p} \left[\langle \hat{n}_i(0) \rangle - \langle \hat{n}_i(t) \rangle \right]. \tag{2.18}$$

The dynamics of $\delta n(t)$ in Figure 2.7(a) shows a clear initial power-law behavior drifting to much slower logarithmic growth at later times, in agreement with the dynamics of $\langle \hat{n}_i(t) \rangle$ in the right part of the chain. At even longer times $\delta n(t)$ saturates to a value proportional to the system size L. Figure 2.7(b) shows the instantaneous dynamical exponent,

$$z(t) = \left(\frac{d \ln \delta n(t)}{d \ln t} \right)^{-1}. \tag{2.19}$$

In this figure, the early time dynamics are characterized by fast transport of particles across the domain wall $i = N_p$ due to the large initial density. On intermediate time-scales $t \approx 10$, a superdiffusive plateau of $1/z(t) \approx 2/3$ is visible. Finally, at longer times the dynamics slow down and become logarithmic, consistent with a vanishing $1/z(t)$. Zooming in the time-window $t \leq 30$, we notice that the extent of the superdiffusive plateau increases linearly with system size, suggesting the persistence of the superdiffusive regime in the thermodynamic limit.

The superdiffusive behavior observed in the dynamics of the domain wall initial state is very peculiar, as one would expect a state close to infinite temperature to show diffusive

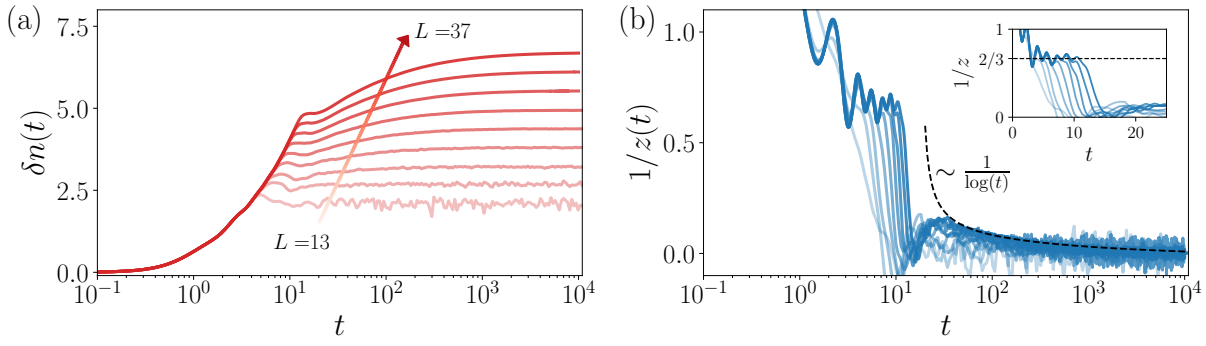

Figure 2.7: (a) The behavior of the particle current across the domain wall shows an initial power-law growth $\delta n(t) \sim t^{1/z(t)}$ followed by a slow-down to logarithmic behavior at later times, in agreement with the density dynamics. (b) The analysis of the dynamical exponent $z(t)$ shows the presence of a super-diffusive plateau $1/z \approx 2/3$ at intermediate times, whose duration grows linearly with system size. At later times, the onset of logarithmic dynamics is signalled by the decay of $1/z(t)$. Data are for $13 \leq L \leq 37$ from more to less transparent..

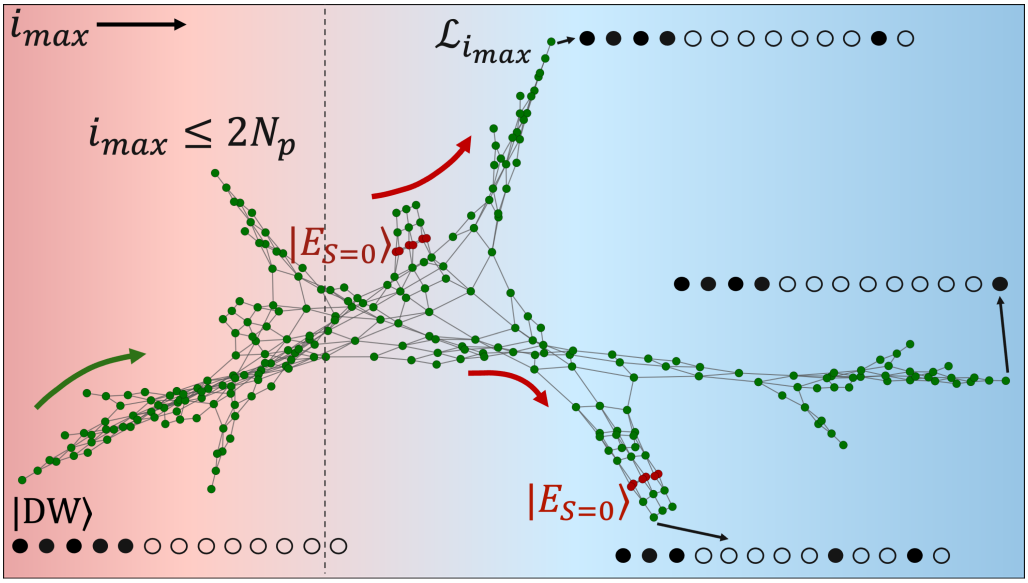

Figure 2.8: The representation of $\hat{H}_2$ as the adjacency graph $\mathcal{G}_r$ for system with $N_p = 5$ particle and $L = 13$ lattice sites. The dense central part – *backbone* – has gradually decreasing number of vertices and connectivity as the position of the rightmost particle increases above $i_{\max} > 2N_p = 10$ (dashed line). The *legs* of the graph emanate from the backbone and correspond to regions where $i_{\max}$ is conserved. The legs end with the product states (an example is labeled as $\mathcal{L}_{i_{\max}}$), where a particular particle is frozen near the end of the chain. Red vertices show product states corresponding to zero-entanglement eigenstates $|E_{S=0}\rangle$, which in this case have weight on 12 out of $\mathcal{D}_{N_p} = 273$ product states contained in the constrained Hilbert space.

transport in an ergodic system as is the one considered here. We further investigated the time-evolution of other initial states with a lower density of particles in the leftmost part of the chain. Appendix A.5 shows that with decreasing density, the transport is drifting from superdiffusion in dense states to diffusion as the density decreases. Such dependence of transport on the density in the initial state suggests that superdiffusive dynamics is related to the special nature of the domain wall state that separates completely empty and full regions, and thus it may lack a coarse-grained hydrodynamics description.

We now focus on capturing the phenomenology of the slow dynamics observed at late times using the structure of the Hamiltonian. Starting from the domain wall initial state, the slow dynamical regime is reached after a time scaling proportionally to the system size. Naively this may preclude the observation of such dynamical regime in the thermodynamic limit. However, our study of transport in more dilute initial states suggests that the onset of logarithmic slow dynamics may depend on the density of particles. In particular, we conjecture that at sufficiently low initial densities, logarithmic dynamics may be observable at timescales that do not depend on the system size. In order to construct a phenomenological picture of slow dynamics, we interpret the Hamiltonian as a graph where the vertices of the graph enumerate the product states contained in a given connected sector of the Hilbert space. The edges of the graph connect product states that are related by any particle hopping process allowed by the constraint. A particular example of such a graph for the system with $N_p = 5$ particles and $L = 13$ sites is shown in Fig. 2.8.

The vertices of the graph in Fig. 2.8 are approximately ordered by the position of the

rightmost occupied site $i_{\max} \geq N_p$, revealing the particular structure emergent due to the constraint. The dense region that follows the domain wall product state has high connectivity, and we refer to it as the *backbone*. In addition to the backbone, the graph has prominent *legs* emanating perpendicularly. The legs are characterized by the conserved position of the rightmost particle that is effectively frozen due to the particles on the left retracting away, as pictorially shown in Fig. 2.8. Since such legs are in one-to-one correspondence with the position of the rightmost particle, $i_{\max}$, their number grows linearly with system size. The number of product state configurations contained within each leg strongly depends on $i_{\max}$. Given that the position of the rightmost particle is frozen within a leg, they cast a strong effect on the dynamics of the model.

In particular, the spreading of particles towards the right probed by $R(t)$ can be related to the presence of an increasing number of configurations within legs at large $i_{\max}$, $\mathcal{N}_{i_{\max}}$. These are characterized by long empty regions as the one depicted in Figure 2.8, which require the collective motion of many particles to allow the hopping of the rightmost boson sitting at $i_{\max}$. The slow dynamics observed, then, can be qualitatively understood as the effect of many states not contributing to the spreading and of the increasingly long empty regions that have to be crossed to activate hopping further to the right. Looking back at the dynamics shown in Figure 2.6, we highlight this effect by rescaling the time-axis by the number of configurations belonging to each leg, $\mathcal{N}_i$. The resulting collapse is shown in the inset of Figure 2.6(b).

2.4.3 Dynamics in constrained classical cellular automata

The anomalous relaxation of the quantum model from the domain wall state reported in Section 2.4.2 invites natural questions about the universality of dynamics in presence of inversion-breaking constraints. To shed light on this question, we introduce a classical cellular automaton model that replaces the unitary time-evolution of the quantum model $\hat{U}(t) = \exp\left(-\imath \hat{H} t\right)$ with a circuit of local unitary gates preserving the same symmetries and constraints of the Hamiltonian [154, 155].

To reproduce correlated hopping in the Hamiltonian (2.2), we introduce two sets of local gates U_1 and U_2 schematically shown in Fig. 2.10(a). The first gate, U_1, acts on 4 sites and implements the hopping facilitated by the next nearest neighbor,

$$U_1 = \exp\left\{ -\imath\theta \left[\hat{n}_j (1 - \hat{n}_{j+1}) \left(c^\dagger_{j+3} c_{j+2} + \text{H.c.} \right) \right] \right\}. \tag{2.20}$$

The second gate, U_2, acts on three sites, and implements the hopping facilitated by the nearest neighbor site:

$$U_2 = \exp\left\{ -\imath\theta \left[\hat{n}_j \left(c^\dagger_{j+2} c_{j+1} + \text{H.c.} \right) \right] \right\}. \tag{2.21}$$

For a generic choice of the rotation angle θ these gates cannot be efficiently simulated classically. However, in what follows we fix θ to the special value, $\theta = \pi/2$, so that gates $U_{1,2}$ map any product state to another product state. This corresponds to a classical cellular automaton which allows for efficient classical simulation.

As each local gate is particle conserving, in order to allow for non-trivial transport, we shift gate position by one site after each layer, as shown in Fig. 2.10(a). Consequently,

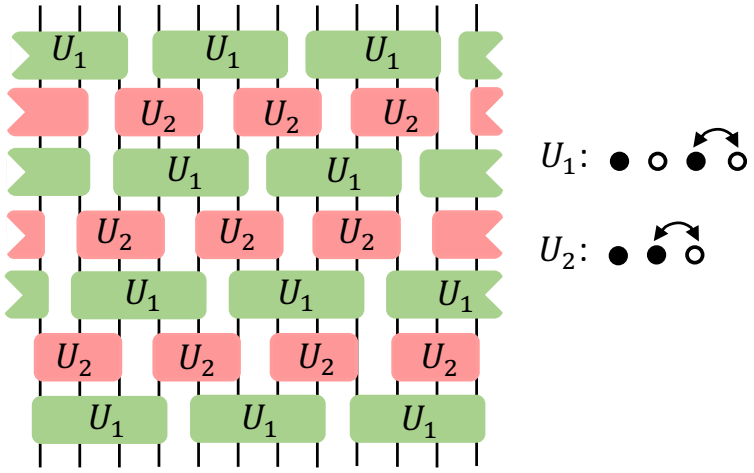

Figure 2.9: Schematic representation of the circuit used to describe the classical dynamics. The continuous time-evolution $\hat{U}(t)$ is decomposed into a series of 4-sites gates U_1 and of 3-sites gates U_2, whose action is shown on the right part of the Figure.

the circuit has a 7-layer unit cell in the time direction. Additionally, the order of gate applications is also important, as the gates $U_{1,2}$ generally do not commute with each other. Alternating the layers of U_1 and U_2 gates proves to be the best choice, as it implements all allowed particle hopping processes, leading to the circuit shown in Fig. 2.10(a).

Using this cellular automaton we are able to simulate the time-evolution of very large systems to extremely long times. As the setup implements the same constraint as the Hamiltonian dynamics, we conjecture that it should present similar features. For instance, initializing the system in a dense-empty configuration similar to the $|\mathrm{DW}\rangle$ state, we expect the dense region to spread quickly into the empty one, until eventually it stretches too much and its propagation slows down due to the constraint.

We study the evolution to the domain-wall initial state for a system of $L = 298$ sites and $N_p = 100$ particles. Since this model is deterministic, the density as a function of circuit depth is a binary function, $n_i(t) \in \{0, 1\}$. Figure 2.10(b) shows the short-time density dynamics ($t < 1000$). We observe ballistic particle transport in the dense regime. On the one hand, the position of the rightmost particle moves to the right. On the other hand, defects (holes) propagate within the dense domain wall state. The simulation reveals notable difference in velocities of holes and spreading of the rightmost particle, that is expected in view of the inversion breaking symmetry within the model.

The ballistic expansion of the particles is followed by a logarithmic slowdown at later times as shown in Fig. 2.10(b). Much akin to the Hamiltonian dynamics, this slowdown is due to the lower density reached at later times as the front moves to the right and more particles become temporarily frozen due to the constraint. To further probe the two distinct behaviors observed in the cellular automaton, in the inset of Fig. 2.10(b) we show the time-evolution of the particle flow across the domain wall $\delta n(t)$ as in Eq. (2.18). From the initial linear behavior, $\delta n(t)$ abruptly enters a logarithmic regime as it exceeds the extent of the ballistic region, corresponding to $i \approx 180$.

The study of the circuit evolution for the domain-wall initial state then shows the overall similar characteristic inhomogeneous dynamics as the quantum system. At early times,

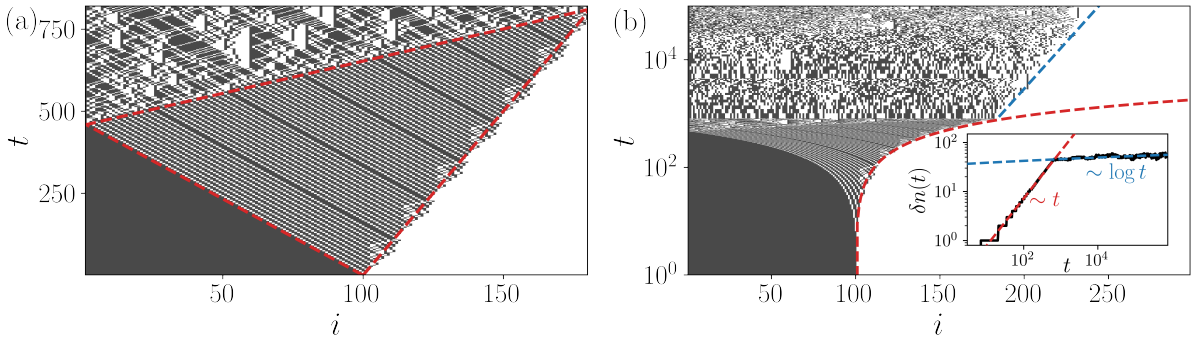

Figure 2.10: (a)-(b): Density evolution of the classical cellular automaton starting from domain wall initial state for a system with $L = 298$ sites and $N_P = 100$. (Black and white dots correspond to occupied and empty sites). (a) At short times particles spread ballistically into the empty region. Scattering events appear at regular time intervals at the boundaries of the red dashed triangle which defines the region of ballistic behavior. (b) At later times when particle density is lower the constraint becomes more effective, leading to the logarithmic spreading of particles into the empty region. The inset shows the dependence of the current across the domain wall on time that has a clear ballistic regime of linear increase with time followed by slow logarithmic growth at later times.

and close to the initial domain wall $i = N_p$, the transport of particles and holes is ballistic as for $t \leq 1$ in the quantum case (see Fig. 2.7). However, as the density spreads and particle density lowers, ballistic spreading is replaced by a logarithmic slow dynamics. We notice, however, that the automaton lacks the super-diffusive plateau observed in the Hamiltonian dynamics.

2.5 Discussion

In this work, we introduced a family of models characterized by a conserved $U(1)$ charge and strong inversion symmetry breaking. We observe that quantum Hilbert fragmentation [36] in such models can be understood from the recursive construction of special weakly entangled eigenstates coexisting with volume-law entangled eigenstates in the spectrum. In addition, we investigate the dynamics of the system in a quantum quench launched from the domain wall initial state. Although the long time saturation value of particle density is consistent with thermalization, we observe two distinct regimes in particles spreading rom the domain wall initial state. An initial superdiffusive particle spreading at high density is dramatically slowed down at lower densities, leading to a logarithmically slow approach of density to its saturation value. While the superdiffudive plateau has an extent in time that increases with system size, its sensitivity to the choice of initial state suggests that it might be related to the particular nature of the domain wall state considered here and may not have a universal hydrodynamic description. The second, slow transport regime, on the other hand, is not so sensitive to the particular initial state and we attribute this to the structure of the constrained Hamiltonian. In addition, we also reproduce the logarithmic dynamics in a classical cellular automaton that features the same symmetries, although at early times the cellular automaton features ballistic dynamics in contrast to slower but still superdiffusive spreading of particles in the Hamiltonian model.

Our work suggests that the interplay of constraints and broken inversion or other spatial symmetries may lead to new universality classes of weak thermalization breakdown and

quantum dynamics. In particular, the quantum Hilbert space fragmentation in the considered model gives rise to a number of weakly entangled eigenstates that can be interpreted as quantum many-body scars [26, 153]. The number of these eigenstates scales exponentially with system size. Moreover these eigenstates may be constructed in a recursive fashion, by reusing eigenstates of a smaller number of particles. This is in contrast to the PXP model, where the number of scarred eigenstates is believed to scale polynomially with system size [28, 30], though existence of a larger number of special eigenstates was also conjectured [41].

Although we presented an analytic construction for certain weakly entangled eigenstates and demonstrated their robustness to certain deformations of the Hamiltonian, a formal definition of recursive quantum Hilbert space fragmentation, beyond our phenomenological observation, remains an interesting direction for future work. The complete enumeration and understanding of weakly entangled eigenstates may give further insights into their structure and requirements for their existence. In addition, a systematic study of the emergence of quantum Hilbert space fragmentation in the largest sector of a classically connected Hilbert space in other constrained systems, like the XNOR or the Fredkin models is desirable [116, 133].

From the perspective of particle transport, the numerical data for the dynamical exponent controlling particle spreading suggests that our family of constrained models features superdiffusive dynamics [41, 156, 157, 158, 159] from a particular domain wall initial state in the largest connected sector of the Hilbert space. Thus, although it is less robust compared to other examples, understanding and quantifying the emergence of superdiffusion in the present and similar models with longer range of assisted hopping remains and interesting question. In particular, the models considered in our work may be implemented using quantum simulator platforms using control-swap gates of various ranges. Thus, an experimental study of such models may reveal novel valuable insights into their physics and the universality of their transport phenomena, which are beyond the reach of current state of the art numerical and theoretical approaches.

CHAPTER 3

Stability of many-body mobility edges in disordered interacting systems

In this Chapter, we introduce a model featuring kinetic constraints, disorder and free hopping. We show the onset of a many-body localized phase at strong disorder and small particle density, coexisting with thermal states at higher density, thus providing an example of many-body mobility edge. The stability of localization to the mobility edge is further explored with large scale numerical simulations. Additionally, the failure in this particular case of the mechanism proposed in Ref. [85] to conjecture the absence of many-body mobility edges is shown, corroborating the conclusion of the stability of localization. The second Section of this chapter is based on

Brighi P., Abanin D. A., Serbyn M. "Stability of mobility edges in disordered interacting systems," Phys. Rev. B **102** 060202(R) (2020)

3.1 Introduction

Many-body localization (MBL) provides a mechanism to avoid thermalization in isolated quantum interacting systems [50, 160]. Despite intensive theoretical [74, 75] and experimental [66, 70, 71, 82, 161, 162, 163] studies, only fully-MBL phase in one spatial dimension is relatively well understood. The fate of MBL in higher dimensions [62, 81, 164, 165, 166] and the possibility of the coexistence of localized and delocalized eigenstates in the same many-body spectrum [85] remain debated.

Similarly to the case of [84], the MBL and delocalized eigenstates cannot coexist at the same energy suggesting the existence of *many-body mobility edge (MBME)* — a certain energy in the spectrum separating localized and delocalized eigenstates [50]. In contrast to the non-interacting case, the energy of MBME scales *extensively* with system size. In the absence of a coupling to a bath, this leads to an exactly vanishing conductivity (in contrast to an exponentially small but finite value in Anderson insulator) until a certain critical temperature [50].

Recently [85] suggested a possible mechanism that may destroy MBME in large systems: a finite region with local energy density above the mobility edge — a "bubble" — may

resonantly spread throughout the system thereby destroying localization everywhere. However, recent experiments [71] and MPS simulations [167] gave evidence of MBME, at least on intermediate timescales. In addition, a number of numerical studies observed a mobility edge [59, 168, 169, 170, 171] using exact diagonalization (ED). Unfortunately, the ED is limited to relatively small system sizes; experiments with MBME in energy density are also challenging since they require energy resolution.

In order to overcome the above challenges, we propose to study MBME *in particle density*. This allows us to directly probe the mechanism of instability suggested in Ref. [85], which equally applies to MBME in any extensive conserved quantity. First, using numerical simulation with matrix product states (MPS), we demonstrate that uniform dilute states remain localized even at system sizes of $L = 40$ sites up to 250 tunneling times (i.e. more than two orders of magnitude larger than the inverse local hopping). Next, we use a region with large particle density to reproduce the bubble described in [85] and track its influence on the dilute remainder of the system in a quantum quench. We do not find any evidence of resonant tunneling of the bubble, at least on experimentally relevant timescales.

In summary, the study of the particle density MBME facilitates the state preparation and analysis and allows us to access the dynamics of much larger systems using time evolution with MPS. We report the stability of the particle density mobility edge on long timescales and suggest that similar physics may be experimentally probed using Bose-Hubbard model.

3.2 Correlated hopping model

We consider hard-core bosons on an open chain of size L, with the following Hamiltonian,

$$\hat{H} = t_1 \sum_{i=1}^{L-1} (c_{i+1}^\dagger c_i + \text{ h.c.}) + \sum_{i=1}^{L} \epsilon_i \hat{n}_i + t_2 \sum_{i=2}^{L-1} (c_{i-1}^\dagger \hat{n}_i c_{i+1} + \text{ h.c.}). \tag{3.1}$$

The first two terms correspond to the non-interacting Anderson's model [48], where random on-site potential has a uniform distribution, $\epsilon_i \in [-W, W]$. The facilitated hopping in the third term enables motion of a *pair of particles* with amplitude t_2, $\bullet\bullet\circ \leftrightarrow \circ\bullet\bullet$, making the model interacting. The Hamiltonian (3.1) has two channels for dynamics: the single particle hopping prevails in dilute states, while the pair hopping is dominant at larger densities.

Employing kinetic constraints, this model is akin to the one introduced in Chapter 2, although the constraint used in this case is completely inversion-symmetric. We note that a similar non-chiral model was discussed in Ref. [85] in two dimensions, although only with two particles. Furthermore, the limit $t_1 = 0$ in the absence of disorder was shown to be integrable [155]. The enhancement of localization length in the case of two interacting particles also received significant attention [172, 173]. In a different direction, the fate of the single particle mobility edge in the presence of interactions was studied [163, 174]. In contrast, we study model (3.1) that does not have a single particle mobility edge and consider the finite particle density regime.

We fix the value of the hopping parameters $t_1 = 0.5$ and $t_2 = 2$ so that the localization length of a single particle $\xi_{\text{SP}} \lesssim 1$ and at the same time a single pair has a localization length $\xi_{\text{P}} \gtrsim 2.5$ for $2.5 \lesssim W \lesssim 6$ as shown in Section 3.3. For such a choice, our model

does not suffer from finite size effects [175] and we establish MBME using eigenstates probes.

3.3 Locallization length and parameter choice

The dynamics generated by the constrained Hamiltonian, Eq. (3.1), strongly depends on the choice of the hopping parameters $t_{1,2}$. In order to choose the most suitable parameters for the study of MBME in particle density, we explore localization lengths for a single particle ξ_{SP} and for one pair of particles ξ_{P}. These localization lengths are evaluated using ED. We calculate the infinite-time average of the occupation number at each site for an initial state where either a single particle or a single pair are initialized at the first site of the chain. We extract the localization lengths ξ_{SP} (ξ_{P}) from an exponential fit of the density curve $\langle n_i \rangle$.

Resulting values of $\xi_{\mathrm{P,SP}}$ for fixed $t_1 = 0.5$ and different disorder values and different values of hopping t_2 are shown in Fig. 3.1. The single particle hopping localization length (dashed line in Fig. 3.1) does not depend on t_2, and becomes smaller than one lattice spacing for $W \gtrsim 4$. The pair localization length is monotonously increasing with t_2 at fixed value of disorder strength, W. Our aim is to have ξ_{P} in the range between 2 and 5. In this regime, the half-filling case is expected to be delocalized, while at lower densities $\nu \sim 1/5$, when the typical distance between pairs is large, we expect MBL phase. This motivates the choice $t_2 = 2$, since at this value of t_2 $\xi_{\mathrm{P}}(W)$ approaches 2 at disorder strength around $W \sim 6$. We note that we avoided further increase of t_2 to keep the model

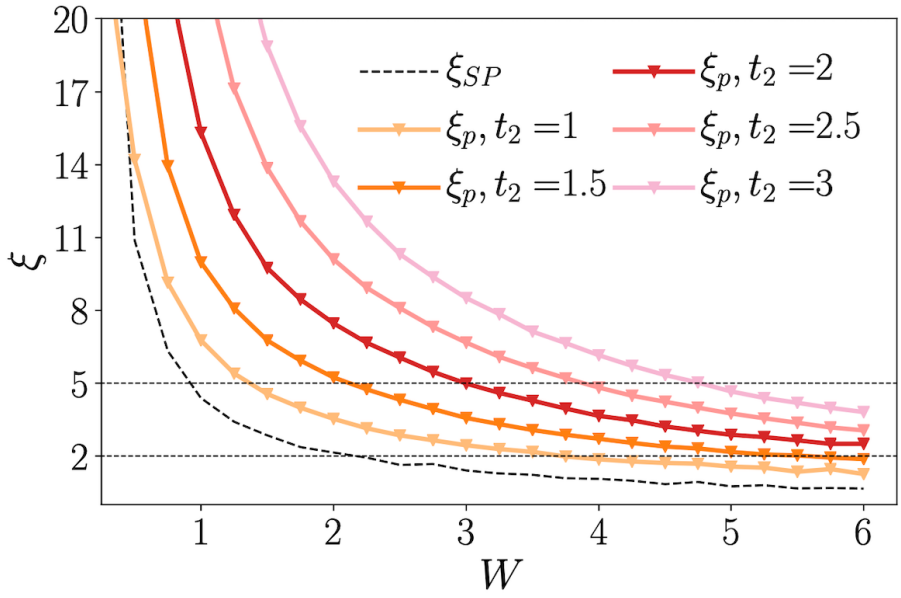

Figure 3.1: The localization length decreases, as expected, with the disorder strength for all the values of t_2. For every constrained hopping amplitude t_2 it is possible to locate the region of disorder where we expect to see a MBME in particle density as the area among the two dashed lines. As the curve crosses the first dashed line, systems with typical particle spacing 5 will be localized. Nevertheless denser states will still be delocalized, having smaller distance among particles. Data were obtained on a lattice of length $L = 50$ and averaged over 5000 disorder realizations.

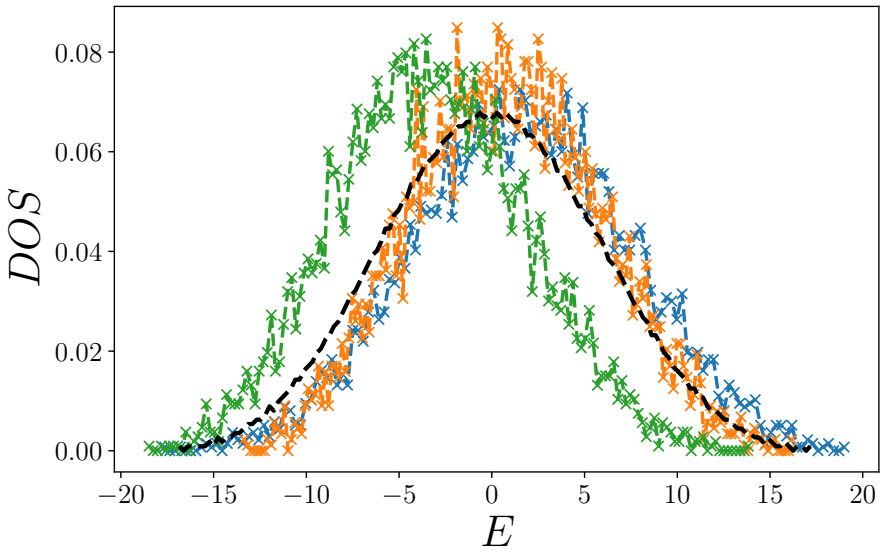

Figure 3.2: The DOS from single disorder realizations show a relatively smooth behavior and a Gaussian shape, thus confirming the absence of strong finite size effects. DOS refers to a chain with $L = 20$ and $\nu = 1/4$. Disorder strength is $W = 5.0$. Green, blue and orange curves correspond to different disorder realizations, while the black dashed line shows disorder-averaged DOS.

away from the constrained limit: in the case when t_2 dominates over t_1, the model would approximately reduce to a kinetically constrained model that has many disconnected sectors in the Hilbert space.

In order to rule out the presence of strong finite size effects, we studied the density of state in individual disorder realizations. In the regime when $t_2 \gg t_1$ the strong finite size effects would give rise to the presence of mini-bands and the DOS would become non-monotonous with numerous peaks corresponding to mini-band structure [175]. Figure 3.2 confirms that at our choice of parameters even individual disorder realizations have a relatively smooth density of states with Gaussian envelope, thus ruling out the presence of strong finite size effects.

3.4 Eigenstate probes of localization

We use exact diagonalization and shift-invert (SI) numerical techniques to provide evidence for MBME in Hamiltonian (3.1). We analyze the average ratio of level spacings, $\delta_i = E_{i+1} - E_i$, in the middle of the spectrum, $r_{\text{av}} = \langle \min(\delta_i, \delta_{i+1}) / \max(\delta_i, \delta_{i+1}) \rangle$. This is a commonly used probe of the MBL transition [53, 59] that attains the value $r_{\text{P}} \simeq 0.39$ for the Poisson level statistics, characteristic of the MBL phase and $r_{\text{GOE}} \simeq 0.53$ for the case of random Gaussian orthogonal ensemble (GOE), typical for chaotic Hamiltonians with time-reversal symmetry.

Figure 3.3 displays that at half-filling, $\nu = N/L = 1/2$, where N is the total number of particles and L is the chain length, the level statistics approaches GOE with increasing system size, which is consistent with the delocalized phase. In contrast, at $\nu = 1/5$ filling r_{av} flows towards r_{P} at strong disorder. In what follows we fix the disorder strength to be

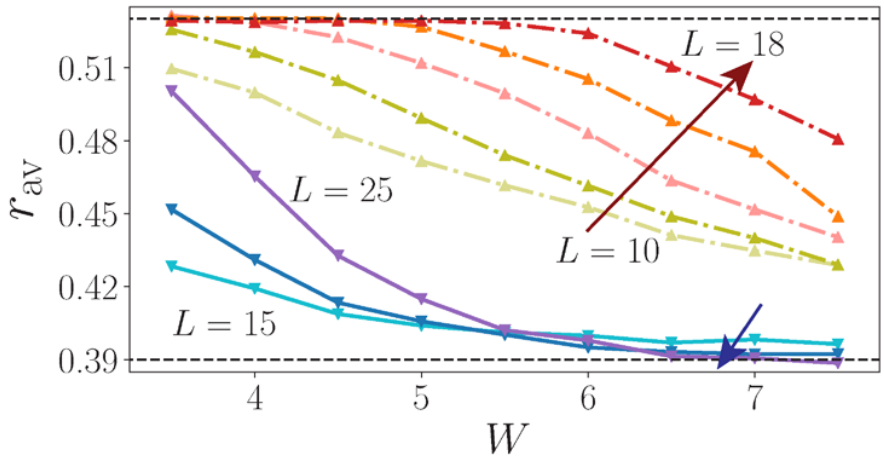

Figure 3.3: Scaling of level spacing ratio demonstrates that at density $\nu = 1/5$ (solid lines, $L = 15, 20, 25$ with $3, 4, 5$ particles) the system enters MBL phase for $W \geq 6.3$. In contrast, at half-filling $\nu = 1/2$ (dashed curves, $L = 10, \ldots 18$) the critical disorder strengths is much larger and in the entire range of disorder $r_{\rm av}$ approaches thermal value with increasing system size. Data is generated from ED/SI simulations with at least 10^3 disorder realizations using approximately 2% of eigenstates in the center of the spectrum.

$W = 6.5$, since at this value the dilute limit is localized while the dense limit clearly flows towards delocalization.

After having focused on the two values of filling, $\nu = 1/2$ and $1/5$, we demonstrate the density dependence of critical disorder. For this purpose we calculate the average ratio of level spacings $r_{\rm av}$ for a single system size $L = 18$ at varying values of density. Figure 3.4 allows to estimate the dependence of the critical disorder on the filling, ν. At low densities ($\nu < \nu_c(W)$) states have $r_{\rm av}$ approaching value characteristic for Poisson distribution of level spacings. In contrast, for dense configurations ($\nu > \nu_c(W)$) the level spacing ratio is close to GOE prediction.

The left panel of figure 3.4 reveals that the most delocalized filling is $\nu = 2/3$, which corresponds to the case when the best packing of pairs in the chain, $\bullet\bullet\circ\bullet\bullet\circ\cdots$, can be achieved. At this filling the Poisson values of $r_{\rm av}$ would be achieved beyond the upper limit of the considered disorder range. Decreasing particle density away from this value causes earlier onset of localization. For instance, fixing disorder value $W = 6.5$ we observe that $\nu = 1/2$ and $\nu = 1/5$ are situated well in delocalized and localized regions.

We further discuss the presence of many-body mobility edge in energy density in a single density sector of the Hamiltonian Eq. (3.1). Given the $U(1)$ symmetry, we would expect that a fixed filling sector presents MBME in energy density, similarly to the case of the random field XXZ spin chain [59]. In the middle of the spectrum the density of states is large and eigenstates may remain delocalized, while at the same disorder strength the states at the edges of the many-body spectrum are localized.

To explore the eventual presence of MBME in energy density in the half filling sector, we studied the energy resolved level spacing ratio $r_{\rm Av}(\epsilon, W)$. The results, displayed in the right panel of figure 3.4, show evidence of many-body mobility edge; the level spacing ratio, as a function of the energy density $\epsilon = \frac{E - E_{\rm min}}{E_{\rm max} - E_{\rm min}}$, where $E_{\rm min}$ and $E_{\rm max}$ are the ground state and the most excited state respectively, increases from the Poisson to the

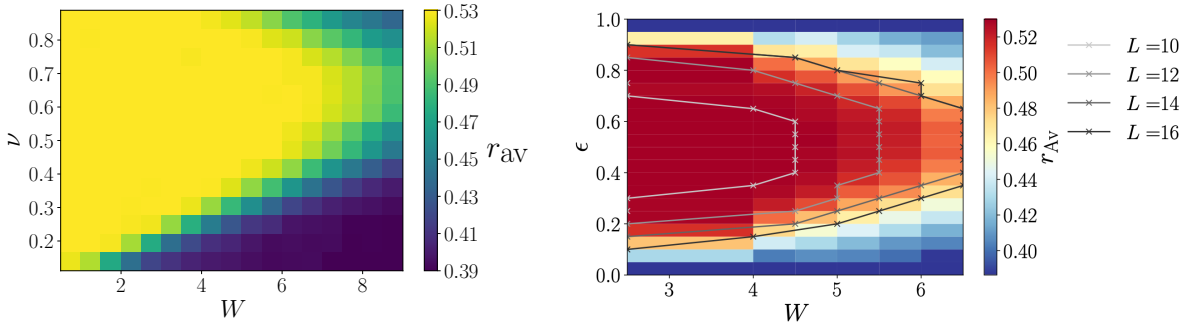

Figure 3.4: Left: the sharp difference of r_{av} obtained for different ν at the same disorder W clearly shows the MBME in our model. Interestingly, the mobility edge curve $W_c(\nu)$ is not symmetric, but is peaked around $\nu = 2/3$, implying that the states with the maximum number of pairs for fixed size are the hardest to localize. The data is obtained for a system of size $L = 18$, using shift-invert method with $10 - 10^3$ states from the middle of the spectrum and $5 \times 10^4 - 10^3$ disorder realizations. Right: the energy resolved level spacing ratio for $L = 16$ in the half filling sector shows clear evidence of MBME. In the center of the band r_{av} approaches the GOE value, while at large and small energy density it is close to the Poisson value. Furthermore, the MBME curves obtained for smaller systems seem to converge at increasing system size, thus suggesting the persistence of the MBME in the thermodynamic limit. The plot was obtained averaging over $n = 10^4,\ 2\times10^3,\ 5\times10^2,\ 10^2$ disorder realizations for increasing system size from $L = 10$ to $L = 16$.

GOE value as ϵ goes from the lower edge to the center of the spectrum and decreases again from the center to the upper edge. This variation is such that at a fixed disorder strength the low and high energy states are localized, while the center of the band is delocalized, thus defining a many-body mobility edge. The scaling of the MBME curves for different system size shows signs of convergence, suggesting stability of the MBME in the thermodynamic limit.

Another complementary probe of many-body localization or ergodicity is the entanglement entropy of eigenstates. While localized eigenstates are known to show area law [56, 79], thus converging to a single value as system size is increased, thermal states present an increasing entanglement which follows volume law and increases roughly linearly with system size [18]. Figure 3.5 illustrates the behavior of bipartite entanglement entropy for different disorder strengths and different fillings. On the one hand, the finite size scaling of entanglement entropy of eigenstates in the middle of the spectrum shows that for $\nu = 1/5$ and disorder $W > W_c \sim 6$ the entanglement is consistent with area-law. On the other hand, the entanglement of dense systems, $\nu = 1/2$, does not show a similar behavior. The finite size scaling, indeed, shows no crossing at these disorder values, thus suggesting volume-law of entanglement entropy for $\nu = 1/2$.

3.5 MPS simulations of quench dynamics

In our MPS simulation, we time evolve dilute states in large systems $L \geq 30$ up to time $T_{\text{max}} = 500$. For this we use the time-evolving block decimation (TEBD) algorithm described in Appendix B with a fourth-order Trotter evolution based on the ITensor library [176]. The main parameter involved in the time evolution algorithm is the time

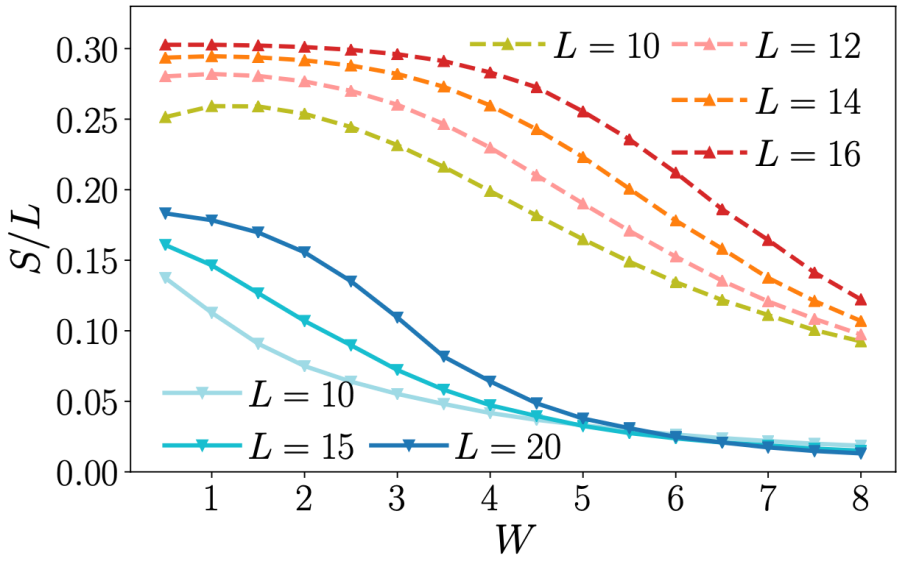

Figure 3.5: The behavior of half-chain entanglement entropy shows very distinct behavior for dilute (blue-shaded curves) and dense (red-shaded curves) states. The crossing in the dilute states implies that they entered the MBL phase, and thus have area-law entanglement entropy. On the other hand, dense states do not show a similar crossing in this range of disorder, suggesting that they are still in the ergodic phase. The data are obtained with shift-invert method for $10 - 10^3$ eigenstates in the middle of the spectrum and averaged over $5 \times 10^4 - 5 \times 10^3$ disorder realizations.

step δt used to split the unitary evolution into a sequence of gates. The error related to the finite size of the time step in the p-th order Trotter expansion grows as δt^p. The other source of error is the finite cutoff, ε, that governs the truncation of singular values in the singular value decomposition (SVD). Choosing a small enough value of the truncation guarantees quasi-exact results up to the times when the bond dimension χ saturates. After this point, the amount of information neglected is uncontrolled and it might affect the expectation values.

As we discuss in Appendix B, our choice of simulation parameters $\delta t = 0.05$, $\varepsilon = 10^{-9}$ and $\chi = 500$ guarantees the reliability of our results up to the times investigated.

3.6 Quench dynamics

Having provided numerical evidence for the coexistence of localized and delocalized phases in small systems, we turn to quantum quench dynamics that distinguishes MBL from ergodic phase [66, 177]. We consider quenches where the system is initially prepared in a product state and then evolved with the Hamiltonian (3.1). Starting with a density wave of period $1/\nu$, a configuration that contains no pairs, we calculate the density profile at late times. For the dilute case, $\nu = 1/5$, we use the time-evolving block decimation (TEBD) with the parameters discussed in the previous Section. This allows to monitor dynamics of systems as large as $L = 40$ sites up to times $T_{\max} = 500$. In the dense case ($\nu = 1/2$) we use ED and Krylov subspace time evolution method. While ED allows to access the infinite-time density profile, with the Krylov method, we simulate quantum dynamics up to $T_{\max} = 1000$.

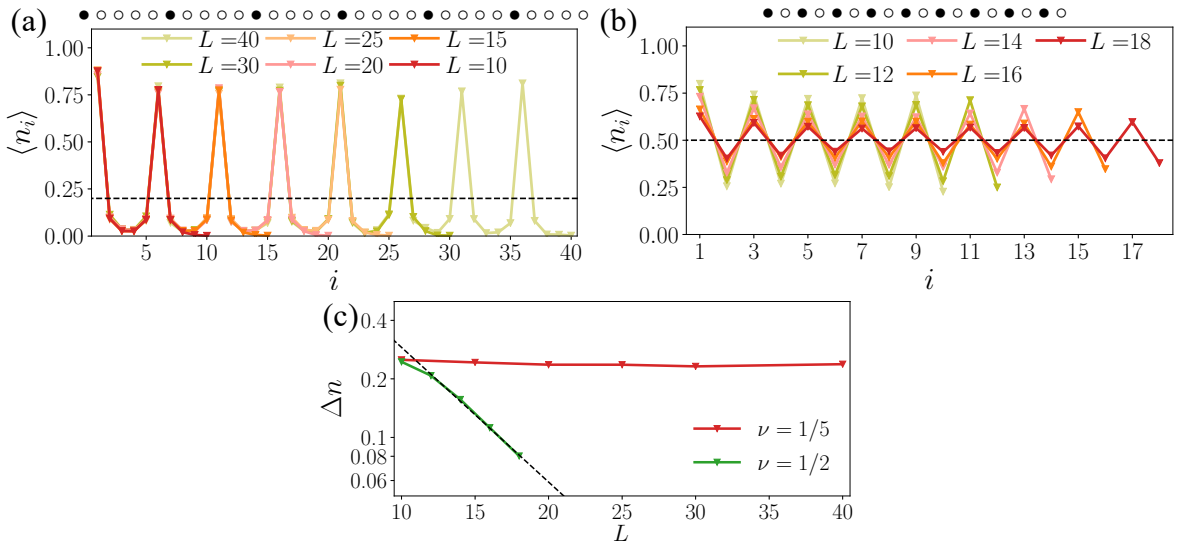

Figure 3.6: The quantum quench from the uniform density wave with period $1/\nu$ reveals memory of the initial state at $\nu = 1/5$ in (a), whereas in the dense case $\nu = 1/2$ (b) the charge pattern relaxes to zero exponentially in the system size. This is shown in (c) through the exponential decay of $\Delta n = (1/L)$. The data are generated using TEBD and Krylov (ED) dynamics using between 5×10^4–100 (dilute) and 3×10^4–10^3 (dense) disorder.

The density profiles at late times look very different in the dense and dilute cases. While in the dilute case the system retains memory of the initial state, see Fig. 3.6(a), at $\nu = 1/2$ quantum dynamics leads to a progressively more uniform density profile with increasing system size, Fig. 3.6(b). In order to quantify the difference in the form of the density profile at late times, in Fig. 3.6(c) we plot the average deviation of the density from the equilibrium thermal value ν,

$$\Delta n = \frac{1}{L} \sum_{i=1}^{L} |\langle \hat{n}_i(T_{\max}) \rangle - \nu|. \tag{3.2}$$

The deviation of late-time density from the thermal value, Δn, in the dense regime decays exponentially with the system size as $\Delta n \sim e^{-L/\xi_{\mathrm{T}}}$, where $\xi_{\mathrm{T}} \simeq 6.27$. In contrast, for the dilute case Δn shows no dependence on the system size, as is apparent in the density profiles. The characteristic length ξ_{T} extracted in the dense case gives the minimum size for genuine egodic bubbles that can destroy the MBME according to Ref. [85].

Having confirmed the coexistence of localized and delocalized states at different values of particle density ν for the same disorder strength, we proceed with a more detailed study of the effect of the presence of a bubble, whose behavior is central to the mechanism proposed in [85]. Figure 3.7(a) illustrates the evolution of a non-uniform initial state, where a dense region represents the bubble. The bubble region consists of 8 sites with two pairs of particles and has a local density of $\nu = 1/2$. The bubble is followed by a period-5 density wave that occupies $L - 10$ sites and two additional empty sites at the end of the chain. Although having $\nu = 8/30 > 1/5$, this state is still in a localized sector, as shown in Figure 3.4. The bubble leaks only weakly into the dilute region even at late times, see Fig. 3.7(a), with particles far away from the bubble not being affected. In contrast, in the dense case, Fig. 3.7(b), the bubble with average density of $\nu = 2/3$ successfully melts the period-3 density wave state throughout the system.

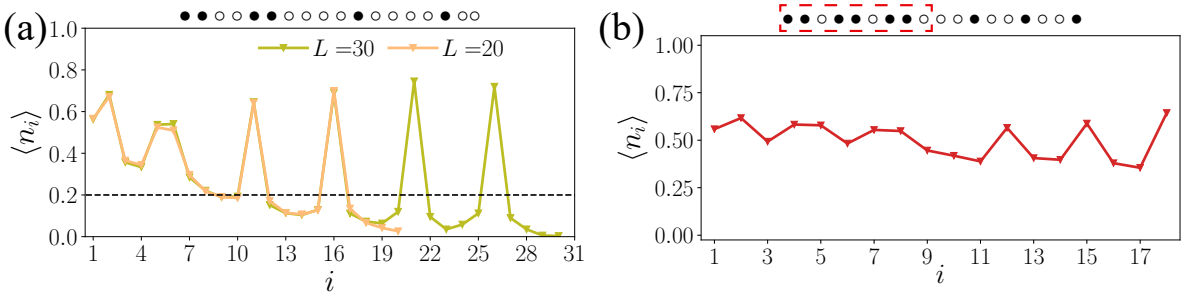

Figure 3.7: (a) The density profile of a quench from a non-homogeneous initial state featuring a dense thermal *bubble* (dashed red rectangle in the top of the figure) remains far from thermal equilibrium in the dilute case. (b) On the contrary, in the dense region of the Hilbert space the bubble is very efficient in restoring thermalization. The data are generated using TEBD and Krylov (ED) dynamics using between 5×10^4–100 (dilute) and 3×10^4–10^3 (dense) disorder.

Next, in Figure. 3.8(a) and (b) we further illustrate the differences between the density dynamics in the dense and dilute cases in presence of a bubble. In both cases we plot the density of particles within subregions of small size k,

$$\tilde{n}_i = \frac{1}{k} \sum_{j=i}^{i+k-1} \langle n_j \rangle, \tag{3.3}$$

as shown at the top of the plot. In the dilute case, Fig. 3.8(a), we observe that $\tilde{n}$ remains far from its thermal value even at late times, in contrast with [85], where an ergodic region larger than ξ_T is expected to delocalize the system. The densities within the bubble regions and adjacent to the bubble seem to saturate, while the far from the bubble we observe very slow dynamics, and on this timescales no thermalization takes place. In contrast, the dense case, Fig. 3.8(b), shows that all expectation values evolve towards equilibrium, although the regions far away from the center of the chain display slow, logarithmic in time, growth of the density.

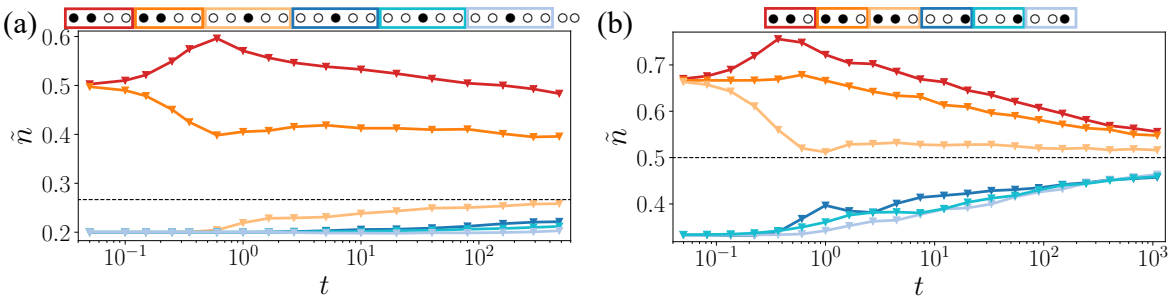

Figure 3.8: Dynamics of the coarse-grained density $\tilde{n}$ in dilute $\nu = 8/30$ and dense $\nu = 1/2$ configurations featuring a thermal bubble. (a) The time dynamics of density in the coarse grained regions (see the legend at the top) shows absence of significant relaxation in regions away from the bubble for dilute states. The density in the region at the boundary with the bubble increases logarithmically in time. (b) On the contrary, in dense configurations saturation to the thermal value (black dashed line) is observed throughout the chain, although logarithmically slow. The data are generated using TEBD and Krylov (ED) dynamics using between 5×10^4–100 (dilute) and 3×10^4–10^3 (dense) disorder.

Finally, we study the dynamics of the bipartite entanglement entropy, S_{vN}, see Fig. 3.9(a) and (b). The entanglement is defined as

$$S_{\mathrm{vN}} = -\operatorname{tr}\rho\ln\rho, \quad \rho = \operatorname{tr}_B[|\psi(t)\rangle\langle\psi(t)|\,, \tag{3.4}$$

where ρ is the reduced density matrix of the left subregion calculated from $|\psi(t)\rangle = e^{-i\hat{H}t}|\psi_0\rangle$. Different entanglement cuts shown at the top of Fig. 3.9(a) and (b) are encoded by their color. Consistent with MBL, the increase of entanglement in the region close to the bubble is logarithmic in time in Fig. 3.9(a) [52, 54, 55, 68]. The entanglement across the cuts further away from the bubble begins to grow at significantly later times. For these more distant cuts, the initial uprise in entanglement corresponds to a slow logarithmic change of density [see Fig. 3.8(a)], and after saturation of density dynamics, we expect the onset of logarithmic growth of entanglement. In contrast, the entanglement dynamics in Fig. 3.9(b) is always faster than logarithmic. In the next Section, we provide more details on the contribution of particle transport to entanglement [68, 178], demonstrating that it is responsible for logarithmic entanglement increase, in agreement with [179], whereas the configurational entanglement grows faster than logarithmic, and total entropy shows power-law increase.

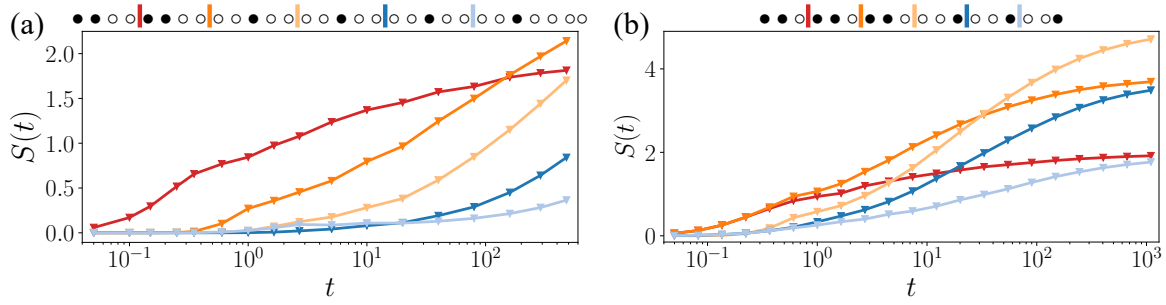

Figure 3.9: Dynamics of entanglement entropy in dilute $\nu = 8/30$ (a) and dense $\nu = 1/2$ (b) configurations featuring a thermal bubble. (a) The onset of logarithmic entanglement dynamics after a transient is visible for all cuts (see the legend at the top) away from the bubble. This is a hallmark of many-body localization, thus suggesting stability of MBL in this configuration. (b) entanglement entropy displays faster than logarithmic growth for all cuts, indicating thermalization. The data are generated using TEBD and Krylov (ED) dynamics using between 5×10^4–100 (dilute) and 3×10^4–10^3 (dense) disorder realizations.

So far, we discussed density and entanglement entropy dynamics in two families of different quantum quenches, namely a uniform state or a bubble joined to a more dilute remainder. Below we present details for the quenches in presence of a bubble, supporting the stability of MBL in this setting. In addition, we discuss the dynamics resulting from an initial state containing a density wave of particle *pairs*.

3.6.1 Pair density and entanglement dynamics in presence of a bubble

Since particle pairs are the most mobile objects, we consider the pair density in quenches that are initialized with the bubble (see Fig. 3.7). The pair density is of special interest in these quenches as Ref. [85] suggested that the instability of the system is ascribed to the ability of the bubble to move. In our model the bubble consists of several pairs, thus motion of the bubble throughout the system would imply the spreading of pairs.

The pair density defined as $\langle n_i n_{i+1} \rangle$ measured at late or infinite times is shown in Fig. 3.10. In the dense case the late time pair density profile supports delocalization: at late times the density of pairs becomes homogeneous throughout the formerly more dilute region of the system. We note, that the pair density is not a conserved quantity, and it can increase in the process of unitary dynamics.

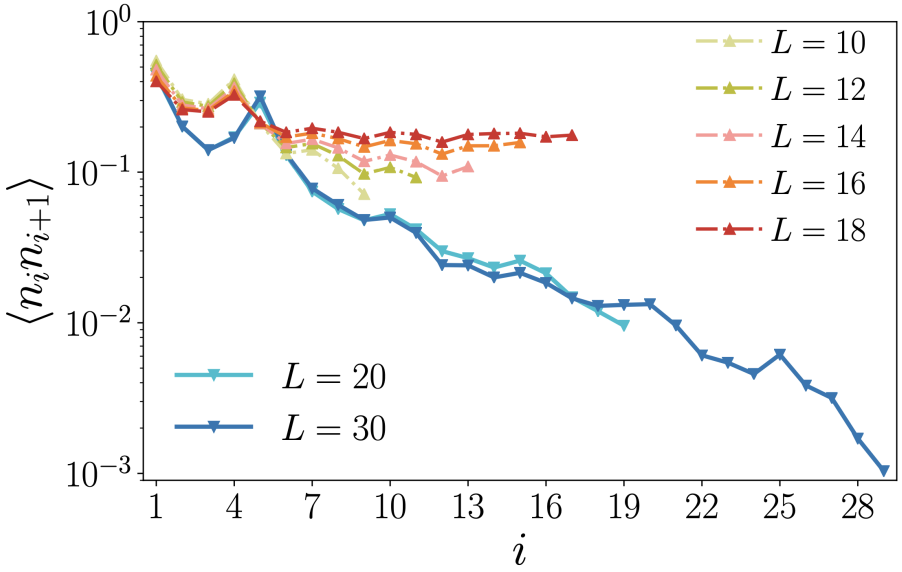

Figure 3.10: The finite size scaling of the pair density $\langle n_i n_{i+1} \rangle$ shows opposite trend for the dense and dilute cases. The red-shaded curves represent $\nu = 1/2$ configurations: increasing the system size (from yellow to dark red) the pair density becomes more uniform and approaches the thermal value, hence in the thermodynamic limit the probability of finding a pair far from the bubble is almost the same as finding it in the bubble. On the contrary, blue curves ($\nu = 1/5$) show exponential vanishing of the pair density and, furhtermore, increasing system size (from light blue to dark blue) the density decreases, suggesting that at the thermodynamic limit there will be no pair outside the thermal region. Data were obtained with ED, Krylov ($T_{\max} = 1000$) and TEBD ($T_{\max} = 500$) algorithms averaging over 100 disorder samples for the largest MPS simulations ($L = 20, 30$), $3 \times 10^4, 10^4, 5 \times 10^3$ and 10^3 for ED (from $L = 10$ to $L = 16$) and over 10^3 for Krylov algorithm ($L = 18$).

In contrast, for the dilute case the pair density profile has a pronounced exponential tail away from the initial ergodic region. This shows that pairs spreading away from the initial bubble do not delocalize when encountering additional particles on their way. Indeed, while the late time pair density profile has small peaks around the initial position of particles, these peaks are not very pronounced. In addition, the study of the pair density profile in the uniform density wave at $\nu = 1/5$ reveals an almost constant behavior, centered around $\langle n_i n_{i+1} \rangle \sim 10^{-3}$, which corresponds to the values reached at the end of the exponential tail in the system with $L = 30$ in Fig. 3.10.

Next, we focus on understanding different contributions to entanglement growth. Exploiting the $U(1)$ symmetry of our model and following Refs. [68, 178], we split the von Neumann entanglement entropy into a configuration and a particle transport contributions. Indeed, due to conservation of the total number of bosons the full reduced density matrix ρ must have a block-diagonal form. Individual blocks within ρ can be written as

$p_n\rho^{(n)}$, where p_n gives the probability to have n particles in the susbsystem A and $\rho^{(n)}$ is normalized such that $\mathrm{tr}\,\rho^{(n)} = 1$. Using such representation of the reduced density matrix we can split the full entropy into $S_{vN} = S_C + S_n$ as:

$$\begin{aligned} S_{vN} &= -\,\mathrm{tr}\,\rho\log\rho = -\sum_n p_n\,\mathrm{tr}\,\rho^{(n)}\log\left(p_n\rho^{(n)}\right) \\ &= -\sum_n p_n\log p_n - \sum_n p_n\,\mathrm{tr}\,\rho^{(n)}\log\rho^{(n)} \\ &= S_n + S_C. \end{aligned} \tag{3.5}$$

In this way the entanglement growth is split into two contributions: one coming from the particle transport, S_n, and another originating from dephasing between different configurations with the same particle number, S_C. Interestingly, Fig. 3.11 shows that while the overall entanglement entropy grows faster than logarithmic, this is due only to the configuration part (yellow curve) and the entanglement due to particle transport has logarithmic growth. The logarithmic growth of S_n is consistent with the logarithmic particle transport presented in Fig. 3.8(b) and with other transport measures presented in the next section. We identify this behavior as a hallmark of MBME, and note that it happens on long, yet experimentally accessible timescales $t \sim 50(\hbar/t_1)$.

Recent work [179] demonstrated that logarithmic growth of the number entropy is expected in the thermal phase, provided there is particle transport over distances that increase as a power-law in time, $l \propto t^{\nu}$. [1] The authors also predict a power-law scaling of the

[1] We note, that although the authors of Ref. [179] report unbounded growth of the number entanglement in the MBL phase, the successive work of Luitz and Bar Lev [180] shows that this is due to rare particle fluctuations around the boundary between the two subsystems and the growth disappears at large enough system size.

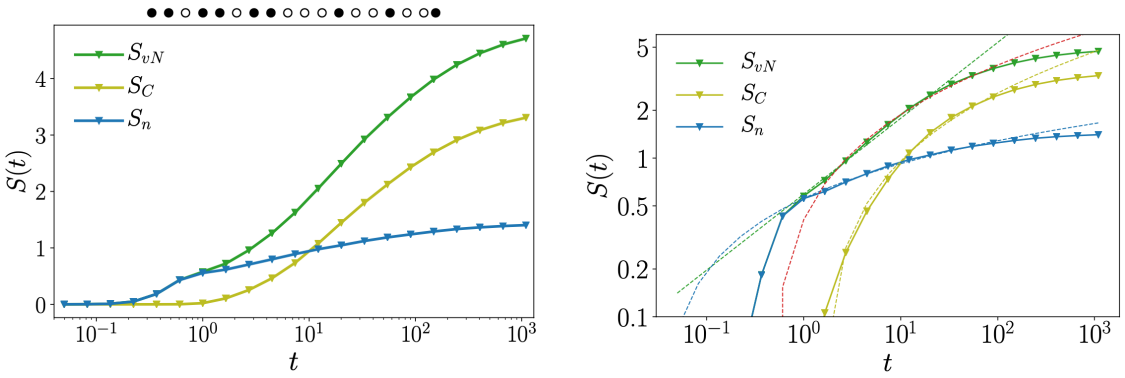

Figure 3.11: The different contributions to the entanglement entropy of the bubble show that the overall behavior of the von Neumann entropy is faster than logarithmic. Nevertheless this behavior can be ascribed to the sole configurational entropy S_C, while the particle transport contributes to the purely logarithmic growth. The log-log plot of the entropies discussed in Eq. (3.5) confirms that only the total entropy is growing as a power-law, while both S_n and S_c grow slower. In particular, S_n grows as a first degree polynomial in $\log(t)$ (dashed green line) and S_C as a second degree polynomial in $\log(t)$ (orange dashed line). The sum of these two behaviors (red dashed line) agrees with the power-law behavior (dashed blue line). The curves are obtained through Krylov evolution up to $T_{\max} = 1000$ averaged over 1000 disorder realizations for $L = 18$ and $W = 6.5$.

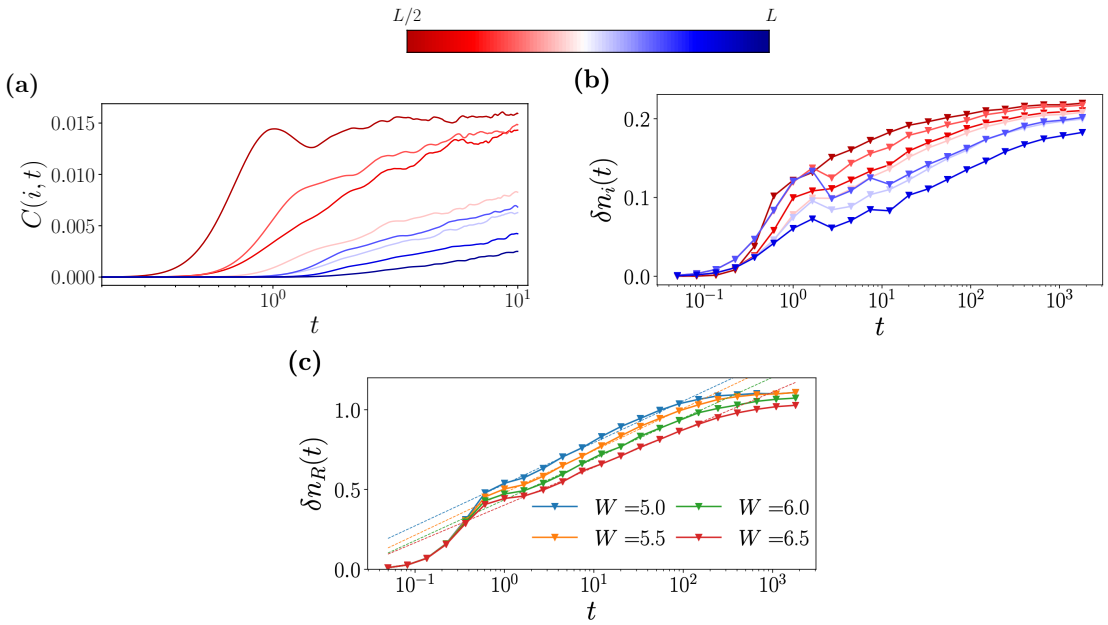

Figure 3.12: Time dynamics of correlation functions (a), local density fluctuations (b) and density fluctuations in the dilute half of the chain (c) all show, after an initial power-law growth, logarithmic increase with time. In particular, correlations far away from the central site (blue curves, as encoded in the legend above) show signs of a logarithmic light-cone. Similarly, local density fluctuations deep in the localized region present slower dynamics. Finally, panel (c) shows how increasing disorder slows the growth of the global density fluctuation of the dilute half. These results were obtained with the Krylov method on system size $L = 18$ for $W = 6.5$ (a), with ED on system size $L = 16$ and $W = 6.5$ (b) and for different disorder values (c), averaging over 200 disorder realizations.

configuration entropy, which we do not observe, as shown in figure 3.11. We attribute the slower than power-law growth of configuration entanglement to the localized nature of the right half of the chain, which in turn reduces the number of possible configurations until the particle transport from the left half leads to delocalization.

Further analysis of the entanglement dynamics shows that S_{vN} grows in a power-law fashion $S_{vN} \approx at^b$, corresponding to the dashed blue fit in the right panel of Fig. 3.11, over a relevant time interval. On the other hand, both S_n and S_c behave as polynomials in $\log(t)$, of first and second degree respectively, and their sum (dashed red line) reasonably approximates the power-law behavior of S_{vN}, as one can expand $t^b \approx 1+b\log(t)+\frac{b^2}{2}\log^2(t)$.

Finally, to support our interpretation of logarithmic increase of S_n as due to transport, we study the dynamics of density correlation functions and fluctuations. Figure 3.12 presents the dynamics of connected correlation functions $C(i,t) = \langle \hat{n}_i \hat{n}_{L/2} \rangle - \langle \hat{n}_i \rangle \langle \hat{n}_{L/2} \rangle$ with respect to the central site of the chain, the local density fluctuations $\delta n_i = \langle \hat{n}_i^2 \rangle - \langle \hat{n}_i \rangle^2$ and the density fluctuations in the dilute part of the chain $\delta n_R = \langle \hat{n}_R^2 \rangle - \langle \hat{n}_R \rangle^2$, where $\hat{n}_R = \sum_{i=L/2}^{L} \hat{n}_i$. The logarithmic dynamics of these quantities is consistent with the behavior of number entropy, thus proving the further support for the existence of slow transport in the dilute part of the chain.

3.6.2 Quench dynamics from a pair density wave state

Finally, we consider quenches from configurations featuring a pair-density wave of period $2/\nu$, as opposed to the single-particle density wave considered above. These configurations accommodate the maximal possible number of pairs in the uniform state. Figure 3.13 confirms that such state is localized at $\nu = 1/5$ and is relaxing in the dense case. Dense systems display strong dependence on the system size and increased tendency towards relaxation at larger system sizes, L. In contrast, at $\nu = 1/5$ the late time density profile has almost no dependence on the size of the system. In particular, even at very large lengths the curves do not approach the average density represented by the dashed black

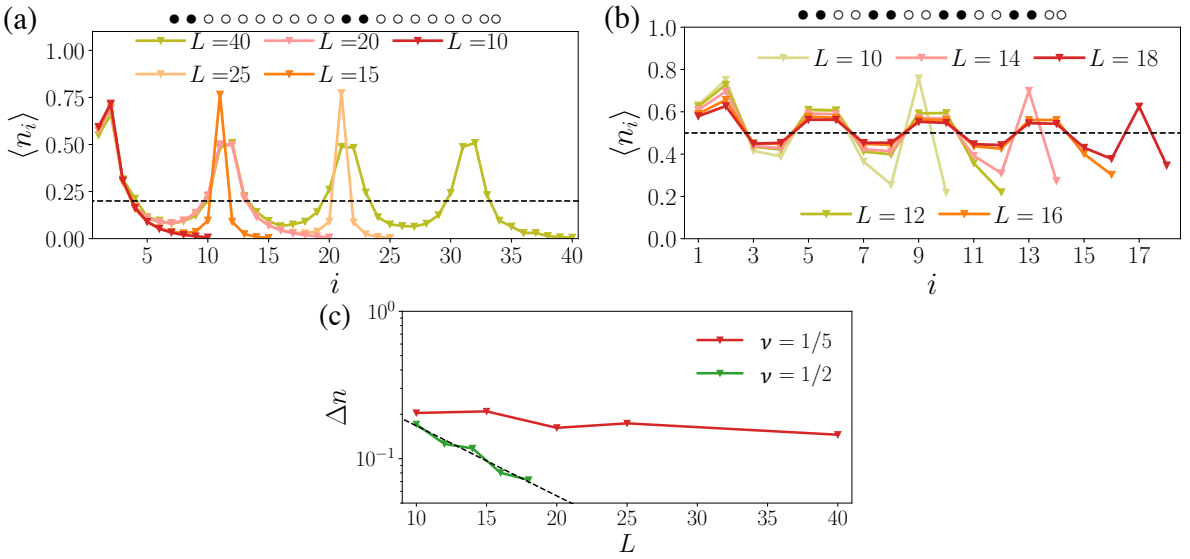

Figure 3.13: The late time density profiles of the pair density waves at dense, $\nu = 1/2$, and dilute, $\nu = 1/5$, fillings show very different behavior. (a) Dilute configurations are essentially frozen, and do not approach the thermal density represented by the black dashed line. (b) In contrast, at $\nu = 1/2$ relaxation is enhanced at larger L. (c) The deviation of late time density from the thermal value decay exponentially with system size as $e^{-L/\xi_T^{\text{pair}}}$ with $\xi_T^{\text{pair}} \approx 8.1$. In contrast for $\nu = 1/5$, the residual density remains nearly constant with system size and naïve fit to the exponential gives an order of magnitude larger scale, $\xi_T^{\text{dilute}} \approx 84$. Data at $\nu = 1/5$ is obtained via ED ($L = 10$, $L = 15$, and $L = 20$ with 5×10^4, 10^4, and 2×10^3 disorder realizations), Krylov time evolution ($L = 25$, $T_{\max} = 10^3$ and 10^3 disorder realizations) and TEBD ($L = 40$, $T_{\max} = 300$ and 100 disorder realizations). For $\nu = 1/2$ we used ED ($L = 10$, 12, 14, and 16 with 3×10^4, 10^4, 5×10^3, and 10^3 disorder realizations) and Krylov time evolution ($L = 18$, $T_{\max} = 10^3$, and 10^3 disorder realizations).

line. The deviation from the thermal value Δn has an oscillatory behavior as system size changes, due to the different number of particle pairs when N is even/odd.

3.7 Bubble tunneling vs. decay processes

The quench dynamics discussed above suggests that a bubble is not able to spread through the entire localized chain and remains in the vicinity of its initial position. At the same time, most of our quench simulations are restricted to finite, albeit long, times. In order

to give a complementary evidence for the bubble localization, we return to eigenstate properties that effectively probe the infinite time limit.

We start with an initial product state in the half-filled case illustrated for $L = 12$,

$$|\psi_1\rangle = \boxed{\bullet\bullet\circ\bullet\bullet\circ}\circ\circ\bullet\circ\circ\bullet, \tag{3.6}$$

that contains a bubble of $k = L/2$ sites with $\nu = 2/3$ filling (boxed region), followed by a sparser region with the same number of sites and density $\nu = 1/3$. To quantify the relation between the probability of the bubble tunneling to the opposite end of the system and the probability of the bubble spreading throughout the system, we use a spatial reflection of $|\psi_1\rangle$ and uniform density wave as a representative of the state with bubble tunneling and spreading, respectively:

$$\left|\psi_2^{\mathrm{t}}\right\rangle = \bullet\circ\circ\bullet\circ\circ\boxed{\circ\bullet\bullet\circ\bullet\bullet}, \tag{3.7}$$

$$|\psi_2^{\mathrm{s}}\rangle = \bullet\circ\bullet\circ\bullet\circ\bullet\circ\bullet\circ\bullet\circ\bullet, \tag{3.8}$$

illustrated for $L = 12$ and $\nu = 1/2$ filling. For dilute configurations at $\nu = 1/5$ we define the bubble as a region of size $2(\nu L - 1)$ with density $\nu = 1/2$, joined with a dilute remainder. For $L = 20$ such a state is:

$$|\psi_1\rangle = \boxed{\bullet\bullet\circ\bullet\circ\circ}\circ\circ\circ\circ\circ\circ\circ\bullet\circ\circ\circ\circ\circ\circ\circ\circ$$

.

It is straightforward to show that the infinite time average probability of finding the system with the wave function $e^{-i\hat{H}t}\,|\psi_1\rangle$ in the product state $|\psi_2\rangle$ is given by

$$\mathcal{P}(|\psi_1\rangle, |\psi_2\rangle) = \sum_{\alpha=1}^{\mathcal{N}} |\langle E_\alpha|\psi_1\rangle \langle E_\alpha|\psi_2\rangle|^2, \tag{3.9}$$

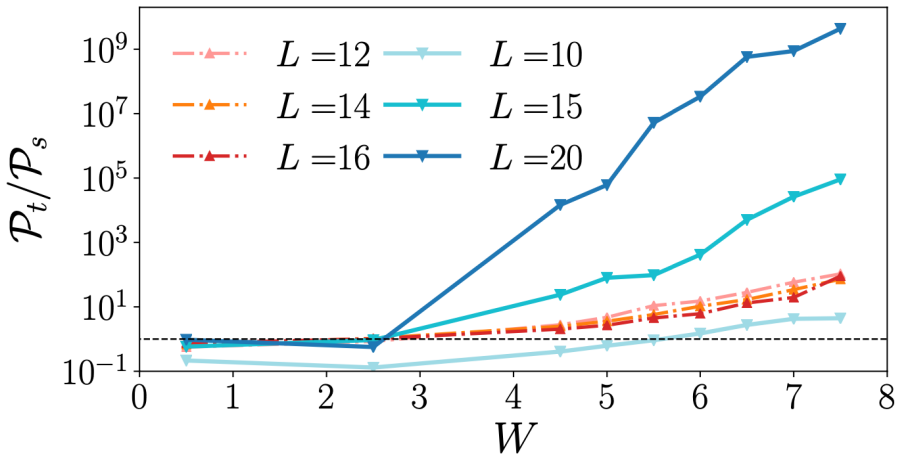

Figure 3.14: The rapid increase of the ratio of $\mathcal{P}_{\mathrm{s}}/\mathcal{P}_{\mathrm{t}}$ with system size and disorder strength reveals that in the dilute case, $\nu = 1/5$ the probability for bubble spreading is strongly enhanced compared to the probability of bubble tunneling to the opposite end of the system. For the dense case these two probabilities are of the same order and approach each other with increasing system size in a broad range of disorders. Averaging is done over at least 2.5×10^3 disorder realizations.

where $\{|E_\alpha\rangle\}$ are the complete set of eigenstates of $\hat{H}$. Eq. (3.9) quantifies the similarity in the expansion of two different states $|\psi_{1,2}\rangle$ over the basis $|E_\alpha\rangle$ and reduces to the conventional participation ratio when $|\psi_1\rangle = |\psi_2\rangle$.

In order to reveal the relation between bubble decay and tunneling processes, we calculate the ratio of probabilities of bubble decaying, $\mathcal{P}_\mathrm{s} = \mathcal{P}(|\psi_1\rangle, |\psi_2^\mathrm{s}\rangle)$, with $|\psi_2^\mathrm{s}\rangle$ from Eq. (3.8), to bubble tunneling, $\mathcal{P}_\mathrm{t} = \mathcal{P}(|\psi_1\rangle, |\psi_2^\mathrm{t}\rangle)$ with $|\psi_2^\mathrm{t}\rangle$ from Eq. (3.7). In the dense case, these two probabilities are of the same order and moreover tend to identity with increasing system size as expected in the delocalized phase, see Fig. 3.14. In the dilute case, the ratio $\mathcal{P}_\mathrm{s}/\mathcal{P}_\mathrm{t}$ is rapidly increasing with both disorder, and system size. This proves that the bubble tunneling processes are strongly suppressed compared to the processes where the bubble spreads throughout the system, calling into question the applicability of the resonance argument of [85].

3.7.1 $\mathcal{P}$ as a function of bubble distance

To further analyze the bubble tunneling, we study the behavior of the mutual inverse participation ratio $\mathcal{P}$ for states where the dense region is displaced by some distance d. The mutual IPR assumes very different values depending on the nature of the two states: values of mIPR $O(\mathcal{N})$ correspond to two vectors that have similar expansion over eigenstates, and are hence connected during the time-evolution. On the other hand, large values of mIPR imply that the two states have different support in the eigenstates basis, suggesting that evolving from one to the other is extremely unlikely.

In our analysis we measure the mIPR, $\mathcal{P}_d^{-1} = \mathcal{P}^{-1}(\psi_L, \psi_d)$, between the following states

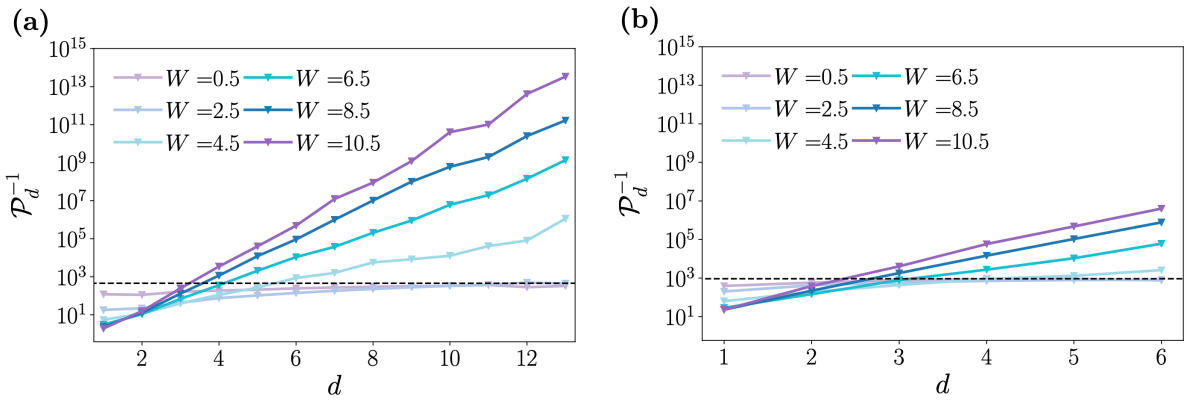

Figure 3.15: The mutual IPR, $\mathcal{P}_d^{-1}$, that quantifies the inverse probability of bubble tunneling d sites, increases exponentially with d at strong disorder. At weak disorder the mIPR approaches the Hilbert space dimension, $\mathcal{N}$, shown by a dashed line. In the dilute system in (b), $W = 4.5$ marks the onset of the exponential growth, suggesting that the thermal bubble is frozen at its initial position. On the other hand, for $\nu = 1/2$, in (a), the clear exponential behavior emerges only at larger disorder. $\mathcal{P}_d^{-1}$ was calculated for system sizes $L = 15$ and $L = 12$ in dilute and dense case respectively and averaged over 10^4 disorder realizations.

in the dense limit (half-filling, $L = 12$),

$$|\psi_L\rangle = \boxed{\bullet\bullet\bullet\bullet\bullet\bullet}\circ\circ\circ\circ\circ\circ, \tag{3.10}$$

$$|\psi_d\rangle = \underbrace{\circ\circ\circ}_{d}\boxed{\bullet\bullet\bullet\bullet\bullet\bullet}\circ\circ\circ\,. \tag{3.11}$$

Here we use a bubble that contains all particles to maximize the range of achievable displacements. For the dilute case, $L = 15$, we use similar pair of states with a bubble containing 3 particles ($\nu = 1/5$).

In the thermal phase, eigenstates are approximately given by random vectors in the Hilbert space and their average overlap with other normalized vectors approaches the value predicted by random matrix theory, irrespective of the state or the eigenstate. In the weak disorder limit, we then expect $\mathcal{P}_d^{-1}$ to be independent on the distance between the two bubbles and to have the same behavior as the conventional IPR: $\mathcal{P}_d^{-1} \sim \mathcal{N}$. This expectation is confirmed by the results presented in fig. 3.15(a) and (b) for $W = 0.5$.

On the other hand, in the MBL phase eigenstates are not similar to random vectors, but instead are characterized by a set of local integrals of motion that have a finite overlap with the local particle density. Thus, two product states with globally different arrangement of particles are expected to have drastically different expansion over eigenstates. Therefore, we expect $\mathcal{P}_d^{-1} \propto \exp[d/\xi]$. As presented in figure 3.15(a) and (b), at strong disorder our results support this hypothesis for both dilute (a) and dense (b) states.

At intermediate disorder strength, we observe a qualitative difference between dense and dilute cases. Dilute configurations, Fig. 3.15(a), show exponential behavior already at $W = 4.5$, whereas dense states in Fig. 3.15(b) need much stronger disorder to clearly present the same trend. This result confirms the presence of mobility edge and is consistent with the observed absence of pair spreading reported in Figure 3.10 and also with the finite size scaling of mIPRs shown in the main text, Fig. 3.14.

3.8 Dynamical probe of the absence of resonances

The discussion on mutual IPR showed how tunneling processes are strongly suppressed in the dilute case of our model. In addition to eigenstates analysis, we also studied long time dynamics of states with a thermal bubble. In this way, it was possible to verify whether a bubble initialized at a certain position can dynamically give rise to a dense region somewhere else in the chain. In order to study this process we defined a projector onto the subset of Hilbert space that has large density in a certain region. More specifically, we define

$$\hat{P}_{\nu_c}(L_0, i) = \sum_{|\phi_\alpha\rangle \in \mathcal{C}} |\phi_\alpha\rangle \langle\phi_\alpha|\,, \tag{3.12}$$

where states $|\phi\rangle$ are all possible product states that satisfy the condition $\nu \geq \nu_c$ in the region $[i, i + L_0]$. This projector selects all configurations where the system is locally above the mobility edge. We notice that $\hat{P}_{\nu_c}(L_0, i)$ takes into account all possible configurations, thus considering also the entropic factor.

In order to understand what is the minimal required size of the region L_0, we use the lengthscale extracted from the decay of Δn. The fit in Fig. 3.6(c) yields $L_0 \simeq 6 \div 7$, while fit in Fig. 3.13(c) gives a somewhat larger scale. We define an initial state $|\psi_0\rangle$ that has

an entangled dense region of size approximately L_0 (described by a linear superposition of product states $|\phi_i\rangle$) followed by a product state:

$$|\psi_0\rangle = \frac{1}{\sqrt{N_C}} \sum_{i=1}^{N_C} |\phi_i\rangle \otimes |\circ\circ\circ\bullet\circ\circ\rangle \,. \tag{3.13}$$

Below, we fix the overall density to $\nu = 1/4$ and $W = 6.5$, which still corresponds to a localized system. The dense region is obtained as a superposition of different configurations with $N-1$ particles in $L_0 = 2(N-1)$ sites. The remaining particle is initialized in the middle of the last segment of the chain. For instance, for $L = 16$ this results into the following initial state:

$$|\psi_0\rangle = \frac{1}{\sqrt{N_C}} \Big[\boxed{\bullet\bullet\circ\bullet\circ\circ} \circ\circ\circ\circ\bullet\circ\circ\circ\circ\circ + \boxed{\bullet\circ\bullet\circ\bullet\circ} \circ\circ\circ\circ\bullet\circ\circ\circ\circ\circ + \boxed{\bullet\bullet\bullet\circ\circ\circ} \circ\circ\circ\circ\bullet\circ\circ\circ\circ\circ + \ldots \Big], \tag{3.14}$$

where the boxed area contains a dense entangled bubble and the remainder is in the dilute state.

The initial state $|\psi_0\rangle$ is then evolved through the Hamiltonian (3.1) in a quench protocol. After time evolution up to a maximum time $T_{\max} = 1000$, we measure $\langle P_{\nu_c}(L_0, d)\rangle = \langle\psi(t)|\, \hat{P}_{\nu_c}(L_0, d)\, |\psi(t)\rangle$, which quantifies the probability of encountering a bubble shifted by d sites from the initial position of the bubble.

Finally, averaging over all different product states in the dilute part of the chain and over disorder we obtain the data in Fig. 3.16. This plot reveals that the probability of

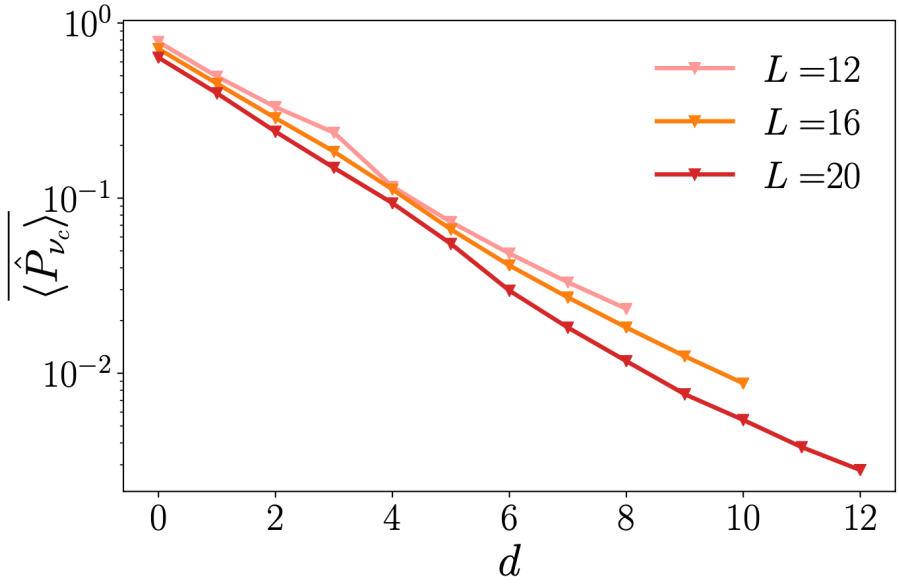

Figure 3.16: The late time evolution of $\overline{\langle P_{n_c}(L_0, d)\rangle}$ shows exponential decay for all the system sizes studied ($L = 12, 16, 20$ at density $\nu = 1/4$). Furthermore, we notice that increasing the system size the exponential vanishing becomes more severe, suggesting that in the thermodynamic limit there would be no motion of the bubble at all. These results were obtained using $10^4, 5 \times 10^3$ and 10^3 disorder realizations for the system sizes from smaller to larger.

having a dense ($\nu > \nu_c$) region decays exponentially with the distance d from its initial location. This is in agreement with our long-time TEBD dynamics, Fig. 3.10, that reveals localization of individual pairs. Thus, we conclude that the bubble does not spread resonantly but rather tunnels throughout the system. Moreover, the finite size scaling analysis shows that increasing the system size the decay of $\overline{\langle P_{\nu_c}(L_0, d)\rangle}$ with distance d is enhanced. Therefore in the dilute regime of our model the bubble remains localized around its initial position.

3.9 Experimental realization

Finally, we discuss a possible way to observe the physics related to MBME in experiments with ultracold atoms. Within the disordered Aubry-André bosonic Hamiltonian,

$$\hat{H} = \sum_i \left[t(a_i^\dagger a_{i+1} + \text{h.c.}) + \epsilon_i n_{i,\sigma} + U n_i(n_i - 1) \right], \tag{3.15}$$

that is actively used to study MBL physics [68, 69], the bubbles can be represented by regions with $\langle a_i^\dagger a_i \rangle = \rho > 1$ bosons per site. A particle within such region has a hopping matrix element enhanced by the Bose-factor of $\langle \rho \rangle$, thus playing the role of hopping t_2 in model (3.1). In the regime of densities and disorder strengths such that the enhanced hopping $\langle \rho \rangle t$ corresponds to localization lengths significantly larger than lattice spacing, $\xi_{\text{dense}} > a$, whereas a single boson localization length is $\xi \lesssim a$, this model will implement similar physics to our toy model. Note that at the same time it is important to keep interaction U low enough, $U \leq t$, to avoid the formation of minibands related to long-lived doublons.

By initializing the system in a product state with a dense region of bosons in the center of the trap along with low density of bosons away from such a region, the dynamics under Hamiltonian (3.15) will probe the ability of the bubble to melt the imbalance [66] away from its original position. From our simulations we expect the absence of imbalance relaxation far away from the bubble. In a different direction, doublons [181, 182] or second species of particles not subject to disorder [70] are also promising candidates that can play a role of the bubble.

3.10 Discussion

We presented a model with MBME in particle density and investigated its properties numerically using ED and time evolution with MPS. We find strong evidence of the persistence of localization at infinite times for small systems and also observe memory of initial configuration until times of $T_{\max} = 500$ for systems with up to $L = 40$ sites. These times are at least two orders of magnitude larger compared to the inverse local hopping, $\hbar/t_1$, and are achievable with cold atoms experiments. While we cannot rule out a residual very slow delocalization at much later times, the constructed model allows us to bound the timescale up to which the localization remains stable in very large systems that are beyond the reach for ED.

The model with MBME in particle density presented in this work allows for direct tests of the arguments about the instability of MBME [85]. In order for bubble to move throughout the system it is important that the bubble does not disappear by spreading and that configurations with bubbles situated at different locations are effectively coupled to each

other. Our simulations reveal that dilute systems have no trace of bubble reemerging at a different location within the system. Moreover, even the expectation value of the pair density $\langle n_i n_{i+1} \rangle$ (pairs are building blocks of the bubble) is exponentially suppressed away from the original location of the dense bubble. In an alternative approach, we directly test the probability of the bubble to emerge at the opposite end of the system at infinite time and find it to be strongly suppressed.

To conclude, we expect that the proposed model will enable further investigations of particle density MBME. Studies of the structure of matrix elements, extension of the theory of LIOMs [56, 57] to systems with MBME in particle density [169], and studies of the effect of a small bath on a localized system [61, 87, 88, 183] using our model represent promising avenues for future work.

CHAPTER 4

Many-body localization proximity effect

This chapter collects our work on many-body localization proximity effect. We introduce a model featuring two species of hard-core bosons, *disordered* bosons form an Anderson insulator, while *clean* bosons are free particles. Upon turning on the interaction among the two bosonic species, we investigate the stability of localization and the onset of many-body localization proximity effect. Via a mean field approach and perturbative arguments, we expect localization of both particle types in the strong interaction limit. Our numerical simulations on large chains in the case of a single clean particle confirm this expectation, showing evidence of MBL proximity effect and non-trivial signatures in entanglement dynamics. We explain these observations through a phenomenological theory of *propagation of MBL* and provide supplemental evidence through the study of highly excited eigenstates.

This chapter is based on the following publications

Brighi P., Michailidis A. A., Abanin D. A., Serbyn M. "Propagation of many-body localization in an Anderson insulator," Phys. Rev. B (Letters) **105** L220203 (2022)

Brighi P., Michailidis A. A., Kirova K., Abanin D. A., Serbyn, M. "Localization of a mobile impurity interacting with an Anderson insulator," Phys. Rev. B **105** 224208 (2022)

Brighi P., Ljubotina M., Abanin D. A., and Serbyn M. " Many-body localization proximity effect in two-species bosonic Hubbard model." In preparation, 2023

4.1 Introduction

The thermalization of isolated quantum systems and its breakdown are fundamental questions of many-body quantum physics. While typical interacting quantum systems are expected to thermalize according to the eigenstate thermalization hypothesis (ETH) [1, 2], the presence of strong disorder can lead to non-ergodic behavior, a phenomenon known as many-body localization (MBL) [49, 50]. MBL is an example of stable dynamical phase of matter avoiding thermal equilibrium, and its existence may be understood from the stability of localization in the Anderson Hamiltonian [48] with respect to

weak but finite interactions [49, 50, 75]. Localization in interacting systems and its phenomenology were thoroughly studied both theoretically [63, 75, 80, 184, 185, 186, 187] and experimentally [66, 67, 68, 69, 162].

A number of dynamical properties of MBL [55, 80] were explained via the existence of an extensive number of quasilocal conserved quantities [56, 57, 60], the so-called LIOMs or l-bits. The existence of these conserved quantity is also the central point of a mathematical proof [60] which, under very mild assumptions, ensures stability of localization in one dimension for the transverse field Ising model (TFIM). However, there are important open questions regarding the nature of MBL, such as its stability in higher dimensions [62, 67, 81, 166, 188, 189] and the possibility of localized and thermalizing eigenstates coexisting in the same system at different energy or particle densities — so-called many-body mobility edges [59, 71, 85, 86, 167, 171, 190], previously discussed in Chapter 3.

At the same time, experiments provided strong support for the stability of the MBL phase on long timescales, verified a number of theoretical predictions, and started exploring regimes where the theoretical understanding is incomplete [66, 68, 69, 191]. In particular, experiments suggested the existence of MBL in higher dimension [67, 83] and probed the many-body mobility edges [71].

Another open question concerns the stability of localization in an MBL system coupled to a so-called quantum bath, represented by another quantum system that would thermalize in absence of the coupling. In the case of a thermodynamically large bath, where the back-action of the localized system can be neglected, the system-bath coupling is expected to result in delocalization, caused by the facilitated transport and energy exchange. However, considering a bath whose dimension is comparable to the localized system, or smaller, can yield distinct outcomes, especially if the back-action on the bath is taken into account. The MBL degrees of freedom can localize the bath – a phenomenon dubbed "MBL proximity effect" by Ref [61]. Alternatively, the bath can thermalize the formerly localized system [87].

This question was addressed in various different settings at a theoretical level [61, 64, 87, 88, 170, 183, 192, 193] and experimentally [70, 72]. Inspired by the avalanche mechanism [62] for the delocalization transition, a number of works studied the effect of a "thermal grain" coupled to a localized system [64, 87, 192]. These works described the bath as a random matrix drawn from the Gaussian orthogonal ensemble (GOE), hence trivially satisfying ETH, and account for the quasi-local nature of integrals of motion while considering coupling between the bath and the localized system. In these models the bath lacks spatial structure, thus it cannot be localized by the MBL system, excluding *a priori* the MBL proximity effect. In order to keep the microscopic structure of the bath, Refs. [61, 88, 170] represented it by a set of thermalizing particles. In this framework, thermal and localized degrees of freedom coexist and are coupled through local interaction. It has been shown [88] numerically that localization can globally persist, if the bandwidth of the thermal particles is small. A related setup, although with both species of particles subject to disorder, was theoretically considered in Ref. [181], which suggested that depending on the localization length, a bath consisting of a single boson can either localize or thermalize other particles. However, the fingerprints of localization of the bath under the influence of the disordered degrees of freedom were not studied in detail and still remain an open question.

All the studies discussed so far relied on the use of exact diagonalization (ED), which dramatically limits the system sizes available. In contrast, recent experimental studies [70,

72] have addressed this problem on bosonic quantum simulators, enabling the study of large systems. In Ref. [70] a “global" setup was used, where the thermal degrees of freedom are homogeneously distributed through a 2d lattice. Varying the number of thermal particles, the experiment showed evidence of the stability of localization when the thermalizing bosons are a small fraction of the total. On the other hand, the authors of Ref. [72] used a different approach. There, a 1d chain is split into a disorder-free segment, that represents a bath, and is connected to a disordered segment. The experiment investigated the stability of localization while changing the size of the disorder-free segment. While localization is stable for small thermal chains, signs of delocalization were observed when the bath constitutes half of the whole system.

In this work inspired by recent experiments [70, 72] we investigate the behavior of a non-interacting Anderson insulator with a finite density of particles interacting with a single clean (not subject to disorder potential) boson that acts as a small quantum bath. We obtain a perturbative condition for the stability of localization, which suggests that at strong disorder and *strong interactions*, the system remains localized. Approaching the dynamics in an approximate way, using a time-dependent Hartree method, which neglects entanglement and quantum correlations among the two particle species, we at first obtain delocalization at long times, supported by the diffusive spreading of the particle constituting the bath and decaying memory of the initial state of the Anderson insulator. However, large scale matrix product state (MPS) [194] simulations of the long-time dynamics of the system reveal that the Anderson insulator localizes the clean boson, providing the first evidence of MBL proximity effect on these length-scales. The contrast of approximated time-dependent Hartree method and quasi-exact TEBD highlights the fundamental role played by entanglement.

Next, we address the effect of the clean boson on the Anderson insulator, showing that by mediating an effective interaction among localized particles it triggers additional relaxation of the density imbalance [66] enhancing particle-particle correlations. Finally, we attribute the non-trivial entanglement dynamics observed in this system to an effective *propagation of MBL* in the Anderson insulator mediated by the clean boson. Finally, we use density-matrix renormalization group for excited states method (DMRG-X) [110, 111, 112], to study highly excited eigenstates of the Hamiltonian in large chains. This effectively allows us to probe localization at infinite times. Analyzing the expectation value of density in eigenstates, we observe localization of the small bath due to the interaction with the Anderson insulator. Furthermore, we find that eigenstates show area-law entanglement, thus providing complementary support for the persistence of localization at strong interactions.

Having established the presence of MBL proximity effect in the strong interaction regime, we proceed and study the system at weaker couplings and in the case of extensively large quantum baths. In the *weak interaction* regime, analytical arguments suggest the possibility of a breakdown of the MBL proximity effect and consequent delocalization of the clean particle. Using state of the art numerical methods and large computational resources, we investigate the time-evolution of the model and additionally consider a related Floquet model with similar properties, which enables the study of much longer timescales. At sufficiently large interaction strengths, we still observe characteristic features of localization, in contrast with the claims of Ref. [195]. Upon decreasing the coupling strength, we observe signatures of delocalization of the clean particle, whereas the disordered bosons still show extremely slow dynamics, making their behavior hard to

capture unambiguously.

After establishing the possibility of delocalization of the single-particle bath, we investigate the effects of increasing the size of the quantum bath. Using operator dynamics, we consider the case when the particle density of the bath is comparable to the density of localized particles. In this case, we find non-vanishing (diffusive or subdiffusive) particle transport for both clean and disordered bosons, providing strong evidence of delocalization. As the density of the clean particles is reduced, such that their average spacing becomes comparable to the localization length of a single clean particle in the case of the MBL proximity effect, we observe dynamics compatible with localization at short times. The rapid growth of entanglement prevents us from reaching longer timescales, where delocalization expected from analytical treatment of related problems may be manifested [196, 197].

By pushing the limits of numerical simulations to large systems, long evolution times, and large entanglement regimes, our work sheds light on the fate of localized system coupled to a bath with varying number of particles. For a weak quantum bath we demonstrate the persistence of localization in systems with much larger number of particles than is accessible to exact diagonalization, suggesting stability of MBL on long timescales and possibly in thermodynamic limit [90, 92]. In the opposite limit of large quantum bath, our investigation of transport shows a surprisingly fast emergence of diffusive behavior of the localized system due to its coupling with the bath, in contrast with observations of subdiffusive transport throughout the delocalized phase of more conventional disordered many-body Hamiltonians with a single species of particles [198, 199]. This is suggestive of a possible effective long-range interaction induced by the clean bosons, bearing a distant analogy to studies of two-level systems coupled to waveguide that mediates long-range interactions [200].

4.2 Model

We consider a one dimensional chain of two species of hard-core bosons moving through nearest neighbor hopping and interacting via an on-site potential. The *disordered* bosons (d-bosons) are further subject to a random potential drawn from a uniform distribution $\epsilon_i \in [-W, W]$ and are governed by the Anderson Hamiltonian $\hat{H}_d$ [48]

$$\hat{H}_d = t_d \sum_{i=1}^{L-1} (\hat{d}_i^\dagger \hat{d}_{i+1} + \text{h.c.}) + \sum_{i=1}^{L} \epsilon_i \hat{n}_{d,i}, \tag{4.1}$$

where $\hat{d}_i$ is the annihilation operator for the d-bosons, $\hat{n}_{d,i} = \hat{d}_i^\dagger \hat{d}_i$ is their density operator, and t_d is the hopping strength. The resulting Anderson insulator [48] is localized at any density of bosons and disorder strength W [201] thereby providing a specific system avoiding thermalization.

The small quantum bath will be represented by the *clean* bosons (c-bosons) described by $\hat{H}_c$,

$$\hat{H}_c = t_c \sum_{i=1}^{L-1} (\hat{c}_i^\dagger \hat{c}_{i+1} + \text{h.c.}), \tag{4.2}$$

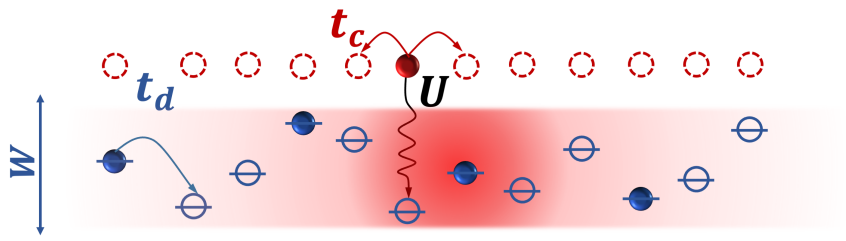

Figure 4.1: A schematic representation of the model described by the Hamiltonian (4.4). Blue dots represent the d-bosons, subject to the disorder potential of strength W, while the red dots illustrate the c-boson interacting with d-bosons via the on-site interaction U.

that are characterized by a single hopping parameter t_c and are not subject to disordered potential. Finally, the two boson species are coupled via the on-site Hubbard interaction,

$$\hat{H}_{\text{int}} = U \sum_{i=1}^{L} \hat{n}_{c,i}\hat{n}_{d,i}, \tag{4.3}$$

where U is the interaction strength and $\hat{n}_{c,i} = \hat{c}_i^\dagger \hat{c}_i$ is the number operator of c-bosons.

The full interacting Hamiltonian then reads:

$$\hat{H} = \hat{H}_d + \hat{H}_c + \hat{H}_{\text{int}}. \tag{4.4}$$

The system described by the Hamiltonian (4.4) is shown schematically in Figure 4.1. The Hamiltonian has $U(1) \times U(1)$ symmetry, as the number of both types of particles, $\hat{N}_{c/d} = \sum_i \hat{n}_{c/d,i}$, is conserved, $[H, N_{d/c}] = 0$. In what follows, we assume a finite density of d-bosons, $\nu_d = N_d/L = 1/3$ unless specified otherwise, and fix the hopping parameters to $t_d = t_c = 1$[1]. In absence of c-bosons the system is in the Anderson insulating phase for any finite disorder. The presence of c-bosons, however, makes the system inherently interacting, leading to the question of stability of Anderson localization with respect to coupling to the small bath represented by c-bosons.

We first approach the problem of a *single* c-boson, that realizes the smallest possible quantum bath with non-trivial spatial structure and local coupling to a localized system. In this respect, our setting resembles the experimental setup of Ref. [70] which was, however, performed on a two dimensional lattice and considered various densities of clean particles. In this setup, at weak interaction strengths we additionally study the time-evolution resulting from a pulsed Floquet driving. The Hamiltonian evolution is generated by the unitary time-evolution operator $\hat{U}(t) = \exp\left(-\imath \hat{H} t\right)$, implemented numerically using a fourth order Suzuki-Trotter decomposition [115] over alternating pairs of sites with time step $\delta t = 0.05$. The Floquet dynamics, instead, are generated by the following time-dependent periodic Hamiltonian

$$\hat{H}(t) = \begin{cases} \hat{H}_{\text{even}} & nT \le t < (n+1/2)T \\ \hat{H}_{\text{odd}} & (n+1/2)T \le t < (n+1)T \end{cases}, \tag{4.5}$$

where $\hat{H}_{\text{even(odd)}}$ represents the Hamiltonian in Eq. (4.4). Here the sum of the hopping terms is restricted to even (odd) sites and the interaction and disorder terms are halved,

[1] We note that the choice of positive hopping parameters corresponds to the dynamics of holes, however we do not expect qualitative changes for negative $t_{c/d}$.

$T = 0.5$ is the period and $n \in \mathbb{N}$. The unitary Floquet operator then describes the dynamics at *stroboscopic times* nT

$$\hat{U}_F = \exp\left(-\imath \hat{H}_{\text{odd}} \frac{T}{2}\right) \exp\left(-\imath \hat{H}_{\text{even}} \frac{T}{2}\right). \tag{4.6}$$

Although the Hamiltonian and Floquet models are, strictly speaking, different, the Floquet dynamics is expected to reduce to the Hamiltonian case in the limit of $\Delta T \to 0$. Moreover, both models are characterized by *exact conservation* of the particle number of the two bosonic species. This allows us to compare the transport and particle spreading between the two models, with the Floquet model being able to achieve much longer evolution times at a comparable computational costs. As we demonstrate below, Floquet and Hamiltonian time evolution show similar phenomenology, with Floquet time evolution enabling us to probe the stability of MBL proximity effect and delocalization on much longer timescales.

Although the boson density is sufficient to specify a particular sector of the Hilbert space, in the single c-boson case we further restrict ourselves to states where d-bosons have a globally homogeneous distribution. In particular, we will study initial states corresponding to a d-bosons density wave, with the single c-boson located on the central site, as exemplified by $|\psi_0\rangle$ below on a system of $L = 18$ sites and with $\nu_d = 1/3$

$$|\psi_0\rangle = |\bullet\circ\circ\bullet\circ\circ\bullet\circ\textcolor{red}{\bullet}\bullet\circ\circ\bullet\circ\circ\bullet\circ\circ\rangle, \tag{4.7}$$

where empty circles represent empty sites, and black (red) circles are sites occupied by d- and c-boson respectively. Such initial state resembles the configurations used in experiments and can be characterized by the so-called imbalance [191, 202], quantifying the memory of the initial density-wave configuration in the system after a quench.

While a strictly periodic arrangement of d-bosons akin to the state (4.7) is not required, we assume that the density of d-bosons is on average distributed uniformly on a scale that is larger than a few lattice spacings. This assumption is important since the presence of large empty/occupied regions in the chain would imply the effective absence of disorder for c-boson in that region. While such configurations could be used to imitate another experimental study of MBL-bath coupling [72], states where extensive regions of the chain are fully empty or occupied by d-bosons are exponentially rare in the size of the region, hence they are far from typical initial product states. On the other hand, typical configurations have approximately uniform density of d-bosons on a scale larger than a few lattice sites, hence our choice of initial density wave state (4.7) is expected to qualitatively capture the typical behavior. Moreover, we expect that if the localization of d-bosons persists, such states are nearly decoupled from spatially homogenous initial states of the type (4.7). Indeed, in order to connect a highly inhomogeneous state such as $|\psi_0\rangle = |\bullet\bullet\bullet\bullet\bullet\circ\circ\circ\circ\circ\textcolor{red}{\bullet}\circ\circ\circ\circ\circ\rangle$ to the density-wave state in Eq. (4.7), the tunneling of an extensive number of d-boson over long distances is required.

In the case of finite c-bosons density, instead, we investigate the dynamics of two different types of initial conditions, to address different regimes in the parameter space of the model. Whenever the density of clean bosons is small, $\nu_c = N_c/L \leq 1/6$, we fix the d-boson density to $\nu_d = 1/3$ and study the evolution of the quantum wave function represented as an MPS from an initial state consisting of clean (disordered) bosons forming a density wave of period $1/\nu_{c/d}$ respectively. Our numerical simulations show that by increasing density of clean particles in the bath the whole system approaches thermalization, thus leading

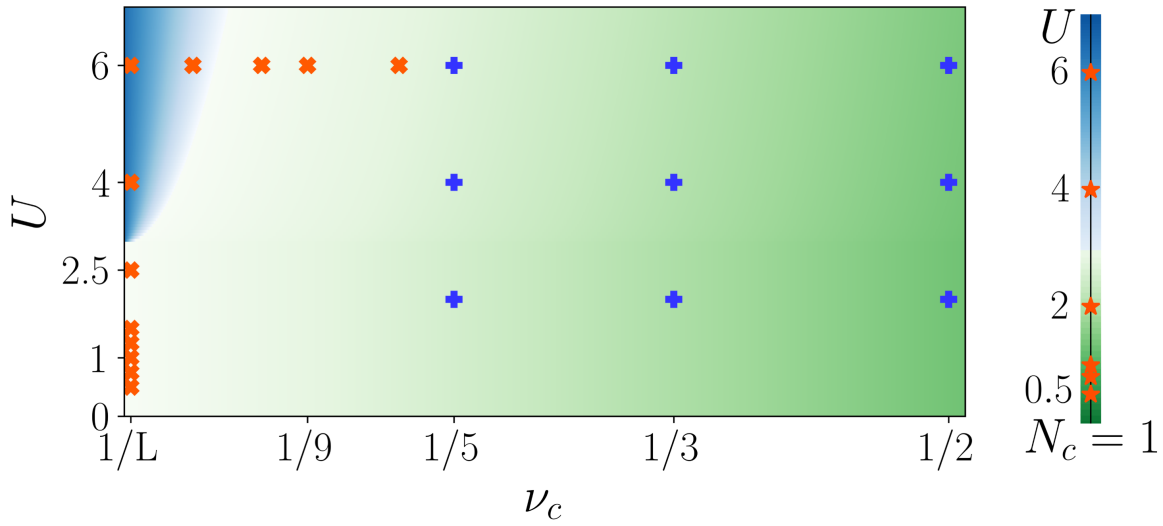

Figure 4.2: Phase diagram for the Hamiltonian system as function of the coupling U and the bath size ν_c, and for the Floquet dynamics in the case of bath consisting of a single particle ($N_c = 1$ or $\nu_c = 1/L$). The markers show different points in parameter space explored in this work, and refer to time evolution that uses Hamiltonian (red crosses) or Floquet (red stars) propagation of wave functions, and Hamiltonian evolution of density matrices (blue crosses). The colors schematically show the different phases, blue representing MBL and green the ergodic phase. The shading corresponds to the putative transition regime, obtained from our numerical simulations. We expect more stable localization in the regime of strong interactions, however in the present study we aim at studying the transition, and hence deliberately choose interaction to be less or equal to disorder strength, $U \leq W = 6.5$.

to rapid entanglement spreading and making the time-evolution of MPS wave function extremely challenging. Thus in regime of $\nu_c > 1/6$ we time-evolve density matrices initialized close to infinite temperature ($\rho_\infty \propto \mathbb{I}$) represented as a matrix product operator (MPO), whose simulation is more efficient in the thermal phase, see Appendix C.4 for details.

In Figure 4.2 we summarize the main results of this Chapter through a tentative phase diagram as a function of interaction strength U and bath size controlled by the density of clean particles, ν_c, for fixed parameters $t_c = t_d = 1$ and $W = 6.5$. First, in Sections 4.3 and 4.4 we study the transition as a function of the interaction strength for the single-particle bath case. The joint results of our numerical simulations and analytical considerations allow us to establish the existence of two phases in this regime, an MBL phase at strong interactions (blue in the phase diagram) and a thermal phase at weak U (light green), characterized by diffusive behavior of the bath particle and extremely slow delocalization of the d-bosons. Close to the putative transition, we use both Hamiltonian and Floquet dynamics, presenting qualitatively similar results.

As the number of c-bosons becomes extensive, $N_c \propto L$, corresponding to finite densitites of clean bosons, we observe, in Section 4.5.2, a weakening of localization, eventually yielding delocalization shown as a crossover from blue to green in the phase diagram in Fig. 4.2. Finally, in Section 4.5.1 we investigate particle transport in the delocalized region of the diagram, finding diffusive spreading of both bosonic species.

4.3 Strong coupling regime

4.3.1 Hartree approximation and criterion for stability of localization

First, we formulate the Hartree approximation and use it to study the Hamiltonian (4.4). This facilitates the choice of parameters in the Hamiltonian, and allows to formulate an analytic criterion for stability of localization with respect to two-particle tunnelling processes.

Effective Disorder

The Hartree approximation adopted in this section consists of replacing the density operator $\hat{n}_{d,i}$ in Eq. (4.4) with its infinite-time average $\langle \hat{n}_{d,i} \rangle$. This approximation would be fully justified in the case of instantaneous relaxation of d-bosons with respect to c-boson dynamics, i.e. if $t_d, W \gg t_c$. Moreover, as in an Anderson insulator the fluctuations of the expectation value $\langle \hat{n}_{d,i} \rangle$ are finite at all times, the Hartree approximation overestimates the degree of localization of the system. In spite of these shortcomings, the Hartree approximation will assist us with the choice of model parameters and will also allow defining an effective disorder strength thus quantifying the analytic criterion for stability of localization.

The infinite-time average of the d-bosons density is given by the diagonal ensemble generated by the eigenstates of $\hat{H}_d$:

$$\begin{aligned} \langle \hat{n}_{d,i} \rangle &= \lim_{T\to\infty} \frac{1}{T} \int_0^T dt \, \langle \psi(t) | \, \hat{n}_{d,i} \, | \psi(t) \rangle \\ &= \sum_n |c_n|^2 \, \langle E_n | \, \hat{n}_{d,i} \, | E_n \rangle \, , \end{aligned} \tag{4.8}$$

where $\{|E_m\rangle\}$ is the eigenbasis of $\hat{H}_d$, $c_n = \langle \psi_0 \, | E_n \rangle$ and $|\psi(t)\rangle = \hat{T} e^{-\imath \int_0^t \hat{H}_d(t')dt'} \, |\psi_0\rangle = e^{-\imath \hat{H}_d t} \, |\psi_0\rangle$. The initial state $|\psi_0\rangle$ is taken to be a density wave, see Eq. (4.7). Due to the random potential in the Anderson Hamiltonian, the d-bosons occupation at infinite times

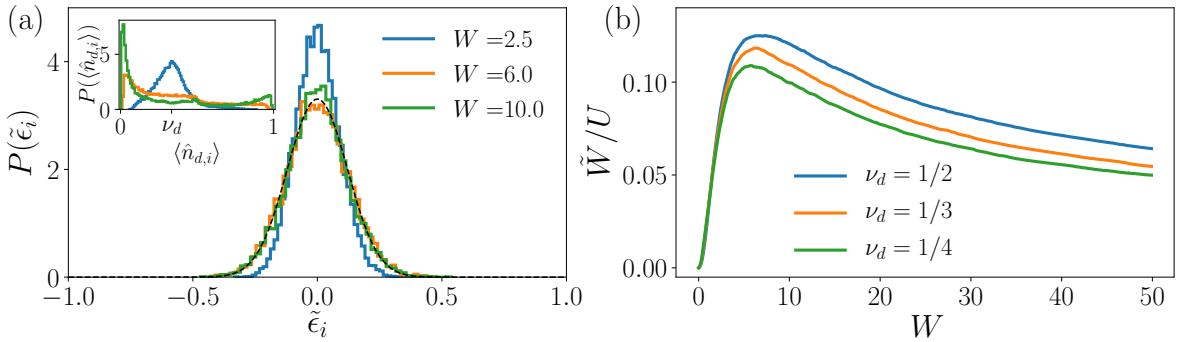

Figure 4.3: (a) Subtracting deterministic components from the distribution of $\langle \hat{n}_{d,i} \rangle$ (inset) results in an approximately Gaussian distribution of the effective disorder potential $\tilde{\epsilon}_i$, shown here for $\nu_d = 1/3$. Standard deviation of this distribution, σ, is used to define the effective disorder strength, $\tilde{W}/U = \sigma$. (b) The effective disorder strength $\tilde{W}$ shows a non-monotonic behavior as a function of W with a maximum at $W^* \approx 5$. The data shown are obtained for $L = 500$ sites and averaged over 50 disorder realizations.

acquires a quasi-random nature and is distributed according to $P(\langle \hat{n}_{d,i} \rangle)$ in the range $[0, 1]$.

Thanks to the noninteracting nature of the problem in the Hartree approximation, the eigenstates in Eq. (4.8) can be written as product states of single particle orbitals $|\ell\rangle$. Then, by going into eigenbasis one can decouple the sum over $\binom{L}{N_d}$ terms in Eq. (4.8) into a double sum over the N_d occupied sites in the initial state and the L single particle orbitals. The problem of finding the infinite time occupation values then reduces to finding eigenstates of a single-particle Hamiltonian, whose Hilbert space scales as L, thus greatly reducing the complexity of the problem. The infinite-time average of the d-bosons density, hence, can be carried out through Eq. (4.8) for very large systems, $L = 500$, where boundary effects on its probability distribution are negligible, and at various disorder strengths.

The infinite-time occupation of the d-bosons plays the role of an effective random chemical potential experienced by the c-boson in the Hartree approximation. As shown in the inset of Figure 4.3(a), when the disorder is strong compared to the hopping parameter, $t_d = 1$, $P(\langle \hat{n}_{d,i} \rangle)$ resembles a bimodal distribution, with two distinct peaks at $\langle \hat{n}_{d,i} \rangle \sim 0, 1$. This behavior can be understood as a consequence of the strong localization of d-bosons for disorder $W = 10$. Thus, even at infinite time, the d-bosons remain close to their initial position and expectation value of $\langle \hat{n}_{d,i} \rangle$ remains close to its initial value, i.e. either 0 or 1, depending on the considered site. As disorder is decreased, the two peak structure gradually disappears, and the distribution acquires a single peak around the average density ν_d.

In order to define the effective disorder $\tilde{\epsilon}_i$ generated by the d-bosons, we need to isolate the random part of the distribution of $\langle \hat{n}_{d,i} \rangle$. To this end, we subtract from $\langle \hat{n}_{d,i} \rangle$ the uniform and the period-$1/\nu_d$ contribution. In Fourier space this corresponds to modifying the Fourier harmonics of density, $\tilde{n}_d(k) = \sum_j \langle \hat{n}_{d,j} \rangle e^{-\imath kj}$, as follows:

$$\tilde{\epsilon}(k) = \tilde{n}_d(k) - (1 - \alpha) L \nu_d \delta_{k,0} - \alpha \sum_{j=1}^{L} f(j, \nu_d) e^{-\imath kj}, \tag{4.9}$$

where $\alpha = \sum_j \langle \hat{n}_{d,j} \rangle e^{-\imath \pi \nu_d j}$ corresponds to the weight of the $1/\nu_d$ harmonic in the particle distribution and $f(j, \nu_d) = \sum_{n=0}^{N_d - 1} \delta_{j, n/\nu_d + 1}$ is a functional representation of the initial density wave configuration. Transforming $\tilde{\epsilon}(k)$ back to the real space, we obtain the effective random potential $\tilde{\epsilon}_i$. Its distribution differs from the one of the infinite-time density, as it can be seen in Figure 4.3(a). In particular, $P(\tilde{\epsilon}_i)$ is centered around zero for all values of disorder, and has an approximately Gaussian shape. Thus, we use the standard deviation of this distribution as the effective disorder strength $\tilde{W} = U \operatorname{std} P(\tilde{\epsilon}_i)$ experienced by c-boson in the Hartree approximation.

The effective disorder strength measured in units of U, $\tilde{W}/U$ is shown as a function of the disorder strength experienced by d-bosons, W, in Figure 4.3(b). First, we note a non-monotonic dependence of $\tilde{W}$ on the d-boson disorder strength, W. The effective disorder strength $\tilde{W}$ presents a maximum around $W^* \approx 5$, whose position depends weakly on the density of d-bosons. This behavior can be naturally explained by considering two opposite limits: at weak W the localization length of d-bosons is much larger and the initial period-2/3/4 density wave configuration is washed out at late times resulting

in weak effective disorder $\tilde{W}$. [2] In the opposite limit of very strong W, the d-bosons remain frozen close to their initial positions resulting in a nearly perfect periodic potential experienced by c-boson. However such periodic potential is unable to localize c-boson and is subtracted in Eq. (4.9), thus again resulting in a weak effective disorder. Given that $\tilde{W}$ is expected to decrease for very large and small W, we expect it to achieve a maximal value at some intermediate disorder W. Finally, we study in Fig. 4.3(b) the dependence of the effective disorder on the d-bosons density ν_d. As ν_d is increased, $\tilde{W}$ increases accordingly due to the fact that the effective random potential $\tilde{\epsilon}_i$ is generated by the d-bosons density. We note, however, that for $\nu_d > 1/2$ the effective disorder would decrease again, because of the hard-core nature of the bosons.

Localization length of the c-boson in Hartree approximation

We demonstrated that in the Hartree approximation the c-boson experiences an approximately Gaussian-distributed random potential with disorder strength $\tilde{W}$ that depends on the initial state and disorder experienced by d-bosons. Since an arbitrary weak disorder potential suffices to localize a single particle in a one-dimensional lattice, the c-boson in the Hartree approximation is always localized. We proceed with the calculation of its localization length ξ_c that provides a characteristic lengthscale of localization and can be compared with the localization length of the d-bosons, ξ_d.

To obtain the localization length for the c-boson we use the weak disorder approximation, justified at weak values of U as the random potentials $\tilde{\epsilon}_i$ are restricted to $[-1, 1]$. Perturbing around the tight-binding limit with the transfer matrix method [203], we obtain $\xi_c(k) \approx 8t_c^2 \sin^2(k)/\langle\tilde{\epsilon}_i^2\rangle$ that depends on the momentum k that determines single particle energy in absence of disorder, $E(k) = -2t_c \cos(k)$. The average localization length is calculated by performing the integral over the complete band

$$\xi_c \approx \frac{8t_c^2}{\langle\tilde{\epsilon}_i^2\rangle} \int_{-2t_c}^{2t_c} d\varepsilon \left[1 - \left(\frac{\varepsilon}{2t_c}\right)^2\right] \rho(\varepsilon), \tag{4.10}$$

where $\rho(\varepsilon)$ is the usual density of states of the tight-binding Hamiltonian. Carrying out the integral we realize that it contributes only to a numerical factor as the c-boson hopping terms cancel out. Recalling that, since $\langle\tilde{\epsilon}_i\rangle = 0$, the variance $\langle\tilde{\epsilon}_i^2\rangle$ corresponds to the definition of the effective disorder strength squared, we obtain

$$\xi_c \approx \frac{4t_c^2}{a\tilde{W}^2}, \tag{4.11}$$

where $a = 1$ is the lattice spacing.

The resulting simple expression for ξ_c, Eq. (4.11), has two main consequences. First, we expect that ξ_c inherits the non-monotonic dependence on W and has a minimum approximately when the effective disorder strengths is maximal in Fig. 4.3. Second, since $\tilde{W} \propto U$, we expect that localization length diverges as $\xi_c \propto 1/U^2$ at small values of U where weak disorder approximation is controllable. To confirm these predictions, we extract the localization length of c-bosons from numerical simulations. Using the effective disorder obtained from the eigenstates of the d-boson Hamiltonian, we use exact

[2] We note, that in the limit of small W dynamics of c-bosons becomes faster, potentially invalidating the static Hartree approximation. Nevertheless, the effective disorder remains well defined even in this case.

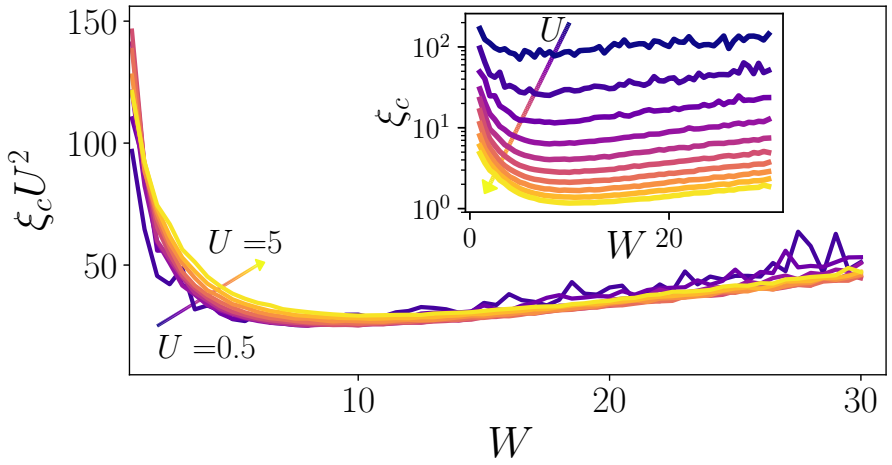

Figure 4.4: The localization length of the c-boson from the Hartree approximation for initial period-3 density wave state of d-bosons. Inset shows bare data, for different values of U ranging from $U = 0.5$ (dark blue) to $U = 5$ (yellow). For a broad range of interaction strength, ξ_c has a minimum at $W^* \approx 5$. The main plot shows the collapse of data, confirming the scaling $\xi_c \sim U^{-2}$.

diagonalization to calculate the single-particle wave functions of c-bosons resulting from the Hamiltonian $H_c^{\text{Hartree}} = H_c + \sum_i U\langle\hat{n}_{d,i}\rangle\hat{n}_{c,i}$. Each eigenstate $|\phi_\varepsilon\rangle$ of this Hamiltonian can be characterized by an (energy-dependent) localization length $\xi_c(\varepsilon)$. After obtaining $\xi_c(\varepsilon)$ for each eigenstate through an exponential fit of its probability distribution in the real space, $|\langle i|\,\phi_\varepsilon\rangle|^2$, we average the localization length over all eigenstates and further over 50 disorder realizations.

The localization length resulting from the numerical simulation is shown in Fig. 4.4, where the non-monotonic behavior of ξ_c and its scaling with the interaction strength becomes apparent. We note that for the adopted choice of hoppings $t_d = t_c = 1$, ξ_c always exceeds the localization length of d-bosons and is tunable by the interaction strength in a broad range. In particular, for disorder strength $W = 6.5$, used in the accompanying paper [65], $\xi_d \approx 0.5$ is smaller than one lattice spacing, while ξ_c takes values from 1.5 to 100 lattice spacings, as the interaction strength is decreased from $U = 5$ to $U = 0.5$ respectively. This result also assists in the choice of disorder strength: in order to facilitate the numerical studies, we fix disorder at $W = 6.5$ so that the localization length of c-bosons is close to its minimum.

Analytic criterion for stability of localization

The drawback of the Hartree approximation presented above is that it ignores fluctuations of d-bosons density, thus always resulting in localization. However, it provides a useful starting point to address the perturbative stability of such localized system. To this end, we use the basis of Anderson localized orbitals provided by Hartree approximation to address the stability of the system with respect to interactions between clean and disordered bosons.

We transform the interaction Hamiltonian (4.3) to the basis of localized orbitals via the relation $\hat{d}_\alpha = \sum_i \psi_{d\alpha}(i)\hat{d}_i$, where $\hat{d}_\alpha$ is the annihilation operator of an Anderson orbital and $\psi_{d\alpha}(i) = \langle\alpha|i\rangle$ is the corresponding wave function and similar expressions hold for

c-bosons. This leads to

$$\hat{H}_{\text{int}} = \sum_{\alpha\beta\gamma\delta} V_{\alpha\beta\gamma\delta} \hat{d}^\dagger_\alpha \hat{c}^\dagger_\beta \hat{d}_\gamma \hat{c}_\delta. \tag{4.12}$$

As shown in the schematic representation in the inset of Figure 4.5, the matrix element $V_{\alpha\beta\gamma\delta}$ corresponds to a correlated hopping process with its value being given by the overlap of the wave functions of the corresponding localized orbitals,

$$V_{\alpha\beta\gamma\delta} = U \sum_{i=1}^{L} \psi^*_{d\alpha}(i)\psi^*_{c\beta}(i)\psi_{d\gamma}(i)\psi_{c\delta}(i), \tag{4.13}$$

where the envelope of the wave functions decays on the scale of the corresponding localization length, $|\psi_{d\alpha}(i)| \sim e^{-|i-x_\alpha|/(2\xi_d)}/\sqrt{2\xi_d}$, where x_α is the site around which the orbital is localized. In order to address the stability of localization with respect to such correlated hoppings triggered by interaction, we compare the matrix element of this process to the corresponding level spacing.

Keeping only the leading behavior of the wave functions, i.e. the exponential decay, and neglecting their oscillatory behavior results in an upper bound for the matrix element in Eq. (4.13) and thus favors delocalization. In this case, the matrix element can be easily estimated as

$$V_{\alpha\beta\gamma\delta} \approx \frac{U}{4\xi_c\xi_d} \sum_{i=1}^{L} e^{-\frac{|x_\alpha - i| + |x_\gamma - i|}{\xi_d}} e^{-\frac{|x_\beta - i| + |x_\delta - i|}{\xi_c}}, \tag{4.14}$$

from where one can immediately realize that it is exponentially suppressed whenever any of terms in the exponents $|x-i|/\xi_{c/d} > 1$ exceeds one. This restricts the localized orbitals that can efficiently participate in the hopping process:

$$\begin{cases} |x_\alpha - x_\gamma| & \lesssim \xi_d, \quad |x_\alpha - x_\beta| \lesssim \max(\xi_c, \xi_d) \\ |x_\beta - x_\delta| & \lesssim \xi_c, \quad |x_\gamma - x_\delta| \lesssim \max(\xi_c, \xi_d). \end{cases} \tag{4.15}$$

Using the fact that $\xi_c \geq \xi_d$, the summation cancels the ξ_d in the denominator resulting in a simple estimate

$$V_{\alpha\beta\gamma\delta} \approx \frac{U}{4\xi_c}. \tag{4.16}$$

The second element needed to understand if such tunnelling processes are resonant is the typical level spacing δ_{cd}, obtained as the ratio of the typical energy difference ΔE to the number of states $\mathcal{N}$ connected by the interaction. Since the two states differ for the position of the two bosons, the typical energy difference is given by the sum of the two disorder strengths: $\Delta E \approx W + \tilde{W}$. To account for the number of states $(|\psi\rangle, |\psi'\rangle)$ connected by the interaction we need to consider the constraints (4.15), which restrict the possible configurations. First, in the initial state the two bosons must lie within a distance ξ_c from one another, as $\xi_c \geq \xi_d$, thus contributing $2\xi_c$ possible configurations. Due to the localized nature of wave functions, the position of the bosons in the final state must lie within a distance ξ_c and ξ_d for the c-boson and the d-bosons respectively. A naïve computation would then give $\mathcal{N} = (2\xi_c)(2\xi_c)(2\xi_d) = 8\xi_c^2\xi_d$. However, one must be careful as also in the final state the two bosons must be separated by at most ξ_c for the matrix element not to vanish. This reduces the total number of states, as not all the moves increasing the distance among the bosons are allowed. A careful computation reveals that for a given d-boson hopping there are only $(3/2)\xi_c$ possible choices, thus reducing the total number of states. Finally, one has to take into account the finite density of the

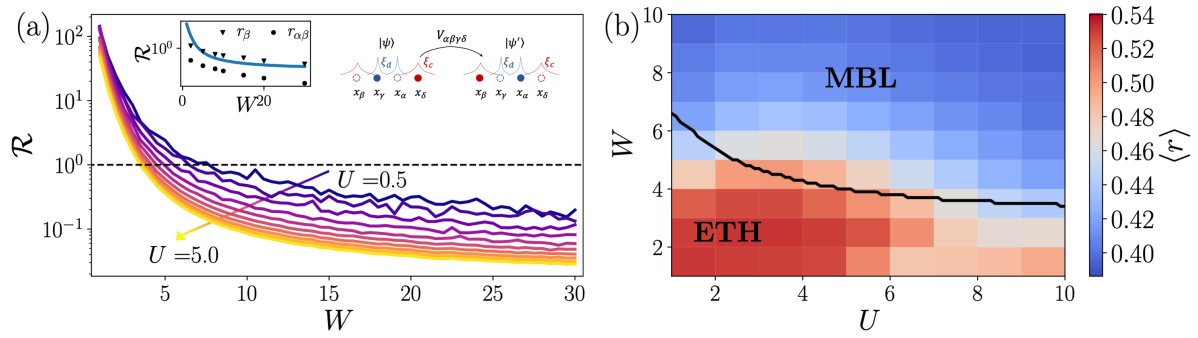

Figure 4.5: (a) The typical ratio between matrix element and level spacing as a function of disorder for different coupling strengths U rapidly decreases as the interaction strength increases. In the left inset we compare analytic expression for $\mathcal{R}$ with its numerical estimate. The right inset shows the tunnelling process induced by $\hat{H}_{\text{int}}$. (b)The phase diagram obtained using the average ratio of adjacent level spacings, $\langle r \rangle$, for the central 500 eigenstates of a system of $L = 15$ sites shows good qualitative agreement with the criterion $\mathcal{R} = 1$ for the transition, especially at strong U. At weak U localization appears to be stable beyond the limit obtained with the criterion, while at intermediate interaction higher-order processes neglected in our analytical estimate lead to a larger extent of delocalized phase.

d-bosons, together with their hard-core nature, that requires that an initially occupied site must be left empty after the hopping and vice versa, leading to

$$\mathcal{N} \approx 6\xi_c^2 \xi_d \nu_d (1-\nu_d), \quad \delta_{cd} = (W + \tilde{W})/\mathcal{N}. \tag{4.17}$$

Gathering the results of Eqs. (4.16)-(4.17) we obtain the expression for the ratio of level spacing to the matrix element,

$$\mathcal{R} = \frac{3}{2} U \frac{\xi_c \xi_d \nu_d (1-\nu_d)}{W + \tilde{W}}. \tag{4.18}$$

Condition $\mathcal{R} < 1$ provides a criterion for stability of localization. Recalling that the c-boson localization length depends on the interaction strength $\xi_c \approx \xi_c^0/U^2$, the criterion $\mathcal{R} < 1$ can be rearranged as

$$(W + \tilde{W})U > \frac{3}{2} \xi_c^0 \xi_d \nu_d (1-\nu_d), \tag{4.19}$$

suggesting that localization remains stable at strong interactions and large disorder. For the disorder strength used in the numerical simulations in the remainder of this work, $W = 6.5$, the criterion (4.19) yields a critical interaction strength $U_c \approx 1.5$, therefore at strong interaction $U = 12$ used in the numerical simulations the system is expected to remain localized.

The typical probability of resonance $\mathcal{R}$ can also be evaluated numerically and compared with the prediction of Eq. (4.18). To this end, after diagonalizing the Hamiltonian in the Hartree approximation, for each c-boson eigenstate we select states lying within the localization lengths ξ_c and ξ_d from one another and evaluate for all of them the matrix element $V_{\alpha\beta\gamma\delta}$ and the energy difference. Then we define the resonance value r_β fixing the initial state of the c-boson, e.g. β, and maximizing the ratio of the matrix element

to the energy difference over all other available states. In a similar way we define the resonance $r_{\alpha\beta}$, where both the initial state of the c-boson (β) and of the d-boson (α) are fixed. Being a more constrained version of r_β, the following inequality holds

$$r_\beta = \max_{\alpha\gamma\delta}\left[\frac{V_{\alpha\beta\gamma\delta}}{\Delta E}\right] \geq r_{\alpha\beta} = \max_{\gamma\delta}\left[\frac{V_{\alpha\beta\gamma\delta}}{\Delta E}\right]. \tag{4.20}$$

Finally, we obtain the typical resonance probability by taking the median of the distribution of r_β and $r_{\alpha\beta}$. The results of this numerical evaluation are shown in the inset of Figure 4.5(a) together with the analytic prediction (4.18) and show an overall agreement. In particular, we notice that $r_{\alpha\beta}$ is always smaller than r_β.

From Figure 4.5(a) we observe that the disorder W at which the condition (4.19) is satisfied decreases as the interaction strength U increases. Taking the disorder value where $\mathcal{R} = 1$ as a critical point, we obtain the transition line shown in Figure 4.5(b). Note, that our considerations assume a homogeneous initial distribution of d-bosons, as discussed at the end of Sec. 4.2. The transition line is compared with the average ratio of adjacent level spacings for a system of $L = 15$ sites. The ratio of adjacent level spacing defined as $r = \min(\delta_i, \delta_{i+1})/\max(\delta_i, \delta_{i+1})$, where δ_i is the energy difference of two neighboring eigenstates, has a well known behavior in the thermal and MBL regimes. Its average for the Gaussian orthogonal ensemble (GOE) reads $r_{\text{GOE}} \approx 0.54$, and is approached in ergodic phase, while for MBL it reaches the Poisson value $r_{\text{P}} = 2\log(2) - 1 \approx 0.39$ [51, 53]. In Fig. 4.5(b), we show results for the average over the central 500 eigenstates, further averaged over 200 disorder realizations. We notice a good qualitative agreement with the transition line obtained through the criterion (4.19), especially at large values of U. Figure 4.5(b) suggests that at disorder $W = 6.5$ the system is expected to be localized for sufficiently large $U \gtrapprox 1.5$. In what follows we explore the properties of the localized system for $U = 12$, a point that is located deep in the localized regime according to our stability condition and results from exact diagonalization for small system sizes.

4.3.2 Quench dynamics as a probe of localization

The static Hartree approximation introduced above allowed to formulate a criterion for the stability of localization. Below we proceed with probing the dynamics of the full model in the localized regime. First, we study the dynamics of a clean boson in the random landscape of the static Hartree disorder, gaining insight in the expected dynamics for localized particles. Next, we extend the Hartree approximation attempting to include dynamical effects in the system via a time-dependent update of the mean field. Finally and more importantly, we study the full quantum dynamics using TEBD.

Numerical simulations

To check the criterion (4.19), we numerically study dynamics of large systems over long times. We fix $W = 6.5$, which is close to the value that maximizes the effective disorder $\tilde{W}$ [89] and typically consider a quantum quench from an initial period-3 density wave of d-bosons corresponding to density $\nu_d = 1/3$, a setup often used in cold atoms experiments on localization [161, 191, 202]. The large local Hilbert space dimension restricts the use of exact diagonalization, hence requiring the use of more advanced techniques.

We first imply a time-dependent version of the Hartree approximation presented above, where the mean fields are updated after each time step. In this approximation $\langle \hat{n}_{c/d}(t) \rangle$

are affecting the dynamics $|\psi(t)\rangle \to |\psi(t+dt)\rangle$, and are then calculated again with the evolved wave function. However, this approach neglects the development of quantum correlations and of entanglement, thus limiting its applicability. The use of matrix product states (MPS) techniques, instead, can be considered almost exact, as far as the bond dimension is not saturated, and the truncation error is kept small enough. As we will show in the following, this system develops a large amount of entanglement, thus requiring a large bond dimension for a faithful description. Hence we study the dynamics using a parallel version of the TEBD algorithm [114] implemented using the ITensor library [176]. The parallelization of the algorithm, although relatively straightforward, allows the study of states with extremely large bond dimension, $\chi = 3000$, enabling us to explore large systems (up to $L = 60$) on experimentally relevant timescale of $T \leq 200$.

Finally, we also investigate the behavior of highly excited eigenstates, which give insight on the fate of the system at infinite times. To go beyond exact diagonalization, again we resort in the powerful MPS methods. In particular, we use the DMRG-X [110, 111, 112] algorithm, an extension of the celebrated DMRG [108], where the operator which is locally minimized corresponds to the shift-inverted Hamiltonian, $(\sigma\mathbb{I} - \hat{H})^{-1}$, with σ the target energy. Details about the DMRG-X and parallel TEBD implementation can be found in appendices C.2 and C.1 respectively.

Clean boson dynamics in static Hartree disorder

The static Hartree approximation discussed in Section 4.3.1, yields an effective disorder acting on the c-boson and consequently its localization. As the effective disorder changes with the filling fraction of the d-bosons, we expect also the localization length to change accordingly. This should lead to a weaker localization whenever the d-bosons density, ν_d, deviates from half filling. This is confirmed by the numerical results shown in Figure 4.6, where we observe stronger localization for $\nu_d = 1/2$. Additionally, we compare the data with the prediction of Eq. (4.11) (dashed lines). Although qualitatively similar,

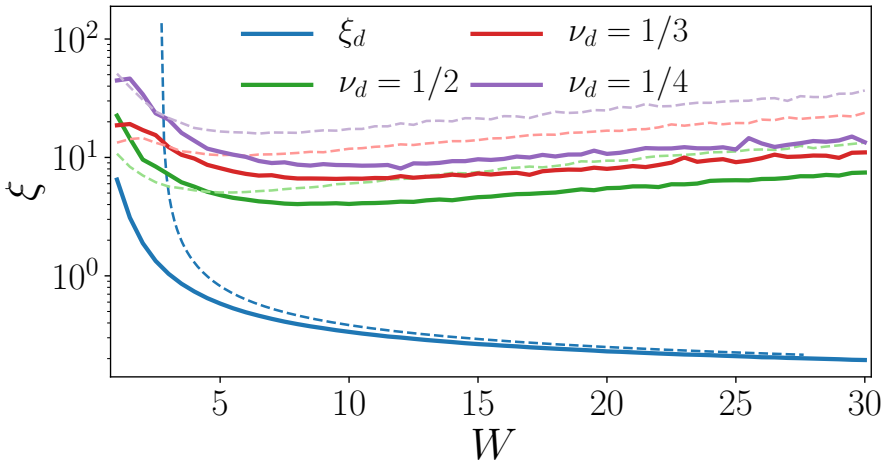

Figure 4.6: Hartree induced localization length compared with the analytic result of Eq.(4.11), dashed lines, reveals good agreement at weak disorder, while at larger W the deviation of $P(\tilde{\epsilon}_i)$ from Gaussian leads to a worse agreement. The localization length ξ_c reflects the behavior of the effective disorder, leading to larger ξ_c for systems far from half filling. The weaker nature of the effective disorder results in $\xi_c \gg \xi_d$ for all the parameters studied, thus highlighting the much weaker localization of the c-boson.

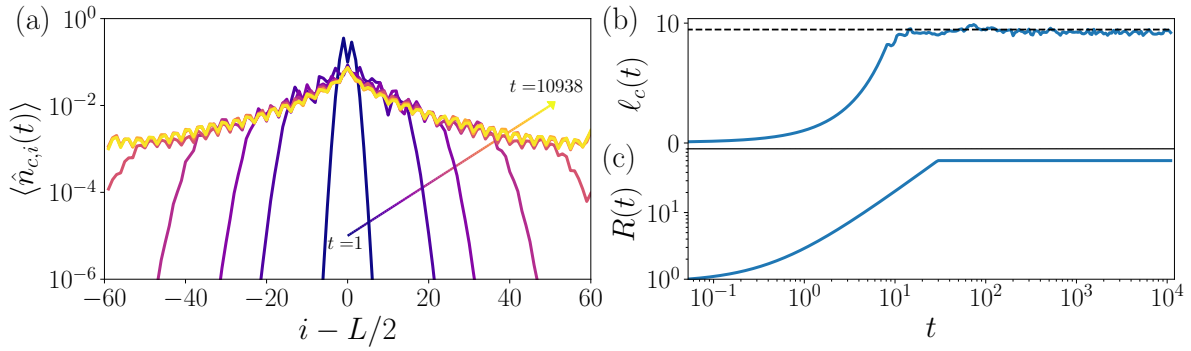

Figure 4.7: The density profiles (a) of the single particle in the static Hartree disorder at $U = 2.5$ show an exponential decay within a range $R(t)$, outside of which they rather have a Gaussian behavior. The exponential decay is characterized by a decay length $\ell_c(t)$ (b), which after an initial transient is constant in time and saturates to the value obtained in Fig. 4.6. The extent of the exponentially suppressed region, $R(t)$, instead grows in a power-law fashion until it reaches the boundaries of the system (c).

the quantitative agreement fails as the disorder strength W increases. We attribute this discrepancy to the deviation of the distribution of effective disorder from Gaussian discussed in Section 4.3.1.

Next, we consider the c-boson dynamics in the static Hartree approximation fixing the disorder strength affecting d-bosons to $W = 6.5$, close to the minimum of the c-boson localization length. After the replacement of $\hat{n}_d$ with its infinite time average, the dynamics can be obtained numerically for large systems without resorting to large computational resources, as the single-particle Hilbert space dimension only scales as the system size L. Therefore, we study the density dynamics of a c-boson initialized in the center of a $L = 120$ chain evolving the initial state up to $t \approx 10^4$. The density profiles obtained in this way in Figure 4.7(a) reveal the presence of two distinct behaviors, depending on the distance from the center. Close to the initial position of the particle, the density in Fig. 4.7(a) decays exponentially, consistently with the expectation for a localized particle. However, further away from the initial location of the particle, the density dependence is consistent with a Gaussian profile. While the Gaussian profile is expected from the diffusive spreading of the particle that could take place at early times for weak disorder (weak localization), the coherent backscattering from static disorder leads to the localization of the particle.

The two distinct regimes in the density profile can be described by introducing two separate lengthscales: the distance $R(t)$ corresponds to crossover from exponential to diffusive behavior, and $\ell_c(t)$ describes the slope of exponential decay. Using these lengthscales, the dynamics of the density can be captured by the following ansatz,

$$n(x,t) \propto \exp\Big(- \frac{|x|}{\ell_c(t) \tanh\Big(R(t)/|x|\Big)} \Big), \tag{4.21}$$

that smoothly interpolates between exponential and Gaussian decays for $x < R(t)$ and $x > R(t)$ respectively.

The ansatz (4.21) can then be used to fit the numerical data and to obtain the behavior of the two parameters $\ell_c(t)$ and $R(t)$, shown in Figure 4.7(b)-(c). We observe that for the static Hartree approximation, the decay length after a transient quickly saturates to the corresponding localization length ξ_c shown in Figure 4.6. The extent of the exponential

decay region around the center, $R(t)$, instead increases as a power-law, before its saturation to half system size, meaning that the localized region extends over the whole chain. Later in this work, we use the same ansatz to study the dynamics in the fully interacting system, obtaining similar results, although interactions result in much more intricate dynamics.

Time-dependent Hartree approximation

The static Hartree approximation relies on the assumption of quick equilibration of the d-boson density and overestimates localization in the system, as we shall demonstrate below comparing with the results obtained in the previous Section. Here, we adopt a different approximation: we assume that the full many-body wave function can be decomposed into a product of c- and d-bosons wave functions respectively. Such representation completely ignores entanglement between the two boson species. However, it allows performing fast and efficient simulation of dynamics on long timescales for large systems. We note here that similar approaches to the approximation of dynamics in MBL system have already been used [204, 205], showing results qualitatively similar to what we present below.

The product state structure of the wave function of the full system allows to reduce the full many-body Schrödinger equation to the simultaneous evolution of two non-interacting but time dependent Hamiltonians. Specifically, the time evolution of c- and d-bosons is governed by time-dependent Hamiltonians $\hat{H}_c^{\mathrm{dH}}(t)$ and $\hat{H}_d^{\mathrm{dH}}(t)$ respectively:

$$\begin{aligned} \hat{H}_d^{\mathrm{dH}}(t) &= t_d \sum_{i=1}^{L-1} (\hat{d}_{i+1}^\dagger \hat{d}_i + \mathrm{h.c.}) + \sum_{i=1}^{L} V_{d,i}(t)\hat{n}_{d,i}, \\ V_{d,i}(t) &= \epsilon_i + U\langle \hat{n}_{c,i}(t)\rangle \end{aligned} \tag{4.22}$$

$$\begin{aligned} \hat{H}_c^{\mathrm{dH}}(t) &= t_c \sum_{i=1}^{L-1} (\hat{c}_{i+1}^\dagger \hat{c}_i + \mathrm{h.c.}) + \sum_{i=1}^{L} V_{c,i}(t)\hat{n}_{c,i}, \\ V_{c,i}(t) &= U\langle \hat{n}_{d,i}(t)\rangle, \end{aligned} \tag{4.23}$$

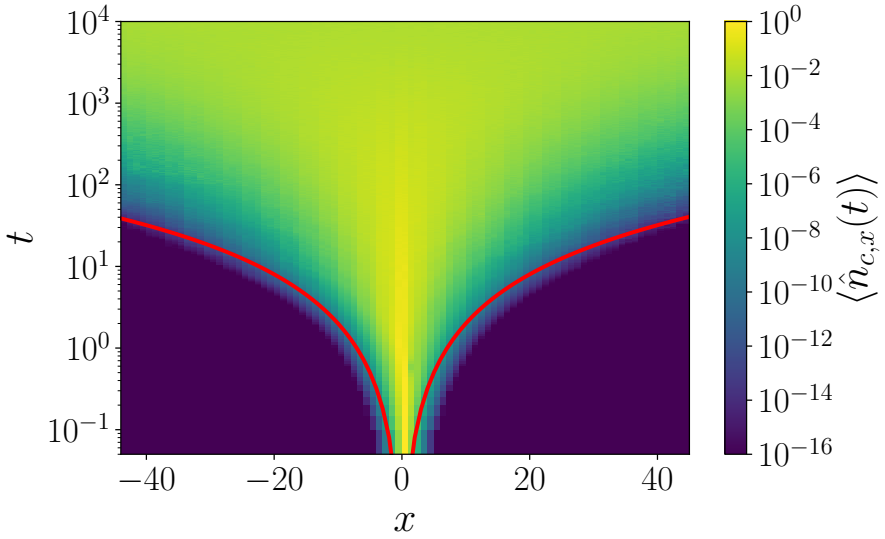

Figure 4.8: Evolution of the density profile of the clean boson in the dynamic Hartree approximation has a clear diffusive behavior. The red line corresponds to the diffusive "lightcone", $\langle \hat{n}_{c,x}(t)\rangle = \sqrt{t/0.02}$, obtained as a fit to the curve where $\langle \hat{n}_{c,x}(t)\rangle > 10^{-10}$. The data is averaged over 400 disorder realizations, $L = 90$.

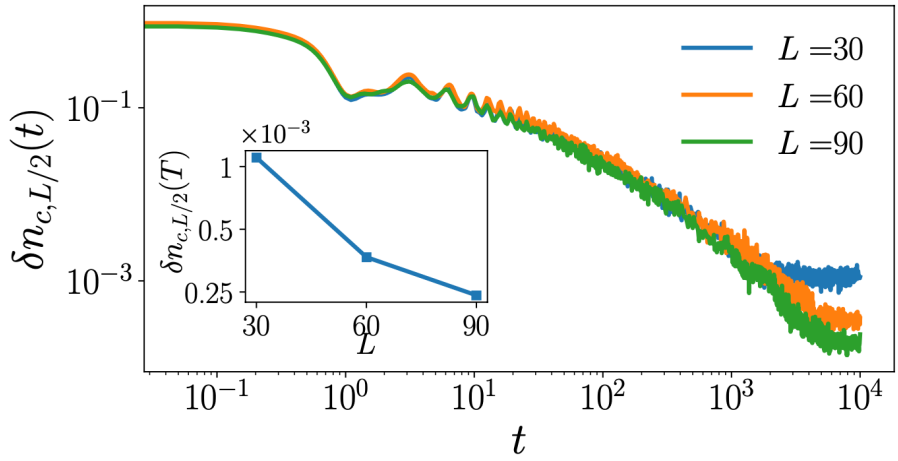

Figure 4.9: Fluctuations of the c-boson density decay slightly faster than polynomially in time. Inset shows that the saturation value of density fluctuations reached at late times decreases monotonically with the system size as $1/L^b$, with $b \approx 1.6$. This data is obtained averaging over 400 disorder realizations.

where the expectation value of densities of corresponding boson species reads $\langle \hat{n}_{c/d,i}(t) \rangle = \left\langle \psi_{c/d}(t) \right| \hat{n}_{c/d} \left| \psi_{c/d}(t) \right\rangle$, and $\left| \psi_{c/d}(t) \right\rangle$ is the wave function obtained from the time-evolution of the initial state (4.7) with the correspondent time-dependent Hamiltonian:

$$\left| \psi_{c/d}(t) \right\rangle = \hat{T} \exp\Big(-\imath \int_0^t dt' \hat{H}^{\mathrm{dH}}_{c/d}(t') \Big) \left| \psi^0_{c/d} \right\rangle . \tag{4.24}$$

Although the d-bosons formally are described by a many-body wave function due to their finite density, one can exploit their non-interacting nature to perform an efficient simulation of dynamics. In fact, as explained after Eq. (4.8), both the initial state and the eigenstates can be written as product states. After rotating the orbitals into the real space basis and back, the time-evolution reduces to a double sum over initially occupied sites and orbitals. The d-bosons can, then, be treated separately as single particles, and their overall wave-function can be reconstructed from the single-particle evolved states, thus reducing the complexity from exponential to poly(L).

First, we study the dynamics of the c-boson, illustrated in Figure 4.8, where we plot the density profile of the clean boson $\langle \hat{n}_{c,x}(t) \rangle$ as a function of distance from its initial location, $x = i - L/2$, and time. We observe that in contrast to the case of static Hartree approximation, where the c-boson spreads within an exponentially localized envelope (see Section 4.3.2), the dynamic Hartree approximation results in a diffusive spreading of c-boson and its complete delocalization over the entire system on a timescale $t \sim L^2$. Once the c-boson spreads over the whole chain, it does not reach a steady state, which can be attributed to the fact that this approximation oversimplifies the true many-body character of the problem.

The fluctuations of the c-boson density result in a time-dependent potential acting on disordered bosons, see Eq. (4.22). In order to quantify the density fluctuations of the clean boson, we average the absolute value of the deviation of its density from the mean value, $\delta n_{c,i}(t) = |\langle \hat{n}_{c,i}(t) \rangle - \overline{\langle \hat{n}_{c,i} \rangle}|$, where $\overline{\langle \hat{n}_{c,i} \rangle}$ corresponds to the average over the interval $t \in [9.9 \times 10^3, 10^4]$. As shown in Figure 4.9, the density fluctuations around the initial position of the c-boson decay in time, until they eventually reach a plateau. Note the long

timescale involved in reaching the saturation value, even for a relatively small system of $L = 30$ this happens at times $t \gtrsim 10^3$.

The dynamics of the d-bosons can be intuitively understood as resulting from an Anderson insulator globally coupled to a weak, non-Markovian, local noise. While it is known [205, 206, 207, 208, 209] that Anderson localization is unstable with respect to global noise, a recent work [193] has demonstrated that coupling of an Anderson insulator to a local Markovian white noise leads to a logarithmically slow particle transport and entanglement growth. Our dynamics differs from that of Ref. [193] in that d-bosons are coupled to fluctuations of the c-boson density globally throughout the entire length of the chain. Another important difference is that the density fluctuations of the clean boson produce a temporally and spatially correlated noise.

In Figure 4.10(a) we show the density profile of d-bosons at late times, $T = 10^4$, for different system sizes $L = 30$, 60, and 90. Although the relaxation is strongest in the middle of the chain, the memory of the initial density wave configuration survives even at late times. To understand the dynamics of relaxation of the density profile, we consider the imbalance $I(t)$ [66]. The imbalance quantifies the memory of the initial state using the difference in occupation among initially occupied and empty sites (N_o and N_e respectively),

$$I(t) = \frac{N_o(t) - N_e(t)}{N_o(t) + N_e(t)}. \tag{4.25}$$

For the initial period-3 density wave state considered here, the explicit form of $N_{o/e}$ reads:

$$N_o = \sum_{i=1}^{L/3} \hat{n}_{d,3i-2}\ , \quad N_e = \frac{1}{2}\sum_{i=1}^{L/3}\Big(\hat{n}_{d,3i} + \hat{n}_{d,3i-1}\Big). \tag{4.26}$$

Figure 4.10(b) reveals that $I(t)$ decays without any signs of saturation even at times $T = 10^4$. As show in Ref. [210], the time-dependent Hartree approximation leads to delocalization in the MBL phase, while it produces accurate results in the ergodic side of the transition. After rescaling the time axis with a factor of $1/L^2$ we observe the collapse

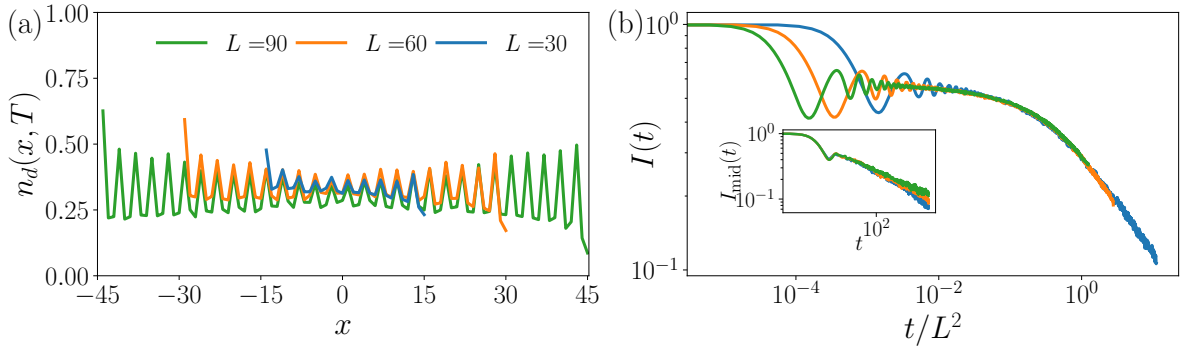

Figure 4.10: (a) The density profile of $d-$bosons at late time $T = 10^4$ retains memory of the initial state. Comparing data for different system sizes, we observe that larger systems keep stronger memory of the initial state. (b) Inset shows that the imbalance in the middle of the chain follows an approximate power-law relaxation without any signs of saturation at late times. The main panel reveals that imbalance dynamics collapses for different system sizes after rescaling of the time axis by $1/L^2$. The averaging is performed over 400 disorder realizations.

of the data, which further supports the intuition that the delocalization observed in this approximate approach is an artifact of the diffusive spreading of the c-boson. In fact, although the imbalance is not a conserved quantity, its relaxation will happen at time $t \propto L^2$. The decay of imbalance, after a plateau extending up to $t \approx 0.1L^2$ follows a power-law scaling, $I(t) \sim (L^2/t)^\beta$. The exponent β is obtained by fitting the behavior of $I(t)$ in a time window $t \in [t_{\min}(L), T]$, with $t_{\min} = 2410,\ 5410,\ 6820$ for $L = 30,\ 60,\ 90$ respectively to account for the different duration of the plateau. The power-law fit results in $\beta \approx 0.4$ as shown in the inset of Fig. 4.15(a). These results however show a significant dependence on the system size, that we attribute to the boundary effects that influence the spreading of the c-boson even at $L = 90$, as shown in Figure 4.8.

In summary, the dynamic Hartree approximation suggests a complete delocalization of the clean particle, that is followed by the melting of the imbalance of disordered bosons. This does not agree with our expectations from the criterion for stability of localization obtained in Sec. 4.3.1, and also disagrees with the results of the TEBD dynamics presented below. It is natural to attribute the delocalization observed here to the nature of dynamic Hartree approximation, that completely neglects the many-body character of the problem and discards the correlations between the two species of bosons. The inclusion of such correlations is expected to lead to a more efficient relaxation of density fluctuations and may stop the diffusive spreading of c-boson as we illustrate below.

MPS simulations and many-body localization proximity effect

After having approached the dynamics of the system using the static and time-dependent Hartree approximation, leading to localization and thermalization respectively, we now tackle the problem using the quasi-exact TEBD algorithm. As discussed in Section 4.3.2, the choice of parameters of our simulation are such that, until saturation of the bond dimension, the results obtained can be considered exact.

Localization of the clean boson We first analyze the dynamics of the c-boson initialized at the center of the chain for strong interaction $U = 12$ so that Eq. (4.19) is satisfied and we expect the c-boson to localize. Indeed, the density profiles $\langle n_{c,i}(t)\rangle$ shown for different times in Fig. 4.11(a) have a clear exponential decay, characterized by a time-dependent decay length $\ell_c(t)$. However, this behavior is limited to a region $R(t)$ beyond which we observe a Gaussian decay of the density [89]. The Gaussian density profile could be interpreted as a signature of diffusive spreading within an exponentially localized profile, and indeed $R(t)$ grows approximately like $\sqrt{t}$ [89]. At the same time, the decay of the c-boson density away from its original position becomes exponential, signaling localization. We notice that this behavior is akin to the one observed in the static Hartree approximation (Sec. 4.3.2), hence an accurate description of the density profile for the considered range of times is given by the ansatz

$$n_c(x,t) \approx \mathcal{N}_c(t) \exp\Big(- \frac{|x|}{\ell_c(t) \tanh\Big(\frac{R(t)}{|x|}\Big)}\Big), \tag{4.27}$$

that depends on two parameters, $\ell_c(t)$ and $R(t)$ and smoothly interpolates between an exponential decay for $x \ll R(t)$, and a Gaussian decay with $\sigma^2 = \ell_c(t)R(t)$ when instead $x \gg R(t)$. $\mathcal{N}_c(t)$ is a normalization factor that depends on values of $\ell_c(t)$ and $R(t)$. To reduce the effect of the period-3 density wave structure originating from the initial state of d-bosons, we coarse-grain the density over a unit cell of three sites $\tilde{n}_{c,i}(t) = \frac{1}{3}\sum_{j=i}^{i+3}\langle \hat{n}_{c,j}(t)\rangle$

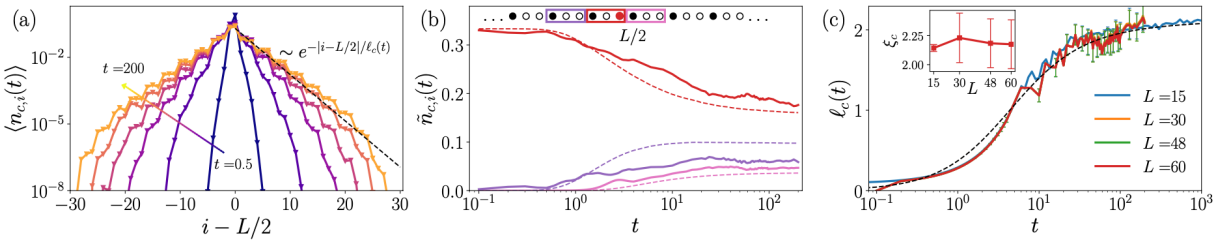

Figure 4.11: (a) The density profile of c-boson at different times reveals an exponential decay with distance from its initial position within a region of size $R(t)$ with decay length $\ell_c(t)$, both changing with time. Color intensity corresponds to time from $t = 0.4$ (darkest) to $t = 200$ (brightest). (b) Dynamics of the coarse-grained density $\tilde{n}_{c,i}$ reveals saturation and agrees reasonably well with the ansatz (4.27). (c) The decay length of c-boson density profile extracted from fit to Eq. (4.27) shows a logarithmic increase for $t \geq 1$ and eventually saturates to a finite value. Dynamics of $\ell_c(t)$ agrees with ansatz (4.28) shown by dashed line. The inset shows the saturation value of $\ell_c(t \to \infty)$ extracted from fit to ansatz that remains constant between different system sizes. The data shown here are obtained averaging over $N_{\rm dis} = 50$ disorder realizations for $L = 30, 48, 60$ and 5000 realizations for $L = 15$. Error bars correspond to standard deviation.

and fit its real-space profile to Eq. (4.27) to extract the time-dependent decay length and $R(t)$. Figure 4.11(b) shows that the prediction of the ansatz (dashed lines) is adequately describing $\tilde{n}_c(i,t)$. The dynamics of the coarse-grained density suggests that both $R(t)$ and $\ell_c(t)$ eventually saturate, confirming the localized nature of the c-boson due to the *MBL proximity effect*.

In Figure 4.12 we compare the time-evolution of the density profile of the clean boson with the ansatz of Eq. (4.27). While at early times $\langle \hat{n}_{c,i}(t)\rangle$ approximately agrees with a diffusive profile extracted from time-dependent Hartree approximation (red line and Fig. 4.8), at times of order one, the density spreading slows down. To describe the envelope of the density profile, we use the fact that when $R(t)$ saturates to $L/2$, the ansatz (4.27) reduces to $n_c(x,t) \approx e^{-|x|/\ell_c(t)}$. By imposing the condition $n_c(x,t) = \text{const}$, we obtain the scaling $|x| \approx \ell_c(t)$ shown in Fig. 4.12 by the blue line, that provides a better description for the envelope of the density profile.

The saturation of $R(t)$ is due to the finite size of the system, which limits its growth to $L/2$ [89]. On the other hand the behavior of the decay length is non-trivial. The plateaus in $\tilde{n}_c(i,t)$ and the slowdown of the growth of $\ell_c(t)$, arising around time $t \approx 10$, suggest a saturation of $\ell_c(t)$ to a finite value $\xi_c = \ell_c(t \to \infty)$ that we take as a proxy for the localization length of c-boson. In Figure 4.11(c) we observe a logarithmic growth of $\ell_c(t)$ that saturates at longer times. In order to extract the saturation value of ℓ_c we fit its time dependence to the following phenomenological ansatz,

$$\ell_c(t) = \xi_c \frac{\log\left(1 + t/T_0\right)}{\alpha + \log\left(1 + t/T_0\right)}, \tag{4.28}$$

where parameter α affects crossover from ballistic growth to logarithmic dynamics and T_0 sets the timescale of saturation to towards ξ_c. The numerical results are in good agreement with the fit to Eq. (4.28), shown as a black dashed line in Fig. 4.11(c), allowing to extract the localization length, shown in the inset of Figure 4.11(c) for $U = 12$. The localization length is constant in L within error bars, suggesting that the system remains localized in the thermodynamic limit.

Figure 4.13 considers the dynamics of decay length of the c-boson depending on the interaction strength. As expected, we observe that weaker interactions lead to much faster increase of $\ell_c(t)$, with its growth becoming faster than logarithmic between $U = 2.5$ and $U = 4$. Moreover, the saturation value of decay length [inset of Fig. 4.13(a)] for $U \leq 4$ is larger than system size, indicating that the available system size is insufficient to determine the fate of the c-boson at this interaction. As shown in [89], these values of interaction strength should satisfy the criterion for localization (4.19), however, higher order effects could enhance delocalization. In addition, we analyze the bipartite entanglement entropy of system including c- and d-bosons $S(i) = -\operatorname{tr} \rho_i \ln \rho_i$, where ρ_i is the reduced density matrix of the first i sites, at fixed time $T = 130$. The large values of $S(L/2)$ for weak interactions in Fig. 4.13(b) highlight the increasing complexity of simulations. In the remainder of this Section we focus on analyzing the regime of $U = 12$. The study of weaker interactions is instead analyzed in detail in Section 4.4

Localization of d-bosons We proceed with the characterization of the effect of the c-boson on the localized d-bosons for large values of U. We study the memory of d-bosons initial state in Fig. 4.14(a), where we show the density profiles at late time $T = 200$ for system sizes $L = 30, 48, 60$. The $\langle n_{d,i} \rangle$ curves immediately suggest that the time evolution did not wash out the initial period-3 density wave structure, providing a clear sign of absence of thermalization, at least on the timescales considered. We notice however an enhanced relaxation close to the center of the chain. This is readily explained by the interaction with the c-boson ($i = L/2$) localized in the central region of the chain.

Next, we consider the dynamics of imbalance of d-bosons, defined in Eq. (4.25) and shown in Fig. 4.15(a). While TEBD and time-dependent Hartree approximation approximately agree at times up to $t \approx 10$, at later times the imbalance obtained from TEBD remains approximately constant, while the time-dependent Hartree approximation predicts a power-law decay of the imbalance. This is further highlighted by the exponent β obtained from the fit of $I(t)$ in the time window $t \in [10, 200]$, shown in the inset, that is compatible

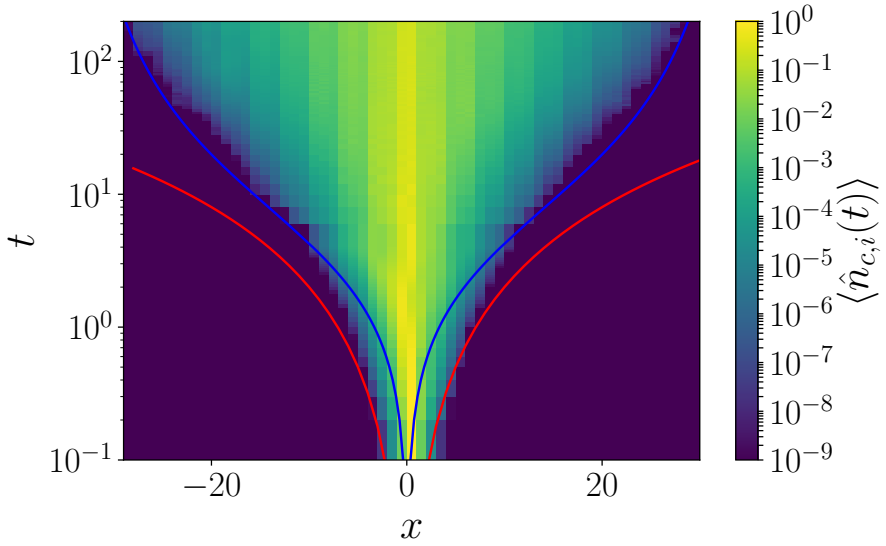

Figure 4.12: The spreading of the c-boson density in the $L = 60$ system is well described by the ansatz of Eq. (4.27) (blue curve), while it deviates from the diffusive behavior (red curve).

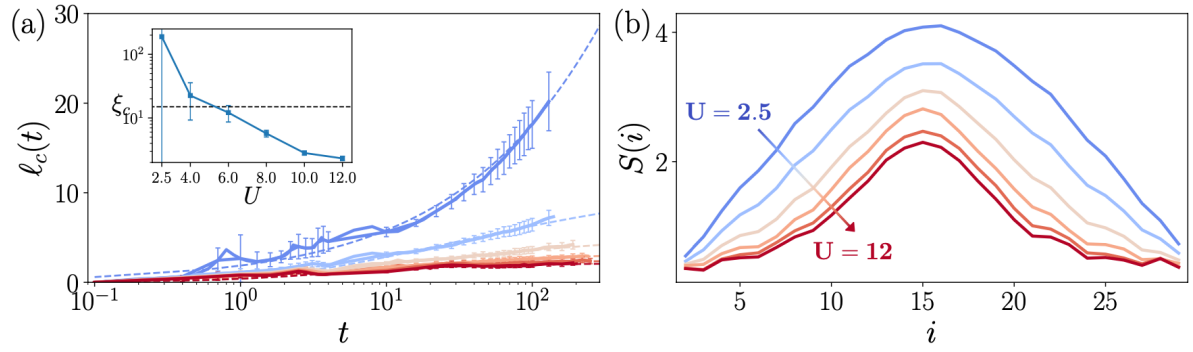

Figure 4.13: (a) Upon decreasing the interaction strength U the growth of decay length $\ell_c(t)$ accelerates and its time dynamics becomes faster than logarithmic for $U = 2.5$. At intermediate values of U the asymptotic value of $\ell_c(t)$ becomes larger than system size as shown in inset. Dashed lines correspond to the fit to Eq.(4.28). (b) The entanglement profile at time $T = 130$ rapidly increases with decreasing U and becomes concave for $U = 2.5$. The deviations from phenomenology that predicts a convex behavior for the entanglement profile imply potential thermalization. The data are for $L = 30$, $N_{\text{dis}} = 50$.

within error bars with value $\beta = 0$ for TEBD dynamics, which corresponds to non-decaying imbalance.

In order to quantify the stronger relaxation close to the center of the chain, triggered by the presence of the clean boson, we also study the local imbalance in the middle of the chain, $I_{\text{mid}}(t)$ defined according to Eq. (4.25) but restraining the sum in Eq. (4.26) to the six central sites. The quantity $I_{\text{mid}}(t)$ shows a stronger decay in Fig. 4.15(b) as compared to its global counterpart in Fig. 4.15(a). However, again TEBD dynamics reveals a much weaker effect of the c-boson compared to the Hartree approximation. Fitting the decay to the power-law form, the resulting exponent remains small and it does not change with system size (inset). Hence, we expect the effect on the central region to be system size independent, thus leaving the boundaries unaffected as $L \to \infty$.

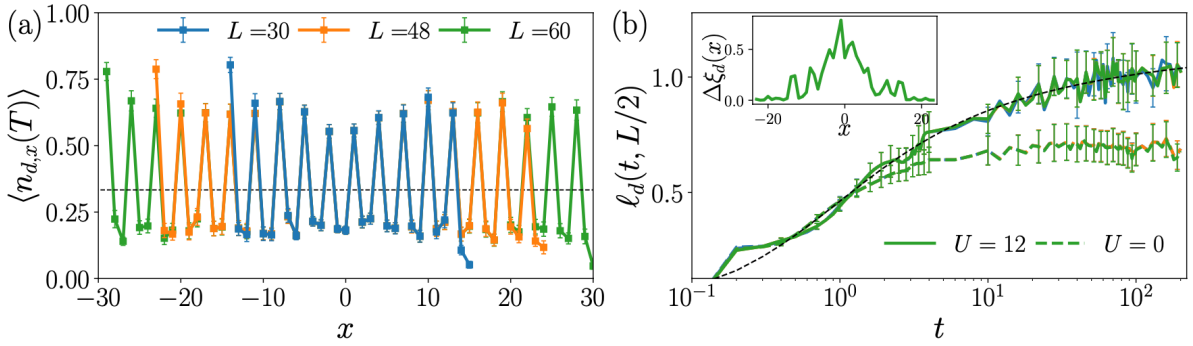

Figure 4.14: (a) The density profiles at late times $T = 200$ show memory of initial state of d-bosons. The c-boson leads to an additional small relaxation of density only near the center of the chain. (b) The decay length of d-bosons also reveals logarithmic in time dynamics and saturates even in the middle of the chain. Inset: the difference between saturation values of $\ell_d(t \to \infty, i)$ for $U = 12$ and $U = 0$ extracted from Eq. (4.28) shows enhancement of the decay length in the central region compared to Anderson insulator. Averaging is done over $N_{\text{dis}} = 50$ disorder realizations.

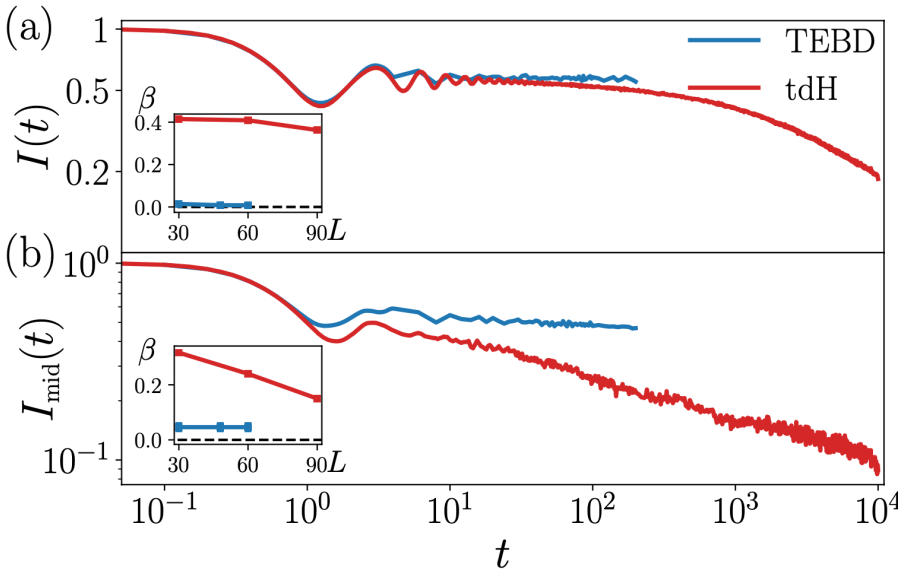

Figure 4.15: (a) TEBD dynamics (blue line) reveals a broad plateau in imbalance at late times, whereas time-dependent Hartree approximation (red line) predicts a power-law decay. (b) The imbalance of central six sites in TEBD dynamics reveals a weak power-law decay. The stronger deviation between TEBD and approximate time-dependent Hartree data highlights the importance of entanglement for the accurate description of the dynamics. Data is shown for $L = 60$ and averaged over 400 and 50 disorder realizations for time-dependent Hartree and TEBD respectively.

As the density dynamics shows, the localized c-boson induces an effective interaction between d-bosons that can be probed via the connected correlation functions

$$\langle n_{d,i}(t) n_{d,j}(t)\rangle_c = \langle n_{d,i}(t) n_{d,j}(t)\rangle - \langle n_{d,i}(t)\rangle\langle n_{d,j}(t)\rangle. \tag{4.29}$$

The exponential decay of the absolute value of the disorder-averaged connected correlation function with distance x,

$$|\langle n_{d,i-x/2}(t) n_{d,i+x/2}(t)\rangle_c| \sim e^{-|x|/\ell_d(t,i)} \tag{4.30}$$

allows to define a time and position dependent decay length of d-bosons, $\ell_d(t,i)$. In Figure 4.14(b) we show the dynamics of $\ell_d(t)$ for the central site, $i = L/2$. Although the value of ℓ_d is larger than the Anderson value (dashed colored lines), it remains close to one lattice spacing even at late times and shows clear signs of saturation. We use the asymptotic value of $\ell_d(t \to \infty, i)$ at large times, obtained from the fit to Eq. (4.28) (black dashed line), as a proxy for the d-bosons localization length, $\xi_d(i)$. Given the inhomogeneity of the system, we expect $\ell_d(t,i)$ to depend on the distance from the middle of the chain. In the inset of Fig. 4.14(b) we show the profile of the difference of $\xi_d(i)$ and the localization length for the Anderson insulator, $\Delta\xi_d$, that confirms that the effect of the interaction is limited to the center of the chain.

Entanglement dynamics Finally, we study the dynamics of entanglement entropy. In the MBL phase, entanglement growth is known to be logarithmic [55, 56, 57] while it quickly saturates to a small value in the Anderson insulator. In our system, despite the absence of interactions between d-bosons, entanglement entropy for different cuts shows logarithmic growth in Fig. 4.16(a). However, the onset of this increase strongly

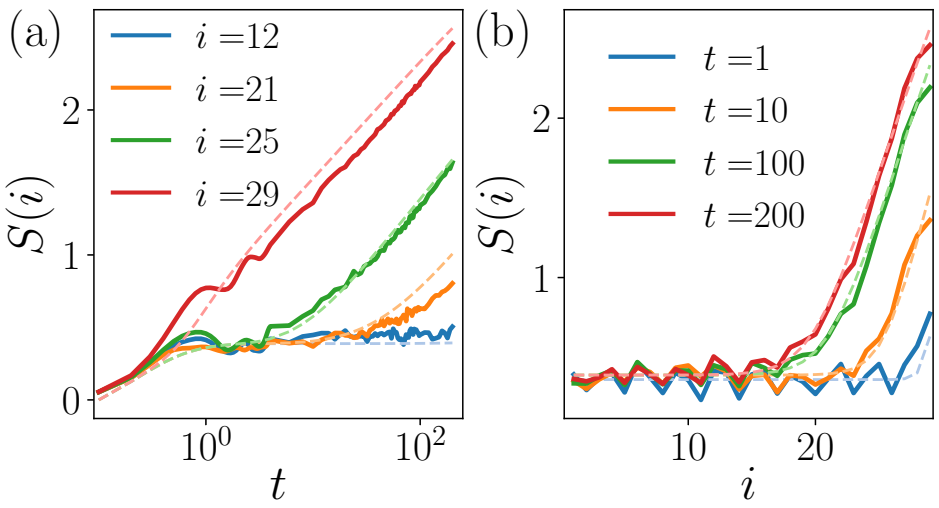

Figure 4.16: (a) The logarithmic entanglement dynamics with the delayed start of the growth away from the center is explained by the interactions triggered by c-boson. (b) The entanglement profile at fixed times has linear growth with distance to the position of c-boson, $|i - L/2|$. Dashed lines in both panels are prediction from Eq. (4.31). System size is $L = 60$, $N_{\text{dis}} = 50$.

depends on the location within the chain. We attribute such entanglement dynamics to the presence of the c-boson. While a single c-boson is incapable of producing more than $\ln 2$ entanglement, the non-zero c-boson density induces effective interactions between d-bosons thus turning the former Anderson insulator into a genuine MBL phase.

Although the c-boson is eventually localized, its density is spreading throughout the chain within an exponential envelope (see Fig. 4.11(b)) effectively triggering *propagation of MBL*. Phenomenologically we describe the entanglement profile as

$$S(i,t) = S_{\text{AI}} + \xi_S \log\Big(1 + U_{\text{eff}}(i - L/2, t)t\Big), \tag{4.31}$$

which captures the logarithmic growth of entanglement in the MBL phase [55, 56, 57] with an effective interaction strength $U_{\text{eff}}(x,t) = Un_c(x,t)$ set by the c-boson density from Eq. (4.27). Eq. (4.31) predicts that far from the center (large $|i - L/2|$) the logarithmic growth starts only when the *many-body localization front* $x_{\text{MBL}}(t)$ reaches the position of the cut. The value of $x_{\text{MBL}}(t)$ obtained from the condition $tU_{\text{eff}}(x,t) \approx 1$ reads $x_{\text{MBL}} \approx \ell_c(t) \log\big(\mathcal{N}_c(t)Ut\big)$, where we used that at late times $\tanh(R(t)/|x|) \approx 1$. The MBL front at first grows as the decay length $\ell_c(t)$ and continues to grow logarithmically, even after the saturation of $\ell_c(t)$, eventually reaching the boundaries of the system.[3] Comparison of the prediction of Eq. (4.31) with data in Fig. 4.16(a) shows good agreement. Furthermore, from Eq.(4.31) the late time entanglement profile can be predicted to be linear in $|x|$, with a slope given by $-\xi_S/\ell_c(t)$. This is supported by Fig. 4.16(b), where the entanglement entropy decreases linearly with the distance from the center of the chain. The linear decrease of the entanglement profile allows us to interpret the curvature of entanglement profile at weak U in Fig. 4.13(b) as a breakdown of this picture, potentially indicating delocalization.

[3]We note that in the thermodynamic limit the transition of the boundaries to MBL is not trivial and depends on ξ_c.

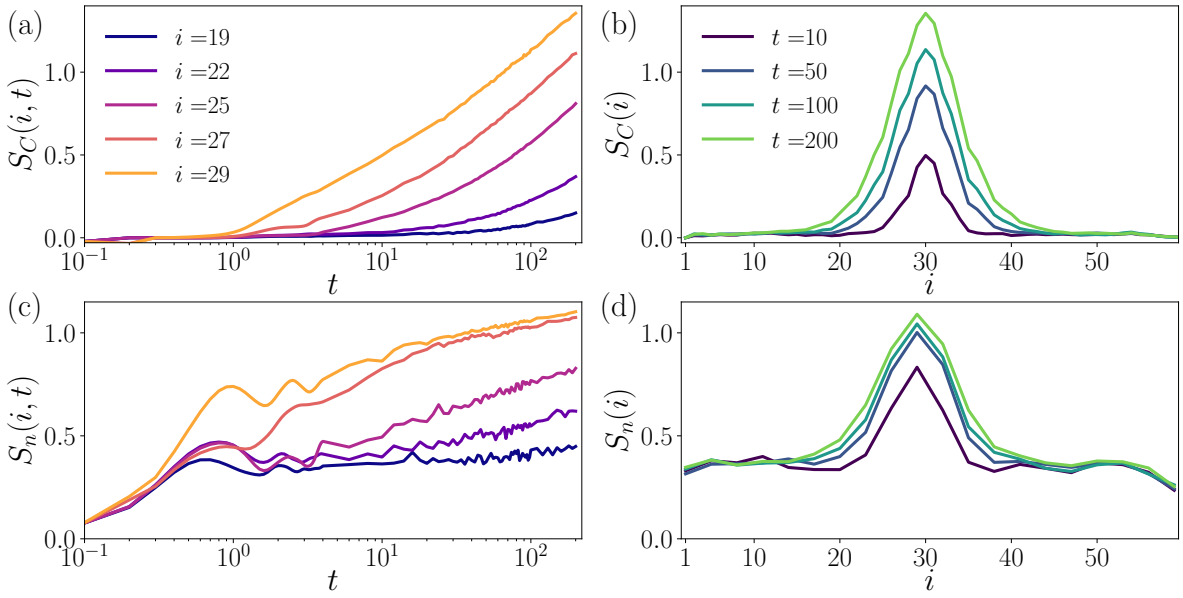

Figure 4.17: (a) The configuration entropy shows a steady logarithmic growth, whose start is delayed as the cut gets farther from the center of the chain, due to the weaker effect of the interaction at the boundaries. (b) The real space profile of the configuration entropy is highly non-uniform, with entropy being maximal in the center of the chain, where the c-boson is localized. Far from the center, $S_C(i)$ is close to zero, indicating the absence of interactions in the boundaries up to late times. (c) The growth of number entropy is similarly delayed with increasing distance from the center of the chain. It shows slow growth, compatible with the weak relaxation of d-bosons observed in the imbalance dynamics. (d) The number entropy also has a non-uniform profile, with its values far from the center being consistent with the particle entropy of the Anderson insulator. This data refer to a system of $L = 60$ sites, averaged over 50 disorder realizations.

Thanks to $U(1)$ conservation, we can write the reduced density matrix of the first i sites from the left, ρ_i, in block-diagonal form, $\rho_i = \sum_n p_i^{(n)} \rho_i^{(n)}$, where $p_i^{(n)}$ corresponds to the weight of the n-particles sector, considering both c- and d-bosons, and $\mathrm{tr}\rho_i^{(n)} = 1$. It is then convenient to separate the total entanglement entropy, $S(i) = -\mathrm{tr}\rho_i \log \rho_i$, in two contributions: the configuration entanglement $S_C(i)$ and the particle entanglement $S_n(i)$ [68]

$$S(i) = S_n(i) + S_C(i) \tag{4.32}$$

$$S_C(i) = -\sum_n p_i^{(n)} \mathrm{tr}\rho_i^{(n)} \log \rho_i^{(n)} \tag{4.33}$$

$$S_n(i) = -\sum_n p_i^{(n)} \log p_i^{(n)}, \tag{4.34}$$

where the two bosonic species are left indistinguishable.

The configuration entropy $S_C(i,t)$ arises from the superposition of different product states in $|\psi(t)\rangle$ and measures the correlation between particle configurations in the two subsystems. The growths of configuration entropy can be attributed to the interacting nature of the system. Thus configuration entropy does not show interesting dynamics in the Anderson insulator, while displaying a logarithmic growth in the many-body localized phase [68] providing the main contribution to the entanglement growth [55]. Particle

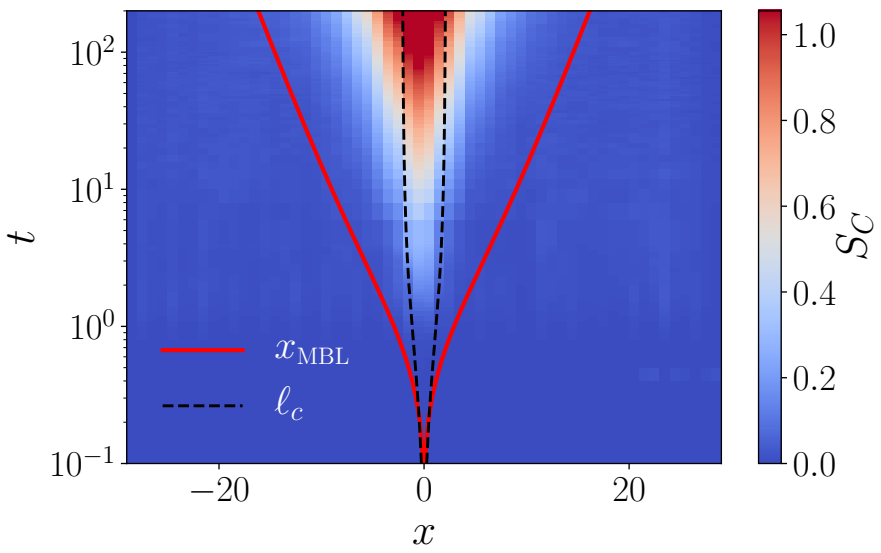

Figure 4.18: The configuration entropy $S_C(i,t)$ at $U = 12$ and $L = 60$, characterizing the interacting nature of the system, presents an extremely inhomogeneous growth. In agreement with the picture of propagation of MBL, its growth is constrained within the "MBL light-front" $x_{\mathrm{MBL}}(t)$ shown by the red line. When $x \gg x_{\mathrm{MBL}}$, the configuration entropy S_C is close to zero, suggesting that system remains effectively non-interacting until late times. For comparison we show also the behavior of $\ell_c(t)$, confirming that the c-boson affects the system on a scale beyond its decay length.

number entanglement entropy $S_n(i)$ arises from the occupation of different sub-sectors of the density matrix ρ_i and hence accounts for the particle transport in the system. Recent studies [179, 211] suggested an extremely slow, albeit finite, growth $S_n(i,t) \sim \log\log t$, which they attributed to slow particle transport. Subsequent work by [180] however suggested absence of such transport and saturating particle number entanglement.

The dynamics of the two contributions to the entanglement in our model is presented in Figure 4.17, where the first row shows the configuration entanglement growth for different cuts in the chain (a) and its profile at different times (b). In the second row, we show the dynamics of particle number entanglement. Similarly to the configuration entropy, $S_n(i,t)$ has a non-homogeneous growth across the system shown in Fig. 4.17(c)-(d).

Separating entanglement $S(i)$ into configurational and particle part, it is clear that the logarithmic growth is due to the configuration entropy, $S_C(i) \sim \xi_S \log(t)$, as clearly shown in Figure 4.17(a). The configuration entanglement growth has a non-homogeneous behavior in the system, explained by the propagation of MBL phenomenology discussed above. Using the effective interaction U_{eff} previously introduced, the dynamics of $S_C(i)$ can be described by the ansatz $S_C(i,t) \approx \xi_S \log(1 + U_{\mathrm{eff}}(i,t)t)$. This explains the delayed onset of the growth of configurational entropy in Fig. 4.17(a) away from the center of the chain. Similarly to the full entanglement entropy, a linearly decreasing entanglement profile away from the center of the chain is predicted, with the following asymptotic behavior of the configurational entanglement

$$S_C(i, t \gg 1) \sim \mathrm{const} - \frac{\xi_S}{\ell_c(t)}|i - L/2|. \tag{4.35}$$

This prediction is confirmed by the numerical results shown in Fig. 4.17(b), yielding the

value of $\xi_S \approx 0.31$.

According to the effective interaction picture describing the propagation of MBL, the interacting nature spreads through the system producing a many-body localization front $x_{\mathrm{MBL}}(t)$[4]. As shown in Figure 4.18, the prediction of the MBL lightcone (red curve) provides an accurate description of the actual behavior of the spread of configuration entropy, thus testing the genuine propagation of the many-body nature through the chain.

4.3.3 Probing eigenstates with DMRG-X

As shown throughout the previous Section, TEBD allowed the accurate simulation of dynamics for large systems. However, the maximal time is limited by entanglement growth, and the fate of the system at late times remains open to interpretation. Below we use the DMRG-X algorithm [110, 111, 112] to probe eigenstates of large systems, providing an effective insight into the infinite time behavior.

c- and d-boson localization

We extract highly excited eigenstates of the Hamiltonian (4.4) with $L = 30$ and 60 sites, $U = 12$ and 1/3 filling of d-bosons. We obtain in total 250 (500) eigenstates in the middle of the spectrum by targeting 25 different energies for each of the 10 (20) disorder realizations considered for $L = 30$ (60) chain respectively. [5] The states are obtained as

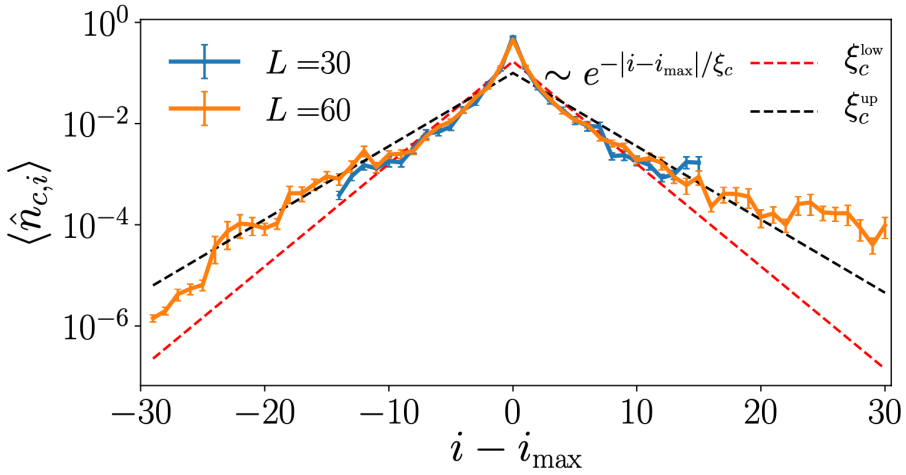

Figure 4.19: The density profile of the c-boson averaged over different eigenstates as a function of the distance from localization center $i_{\max}$ shows an exponential decay for both the system sizes considered. Through a fit to the density in different regions we obtain an upper and lower bound for the localization length, with $\xi_c^{\mathrm{low}} \approx 2.1$ (red dashed line) corresponding to the fit excluding the central site and $\xi_c^{\mathrm{up}} \approx 3$ (black dashed line) obtained from the fit that exclude 12 central sites.

[4] In the thermodynamic limit there might be the possibility of the boundaries of the system remaining Anderson localized. For a system of size L, the time on which the edges of the system see interactions and become MBL reads $t_{\mathrm{MBL}} \approx e^{L/(2\xi_c)}$. Comparison of the Heisenberg time, $t_H \approx e^{cL}$, with c given by $\log \frac{3}{2^{2/3}}$, with t_{MBL} then suggests that true propagation of MBL takes place whenever the localization length of clean particles measured in units of lattice spacing is $\xi_c > 1/2c \approx 0.58$.

[5] We note, that the first 10 disorder realizations for $L = 60$ system are chosen in such a way that the values of the random energies of the 30 central sites agree with those for $L = 30$ system. Such choice of disorder is motivated by possibility of direct comparison with the data from smaller system sizes.

a result of 100 sweeps where the targeted eigenstate is variationally approximated by an MPS of maximum bond dimension $\chi = 500$ and 250 for systems of size 30 and 60, respectively. The algorithm is initialized with different copies of the initial state (4.7), where the c-boson initial position is chosen among empty sites in the central region. We refer the reader to Appendix C.2 for details on the implementation of the algorithm as well as its performance metrics.

For each of the eigenstates we extract the position where the c-boson density is maximal, $i_{\max}$. This position may be viewed as a localization center of c-boson. When averaging over different eigenstates, the distances are measured with respect to the localization center $i_{\max}$. For instance, density is calculated as a function of $i - i_{\max}$ for each individual disorder realization and then resulting function is averaged over disorder. The average c-boson density plotted as a function of the distance from its peak presents an exponential profile, as shown in Fig. 4.19. We notice that the density profile around the peak is enhanced with respect to the tails, which can be potentially attributed to the large value of U producing stable doublons. The exponentially decaying density confirms the localization of the clean particle and allows us to extract the upper and lower bound on the localization length, $\xi_c^{\text{low}} \approx 2.1$ and $\xi_c^{\text{up}} \approx 3$ resulting from fitting its profile close to the center (excluding the central site) and at the edges of the chain. The two bounds quantitatively agree with the lengthscale $\ell_c(t \to \infty) = \xi_c = 2.5$ *extrapolated* from TEBD dynamics in Section 4.3.2 suggesting that the localization of the c-boson observed in dynamics is not a transient effect, but it is a property of the system, provided the correct sector of the Hilbert space is explored.

Probing potential localization of d-bosons in eigenstates is more complicated: the finite particle density does not allow to define a localization center. Therefore, we consider the average deviations of the d-bosons density from the thermal value given by their average density $\nu_d = 1/3$ as a function of the distance from $i_{\max}$. In Figure 4.20, we show the averaged absolute value of the deviation of the density expectation value from ν_d, which is limited to the range of values $0 < \langle|\hat{n}_{d,i} - \nu|\rangle < 1 - \nu_d$. While in a thermalizing system we expect this quantity to be small and decrease exponentially with the system size, the eigenstates of our problem have on average large expectation value of $\langle|\hat{n}_{d,i} - \nu|\rangle$. In

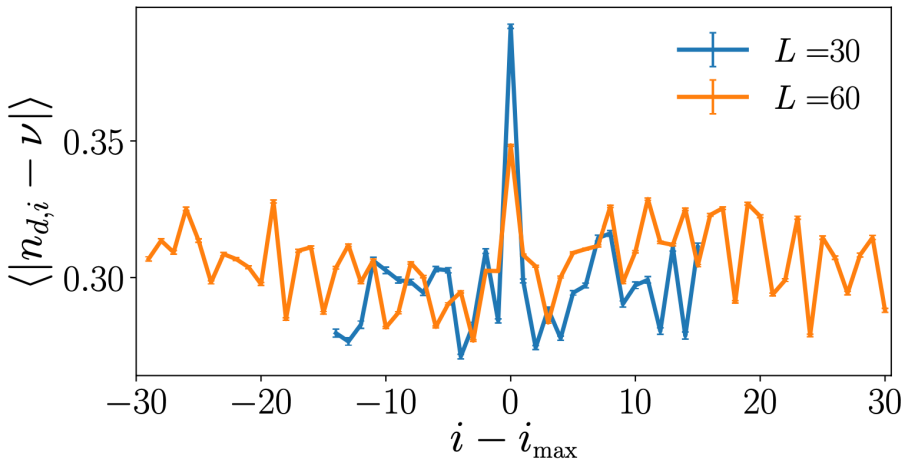

Figure 4.20: Strong deviation of the d-bosons density away from the thermal value $\nu_d = 1/3$ consistent between different system sizes indicates the breakdown of thermalization in eigenstates.

addition, increasing the system size does not lead to a decrease of the average distance from the thermal value, thus suggesting that the d-bosons density strongly fluctuates around ν_d in eigenstates due to their localization. Interestingly, we notice a slight peak of this quantity at $i = i_{\max}$, which is in agreement with the enhancement of the c-boson density observed in Fig. 4.19 and may be attributed to the effect of doublons. In the region around the center, however, we observe a slight weakening of localization, corresponding to smaller values of $\langle|\hat{n}_{d,i} - \nu|\rangle$. This can be attributed to the fact that in the vicinity of the peak of the c-boson, the interactions are effectively stronger, leading to an increased relaxation of the d-bosons.

Further evidence of localization for both types of particles is found in the spectrum of the single-particle correlation matrices $C_{ij} = (1/N_c)\langle\hat{c}_i^\dagger\hat{c}_j\rangle$ ($D_{ij} = (1/N_d)\langle\hat{d}_i^\dagger\hat{d}_j\rangle$) [76, 212]. In the particular case treated here, the von Neumann entropy of C corresponds to the intra-species entanglement $S_{cd} = -\operatorname{tr} C \log C$. We study its distribution and average value among eigenstates, obtaining average entropy of $S_{cd} \approx 0.85$ for both system sizes. Furthermore, the eigenvalues of $C(D)$, $w_{c,i}(w_{d,i})$, sorted by decreasing value, can be interpreted as occupation numbers of single-particle orbitals [76, 212]. In the case of an MBL system, it is expected that particles sit on almost localized sites, hence only the first $N_{c/d}$ orbitals should be significantly occupied. In Figure 4.21 we show the average, $\langle\cdot\rangle$, and log-average, $\overline{x} = e^{\langle \ln x\rangle}$, value of the ordered eigenvalues for D and C respectively. The scaling of $N_d\langle w_{d,i}\rangle$ exhibits a step behavior with the value of $\langle w_{d,i}\rangle$ dropping to zero for $i > N_d$, consistent with the localization of the d-bosons. Similarly, the typical value $\overline{w}_{c,i}$ presents a single large eigenvalue, while the rest decay exponentially.

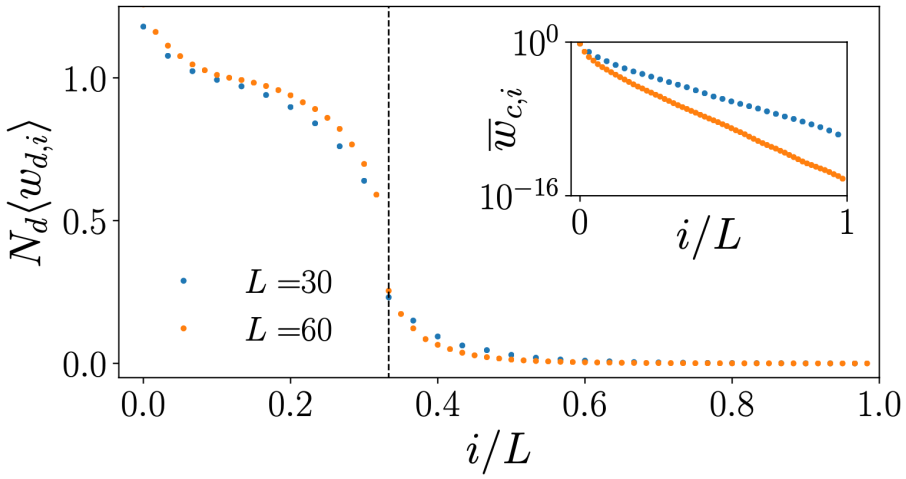

Figure 4.21: The spectrum of D shows a step behavior, dropping quickly to small values at $i/L = \nu_d = 1/3$ (dashed line). This corresponds to the presence of N_d occupied single-particle orbitals, thus confirming localization. Here we show the spectrum of D multiplied by the total number of particles N_d to highlight the similarity between the two system sizes. We note that $N_d w_{d,i} > 1$ is due to the bosonic nature of these particles. The inset shows the log-averaged spectrum of C on a logarithmic scale, revealing that there is a single significantly occupied orbital, while all the others have an exponentially decaying weight.

Entanglement structure of eigenstates

In Figure 4.22(a) we show the bipartite entanglement profile averaged as a function of the position of the cut i. While the entanglement profile of eigenstates suggests an area-law

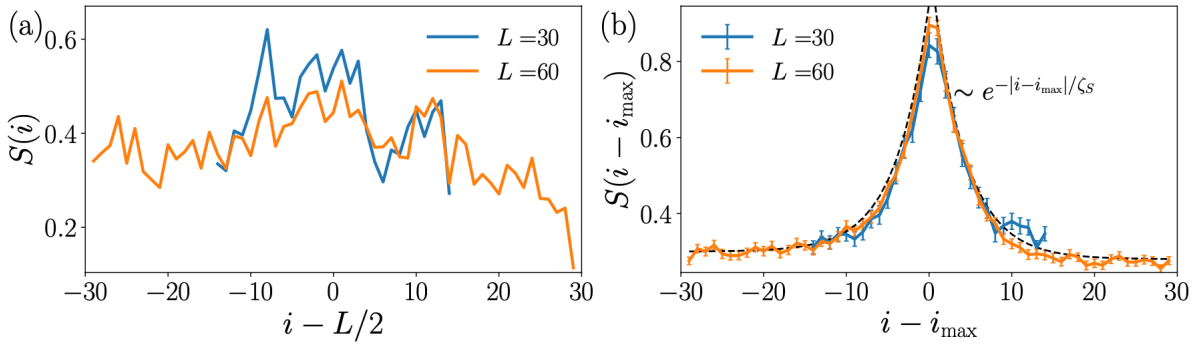

Figure 4.22: (a) Average entanglement as a function of the cut position results in a featureless profile. The agreement in entanglement between different system sizes where they overlap is due to particular disorder choice. (b) Averaging the entanglement profile as a function of the distance from the center of localization of c-boson, $i_{\max}$, shows enhancement in entanglement caused by the presence of the clean boson. The dashed line shows the comparison to an exponential fit. The collapse of entanglement profile between different system sizes suggests area-law entanglement scaling.

entanglement scaling characteristic of many-body localization [56, 79], this representation of data does not show any effect from the presence of the clean boson. To observe the influence of the c-boson, we average the entanglement profile defined with respect to the distance from the localization site of the c-boson, $i - i_{\max}$. Figure 4.22(b) reveals a peak in $S(i - i_{\max})$ around zero, indicating that the clean boson is responsible for additional entanglement in eigenstates. Away from $i_{\max}$ entanglement saturates to a constant value, revealing a clear area-law scaling. Fitting the decay of entanglement away from the center with an exponential of the type $S_0 + ce^{-|i-i_{\max}|/\zeta_S}$ allows to extract the value of $\zeta_S \approx 4$, suggesting that the single c-boson is capable of generating non-trivial entanglement patterns on a scale larger than its localization length. This is due to the fact that entanglement entropy is a very sensitive measure of the interacting nature of the system, hence even a small coupling introduced at $i > \xi_c$ produces an enhancement in entanglement.

The increase in entanglement of eigenstates that decays exponentially with the distance away from the location of c-boson provides further support to the localized nature of eigenstates. Moreover, this provides a complementary view on the picture of the inhomogeneous effective interaction triggered by the presence of c-boson and resulting in the dynamical "propagation of MBL" presented in [65] and in Section 4.3.2 of this thesis.

4.4 Weak coupling regime

As we already showed in the previous Section, at strong interactions the disordered bosons induce localization of the small bath. Here we address the presence of a transition to thermal phase as the interaction strength is decreased, using both quasi-exact large scale numerical simulations and analytical considerations.

4.4.1 Delocalization of clean boson

Using the highly efficient parallel implementation of the time-evolving block decimation (TEBD) algorithm [114] with large bond dimension $\chi = 5000$ and small truncation error

$\varepsilon = 10^{-9}$, we simulate the dynamics generated by the Hamiltonian (4.4) in large systems of $L = 252$ sites. This choice of parameters, together with the fourth order Suzuki-Trotter decomposition with small time-step used, guarantees almost exact numerical results up to the times when bond dimension saturates. We further explore Floquet dynamics of matrix product states of maximal bond dimension $\chi = 2048$ and systems with up to $L = 2000$ sites. The large system sizes studied and the long timescales achieved in our work allow to exclude boundary effects due to the finite size of the system and achieve high entanglement regime. As we shall demonstrate below, this is particularly important in the weak interaction case due to delocalization and spreading of the clean boson to large distances.

In both the Hamiltonian and Floquet case, we focus on the dynamics of an initial product state corresponding to a d-bosons density wave of period $1/\nu_d = 3$ and a single clean boson initialized in the middle of the system at site $i = L/2$, as explained in Section 4.2

Diffusive behavior of the bath at weak interaction

We analyze the behavior of the clean particle that constitutes the bath by studying the evolution of its density profile $\langle \hat{n}_{c,i}(t) \rangle = \langle \psi(t) | \, \hat{n}_{c,i} \, | \psi(t) \rangle$ with time. In the localized and ergodic phases, the bath spreading is expected to show very different characteristic properties. When the c-boson gets localized through the MBL proximity effect, the density profile decays exponentially away from the initial position and localization lengths is expected to saturate at long times. In contrast, when the MBL proximity effect fails to localize the bath, the clean boson is expected to spread diffusively due to the influence of the disordered system, hence showing a Gaussian density profile with the density at the original site decaying as $\propto 1/\sqrt{t}$.

To characterize the dynamics of the c-boson, we perform collapses of its density profile at different times, using the following scaling form:

$$\langle \hat{n}_{c,i}(t) \rangle = t^{-\alpha} f\left(\frac{i - L/2}{t^{\alpha}} \right). \tag{4.36}$$

The value of the exponent $\alpha(U)$ can be thought as a proxy for the inverse dynamical exponent and is used to distinguish the diffusive and localized behavior of the bath. These density profile collapses are shown in Figure 4.23(a)-(b) for Floquet dynamics and in Figure 4.23(e)-(f) for Hamiltonian evolution. At weak interaction strength U, the value of $\alpha \approx 0.5$ in both Hamiltonian and Floquet cases suggests a delocalized bath. At strong U, instead, in the Floquet case the small exponent $\alpha \approx 0$ highlights the saturation of the c-boson spreading, thus confirming the MBL proximity effect already observed at stronger interactions in the previous Section. In the Hamiltonian time-evolution, however, the exponent α attains a larger value, that can be ascribed to the shorter times achieved in this regime. Indeed, comparison with the collapse in the corresponding time-window of the Floquet evolution results in good agreement of the value of α as shown in Fig. 4.23(c), suggesting that at later times the exponent will eventually decay also in the Hamiltonian case.

In addition to different values of α obtained from the rescaling, the density profiles of clean boson in Figure 4.23(a)-(b) and (e)-(f) also have a qualitatively different form. In the delocalized phase, the boson density shows a characteristic Gaussian profile, as opposed to the exponential decay at strong interactions.

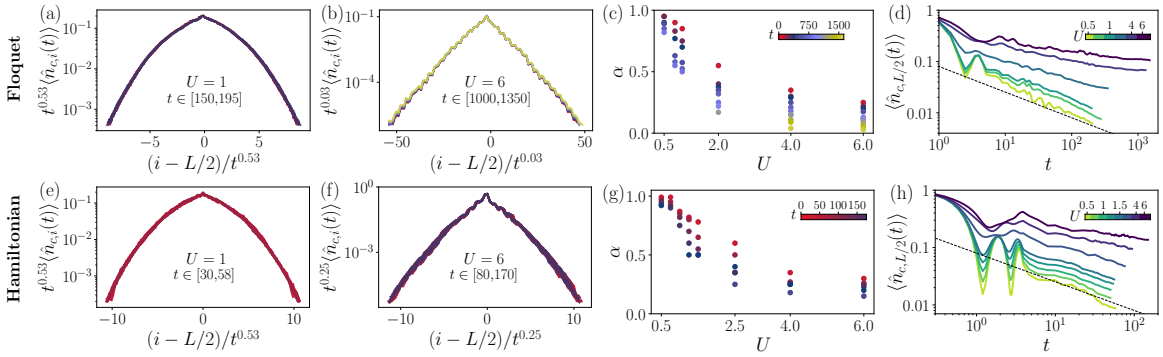

Figure 4.23: Top row: Floquet dynamics. (a) At $U = 1$ the density profiles at long times $150 \leq t \leq 200$ collapse when rescaling the space axis by $\sqrt{t}$ indicating diffusive behavior of the c-boson. (b) At $U = 6$, a similar collapse of the density profile is obtained with a much smaller exponent $\alpha = 0.03$, a value that could be consistent with zero suggesting localization. (c) The exponent $\alpha(U)$ as a function of interaction strength U shows that diffusive spreading of c-bosons at weak interactions $\alpha \approx 1/2$ slows down and it becomes localized at strong U as is witnessed by $\alpha \to 0$. Color indicates the time range used to obtain the exponent, range of accessible times is limited at weak U by entanglement growth. (d) Decay of the c-boson density at its original site $i = L/2$ is consistent with $1/\sqrt{t}$ (black dashed line) in the delocalized phase, and it shows signatures of saturation at strong interaction $U \geq 4$. Bottom row shows similar data but for Hamiltonian dynamics limited to shorter times. (e) Hamiltonian dynamics show a similar behavior indicating diffusion of the c-boson at weak interaction. (f) At larger U, density profiles collapse with a larger exponent α than in the Floquet case. This can be attributed to the shorter times achieved in Hamiltonian dynamics, as Floquet dynamics shows comparable values of α at earlier times, see panels (g)-(h). System size is $L = 252$, data are averaged over 10 disorder realizations.

The study of the exponent α at different times and as a function of U is presented in Figure 4.23(c) and (g). Saturation towards $\alpha = 1/2$ is observed at $U < 2$, and is especially apparent for Floquet evolution. For Hamiltonian dynamics the values of the exponent remains close to $\alpha = 1$ at times $t \approx 150$. This suggests that a much longer time evolution is needed to see the crossover to diffusion. In contrast, for $U \geq 2.5$ the value of α decreases with increasing evolution time. This suggests that a transition from delocalization to localization occurs in the window of interaction strengths $1 \lesssim U \lesssim 2.5$. Due to the fast entanglement growth observed in it, this critical region is also the most challenging to treat numerically, thus preventing a more accurate estimate of the transition point. The transition in the behavior of the bath can also be captured by the different dynamics of the central site density decaying as $\approx 1/\sqrt{t}$ in the delocalized case and saturating to a finite value at strong U, as shown in Fig. 4.23(d) and (h). Note, that the saturation of the density in the Floquet dynamics for $U = 2$ in Fig. 4.23(d) at long times may suggest that the bath localized at this interaction strength. The range of times in the Hamiltonian dynamics is insufficient to decide on the fate of the system. Finally, in Appendix C.3.2 we provide further evidence of the c-boson transition by showing a diverging decay length at $U < 2$.

Slow delocalization of disordered bosons

Due to the small bath size, changing the interaction strength U has a much weaker influence on the density profiles of d-bosons. Indeed, comparing the density profiles and the imbalance at different values of U naïvely suggests that the disordered particles remain localized throughout all the values of interaction strengths, at least on the accessible timescales. A deeper investigation of more sensitive probes, provided by the entanglement entropy and the connected correlation functions of d-bosons, however, reveals the existence of two contrasting behaviors at weak and strong U.

As shown in Appendix C.3.3, the global half-chain entanglement entropy grows algebraically for weak values of the interaction, characterized by a universal behavior $S_{L/2}(t) \propto (tU^{\beta})^{\gamma}$, with $\gamma \approx 0.39$ and $\beta \approx 1.1$ in the Floquet case. In the Hamiltonian case a qualitatively similar picture holds, although the value of β suddenly drops to ≈ 0.6 as $U > 1$. This deviation from the logarithmic growth of the entanglement entropy indicates that the system cannot be fully localized. The analysis of the entanglement profile provides further evidence in favor of delocalization, as its growth is not limited to the central part of the chain, but it propagates to regions far from the initial position of the clean particle. The emergence of large regions where entanglement grows fast can then be a possible mechanism destabilizing localization [62].

To further probe the behavior of the d-bosons, we analyze their density-density connected correlations

$$\langle \hat{n}_{d,i}\hat{n}_{d,j}\rangle_c = \langle \hat{n}_{d,i}\hat{n}_{d,j}\rangle - \langle \hat{n}_{d,i}\rangle\langle \hat{n}_{d,j}\rangle, \tag{4.37}$$

shown in Figure 4.24 (Floquet (a)-(c), Hamiltonian (d)-(f)) as a function of the distance from the center and at different times. At weak interactions below the transition $U < U_c$, the connected correlations present a slow $1/i$ decay in space (black dashed line) and

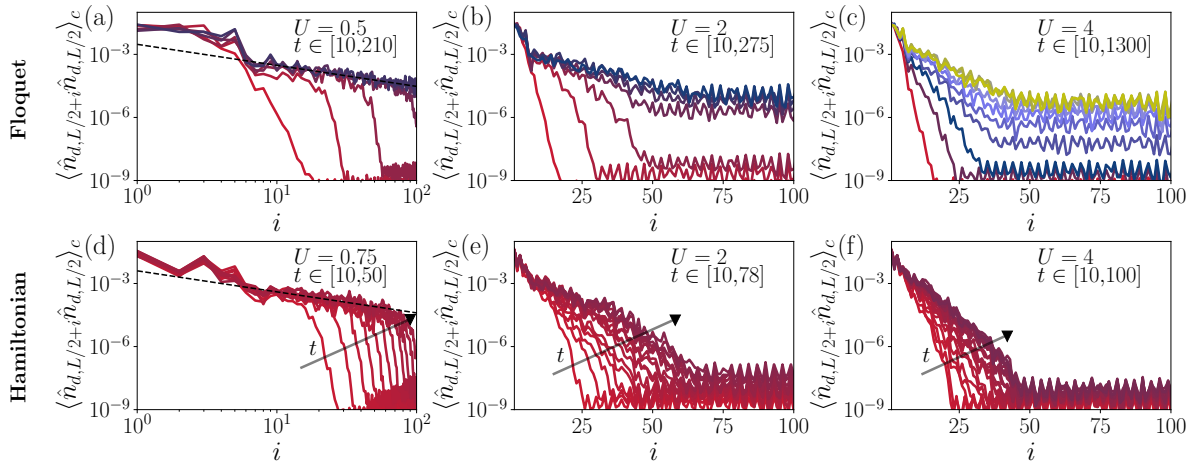

Figure 4.24: Density-density connected correlation functions for d-bosons in Floquet (a)-(c) and Hamiltonian (d)-(f) time evolution. At weak interactions, (a) and (d), correlations decay algebraically with distance, consistent with $1/i$ dependence (black dashed line). Such algebraic decay of connected correlation functions suggests delocalization of d-bosons on long timescales. As U is increased, however, the localized behavior is eventually recovered, and panels (b)-(c) and (e)-(f) show exponentially decaying correlation functions for $U = 4$. We notice the emergence of a plateau far from $i = L/2$ in the Floquet case, which is due to the truncation error arising from the faster saturation of bond dimension in this type of time-evolution.

spread in time to regions far from the center, confirming the slow delocalization of the d-bosons. On the other hand, in the MBL proximity effect phase, density correlations decay exponentially, with a decay length slowly increasing in time and eventually saturating, as highlighted by the collapse of the curves at late times. For values of $U \geq 4$ we notice that the decay length of the d-bosons correlations, $\ell_d(t)$, seems to saturate to a value comparable with the lengthscale of the exponential suppression of the c-boson density, $\ell_c(t)$. The saturation value of $\ell_{c,d} \approx 5$ obtained for $U = 4$, is much smaller compared to the simulated system size, thus confirming the localization of c and d-bosons.

In conclusion, our large scale numerical simulations reveal two qualitatively different behaviors in the system at large and weak interaction strengths. Such distinction would be hard to make in smaller systems where the finite size affects the spreading of both particle types. In the regime of large U, both boson species are localized. At weak U, while we observe a spreading of c-bosons over the distances comparable to hundreds of lattice sites, the dynamics of d-bosons is much slower, and we are unable to decide their fate despite reaching long times $t \geq 200$ in our simulations.

4.4.2 Estimate for the critical coupling from mapping to Bethe lattice

After identifying numerically the existence of two different phases, we construct a phenomenological picture of the transition that allows to obtain analytical estimates. To analyze the behavior of our model in the weak interaction regime, we first consider the Hartree picture presented in Sec 4.3.1, where both the bath and the d-bosons are localized with localization length $\xi_c \gg \xi_d$ at weak coupling. As explained in Section 4.3.1 the interaction in the Anderson orbitals basis corresponds to simultaneous c- and d-bosons hopping among different localized orbitals

$$U \sum_i \hat{n}_{c,i}\hat{n}_{d,i} = \sum_{\alpha\beta\gamma\delta} V_{\alpha\beta}^{\gamma\delta} \hat{d}_\alpha^\dagger \hat{d}_\beta \hat{c}_\gamma^\dagger \hat{c}_\delta. \tag{4.38}$$

In particular, we focus on the motion of the clean boson comprising the quantum bath. The hopping between different orbitals, arising from the interaction term in Eq. (4.38) can be depicted on a graph representing the Fock space. Each node in this graph corresponds to a certain filling of localized orbitals, and edges connect different configurations with the matrix element obtained from Eq. (4.38). While long-range hoppings are allowed, they are exponentially suppressed due to the localization of both particle species in the Hartree limit. Therefore, neglecting the edges connecting configurations where the particles move farther than their localization length, we approximate the full Fock space as a graph of connectivity $K \approx \xi_c^2 \xi_d \nu_d(1-\nu_d)$, where the $\nu_d(1-\nu_d)$ term accounts for the finite density of d-bosons and their hard-core nature as derived in Section 4.3.1.

A second, crucial, approximation corresponds to neglecting all loops in the graph, resulting in a Bethe lattice with coordination number K, as shown pictorially in Figure 4.25 for $K = 4$. In this graph we distinguish two types of hopping processes for the clean boson, *elastic* and *inelastic*. In *elastic* hoppings, the c-boson moves without changing the pattern of occupation of d-bosons orbitals, i.e. $\alpha = \beta$ in Eq. (4.38). These processes, depicted by solid arrows in Figure 4.25, correspond to the motion of the clean-particle in the random environment created by the d-bosons. Alternatively, the c-boson motion can simultaneously produce a scattering of d-boson from one orbital to another. We refer

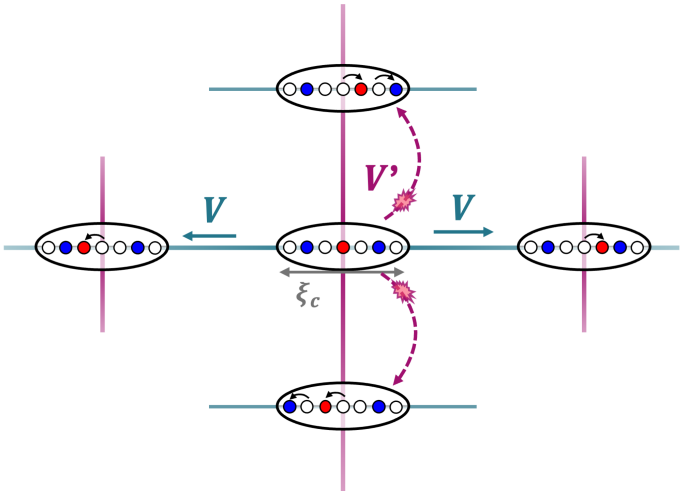

Figure 4.25: Schematic representation of the Bethe lattice, where a small $K = 4$ is chosen for clarity. Each node represents a different boson configuration in Fock space. *Elastic* scattering (horizontal edges) connects nodes where only the c-boson moves with a hopping amplitude V. The simultaneous hopping of clean and disordered bosons, instead, gives rise to *inelastic* processes (vertical edges) with amplitude V'.

to this second type of processes as *inelastic* and represent them as dashed arrows in Figure 4.25.

A phenomenological mapping of the motion of the c-boson to a finite coordination number Bethe lattice allows us to use the results of [213] and obtain a condition for the stability of localization. The stability of the localized phase is controlled by the interplay of the disorder strength on the lattice $\mathcal{W}$, the connectivity, K, and the matrix element of the hopping processes, V. Ref. [213] derives a trascendental equation for the critical value of the matrix element V_c, $\frac{2KeV_c}{\mathcal{W}} \log\left(\frac{\mathcal{W}}{2V_c}\right) = 1$, such that the localized phase is stable for $V < V_c$. To apply this result to our model, we estimate the typical matrix element V, the disorder strength $\mathcal{W}$ and the connectivity K. In order to establish the typical matrix element V, we first consider its approximate expression

$$V_{\alpha\beta}^{\gamma\delta} \approx \frac{U}{\xi_c \xi_d} \sum_i e^{-\frac{|i-x_\alpha|+|i-x_\beta|}{\xi_d}} e^{-\frac{|i-x_\gamma|+|i-x_\delta|}{\xi_c}}, \tag{4.39}$$

where we replace the orbital-specific localization length with its average and neglect the oscillatory part of the wave function. In Appendix C.3.4, we estimate the typical value of V, which in the case of $\xi_c \gg \xi_d \approx 1$ can be approximated as $V \approx U/(2\xi_d)$. Finally, using the estimate for the connectivity $K \approx \xi_c^2 \xi_d \nu_d (1-\nu_d)$, we can estimate the transition solving numerically the equation for the critical hopping amplitude on the Bethe lattice at fixed $t_c = t_d = 1$ and $W = 6.5$. In the Hartree approximation the effective disorder results from the interaction with the d-bosons, and it is thus proportional to the coupling strength, $\mathcal{W} \propto U$. Also, the localization length of the c-boson scales as $\xi_c \propto U^{-2}$, as shown in the previous Section. Thus, the decrease of the hopping amplitude at weak U is counteracted by a larger effective connectivity and weaker effective disorder, leading to instability of localization below a certain critical value of interaction strength. The numerical estimate suggests that in this parameter range, localization becomes unstable at a critical value of the coupling $U_c \approx 3$, in good agreement with the transition window inferred from the numerical results of Section 4.4.1.

In summary, the phenomenological mapping of the hopping of the single clean boson to the Bethe lattice discussed above predicts an instability of localization at sufficiently weak interactions U in agreement with our numerical simulations. The present approach differs from the method used in Section 4.3.1, where the ratio of the typical matrix element to the level spacing was used as a criterion for delocalization. While the resulting critical curves are qualitatively similar, we expect the current mapping to the Bethe lattice to be more accurate in the weak coupling regime. Indeed, in the present work we focus primarily on the behavior of the c-boson in the case of $\xi_c \gg \xi_d \approx 1$, where the problem can be interpreted as a weakly localized single particle occasionally perturbed by the inelastic scattering of d-bosons. Additionally, considering the motion of the c-boson in the Bethe lattice gives an intuitive explanation of the diffusive behavior observed in Section 4.4.1. In the standard picture of single particle localization on the Bethe lattice, the motion of the particle in the delocalized phase is ballistic, since the majority of steps increase the distance of the particle to the origin. In contrast, our mapping naturally reproduces diffusion in the delocalized phase, since at each point half of the hopping processes move the c-boson to the left, and the remaining half moves it to the right, see Fig. 4.25. Understanding if the present phenomenological mapping to the Bethe lattice is capable of reproducing other aspects of numerical simulations, such as entanglement dynamics or very slow relaxation of d-bosons in the delocalized phase remains an interesting open question.

4.5 Extensive bath

In the previous Section we provided evidence of a transition between regimes of localized and delocalized small bath, tuned by the interaction strength, U. In this Section we study the effect of increasing the density of c-bosons that constitute the bath to a finite value. First, in Subsec. 4.5.1 we consider the case when the density of c-bosons is close to half-filling, and investigate the transport of bosons. Afterwards, we study the regime of finite but small density of clean bosons in Section 4.5.2.

4.5.1 Large particle density in the bath and charge transport

We first approach the regime where the clean-particles composing the bath have a large overall density $\nu_c \geq 1/5$. In this regime we expect that the bath triggers delocalization of the d-bosons. To characterize the resulting delocalized phase, we study the transport of bosons using the time-evolution of density matrices close to infinite temperature represented as MPOs. This has several advantages over simulating states directly, which we discuss in Appendix C.4.

Following a well-established approach [156], we initialize the system in a density matrix characterized by a small step in the center of the particle density profile. Figure 4.26 illustrates such an initial density profile, with density in the left (right) part of the chain being set to $\nu_{c/d} \pm \mu_{c/d}$. This condition translates to an initial density matrix written as a tensor product of density matrices on individual sites. The density matrix of individual site of c-bosons (and analogously, d-bosons) can be written as

$$\rho_c^{(i)} = \begin{pmatrix} 1-\nu_c-\mu_c(i) & 0 \\ 0 & \nu_c+\mu_c(i) \end{pmatrix}, \tag{4.40}$$

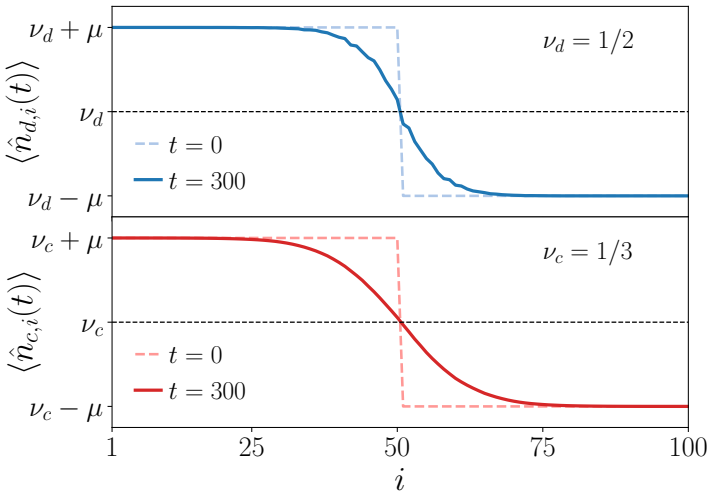

Figure 4.26: Density profile of disordered and clean bosons at late (solid lines) and initial (dashed lines) times. The small density step of magnitude 2μ slowly melts due to the particle current running from the left to the right part of the chain. Data are averaged over 30 disorder realizations, other parameters of numerical simulation are specified in the main text.

where $\mu_c(i) = \pm 0.01$ in the left and right half respectively. Since the time-evolution of density matrices represented as MPOs is most efficient when they are close to infinite temperature, we fix the d-bosons density to be $\nu_d = 1/2$. We then apply operator TEBD to large chains of $L = 100$ sites up to times $T = 300$, using a maximal bond dimension in the range $\chi \in [128, 192]$, depending on the convergence of the results, shown in Appendix C.4.1.

To characterize particle transport, we study the evolution of the transferred particle number, $\delta n_{d/c}(t)$, defined as a difference between the density profile at zero time and time t, $\langle \hat{n}_{d/c,i}(t) \rangle$,

$$\delta n_{d/c}(t) = \sum_{i=1}^{L/2} \left[\langle \hat{n}_{d/c,i}(0) \rangle - \langle \hat{n}_{d/c,i}(t) \rangle \right]. \tag{4.41}$$

The change of density with time corresponds to the current across the central site, integrated over time, thus quantifying the transport of particles. In particular, the logarithmic derivative of $\delta n_{c/d}$ with respect to time can be related to the instantaneous inverse dynamical exponent $1/z(t)$,

$$\frac{1}{z(t)} = \frac{d \ln \delta n(t)}{d \ln t}. \tag{4.42}$$

We study the particle flow as a function of interaction strength U and density of particles in the bath, ν_c. As we show in Figure 4.27, $\delta n_{c/d}(t)$ at times larger than $t \geq 10$ has a clear power-law behavior for both particle species, confirming the delocalization of the originally Anderson localized d-bosons due to the coupling to the bath. However, the fact that d-bosons without coupling to the bath are localized, is reflected by the qualitatively different behavior of the transported number of particles with changing U apparent in Fig. 4.27(a)-(b). With increasing interaction strength, the c-bosons exhibit slower transport, whereas the d-bosons are characterized by faster transport.

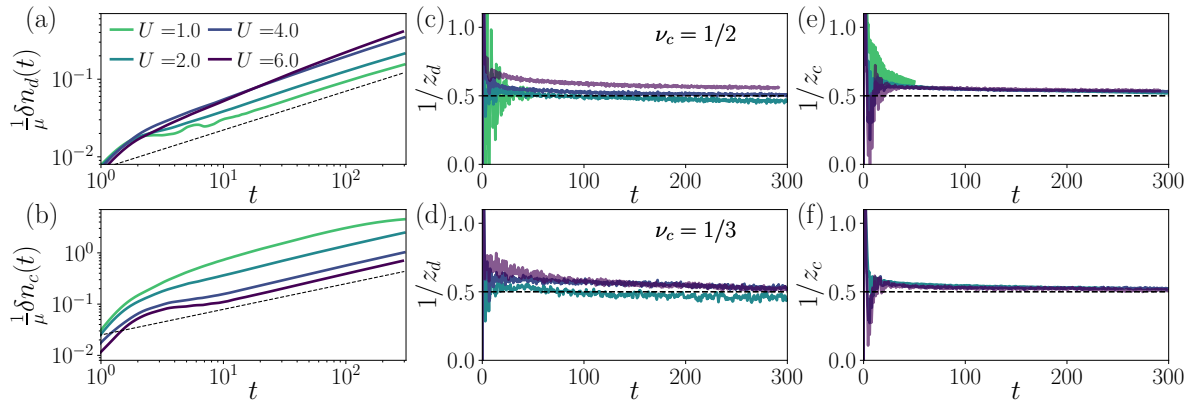

Figure 4.27: (a)-(b) Dynamics of the particles flow across the central site for d and c-bosons at large $\nu_c = 1/2$, and $\nu_d = 1/2$, $W = 6.5$. In both cases $\delta n(t)$ shows a clear power-law behavior close to diffusion $\approx \sqrt{t}$ (dashed line). However, while for the c-bosons δn_c increases as the interaction strength decreases, in agreement with their free nature at $U = 0$, for the disordered particles the opposite behavior is observed. (c)-(f) Inverse dynamical exponent of d-bosons $1/z_d(t)$ and c-bosons $1/z_c(t)$ for different values of the bath size $\nu_c = 1/2$ (c),(e) and $\nu_c = 1/3$ (d)-(f). At large U, $1/z_d(t)$ saturates to a diffusive value $z_d = 2$ for both clean particle densities. As U is decreased and the Anderson localized phase is approached, however, d-boson transport shows signatures of subdiffusive behavior. On the other hand, c-boson transport is almost unaffected by the coupling strength, always showing diffusive behavior, except for $U = 1$. In this case $1/z_c$ vanishes at late times due to the finite size of the system, thus requiring larger systems to properly evaluate the dynamical exponent.

In Figure 4.27(c)-(f), we show the instantaneous dynamical exponent $z_{c/d}(t)$ extracted using Eq. (4.42). We report results for two different particle densities in the bath, $\nu_c = 1/2$ in panels (c)-(e) and $\nu_c = 1/3$ in panels (d)-(f), at different coupling strengths U. Panels (e)-(f) show that the transport features of the bath are unaffected by the variation of the bath particle density and interaction strength, U, with $1/z_c(t)$ always rapidly converging to a value of $1/z_c \approx 1/2$ at late times. Note, that at $U = 1$ and $\nu_c = 1/2$ the transport of c-bosons is affected by the boundaries, as highlighted by the slowdown of the growth of $\delta n_c(t)$ shown in panel (b), thus requiring larger systems to properly assess its value.

In contrast to the c-bosons, the transport of the disordered bosons is more sensitive to the choice of the parameters. In particular, the value of the inverse dynamical exponent systematically decreases as the interaction strength and the density of particles in the bath are lowered, as indicated by the weakly subdiffusive behavior observed for $U \leq 2$. This slight subdiffusive behavior, however, is in contrast with previous results showing strong subdiffusion in a wide parameter range in the vicinity of the transition in the ergodic phase of disordered Hamiltonians [198, 199, 214].

In order to highlight the difference between transport observed in the present model to standard many-body localized systems, we investigate transport in the the disordered Heisenberg chain [52, 53]. In the two-species Hubbard model considered here interactions and hopping are of the same order, while disorder is larger and fixed to $W = 6.5$. Inspired by these values of parameters, we consider the disordered Heisenberg chain with fixed disorder $W = 6.5$ and hopping $J = 1$. We use interaction strength as a control parameter to tune delolcalization. Indeed, at weak values of $J_z \leq 1$ the model is allegedly localized,

whereas for larger J_z delocalization is expected.

Using density matrix simulation of the Heisenberg chain, as shown in Appendix C.4.2, we first confirm that the inverse dynamical exponent $1/z(t)$ decreases with increasing time at small values of J_z, consistent with localization. For larger values of J_z we observe a reversal of this trend, with $1/z(t)$ increasing with time. Nevertheless, even for longest accessible times $100 \leq t \leq 250$ and for the considered broad range of $J_z = 1.5 \ldots 10$, the value of $1/z(t)$ remains well below one half. This is consistent with previous numerical studies [198, 199, 214] that suggested the presence of a broad subdiffusive regime even for parameter values for which the model is deep into the delocalized phase. Since interaction, disorder strength and hopping are comparable in the two Hamiltonians, this result suggests that the presence of the bath in our model cannot simply be replaced by an effective local interaction. Intuitively, the rapid onset of diffusion for the disordered bosons in the present model may be attributed to an effective long-range coupling among them, mediated via the particles in the quantum bath, thus providing a faster transport channel. Quantifying such emergent long-range interaction via specific observables that can be probed in TEBD time evolution remains an interesting avenue for the future work.

4.5.2 Potential delocalization at small particle density in the bath

The ergodic behavior observed in the previous Section suggests the presence of a transition as function of the bath size. In order to capture this transition, we explore the parameter space close to the MBL phase, fixing $U = 6$ and slowly increasing the bath size $\nu_c = 1/24, 1/12 \ldots 1/6$.

As the clean particle density decreases, density matrices as Eq. (4.40) are too far from infinite temperature and give rise to large operator entanglement, thus becoming inefficient. We hence again use MPS time-evolution, which can still capture the dynamics of the system, although the timescales may be limited by the relatively fast entanglement growth. In this framework, we modify the initial state defined in Eq. (4.7) by replacing the single c-boson with a density wave of period $1/\nu_c$

$$|\psi_0\rangle = |\underbrace{\bullet\bullet\circ}_{1/\nu_d}\bullet\circ\circ\bullet\underbrace{\bullet\circ\bullet\circ\circ\bullet}_{1/\nu_c}\bullet\circ\bullet\circ\circ\bullet\bullet\circ\bullet\ldots\rangle, \tag{4.43}$$

so that it can accommodate an extensive number of clean bosons. We further choose a large system size $L = 126$ such that even at the smallest density, $\nu_c = 1/24$, the bath hosts a significant number of clean bosons, $N_c = \lfloor L/24 \rfloor$.

In Appendix C.4.3, we report on the behavior of density profiles and imbalance, confirming delocalization at large ν_c characterized by relaxation of the initial density wave pattern. At smaller bath densities, however, signatures of thermalization are absent up to the timescales $T \approx 50$. In order to capture the transition, then, we analyze the behavior of the more sensitive probe – entanglement entropy.

Since entanglement growth is influenced by the distance to the closest c-boson, we compare bipartite entanglement across a cut l_p such that $\langle \hat{n}_{c,l_p}(t=0)\rangle = 1$ for all considered densities of clean bosons. This comparison is shown in Figure 4.28(a), together with the entanglement entropy relative to the single-particle bath. After an initial transient logarithmic regime, entanglement entropy eventually curves upwards, indicating a faster

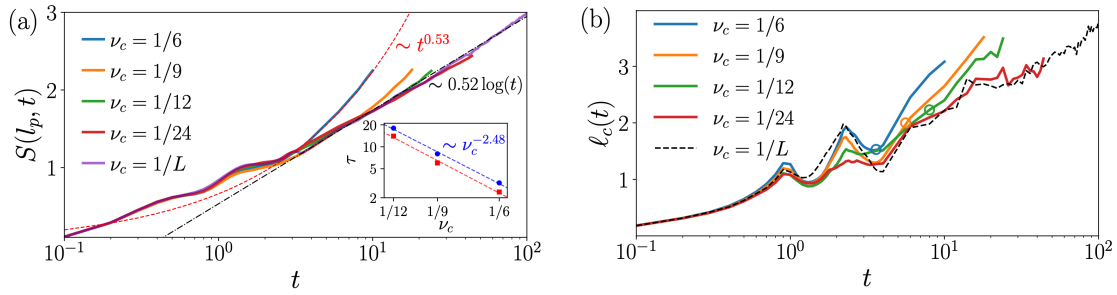

Figure 4.28: (a): Entanglement entropy across a cut between sites l_p and $l_p + 1$, where $\langle \hat{n}_{c,l_p}(t = 0) \rangle = 1$ for all the densities studied. For densities $\nu_c \geq 1/12$ we observe a deviation from the corresponding curve for a single c-boson (purple line) at a time $\tau_S(\nu_c)$. In the inset we show the behavior of this characteristic timescale as a function of density, suggesting a power-law behavior. Comparison of τ obtained from the entanglement entropy (blue dots) and the one obtained from the growth of the correlation functions (red squares) suggests that both timescales behave in a similar way. (b): The decay length $\ell_c(t)$ averaged among all c-bosons composing the bath also deviates from a decay length of a single clean boson (black dashed line) at late times for $\nu_c \geq 1/12$.

power-law growth with time. We observe such deviation from the single-particle case for all values $\nu_c \geq 1/12$ and track its characteristic onset time $\tau_S(\nu_c)$. The scaling of $\tau_S(\nu_c)$ is shown in the inset of Fig. 4.28(a). Within the considered range of densities, behavior of $\tau_S(\nu_c)$ is consistent with the power-law increase at low ν_c, $\tau_S(\nu_c) \propto 1/\nu_c^{-2.48}$, that implies eventual delocalization at any finite density of clean bosons. Of course, limited data range does not allow us to rule the possibility that $\tau_S(\nu_c)$ diverges at a finite value of ν_c, signaling stability of localization at a finite density of clean bosons.

The analysis of the density-density correlation functions of the c-bosons shown in Appendix C.4.3, provides a possible explanation for the power-law entanglement growth. We notice that the correlations among two initially occupied sites l_p and l'_p become relevant at a timescale scaling with the bath density with the same power-law exponent observed for τ_S, as shown by the red line in the inset of Fig. 4.28(a). The agreement between the scaling of the two timescales implies that the faster entanglement growth is triggered only when c-boson correlations become significant. As a consequence of strong suppression of the spreading of clean bosons degrees of freedom, correlations may saturate to a very small value when ν_c is small enough, thus possibly leading to a localized phase even at the finite density of clean bosons.

Deviations from single-particle behavior can also be observed in the time-evolution of the c-boson density profiles. In particular, we probe this by studying the decay length $\ell_c(t)$ of each individual c-boson obtained by fitting the density profile in the vicinity of each l_p to the Ansatz proposed in Eq. (4.27). In the present case, we average the results for $\ell_c(t)$ obtained for each clean boson. As shown in Figure 4.28(b), at early times the decay length behaves in agreement with the single-particle case for all densities ν_c (note that the deviations from the dashed curve can be ascribed to the additional averaging for finite ν_c). At later times marked by the circles, however, for all bath sizes $\nu_c \geq 1/12$ the decay length grows consistently faster than in the case of an intensive bath.

While the scaling of τ shown in the inset of Fig. 4.28(a) seems to suggest thermalization at all finite ν_c, the potential localization of the individual c-bosons indicated by the agreement of the decay length for $\nu_c = 1/24$ with the single c-boson curve might lead

to a breakdown of the delocalization mechanism at small, albeit extensive, bath sizes. Unfortunately, on the timescales available to our numerical simulations, we are not able to confirm that the $\nu_c = 1/24$ bath leads to power-law growth of entanglement or to deviations in the growth of $\ell_c(t)$. Using the power-law fit for $\tau_S(\nu_c)$, we can estimate that the deviation from logarithmic growth at small bath size would take place at a time $T \approx 100$, corresponding to a nearly uniform entanglement entropy $S \geq 3$ – an extremely challenging albeit potentially achievable regime in TEBD simulations.

4.6 Discussion

In this Chapter, we investigate novel physical aspects of localization that can be studied using multi-species lattice models. First, we investigated the fate of an Anderson localized system coupled to a small local bath, represented by a single disorder-free particle, showing evidence of a phase transition driven by the interaction strength.

In the strong coupling regime, we used a static Hartree approximation that overestimates localization to obtain the parameters range most favorable for localization. In addition, we analyzed the effect of two-particle resonances triggered by the interaction, estimating the region of parameters where localization is perturbatively stable with respect to such resonances. Focusing on the parameter values where the perturbative criterion predicts localization, we studied the dynamics in the coupled system. We demonstrated that the time-dependent Hartree approximation, which neglects entanglement between the localized particles and the degree of freedom representing the bath, predicts a slow delocalization of the system consistent with diffusion. In contrast, unbiased TEBD numerical simulations, which take into account all quantum correlations among the two bosonic species, shows evidence of MBL proximity effect within the experimentally relevant timescales achieved and confirm our analytic criterion for the stability of localization. In addition, our MPS simulations reveal potential delocalization at weak interactions, in agreement with the picture of resonances-driven instability. At strong interactions, when the system is localized, the imbalance of disordered particles saturates, suggesting that memory of the initial density-wave configuration is retained even at long times. Furthermore, simulations reveal logarithmic growth of entanglement, in agreement with the MBL phenomenology, and extremely slow growth of particle number entanglement, ascribed to the weak relaxation of the disordered particles due to the interaction with the small bath.

Based on these observations, we propose a phenomenological picture of *propagation of MBL* in the Anderson insulator, triggered by the localized c-boson. We explain the retarded growth of entanglement far from the initial position of the c-boson and the enhanced relaxation in the region close to it. Evidence of the localized behavior of the system is also found in the analysis of highly excited eigenstates obtained numerically with the DMRG-X method [110, 111, 112]. We observe that the clean boson remains localized in eigenstates, confirming the intuition gained from the study of dynamics. We further notice area-law scaling of the entanglement entropy of eigenstates, with an enhancement in the vicinity of the localization site of the c-boson, $i_{\max}$. These results provide evidence for the effective stability of localization even at infinite times and further support the picture proposed.

We then analyzed the stability of localization as the interaction strength is decreased. Using both Hamiltonian and Floquet dynamics, we investigate the behavior of both particle species in extremely large systems and up to experimentally relevant timescales.

Finding qualitatively different behavior of both particle species at weak and strong interaction, we demonstrate the presence of a phase transition separating the two distinct regimes.

In addition to the single particle bath case, we also study the effect of introducing a bath whose number of particles increases proportionally to the system size. Our study of transport highlights that at large densities of clean particles the system is delocalized, showing clear signatures of diffusive dynamics. The investigation of the putative delocalization transition at small but finite density of clean bosons, however, is not conclusive due to rapid entanglement growth preventing our simulation from reaching long times. Thus, further studies are needed in order to understand if there exists a critical density of clean particles below which the entire system stays localized [215], or if delocalization happens at any finite density of clean particles akin to scenario suggested by Refs. [196, 197].

In summary, our work provides evidence for MBL proximity effect and a phenomenological picture of dynamics [65] for large systems that are beyond the reach of numerical exact diagonalization. Our predictions are readily verifiable in state of the art experimental setups [70, 72] that are capable of probing the particle dynamics with a single-site resolution, although probing the long-time behavior of the boundaries of the system may be beyond the reach of currently available resources.

Numerous other questions remain open. In particular, although the single clean particle spreads diffusively at weak interactions, the disordered bosons show extremely slow relaxation. Such behavior is intuitively similar to the delocalized yet non-ergodic phase suggested to exist on Bethe lattices [216, 217]. It remains to be understood, if our phenomenological mapping of the two-species Hubbard model to the Bethe lattice can reproduce the relaxation of disordered bosons, entanglement dynamics, and other physical properties, such as the behavior of connected correlation functions. More broadly, the delocalization of a single particle atop of the infinite sea of localized bosons presents a deviation from the standard thermodynamic limit, where typically densities of all particle species are assumed to be finite. Building a theory of the delocalization transition for such a system remains an interesting challenge. Also, the role of interactions between disordered particles and of the nature of disorder (random or quasiperiodic) provide a complementary set of control parameters, that was not explored in our work.

In a different direction, consideration of the finite density of clean particles allows for a standard thermodynamic limit, but turns out to be an extremely challenging problem for numerical simulations. In this regime, although we were able to confirm delocalizaiton at large density of clean particles, the intermediate density regime proved to be hard to access due to entanglement growth. Understanding the structure of this entanglement and searching for a quasi-local basis transformation may potentially assist one in reaching longer simulation times. This may be crucial for getting insights into microscopic processes and structure of resonances created by the clean particles that drive the delocalization of the entire system. Additionally, further investigation of the diffusive transport at large densities of particles in the bath may provide useful insight for a better understanding of the subdiffusion observed in standard disordered models used to study many-body localization [198, 199, 214].

Finally, modern experiments with ultracold atoms motivate study of other geometries and setups for the many-body lozalization proximity effect. In particular, the study involving the two dimensional cold atom microscope [70], that inspired our work, calls

for extension of our results to two-dimensional systems. While simulating dynamics with two-dimensional tensor network ansatzes is extremely challenging, the study of the present model on ladders with MPS methods may provide useful insights into the qualitative difference between one- and two-dimensional systems. Likewise, large scale numerical studies of models where the coupling between localized system and the bath is local [72] may provide useful insights for the theory of many-body localization and its potential instabilities known as bubbles or avalanches [62, 87, 94, 218].

Bibliography

[1] J. M. Deutsch, "Quantum statistical mechanics in a closed system," Phys. Rev. A **43**, 2046–2049 (1991).

[2] M. Srednicki, "Chaos and quantum thermalization," Phys. Rev. E **50**, 888–901 (1994).

[3] M. Lewenstein, A. Sanpera, V. Ahufinger, B. Damski, A. Sen(De), and U. Sen, "Ultracold atomic gases in optical lattices: mimicking condensed matter physics and beyond," Advances in Physics **56**, 243–379 (2007), https://doi.org/10.1080/00018730701223200 .

[4] I. Bloch, J. Dalibard, and W. Zwerger, "Many-body physics with ultracold gases," Rev. Mod. Phys. **80**, 885–964 (2008).

[5] P. Schauß, M. Cheneau, M. Endres, T. Fukuhara, S. Hild, A. Omran, T. Pohl, C. Gross, S. Kuhr, and I. Bloch, "Observation of spatially ordered structures in a two-dimensional rydberg gas," Nature **491**, 87 (2012).

[6] N. Malvania, Y. Zhang, Y. Le, J. Dubail, M. Rigol, and D. S. Weiss, "Generalized hydrodynamics in strongly interacting 1d bose gases," Science **373**, 1129–1133 (2021), https://www.science.org/doi/pdf/10.1126/science.abf0147 .

[7] R. Blatt and C. F. Roos, "Quantum simulations with trapped ions," Nature Physics **8**, 277–284 (2012).

[8] J. G. Bohnet, B. C. Sawyer, J. W. Britton, M. L. Wall, A. M. Rey, M. Foss-Feig, and J. J. Bollinger, "Quantum spin dynamics and entanglement generation with hundreds of trapped ions," Science **352**, 1297–1301 (2016), https://www.science.org/doi/pdf/10.1126/science.aad9958 .

[9] J. Zhang, G. Pagano, P. W. Hess, A. Kyprianidis, P. Becker, H. Kaplan, A. V. Gorshkov, Z.-X. Gong, and C. Monroe, "Observation of a many-body dynamical phase transition with a 53-qubit quantum simulator," Nature **551**, 601–604 (2017).

[10] H. Bernien, S. Schwartz, A. Keesling, H. Levine, A. Omran, H. Pichler, S. Choi, A. S. Zibrov, M. Endres, M. Greiner, V. Vuletić, and M. D. Lukin, "Probing many-body dynamics on a 51-atom quantum simulator," Nature **551**, 579 (2017).

[11] P. Scholl, M. Sculler, H. J. Williams, A. A. Eberharter, D. Barredo, K.-N. Scymik, V. Lienhard, L.-P. Henry, T. C. Lang, T. Lahaye, A. M. Läuchli, and A. Browaeys, "Quantum simulation of 2d antiferromagnets with hundreds of rydberg atoms," Nature **595**, 233–238 (2021).

[12] P. Scholl, H. J. Williams, G. Bornet, F. Wallner, D. Barredo, L. Henriet, A. Signoles, C. Hainaut, T. Franz, S. Geier, A. Tebben, A. Salzinger, G. Zürn, T. Lahaye, M. Weidemüller, and A. Browaeys, "Microwave engineering of programmable xxz hamiltonians in arrays of rydberg atoms," PRX Quantum **3**, 020303 (2022).

[13] M. H. Devoret and R. J. Schoelkopf, "Superconducting circuits for quantum information: An outlook," Science **339**, 1169–1174 (2013), https://www.science.org/doi/pdf/10.1126/science.1231930 .

[14] K. Satzinger, Y.-J. Liu, A. Smith, C. Knapp, M. Newman, N. C. Jones, Z. Chen, *et al.*, "Realizing topologically ordered states on a quantum processor," Science **374**, 1237–1241 (2021).

[15] X. Mi, M. Ippoliti, C. Quintana, A. Greene, Z. Chen, *et al.*, "Realizing topologically ordered states on a quantum processor," Science **374**, 1237–1241 (2021).

[16] E. Altman, K. R. Brown, G. Carleo, L. D. Carr, E. Demler, C. Chin, *et al.*, "Quantum simulators: Architectures and opportunities," PRX Quantum **2**, 017003 (2021).

[17] O. Penrose, "Foundations of statistical mechanics," Reports on Progress in Physics **42**, 1937 (1979).

[18] L. D'Alessio, Y. Kafri, A. Polkovnikov, and M. Rigol, "From quantum chaos and eigenstate thermalization to statistical mechanics and thermodynamics," Advances in Physics **65**, 239–362 (2016), https://doi.org/10.1080/00018732.2016.1198134 .

[19] E. P. Wigner, "On the statistical distribution of the widths and spacings of nuclear resonance levels," Mathematical Proceedings of the Cambridge Philosophical Society **47**, 790–798 (1951).

[20] E. P. Wigner, "Characteristic vectors of bordered matrices with infinite dimensions," Ann. of Math. **62**, 548–564 (1955).

[21] F. J. Dyson, "A brownian-motion model for the eigenvalues of a random matrix," Journal of Mathematical Physics **3**, 1191–1198 (1962), https://doi.org/10.1063/1.1703862 .

[22] O. Bohigas, M. J. Giannoni, and C. Schmit, "Characterization of chaotic quantum spectra and universality of level fluctuation laws," Phys. Rev. Lett. **52**, 1–4 (1984).

[23] T. A. Brody, J. Flores, J. B. French, P. A. Mello, A. Pandey, and S. S. M. Wong, "Random-matrix physics: spectrum and strength fluctuations," Rev. Mod. Phys. **53**, 385–479 (1981).

[24] M. Srednicki, "The approach to thermal equilibrium in quantized chaotic systems," Journal of Physics A: Mathematical and General **32**, 1163 (1999).

[25] C. J. Turner, A. A. Michailidis, D. A. Abanin, M. Serbyn, and Z. Papić, "Weak ergodicity breaking from quantum many-body scars," Nature Physics **14**, 745 (2018).

[26] M. Serbyn, D. A. Abanin, and Z. Papić, "Quantum many-body scars and weak breaking of ergodicity," Nature Physics **17**, 675 (2021).

[27] S. Moudgalya, N. Regnault, and B. A. Bernevig, "Entanglement of exact excited states of affleck-kennedy-lieb-tasaki models: Exact results, many-body scars, and violation of the strong eigenstate thermalization hypothesis," Phys. Rev. B **98**, 235156 (2018).

[28] C. J. Turner, A. A. Michailidis, D. A. Abanin, M. Serbyn, and Z. Papić, "Quantum scarred eigenstates in a rydberg atom chain: Entanglement, breakdown of thermalization, and stability to perturbations," Phys. Rev. B **98**, 155134 (2018).

[29] S. Choi, C. J. Turner, H. Pichler, W. W. Ho, A. A. Michailidis, Z. Papić, M. Serbyn, M. D. Lukin, and D. A. Abanin, "Emergent su(2) dynamics and perfect quantum many-body scars," Phys. Rev. Lett. **122**, 220603 (2019).

[30] T. Iadecola, M. Schecter, and S. Xu, "Quantum many-body scars from magnon condensation," Phys. Rev. B **100**, 184312 (2019).

[31] W. W. Ho, S. Choi, H. Pichler, and M. D. Lukin, "Periodic orbits, entanglement, and quantum many-body scars in constrained models: Matrix product state approach," Phys. Rev. Lett. **122**, 040603 (2019).

[32] F. Ritort and P. Sollich, "Glassy dynamics of kinetically constrained models," Advances in Physics **52**, 219–342 (2003), https://doi.org/10.1080/0001873031000093582 .

[33] J. R. Schrieffer and P. A. Wolff, "Relation between the anderson and kondo hamiltonians," Phys. Rev. **149**, 491–492 (1966).

[34] P. Sala, T. Rakovszky, R. Verresen, M. Knap, and F. Pollmann, "Ergodicity breaking arising from hilbert space fragmentation in dipole-conserving hamiltonians," Phys. Rev. X **10**, 011047 (2020).

[35] V. Khemani, M. Hermele, and R. Nandkishore, "Localization from hilbert space shattering: From theory to physical realizations," Phys. Rev. B **101**, 174204 (2020).

[36] S. Moudgalya and O. I. Motrunich, "Hilbert space fragmentation and commutant algebras," Phys. Rev. X **12**, 011050 (2022).

[37] Z.-C. Yang, F. Liu, A. V. Gorshkov, and T. Iadecola, "Hilbert-space fragmentation from strict confinement," Phys. Rev. Lett. **124**, 207602 (2020).

[38] P. A. McClarty, M. Haque, A. Sen, and J. Richter, "Disorder-free localization and many-body quantum scars from magnetic frustration," Phys. Rev. B **102**, 224303 (2020).

[39] W.-H. Li, X. Deng, and L. Santos, "Hilbert space shattering and disorder-free localization in polar lattice gases," Phys. Rev. Lett. **127**, 260601 (2021).

[40] P. Brighi, M. Ljubotina, and M. Serbyn, "Hilbert space fragmentation and slow dynamics in particle-conserving quantum east models," arXiv e-prints , arXiv:2210.15607 (2022), arXiv:2210.15607 [quant-ph] .

[41] M. Ljubotina, J.-Y. Desaules, M. Serbyn, and Z. Papić, "Superdiffusive energy transport in kinetically constrained models," (2022).

[42] B. Mukherjee, D. Banerjee, K. Sengupta, and A. Sen, "Minimal model for hilbert space fragmentation with local constraints," Phys. Rev. B **104**, 155117 (2021).

[43] E. Lieb, T. Schultz, and D. Mattis, "Two soluble models of an antiferromagnetic chain," Annals of Physics **16**, 407–466 (1961).

[44] B. Sutherland, *Beautiful models: 70 years of exactly solved quantum many-body problems* (World Scientific, 2004).

[45] M. Rigol, A. Muramatsu, and M. Olshanii, "Hard-core bosons on optical superlattices: Dynamics and relaxation in the superfluid and insulating regimes," Phys. Rev. A **74**, 053616 (2006).

[46] M. Rigol, V. Dunjko, V. Yurovsky, and M. Olshanii, "Relaxation in a completely integrable many-body quantum system: An ab initio study of the dynamics of the highly excited states of 1d lattice hard-core bosons," Phys. Rev. Lett. **98**, 050405 (2007).

[47] L. Vidmar and M. Rigol, "Generalized gibbs ensemble in integrable lattice models," Journal of Statistical Mechanics: Theory and Experiment **2016**, 064007 (2016).

[48] P. W. Anderson, "Absence of diffusion in certain random lattices," Phys. Rev. **109**, 1492–1505 (1958).

[49] I. V. Gornyi, A. D. Mirlin, and D. G. Polyakov, "Interacting electrons in disordered wires: Anderson localization and low-t transport," Phys. Rev. Lett. **95**, 206603 (2005).

[50] D. M. Basko, I. L. Aleiner, and B. L. Altshuler, "Metal-insulator transition in a weakly interacting many-electron system with localized single-particle states," Annals of Physics **321**, 1126–1205 (2006).

[51] V. Oganesyan and D. A. Huse, "Localization of interacting fermions at high temperature," Phys. Rev. B **75**, 155111 (2007).

[52] M. Znidaric, T. Prosen, and P. Prelovsek, "Many-body localization in the heisenberg xxz magnet in a random field," Phys. Rev. B **77**, 064426 (2008).

[53] A. Pal and D. A. Huse, "Many-body localization phase transition," Phys. Rev. B **82**, 174411 (2010).

[54] J. H. Bardarson, F. Pollmann, and J. E. Moore, "Unbounded growth of entanglement in models of many-body localization," Phys. Rev. Lett. **109**, 017202 (2012).

[55] M. Serbyn, Z. Papić, and D. A. Abanin, "Universal slow growth of entanglement in interacting strongly disordered systems," Phys. Rev. Lett. **110**, 260601 (2013).

[56] M. Serbyn, Z. Papić, and D. A. Abanin, "Local conservation laws and the structure of the many-body localized states," Phys. Rev. Lett. **111**, 127201 (2013).

[57] D. A. Huse, R. Nandkishore, and V. Oganesyan, "Phenomenology of fully many-body-localized systems," Phys. Rev. B **90**, 174202 (2014).

[58] V. Ros, M. Müller, and A. Scardicchio, "Integrals of motion in the many-body localized phase," Nuclear Physics B **891**, 420–465 (2015).

[59] D. J. Luitz, N. Laflorencie, and F. Alet, "Many-body localization edge in the random-field heisenberg chain," Phys. Rev. B **91**, 081103 (2015).

[60] J. Z. Imbrie, "On Many-Body Localization for Quantum Spin Chains," Journal of Statistical Physics **163**, 998–1048 (2016).

[61] R. Nandkishore, "Many-body localization proximity effect," Phys. Rev. B **92**, 245141 (2015).

[62] W. De Roeck and F. Huveneers, "Stability and instability towards delocalization in many-body localization systems," Phys. Rev. B **95**, 155129 (2017).

[63] A. Goremykina, R. Vasseur, and M. Serbyn, "Analytically solvable renormalization group for the many-body localization transition," Phys. Rev. Lett. **122**, 040601 (2019).

[64] E. Wybo, M. Knap, and F. Pollmann, "Entanglement dynamics of a many-body localized system coupled to a bath," Phys. Rev. B **102**, 064304 (2020).

[65] P. Brighi, A. A. Michailidis, D. A. Abanin, and M. Serbyn, "Propagation of many-body localization in an anderson insulator," Phys. Rev. B **105**, L220203 (2022).

[66] M. Schreiber, S. S. Hodgman, P. Bordia, H. P. Lüschen, M. H. Fischer, R. Vosk, E. Altman, U. Schneider, and I. Bloch, "Observation of many-body localization of interacting fermions in a quasirandom optical lattice," Science **349**, 842–845 (2015).

[67] J.-y. Choi, S. Hild, J. Zeiher, P. Schauß, A. Rubio-Abadal, T. Yefsah, V. Khemani, D. A. Huse, I. Bloch, and C. Gross, "Exploring the many-body localization transition in two dimensions," Science **352**, 1547–1552 (2016).

[68] A. Lukin, M. Rispoli, R. Schittko, M. E. Tai, A. M. Kaufman, S. Choi, V. Khemani, J. Léonard, and M. Greiner, "Probing entanglement in a many-body–localized system," Science **364**, 256–260 (2019).

[69] M. Rispoli, A. Lukin, R. Schittko, K. Sooshin, M. E. Tai, J. Léonard, and M. Greiner, "Quantum critical behaviour at the many-body localization transition," Nature **573**, 385–389 (2019).

[70] A. Rubio-Abadal, J.-y. Choi, J. Zeiher, S. Hollerith, J. Rui, I. Bloch, and C. Gross, "Many-body delocalization in the presence of a quantum bath," Phys. Rev. X **9**, 041014 (2019).

[71] Q. Guo, C. Cheng, Z.-H. Sun, Z. Song, H. Li, *et al.*, "Observation of energy resolved many-body localization," Nature Physics **17** (2021), 10.1038/s41567-020-1035-1.

[72] J. Léonard, S. Kim, M. Rispoli, A. Lukin, R. Schittko, J. Kwan, E. Demler, D. Sels, and M. Greiner, "Probing the onset of quantum avalanches in a many-body localized system," Nature Physics (2023).

[73] F. Alet and N. Laflorencie, "Many-body localization: An introduction and selected topics," Comptes Rendus Physique **19**, 498–525 (2018), quantum simulation / Simulation quantique.

[74] R. Nandkishore and D. A. Huse, "Many-body localization and thermalization in quantum statistical mechanics," Annual Review of Condensed Matter Physics **6**, 15–38 (2015).

[75] D. A. Abanin, E. Altman, I. Bloch, and M. Serbyn, "Colloquium: Many-body localization, thermalization, and entanglement," Rev. Mod. Phys. **91**, 021001 (2019).

[76] S. Bera, H. Schomerus, F. Heidrich-Meisner, and J. H. Bardarson, "Many-body localization characterized from a one-particle perspective," Phys. Rev. Lett. **115**, 046603 (2015).

[77] Y. Bar Lev, G. Cohen, and D. R. Reichman, "Absence of diffusion in an interacting system of spinless fermions on a one-dimensional disordered lattice," Phys. Rev. Lett. **114**, 100601 (2015).

[78] J. Goold, C. Gogolin, S. R. Clark, J. Eisert, A. Scardicchio, and A. Silva, "Total correlations of the diagonal ensemble herald the many-body localization transition," Phys. Rev. B **92**, 180202 (2015).

[79] B. Bauer and C. Nayak, "Area laws in a many-body localized state and its implications for topological order," Journal of Statistical Mechanics: Theory and Experiment **2013**, P09005 (2013).

[80] J. H. Bardarson, F. Pollmann, and J. E. Moore, "Unbounded growth of entanglement in models of many-body localization," Phys. Rev. Lett. **109**, 017202 (2012).

[81] E. V. H. Doggen, I. V. Gornyi, A. D. Mirlin, and D. G. Polyakov, "Slow many-body delocalization beyond one dimension," Phys. Rev. Lett. **125**, 155701 (2020).

[82] J.-y. Choi, S. Hild, J. Zeiher, P. Schauß, A. Rubio-Abadal, T. Yefsah, V. Khemani, D. A. Huse, I. Bloch, and C. Gross, "Exploring the many-body localization transition in two dimensions," Science **352**, 1547–1552 (2016).

[83] P. Bordia, H. Lüschen, S. Scherg, S. Gopalakrishnan, M. Knap, U. Schneider, and I. Bloch, "Probing slow relaxation and many-body localization in two-dimensional quasiperiodic systems," Phys. Rev. X **7**, 041047 (2017).

[84] N. Mott, "Electrons in disordered structures," Advances in Physics **16**, 49–144 (1967).

[85] W. De Roeck, F. Huveneers, M. Müller, and M. Schiulaz, "Absence of many-body mobility edges," Phys. Rev. B **93**, 014203 (2016).

[86] P. Brighi, D. A. Abanin, and M. Serbyn, "Stability of mobility edges in disordered interacting systems," Phys. Rev. B **102**, 060202 (2020).

[87] D. J. Luitz, F. Huveneers, and W. De Roeck, "How a small quantum bath can thermalize long localized chains," Phys. Rev. Lett. **119**, 150602 (2017).

[88] K. Hyatt, J. R. Garrison, A. C. Potter, and B. Bauer, "Many-body localization in the presence of a small bath," Phys. Rev. B **95**, 035132 (2017).

[89] P. Brighi, A. A. Michailidis, K. Kirova, D. A. Abanin, and M. Serbyn, "Localization of a mobile impurity interacting with an anderson insulator," Phys. Rev. B **105**, 224208 (2022).

[90] J. Šuntajs, J. Bonča, T. c. v. Prosen, and L. Vidmar, "Quantum chaos challenges many-body localization," Phys. Rev. E **102**, 062144 (2020).

[91] D. Sels and A. Polkovnikov, "Dynamical obstruction to localization in a disordered spin chain," Phys. Rev. E **104**, 054105 (2021).

[92] D. Abanin, J. Bardarson, G. De Tomasi, S. Gopalakrishnan, V. Khemani, S. Parameswaran, F. Pollmann, A. Potter, M. Serbyn, and R. Vasseur, "Distinguishing localization from chaos: Challenges in finite-size systems," Annals of Physics **427**, 168415 (2021).

[93] P. J. D. Crowley and A. Chandran, "Avalanche induced coexisting localized and thermal regions in disordered chains," Phys. Rev. Research **2**, 033262 (2020).

[94] A. Morningstar, L. Colmenarez, V. Khemani, D. J. Luitz, and D. A. Huse, "Avalanches and many-body resonances in many-body localized systems," Phys. Rev. B **105**, 174205 (2022).

[95] F. Pietracaprina, N. Macé, D. J. Luitz, and F. Alet, "Shift-invert diagonalization of large many-body localizing spin chains," SciPost Phys. **5**, 045 (2018).

[96] A. Pieper, M. Kreutzer, A. Alvermann, M. Galgon, H. Fehske, G. Hager, B. Lang, and G. Wellein, "High-performance implementation of chebyshev filter diagonalization for interior eigenvalue computations," Journal of Computational Physics **325**, 226–243 (2016).

[97] P. Sierant, M. Lewenstein, and J. Zakrzewski, "Polynomially filtered exact diagonalization approach to many-body localization," Phys. Rev. Lett. **125**, 156601 (2020).

[98] T. J. Park and J. C. Light, "Unitary quantum time evolution by iterative lanczos reduction," The Journal of Chemical Physics **85**, 5870–5876 (1986), https://doi.org/10.1063/1.451548 .

[99] M. Fannes, B. Nachtergaele, and R. F. Werner, "Finitely correlated states on quantum spin chains," Communications in Mathematical Physics **144**, 443–490 (1992).

[100] A. Klümper, A. Schadschneider, and J. Zittartz, "Matrix product ground states for one-dimensional spin-1 quantum antiferromagnets," Europhysics Letters **24**, 293 (1993).

[101] D. Perez-Garcia, F. Verstraete, M. M. Wolf, and J. I. Cirac, "Matrix product state representations," arXiv e-prints , quant-ph/0608197 (2006), arXiv:quant-ph/0608197 [quant-ph] .

[102] U. Schollwöck, "The density-matrix renormalization group in the age of matrix product states," Annals of Physics **326**, 96–192 (2011), january 2011 Special Issue.

[103] F. Verstraete and J. I. Cirac, "Renormalization algorithms for quantum-many body systems in two and higher dimensions," arXiv e-prints , cond-mat/0407066 (2004), arXiv:cond-mat/0407066 [cond-mat.str-el] .

[104] F. Verstraete, M. M. Wolf, D. Perez-Garcia, and J. I. Cirac, "Criticality, the area law, and the computational power of projected entangled pair states," Phys. Rev. Lett. **96**, 220601 (2006).

[105] N. Schuch, M. M. Wolf, F. Verstraete, and J. I. Cirac, "Computational complexity of projected entangled pair states," Phys. Rev. Lett. **98**, 140506 (2007).

[106] R. Orús, "A practical introduction to tensor networks: Matrix product states and projected entangled pair states," Annals of Physics **349**, 117–158 (2014).

[107] M. B. Hastings, "An area law for one-dimensional quantum systems," Journal of Statistical Mechanics: Theory and Experiment **2007**, P08024 (2007).

[108] S. R. White, "Density matrix formulation for quantum renormalization groups," Phys. Rev. Lett. **69**, 2863–2866 (1992).

[109] F. Verstraete, D. Porras, and J. I. Cirac, "Density matrix renormalization group and periodic boundary conditions: A quantum information perspective," Phys. Rev. Lett. **93**, 227205 (2004).

[110] V. Khemani, F. Pollmann, and S. L. Sondhi, "Obtaining highly excited eigenstates of many-body localized hamiltonians by the density matrix renormalization group approach," Phys. Rev. Lett. **116**, 247204 (2016).

[111] M. Serbyn, A. A. Michailidis, D. A. Abanin, and Z. Papić, "Power-law entanglement spectrum in many-body localized phases," Phys. Rev. Lett. **117**, 160601 (2016).

[112] X. Yu, D. Pekker, and B. K. Clark, "Finding matrix product state representations of highly excited eigenstates of many-body localized hamiltonians," Phys. Rev. Lett. **118**, 017201 (2017).

[113] J. Haegeman, J. I. Cirac, T. J. Osborne, I. Pižorn, H. Verschelde, and F. Verstraete, "Time-dependent variational principle for quantum lattices," Phys. Rev. Lett. **107**, 070601 (2011).

[114] G. Vidal, "Efficient classical simulation of slightly entangled quantum computations," Phys. Rev. Lett. **91**, 147902 (2003).

[115] N. Hatano and M. Suzuki, "Finding exponential product formulas of higher orders," in *Quantum Annealing and Other Optimization Methods*, edited by A. Das and B. K. Chakrabarti (Springer Berlin Heidelberg, Berlin, Heidelberg, 2005) pp. 37–68.

[116] H. Singh, B. A. Ware, R. Vasseur, and A. J. Friedman, "Subdiffusion and many-body quantum chaos with kinetic constraints," Phys. Rev. Lett. **127**, 230602 (2021).

[117] V. Khemani, A. Lazarides, R. Moessner, and S. L. Sondhi, "Phase structure of driven quantum systems," Phys. Rev. Lett. **116**, 250401 (2016).

[118] F. Nathan, D. Abanin, E. Berg, N. H. Lindner, and M. S. Rudner, "Anomalous floquet insulators," Phys. Rev. B **99**, 195133 (2019).

[119] T. E. Lee, S. Gopalakrishnan, and M. D. Lukin, "Unconventional magnetism via optical pumping of interacting spin systems," Phys. Rev. Lett. **110**, 257204 (2013).

[120] S. Choi, Y. Bao, X.-L. Qi, and E. Altman, "Quantum error correction in scrambling dynamics and measurement-induced phase transition," Phys. Rev. Lett. **125**, 030505 (2020).

[121] T. Müller, S. Diehl, and M. Buchhold, "Measurement-induced dark state phase transitions in long-ranged fermion systems," Phys. Rev. Lett. **128**, 010605 (2022).

[122] S. Roy, J. T. Chalker, I. V. Gornyi, and Y. Gefen, "Measurement-induced steering of quantum systems," Phys. Rev. Research **2**, 033347 (2020).

[123] F. Arute, K. Arya, R. Babbush, D. Bacon, J. C. Bardin, R. Barends, *et al.*, "Quantum supremacy using a programmable superconducting processor," Nature **574**, 505–510 (2019).

[124] J. P. Garrahan, R. L. Jack, V. Lecomte, E. Pitard, K. van Duijvendijk, and F. van Wijland, "Dynamical first-order phase transition in kinetically constrained models of glasses," Phys. Rev. Lett. **98**, 195702 (2007).

[125] C. Toninelli, G. Biroli, and D. S. Fisher, "Spatial structures and dynamics of kinetically constrained models of glasses," Phys. Rev. Lett. **92**, 185504 (2004).

[126] B. Olmos, I. Lesanovsky, and J. P. Garrahan, "Out-of-equilibrium evolution of kinetically constrained many-body quantum systems under purely dissipative dynamics," Phys. Rev. E **90**, 042147 (2014).

[127] J. P. Garrahan, "Aspects of non-equilibrium in classical and quantum systems: Slow relaxation and glasses, dynamical large deviations, quantum non-ergodicity, and open quantum dynamics," Physica A: Statistical Mechanics and its Applications **504**, 130–154 (2018), lecture Notes of the 14th International Summer School on Fundamental Problems in Statistical Physics.

[128] S. Scherg, T. Kohlert, P. Sala, F. Pollmann, B. Hebbe Madhisidhana, I. Bloch, and M. Aidelsburger, "Observing non-ergodicity due to kinetic constraints in tilted fermi-hubbard chains," Nature communications **12**, 4490 (2021).

[129] R. J. Valencia-Tortora, N. Pancotti, and J. Marino, "Kinetically constrained quantum dynamics in superconducting circuits," PRX Quantum **3**, 020346 (2022).

[130] Z. Lan, M. van Horssen, S. Powell, and J. P. Garrahan, "Quantum slow relaxation and metastability due to dynamical constraints," Phys. Rev. Lett. **121**, 040603 (2018).

[131] J. Feldmeier, P. Sala, G. De Tomasi, F. Pollmann, and M. Knap, "Anomalous diffusion in dipole- and higher-moment-conserving systems," Phys. Rev. Lett. **125**, 245303 (2020).

[132] A. Morningstar, V. Khemani, and D. A. Huse, "Kinetically constrained freezing transition in a dipole-conserving system," Phys. Rev. B **101**, 214205 (2020).

[133] Z.-C. Yang, "Distinction between transport and rényi entropy growth in kinetically constrained models," arXiv e-prints , arXiv:2208.07480 (2022), arXiv:2208.07480 [cond-mat.stat-mech] .

[134] J. Feldmeier, W. Witczak-Krempa, and M. Knap, "Emergent tracer dynamics in constrained quantum systems," Phys. Rev. B **106**, 094303 (2022).

[135] N. Pancotti, G. Giudice, J. I. Cirac, J. P. Garrahan, and M. C. Bañuls, "Quantum east model: Localization, nonthermal eigenstates, and slow dynamics," Phys. Rev. X **10**, 021051 (2020).

[136] R. M. Nandkishore and M. Hermele, "Fractons," Annual Review of Condensed Matter Physics **10**, 295–313 (2019), https://doi.org/10.1146/annurev-conmatphys-031218-013604 .

[137] S. Pai, M. Pretko, and R. M. Nandkishore, "Localization in fractonic random circuits," Phys. Rev. X **9**, 021003 (2019).

[138] T. Rakovszky, P. Sala, R. Verresen, M. Knap, and F. Pollmann, "Statistical localization: From strong fragmentation to strong edge modes," Phys. Rev. B **101**, 125126 (2020).

[139] L. Zadnik and M. Fagotti, "The Folded Spin-1/2 XXZ Model: I. Diagonalisation, Jamming, and Ground State Properties," SciPost Phys. Core **4**, 010 (2021).

[140] L. Zadnik, K. Bidzhiev, and M. Fagotti, "The folded spin-1/2 XXZ model: II. Thermodynamics and hydrodynamics with a minimal set of charges," SciPost Phys. **10**, 099 (2021).

[141] B. Pozsgay, T. Gombor, A. Hutsalyuk, Y. Jiang, L. Pristyák, and E. Vernier, "Integrable spin chain with hilbert space fragmentation and solvable real-time dynamics," Phys. Rev. E **104**, 044106 (2021).

[142] A. Hudomal, I. Vasić, N. Regnault, and Z. Papić, "Quantum scars of bosons with correlated hopping," Communications Physics **3**, 99 (2020).

[143] T. Iadecola and M. Schecter, "Quantum many-body scar states with emergent kinetic constraints and finite-entanglement revivals," Phys. Rev. B **101**, 024306 (2020).

[144] K. Tamura and H. Katsura, "Quantum many-body scars of spinless fermions with density-assisted hopping in higher dimensions," Phys. Rev. B **106**, 144306 (2022).

[145] M. van Horssen, E. Levi, and J. P. Garrahan, "Dynamics of many-body localization in a translation-invariant quantum glass model," Phys. Rev. B **92**, 100305 (2015).

[146] S. Roy and A. Lazarides, "Strong ergodicity breaking due to local constraints in a quantum system," Phys. Rev. Research **2**, 023159 (2020).

[147] A. Geißler and J. P. Garrahan, "Slow dynamics and non-ergodicity of the bosonic quantum East model in the semiclassical limit," arXiv e-prints , arXiv:2209.06963 (2022), arXiv:2209.06963 [cond-mat.stat-mech] .

[148] J. Jäckle and S. Eisinger, "A hierarchically constrained kinetic ising model," Zeitschrift für Physik B Condensed Matter **84**, 115 (1991).

[149] J. Richter and A. Pal, "Anomalous hydrodynamics in a class of scarred frustration-free hamiltonians," Phys. Rev. Research **4**, L012003 (2022).

[150] M. S. Bahovadinov, D. V. Kurlov, S. I. Matveenko, B. L. Altshuler, and G. V. Shlyapnikov, "Many-body localization transition in a frustrated xy chain," Phys. Rev. B **106**, 075107 (2022).

[151] C.-J. Lin and O. I. Motrunich, "Exact quantum many-body scar states in the rydberg-blockaded atom chain," Phys. Rev. Lett. **122**, 173401 (2019).

[152] H. Zhao, J. Vovrosh, F. Mintert, and J. Knolle, "Quantum many-body scars in optical lattices," Phys. Rev. Lett. **124**, 160604 (2020).

[153] S. Moudgalya, B. A. Bernevig, and N. Regnault, "Quantum many-body scars and hilbert space fragmentation: a review of exact results," Reports on Progress in Physics **85**, 086501 (2022).

[154] J. Iaconis, S. Vijay, and R. Nandkishore, "Anomalous subdiffusion from subsystem symmetries," Phys. Rev. B **100**, 214301 (2019).

[155] B. Pozsgay, "A yang–baxter integrable cellular automaton with a four site update rule," Journal of Physics A: Mathematical and Theoretical **54**, 384001 (2021).

[156] M. Ljubotina, M. Žnidarič, and T. Prosen, "Spin diffusion from an inhomogeneous quench in an integrable system," Nature Communications **8**, 16117 (2017).

[157] J. De Nardis, S. Gopalakrishnan, R. Vasseur, and B. Ware, "Stability of superdiffusion in nearly integrable spin chains," Phys. Rev. Lett. **127**, 057201 (2021).

[158] E. Ilievski, J. De Nardis, S. Gopalakrishnan, R. Vasseur, and B. Ware, "Superuniversality of superdiffusion," Phys. Rev. X **11**, 031023 (2021).

[159] V. B. Bulchandani, S. Gopalakrishnan, and E. Ilievski, "Superdiffusion in spin chains," Journal of Statistical Mechanics: Theory and Experiment **2021**, 084001 (2021).

[160] P. W. Anderson, D. J. Thouless, E. Abrahams, and D. S. Fisher, "New method for a scaling theory of localization," Phys. Rev. B **22**, 3519–3526 (1980).

[161] P. Bordia, H. P. Lüschen, S. S. Hodgman, M. Schreiber, I. Bloch, and U. Schneider, "Coupling identical one-dimensional many-body localized systems," Phys. Rev. Lett. **116**, 140401 (2016).

[162] B. Chiaro, C. Neill, A. Bohrdt, M. Filippone, F. Arute, K. Arya, *et al.*, "Direct measurement of nonlocal interactions in the many-body localized phase," Phys. Rev. Research **4**, 013148 (2022).

[163] T. Kohlert, S. Scherg, X. Li, H. P. Lüschen, S. Das Sarma, I. Bloch, and M. Aidelsburger, "Observation of many-body localization in a one-dimensional system with a single-particle mobility edge," Phys. Rev. Lett. **122**, 170403 (2019).

[164] T. B. Wahl, A. Pal, and S. H. Simon, "Signatures of the many-body localized regime in two dimensions," Nature Physics **15**, 164–169 (2019).

[165] I.-D. Potirniche, S. Banerjee, and E. Altman, "Exploration of the stability of many-body localization in $d > 1$," Phys. Rev. B **99**, 205149 (2019).

[166] A. Kshetrimayum, M. Goihl, and J. Eisert, "Time evolution of many-body localized systems in two spatial dimensions," Phys. Rev. B **102**, 235132 (2020).

[167] T. Chanda, P. Sierant, and J. Zakrzewski, "Many-body localization transition in large quantum spin chains: The mobility edge," Phys. Rev. Research **2**, 032045 (2020).

[168] M. Serbyn, Z. Papić, and D. A. Abanin, "Criterion for many-body localization-delocalization phase transition," Phys. Rev. X **5**, 041047 (2015).

[169] S. D. Geraedts, R. N. Bhatt, and R. Nandkishore, "Emergent local integrals of motion without a complete set of localized eigenstates," Phys. Rev. B **95**, 064204 (2017).

[170] M. Goihl, J. Eisert, and C. Krumnow, "Exploration of the stability of many-body localized systems in the presence of a small bath," Phys. Rev. B **99**, 195145 (2019).

[171] R. Yao and J. Zakrzewski, "Many-body localization in the bose-hubbard model: Evidence for mobility edge," Phys. Rev. B **102**, 014310 (2020).

[172] D. L. Shepelyansky, "Coherent propagation of two interacting particles in a random potential," Phys. Rev. Lett. **73**, 2607–2610 (1994).

[173] Y. Imry, "Coherent propagation of two interacting particles in a random potential," Europhysics Letters (EPL) **30**, 405–408 (1995).

[174] X. Li, S. Ganeshan, J. H. Pixley, and S. Das Sarma, "Many-body localization and quantum nonergodicity in a model with a single-particle mobility edge," Phys. Rev. Lett. **115**, 186601 (2015).

[175] Z. Papić, E. M. Stoudenmire, and D. A. Abanin, "Many-body localization in disorder-free systems: The importance of finite-size constraints," Annals of Physics **362**, 714 – 725 (2015).

[176] M. Fishman, S. R. White, and E. M. Stoudenmire, "The ITensor Software Library for Tensor Network Calculations," SciPost Phys. Codebases , 4 (2022).

[177] M. Serbyn, Z. Papić, and D. A. Abanin, "Quantum quenches in the many-body localized phase," Phys. Rev. B **90**, 174302 (2014).

[178] R. Islam, R. Ma, P. M. Preiss, M. E. Tai, A. Lukin, M. Rispoli, and M. Greiner, "Measuring entanglement entropy in a quantum many-body system," Nature **528**, 77 (2015).

[179] M. Kiefer-Emmanouilidis, R. Unanyan, M. Fleischhauer, and J. Sirker, "Evidence for unbounded growth of the number entropy in many-body localized phases," Phys. Rev. Lett. **124**, 243601 (2020).

[180] D. J. Luitz and Y. B. Lev, "Absence of slow particle transport in the many-body localized phase," Phys. Rev. B **102**, 100202 (2020).

[181] U. Krause, T. Pellegrin, P. W. Brouwer, D. A. Abanin, and M. Filippone, "Nucleation of ergodicity by a single mobile impurity in supercooled insulators," Phys. Rev. Lett. **126**, 030603 (2021).

[182] M. Schecter, T. Iadecola, and S. Das Sarma, "Configuration-controlled many-body localization and the mobility emulsion," Phys. Rev. B **98**, 174201 (2018).

[183] P. J. D. Crowley and A. Chandran, "Avalanche induced coexisting localized and thermal regions in disordered chains," Phys. Rev. Research **2**, 033262 (2020).

[184] R. Vosk, D. A. Huse, and E. Altman, "Theory of the many-body localization transition in one-dimensional systems," Phys. Rev. X **5**, 031032 (2015).

[185] R. Nandkishore and D. A. Huse, "Many-body localization and thermalization in quantum statistical mechanics," Annual Review of Condensed Matter Physics **6**, 15–38 (2015).

[186] E. V. H. Doggen, F. Schindler, K. S. Tikhonov, A. D. Mirlin, T. Neupert, D. G. Polyakov, and I. V. Gornyi, "Many-body localization and delocalization in large quantum chains," Phys. Rev. B **98**, 174202 (2018).

[187] A. Morningstar and D. A. Huse, "Renormalization-group study of the many-body localization transition in one dimension," Phys. Rev. B **99**, 224205 (2019).

[188] I.-D. Potirniche, S. Banerjee, and E. Altman, "Exploration of the stability of many-body localization in $d > 1$," Phys. Rev. B **99**, 205149 (2019).

[189] T. B. Wahl, A. Pal, and S. H. Simon, "Signatures of the many-body localized regime in two dimensions," Nature Phys **15**, 164–169 (2019).

[190] N. Pomata, S. Ganeshan, and T.-C. Wei, "In search of a many-body mobility edge with matrix product states in a Generalized Aubry-André model with interactions," arXiv e-prints , arXiv:2012.09853 (2020), arXiv:2012.09853 [cond-mat.dis-nn] .

[191] H. P. Lüschen, P. Bordia, S. Scherg, F. Alet, E. Altman, U. Schneider, and I. Bloch, "Observation of slow dynamics near the many-body localization transition in one-dimensional quasiperiodic systems," Phys. Rev. Lett. **119**, 260401 (2017).

[192] D. A. Huse, R. Nandkishore, F. Pietracaprina, V. Ros, and A. Scardicchio, "Localized systems coupled to small baths: From anderson to zeno," Phys. Rev. B **92**, 014203 (2015).

[193] T. L. M. Lezama and Y. B. Lev, "Logarithmic, noise-induced dynamics in the Anderson insulator," SciPost Phys. **12**, 174 (2022).

[194] F. Verstraete and J. I. Cirac, "Matrix product states represent ground states faithfully," Phys. Rev. B **73**, 094423 (2006).

[195] P. Sierant, T. Chanda, M. Lewenstein, and J. Zakrzewski, "Slow dynamics of a mobile impurity interacting with an anderson insulator," arXiv e-prints (2022), arXiv:2212.07107 [cond-mat.dis-nn] .

[196] M. Müller, "Purely electronic transport and localization in the Bose glass," Annalen der Physik **521**, 849–855 (2009), arXiv:0909.2260 [cond-mat.supr-con] .

[197] I. V. Gornyi, A. D. Mirlin, M. Müller, and D. G. Polyakov, "Absence of many-body localization in a continuum," Annalen der Physik **529**, 1600365 (2017).

[198] K. Agarwal, S. Gopalakrishnan, M. Knap, M. Müller, and E. Demler, "Anomalous diffusion and griffiths effects near the many-body localization transition," Phys. Rev. Lett. **114**, 160401 (2015).

[199] M. Žnidarič, A. Scardicchio, and V. K. Varma, "Diffusive and subdiffusive spin transport in the ergodic phase of a many-body localizable system," Phys. Rev. Lett. **117**, 040601 (2016).

[200] N. Fayard, L. Henriet, A. Asenjo-Garcia, and D. E. Chang, "Many-body localization in waveguide quantum electrodynamics," Phys. Rev. Res. **3**, 033233 (2021).

[201] E. Abrahams, P. W. Anderson, D. C. Licciardello, and T. V. Ramakrishnan, "Scaling theory of localization: Absence of quantum diffusion in two dimensions," Phys. Rev. Lett. **42**, 673–676 (1979).

[202] H. P. Lüschen, P. Bordia, S. S. Hodgman, M. Schreiber, S. Sarkar, A. J. Daley, M. H. Fischer, E. Altman, I. Bloch, and U. Schneider, "Signatures of many-body localization in a controlled open quantum system," Phys. Rev. X **7**, 011034 (2017).

[203] D. J. Thouless, "A relation between the density of states and range of localization for one dimensional random systems," Journal of Physics C: Solid State Physics **5**, 77–81 (1972).

[204] S. Nandy, F. Evers, and S. Bera, "Dephasing in strongly disordered interacting quantum wires," Phys. Rev. B **103**, 085105 (2021).

[205] S. Gopalakrishnan, K. R. Islam, and M. Knap, "Noise-induced subdiffusion in strongly localized quantum systems," Phys. Rev. Lett. **119**, 046601 (2017).

[206] S. Lorenzo, T. Apollaro, G. M. Palma, R. Nandkishore, A. Silva, and J. Marino, "Remnants of anderson localization in prethermalization induced by white noise," Phys. Rev. B **98**, 054302 (2018).

[207] Y. Gefen and G. Schön, "Effect of inelastic processes on localization in one dimension," Phys. Rev. B **30**, 7323–7325 (1984).

[208] D. E. Logan and P. G. Wolynes, "Dephasing and anderson localization in topologically disordered systems," Phys. Rev. B **36**, 4135–4147 (1987).

[209] S. R. Taylor and A. Scardicchio, "Subdiffusion in a one-dimensional anderson insulator with random dephasing: Finite-size scaling, griffiths effects, and possible implications for many-body localization," Phys. Rev. B **103**, 184202 (2021).

[210] P. Pöpperl, E. V. Doggen, J. F. Karcher, A. D. Mirlin, and K. S. Tikhonov, "Dynamics of many-body delocalization in the time-dependent hartree–fock approximation," Annals of Physics **435**, 168486 (2021), special Issue on Localisation 2020.

[211] M. Kiefer-Emmanouilidis, R. Unanyan, M. Fleischhauer, and J. Sirker, "Slow delocalization of particles in many-body localized phases," Phys. Rev. B **103**, 024203 (2021).

[212] T. L. M. Lezama, S. Bera, H. Schomerus, F. Heidrich-Meisner, and J. H. Bardarson, "One-particle density matrix occupation spectrum of many-body localized states after a global quench," Phys. Rev. B **96**, 060202 (2017).

[213] R. Abou-Chacra, D. J. Thouless, and P. W. Anderson, "A selfconsistent theory of localization," Journal of Physics C: Solid State Physics **6**, 1734 (1973).

[214] S. Bera, G. De Tomasi, F. Weiner, and F. Evers, "Density propagator for many-body localization: Finite-size effects, transient subdiffusion, and exponential decay," Phys. Rev. Lett. **118**, 196801 (2017).

[215] R. Nandkishore, "Many-body localization and delocalization in the two-dimensional continuum," Phys. Rev. B **90**, 184204 (2014).

[216] V. Kravtsov, B. Altshuler, and L. Ioffe, "Non-ergodic delocalized phase in anderson model on bethe lattice and regular graph," Annals of Physics **389**, 148–191 (2018).

[217] W. Tang and I. M. Khaymovich, "Non-ergodic delocalized phase with Poisson level statistics," Quantum **6**, 733 (2022).

[218] T. Thiery, F. m. c. Huveneers, M. Müller, and W. De Roeck, "Many-body delocalization as a quantum avalanche," Phys. Rev. Lett. **121**, 140601 (2018).

[219] M. Inui, S. A. Trugman, and E. Abrahams, "Unusual properties of midband states in systems with off-diagonal disorder," Phys. Rev. B **49**, 3190–3196 (1994).

[220] V. Karle, M. Serbyn, and A. A. Michailidis, "Area-law entangled eigenstates from nullspaces of local hamiltonians," Phys. Rev. Lett. **127**, 060602 (2021).

[221] E. V. H. Doggen, F. Schindler, K. S. Tikhonov, A. D. Mirlin, T. Neupert, D. G. Polyakov, and I. V. Gornyi, "Many-body localization and delocalization in large quantum chains," Phys. Rev. B **98**, 174202 (2018).

APPENDIX A

Appendices to Chapter 2

A.1 Thermalization within the largest subsector of the Hilbert space

In order to show the ergodic behavior of the eigenstates of the Hamiltonian, we study the distribution $P(s)$ of the energy differences in the sorted eigenspectrum weighted by the mean level spacing Δ, $s_i = (\epsilon_i - \epsilon_{i-1})/\Delta$. It is known that thermal systems which satisfy the eigenstate thermalization hypothesis are characterized by level statistics in agreement with the prediction of the Gaussian orthogonal ensemble (GOE), $P_{\text{GOE}}(s) = \frac{\pi}{2} s e^{-\frac{\pi}{4}s^2}$.

However, before discussing the level statistics, the discussion of the density of states is in order. The Hamiltonian $\hat{H}_2$ has a spectral reflection property with respect to $E = 0$ and it presents an exponentially large in system size number of zero modes, as highlighted by the peak in the density of states $\rho(0)$ shown in Figure A.1(a). The large number of zero energy eigenstates is explained by the bipartite nature of the adjacency graph that describes the Hamiltonian, see Figure 2.8 for an example. In a bipartite graph there exist two sets of nodes $\mathcal{P}_{1,2}$ labeled by different product states, such that the action of the Hamiltonian on states belonging to the set $\mathcal{P}_1$ yields a state in the set $\mathcal{P}_2$ and

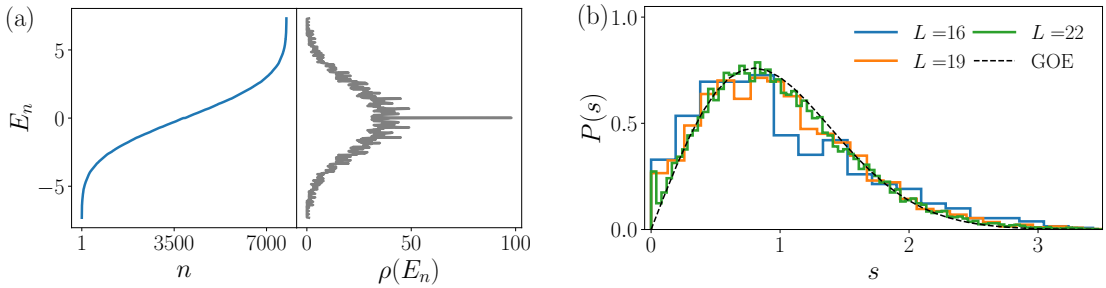

Figure A.1: (a): As shown in the left sub-panel, the spectrum is symmetric with respect to $E_n = 0$, such that for any eigenstate with eigenvalue E_n there is a second state with energy $-E_n$. Additionally, the model has a large number of zero energy eigenstates, as highlighted by the peak of the density of states $\rho(E_n)$ in the right sub-panel. We show data for $N_p = 7$ and $L = 19$. (b): The level spacing distribution $P(s)$ shows good agreement with the GOE prediction, shown as a black dashed line, thus confirming the presence of level repulsion within the largest subsector.

vice versa. These two partitions are identified by the eigenvalue of the parity operator $\hat{\mathcal{P}} = \prod_j (1 - 2\hat{n}_j)^j = \prod_j (-\sigma_j^z)^j$, where $\sigma_j^z = 2\hat{n}_j - 1$ is the corresponding Pauli matrix. It is known that a bipartite graph has a number of zero modes bounded from below by the difference in the size of the two sets P_1 and P_2 [219].

In fact, when the two partitions have a different number of states, a non-trivial solution of the Schrödinger equation for a zero energy eigenstate can be expressed as a system of n_1 linear equations for n_2 variables. If $n_2 > n_1$, there are at least $n_2 - n_1$ linearly independent solutions. In this case, in spite of the bound not being tight, both the number of zero modes and the lower bound from the bipartite structure of the graph describing the Hamiltonian increase exponentially with system size, albeit with different prefactors in the exponent. This suggests that the present understanding of the zero mode subspace is incomplete, inviting further research. In particular, using the disentangling algorithm [220] may give valuable insights. This may also help to develop a more complete understanding of the recursive Hilbert space fragmentation, since its mechanism relies on the zero energy eigenstates with vanishing particle density on the last sites of the system, see Section 2.3.2.

In Figure A.1(b) we show the level spacing distribution for $L \in [16, 22]$ in the interval $[E_{\mathrm{GS}}, -0.1]$, where E_{GS} corresponds to the ground state energy. Note that due to the spectral reflection property of the Hamiltonian, taking into account only negative energies yields the same results as considering the whole spectrum. To obtain $P(s)$, we unfold the spectrum in the given interval through polynomial interpolation of the integrated density of states. The agreement with the GOE prediction suggests that despite the presence of a constraint, the levels develop repulsion within the largest connected sector of the Hilbert space and the model is not integrable.

A.2 Ground state characterization

In this Appendix we characterize the ground state, studying the scaling of the energy gap and of the entanglement entropy. As the Hamiltonian (refEq: East-Hr) only has hopping terms, the low lying eigenstates need to have a large overlap with product states

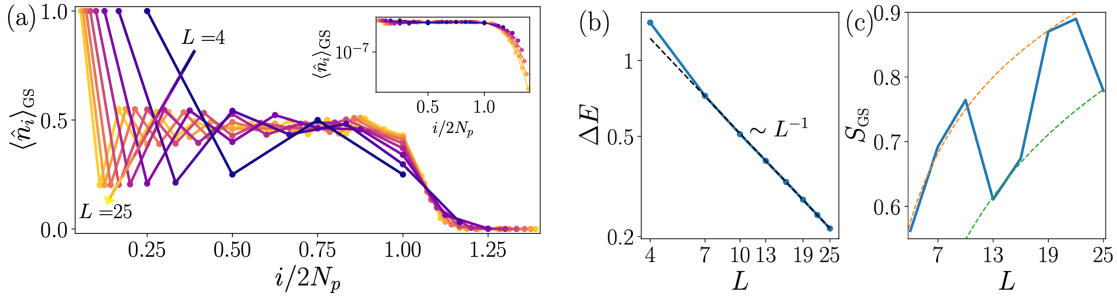

Figure A.2: (a): The density profile of the ground state $\langle \hat{n}_i \rangle_{\mathrm{GS}}$ shows large particle occupation up to $i = 2N_p$. Outside this region, the density starts decaying exponentially, as shown in the inset. (b):The finite size scaling of the energy gap ΔE shows that it vanishes as $1/L$, thus indicating that the model is gapless in the thermodynamic limit. (c): Entanglement entropy across the central cut grows logarithmically with strong finite size corrections (dashed orange and green lines show logarithmic fits), providing additional evidence that the ground state is critical.

that maximize a number of configurations to which hopping is allowed to. In graph language, see Figure 2.8 for an example, these product states correspond to vertices with the largest possible connectivity. For $r = 2$, the state with highest connectivity is $|\underbrace{\bullet\circ\bullet\circ\bullet\cdots\bullet}_{2N_p}\underbrace{\circ\circ\circ\cdots\circ}_{L-2N_p}\rangle$, with connectivity $2N_p - 1$, hence we expect the ground state to have a large weight on the initial $2N_p$ sites. In Figure A.2(a) we plot the density profile of the ground state of the Hamiltonian (2.2) for different system sizes from $L = 4$ to $L = 25$ against a rescaled x-axis $i/2N_p$. The figure confirms the prediction, the ground state is confined within the first $2N_p$ sites, with an exponentially decaying density outside of this region, as shown in the inset. This behavior is different from the one observed in the quantum East model in absence of particle conservation [129, 135], where occupation immediately decays exponentially.

We further study the scaling of the energy gap and of the entanglement entropy. As clearly shown in Figure A.2(b), the energy gap ΔE vanishes as the inverse system size, suggesting that model is in a gapless phase in the thermodynamic limit. Additionally, the entanglement entropy of the ground state across the central cut in the chain presents a slow logarithmic growth. These results suggest that the ground state is critical.

A.3 Construction of left parts of separable eigenstates

In this section we report the left-restricted eigenvectors entering Eq. (refEq: East-zero S evec) for all sub-system sizes we were able to investigate numerically for $r = 2$. These were used in the main text to correctly count the global number of zero entanglement eigenstates $\mathcal{N}_S$ shown in Figure 2.3(b). We remind here that these eigenstates have to fulfill two conditions

(i) they have to be an eigenstate on the problem restricted to m particles in ℓ sites, with $\ell \leq 3m - 2$.

(ii) They must have zero density on the boundary site ℓ: $\left\langle \psi_m^\ell \right| \hat{n}_\ell \left| \psi_m^\ell \right\rangle = 0$.

Additionally we observe that these left-restricted eigenvectors always correspond to zero energy.

To obtain these states, we take advantage of the large number of zero modes of the Hamiltonian (refEq: East-Hr=2). Within the degenerate sub-space, one can perform unitary transformations and obtain a new set of zero energy eigenstates where at least one satisfies the condition (ii) above. To find the correct states in an efficient way, we build the matrix $N_{\alpha,\beta} = \left\langle E_\alpha^{m,\ell} \right| \hat{n}_\ell \left| E_\beta^{m,\ell} \right\rangle$ of the expectation values of the density on the last site on eigenstates of the Hamiltonian reduced to (m, ℓ). We then diagonalize $N_{\alpha,\beta}$ and check whether it has zero eigenvalues. If so, the corresponding eigenvector is still an eigenstate of the reduced Hamiltonian, and, by construction, it satisfies condition (ii). We notice that this method implements a sufficient condition, which implies that there could be other states that fulfill the same set of restrictions. However, our goal here is merely to provide evidence of existence of these states in several different system sizes.

In the following, we list the states for $m = 3, 4, 5$ and $\ell = 6, 9, 11$ respectively.

$$
\begin{aligned}
\left|\psi_3^6\right\rangle &= \frac{1}{\sqrt{2}}\Big(|\bullet\bullet\circ\circ\bullet\circ\rangle - |\bullet\circ\bullet\bullet\circ\circ\rangle\Big) \\
\left|\psi_4^9\right\rangle &= \frac{1}{2}\Big(|\bullet\bullet\circ\circ\bullet\circ\circ\bullet\circ\rangle - |\bullet\bullet\bullet\circ\circ\circ\circ\bullet\circ\rangle\Big) + \frac{1}{4}\Big(|\bullet\circ\circ\bullet\bullet\bullet\circ\circ\circ\rangle + |\bullet\circ\bullet\bullet\circ\bullet\circ\circ\circ\rangle \\
&\quad + |\bullet\circ\circ\bullet\circ\bullet\bullet\circ\circ\rangle + |\bullet\bullet\bullet\circ\circ\bullet\circ\circ\circ\rangle - |\bullet\bullet\circ\bullet\bullet\circ\circ\circ\circ\rangle - |\bullet\bullet\circ\circ\bullet\bullet\circ\circ\circ\rangle \\
&\quad - |\bullet\circ\circ\bullet\bullet\circ\circ\bullet\circ\rangle - |\bullet\circ\bullet\circ\bullet\circ\bullet\circ\circ\rangle\Big) \\
\left|\psi_5^{11}\right\rangle &= \frac{1}{\sqrt{6}}\Big(|\bullet\circ\circ\bullet\bullet\bullet\bullet\circ\circ\circ\circ\rangle + |\bullet\circ\bullet\bullet\circ\circ\bullet\bullet\circ\circ\circ\rangle + |\bullet\bullet\circ\circ\bullet\bullet\circ\circ\bullet\circ\circ\rangle \\
&\quad + |\bullet\bullet\bullet\circ\circ\circ\bullet\circ\circ\bullet\circ\rangle - |\bullet\circ\bullet\circ\bullet\bullet\circ\bullet\circ\circ\circ\rangle - |\bullet\bullet\circ\bullet\circ\circ\bullet\circ\bullet\circ\circ\rangle\Big)
\end{aligned}
\tag{A.1}
$$

Additional states are present, which we do not write down for the sake of brevity. However, we point out the existence of recursively stacked eigenstates, as mentioned in the main text, and of states where the right part corresponds to a single isolated particle.

A.4 Quantum Hilbert space fragmentation for generic Hamiltonian parameters

Throughout the main text, we often mentioned that the results regarding quantum fragmentation hold irrespective of the range of the constraint r and of the values of the hopping amplitudes t_ℓ. In the following, we provide evidence in support of the generality of recursive fragmentation.

In Figure A.3, we first show the entanglement entropy of eigenstates for $r = 2$ and Hamiltonian

$$
\hat{H} = \sum_{i=2}^{L-1} (t_1 \hat{n}_{i-1} + t_2 \hat{n}_{i-2} - t_2 \hat{n}_{i-1}\hat{n}_{i-2})(\hat{c}_{i+1}^\dagger \hat{c}_i + \text{H.c.}), \tag{A.2}
$$

with generic, although homogeneous, hopping amplitudes t_1, t_2. In the leftmost panel, we highlight the presence of zero entanglement eigenstates in the half-chain cut for a random choice of the hopping parameters. The density profile of these special eigenstates is similar to the one showed in Figure 2.3(a), although the density profile in the left region has more complicated pattern due to the different values of $t_{1,2}$.

Next, we show the presence of recursive fragmentation in the generic Hamiltonian (2.3). In the central and right panels of Figure A.3 zero entanglement eigenstates (red crosses) appear across the central cut for both $r = 1$ and $r = 3$. As for the random $t_{1,2}$ case, the structure of these eigenstates is akin to the one obtained in Eq. (2.11), featuring an empty region of $r + 1$ sites disconnecting the left region from the right one. Thus we provide numerical evidence in support of the generic form of the zero entropy eigenstates $|E_{S=0}\rangle$ proposed in the main text.

A.5 Transport in different initial states

In the main text, we discuss the transport properties of the domain wall initial state, observing an unexpected superdiffusive behavior. Although at a finite time t^*, the

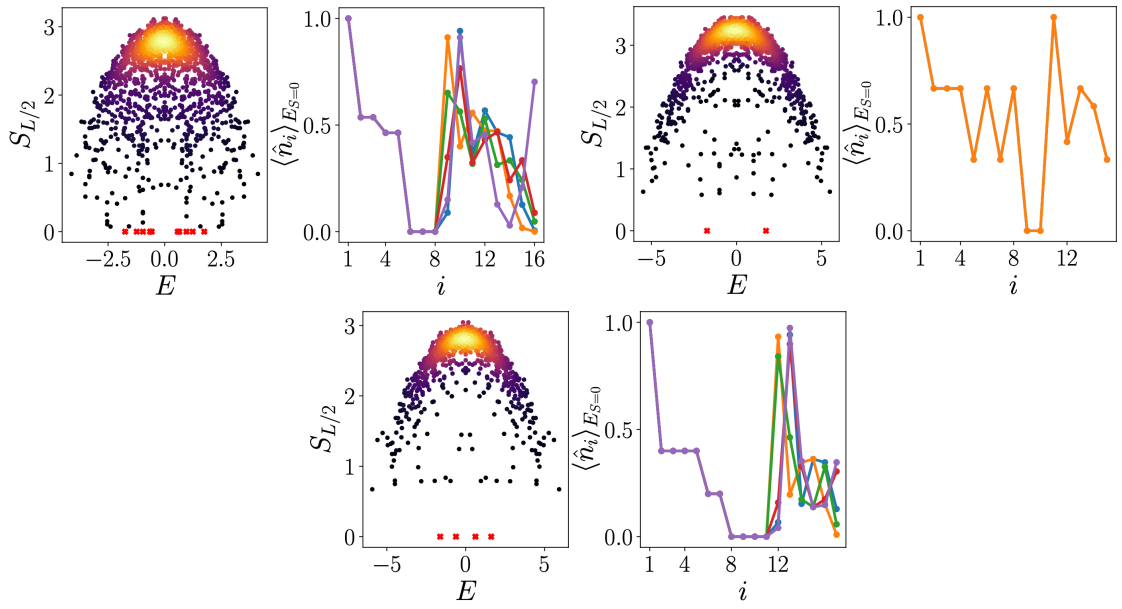

Figure A.3: Top left: entanglement entropy of the eigenstates of the Hamiltonian for range $r = 2$, random hopping parameters $t_1 = 0.84$, $t_2 = 0.49$, and system size $L = 16$. The presence of zero entanglement eigenstates, highlighted by the red crosses, confirms that quantum fragmentation is insensitive to the value of the hopping amplitudes. Top right and bottom: A similar result is obtained for different values of the range r. The central panels refer to $r = 1$, $N_p = 8$ and $L = 15$, while the right ones show $r = 3$, $N_p = 5$ and $L = 17$.

dynamics slow down, showing signatures of logarithmically slow transport, the linear increase of t^* with system size suggests that this feature persists in the thermodynamic limit. In this Appendix, we explore the dynamics of random initial states with varying density to understand the generality of the dynamics observed in the $|\mathrm{DW}\rangle$ initial state.

To this end, we initialize the system in a random superposition of all product states $|\varphi_i\rangle$ with average particle density $\nu = 3/4$ in the leftmost sites

$$|\psi_0\rangle = \frac{1}{N} \sum_i c_i e^{\imath \phi_i} |\varphi_i\rangle \,, \tag{A.3}$$

where the amplitude c_i and the phase ϕ_i are drawn randomly from a uniform distribution in $[0, \pi]$ and N is the normalization factor. After running the dynamics up to time $t = 100$ for 10 different random initial states, we obtain the inverse dynamical exponent $1/z$ as in the main text and average among the different states.

As shown in Figure A.4, the inverse dynamical exponent presents a behavior qualitatively similar to the one observed for the $|\mathrm{DW}\rangle$ initial state, with a plateau extending up to time $t^*(\nu)$ before eventually slowing down to a logarithmic behavior. In this case, however, the plateau suggests diffusive dynamics, suggesting the possibility of a density-dependent transport exponent. In panel (b) of the same Figure, we show the average $t^*(\nu)$ as a function of system size, clearly showing that the plateau becomes longer as L increases both for the $|\mathrm{DW}\rangle$ initial state ($\nu = 1$) and for the present case. Finally, we study the value of the dynamical exponent within the plateau, $\overline{1/z}$, by averaging $1/z(t)$ in a time window $[t_0(L), t_1(L)]$ for each realization of the initial state. The values of $t_0(L)$ and $t_1(L)$ are given in the following table.

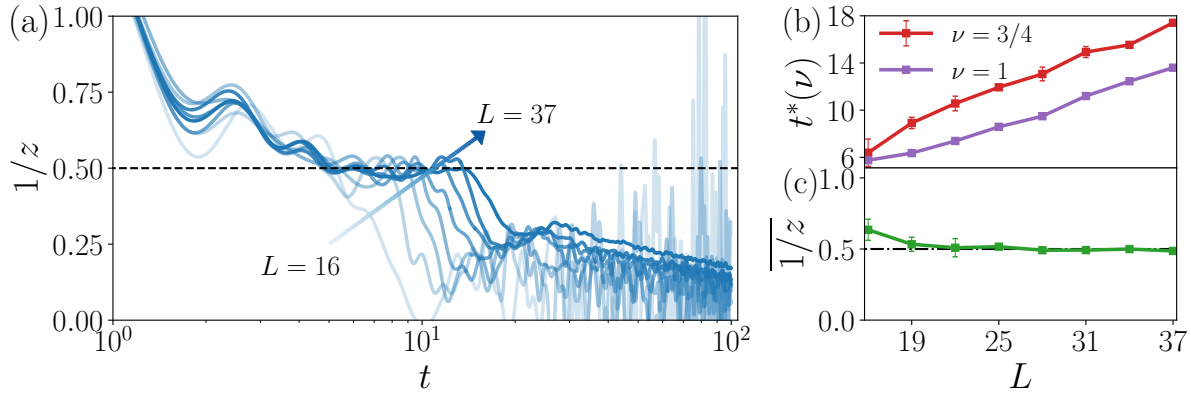

Figure A.4: (a) The inverse dynamical exponent for different system sizes ($L \in [16, 37]$ from more to less opaque) averaged over 10 random initializations. The behavior of $1/z$ is qualitatively similar to the one observed for the $|\mathrm{DW}\rangle$ initial state, although the plateau is compatible with diffusion in this case. (b) The onset time of the logarithmic behavior, $t^*(\nu)$, averaged over the different choices of $|\psi_0\rangle$ ($\nu = 3/4$) and for the domain wall initial state ($\nu = 1$), shows a clear increase with system size. (c) The average value of the inverse dynamical exponent within the plateau $\overline{1/z}$ shows an initial decrease with system size, before eventually saturating to a value compatible with $1/z = 0.5$ (black dashed line).

L	t_0	t_1
16	1	5
19	2.5	7.5
22	3	8
25	4	9.5

L	t_0	t_1
28	5	10
31	5	12
34	5	13
37	5	13

As shown in panel (c), after a decrease with system size at small values of L, the average inverse dynamical exponent $\overline{1/z}$ among different $|\psi_0\rangle$ realizations stabilizes to a value compatible with diffusion $1/z = 0.5$. We also notice that the small standard deviation, represented by the error bars, suggests that this behavior is typical among the studied states.

A.6 Dynamics of the domain wall initial state for different values of r

In the main text we provided evidence of slow dynamics from the time-evolution of the density operator in large systems and from the behavior of the root-mean-square displacement. Here, we present some additional data regarding system size scaling of the density dynamics as well as the observation of slow dynamics for generic r. Finally, we present an additional measure for the logarithmic behavior of the particles spreading.

In Figure A.5(a) we show the system size scaling of the dynamics of the density on the last site of the chain, $\langle \hat{n}_L(t) \rangle$. All the curves present logarithmic growth, and for larger system sizes $L \geq 19$ the slope becomes roughly constant. The absence of logarithmic behavior for smaller system sizes $L < 16$ is in agreement with the data shown in the main text, where $R(t)$ quickly saturates for $L = 13$.

Similar slow dynamics are observed in the time-evolution generated by Hamiltonians with generic constraint range r. In Figure A.5(b) we present the growth of the density in the last three sites of two chains of length $L = 17$ and $L = 21$ for $r = 1$ and $r = 3$ respectively. As the data suggest, the dynamics in the rightmost part of the chain always presents logarithmic behavior, irrespective of the range of the constraint. However, the quantitative details are affected by r.

To analyze the spreading of the density, in the main text we presented the behavior of the root-mean-square displacement $R(t)$ together with the respective dynamical exponent $z_R(t)$. Here, we approach the same question using a different measure, namely the time-dependence of the expansion of the density profile. This spreading distance δr is defined as the distance from the domain wall boundary, $i = N_p$, at which density becomes larger than a certain threshold $\varepsilon \ll 1$. The spreading distance δr is expected to asymptotically behave as a power-law in time, defining a dynamical exponent z_r such that $\delta r \approx t^{1/z_r}$. However, the limited system sizes available to our numerical study do not allow us to reach the asymptotic regime, and we are forced to study the time-dependent analogue $z_r(t)$, obtained through the logarithmic derivative of the spreading distance with respect to time, $(z_r(t))^{-1} = d \ln \delta r / d \ln t$.

In panel (a) of Figure A.6 we show a heat-map of the density dynamics for $L = 37$ sites, superimposed with curves of constant $\langle \hat{n}_i(t) \rangle = \varepsilon$, for values of $\varepsilon \in [0.1, 10^{-10}]$, above the accuracy limit $O(10^{-12})$ of the 4-th order Runge-Kutta algorithm. For each threshold, we show in panel (b) the time-dependent dynamical exponent. For the largest values of ε the dynamical exponent has a super-diffusive plateau at $1/z_r(t) \approx 0.7$ before quickly vanishing as expected from the logarithmic dynamics of the density. On the other hand, at smaller thresholds the dynamical exponent seems to saturate to a finite value, before it eventually starts decreasing due to boundary effects.

The saturation value of the time-dependent dynamic exponent for small thresholds has a weak dependence on the value of ε. As $\varepsilon \to 0$, $1/z_r$ approaches a r-dependent saturation value, monotonically increasing as the range of the constraint becomes larger, as shown in the right panel of Figure A.6(b). This behavior is in agreement with the expectation that

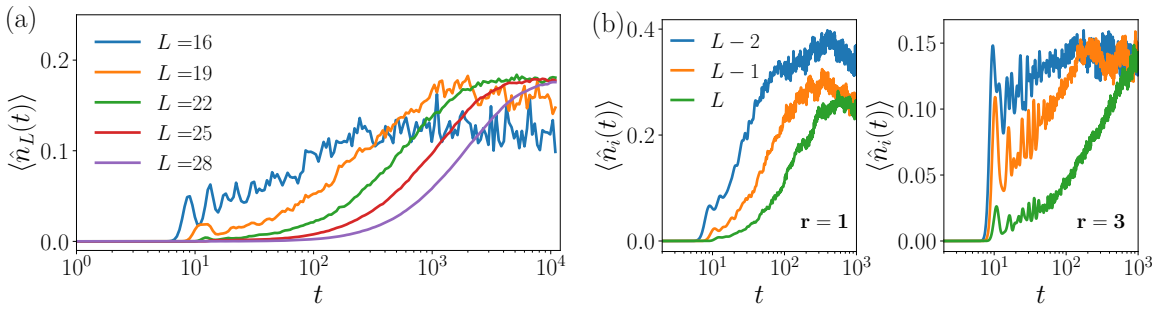

Figure A.5: (a): The dynamics of the density on the last site $\langle \hat{n}_L(t) \rangle$ for several different system sizes. The slow logarithmic growth is evident for all $L \geq 16$. At larger system sizes $L \geq 19$ the slope becomes independent of system size, as well as the saturation value, thus suggesting a universal behavior. (b): The density dynamics for different values of the range r shows always a logarithmic behavior. While the quantitative details change between different values of r, the qualitative feature of the logarithmic growth is a constant, thus confirming our claim of generality of the results. The data are obtained on a chain of $N_p = 9$ and $L = 17$ for $r = 1$, and $N_p = 6$ and $L = 21$ for $r = 3$.

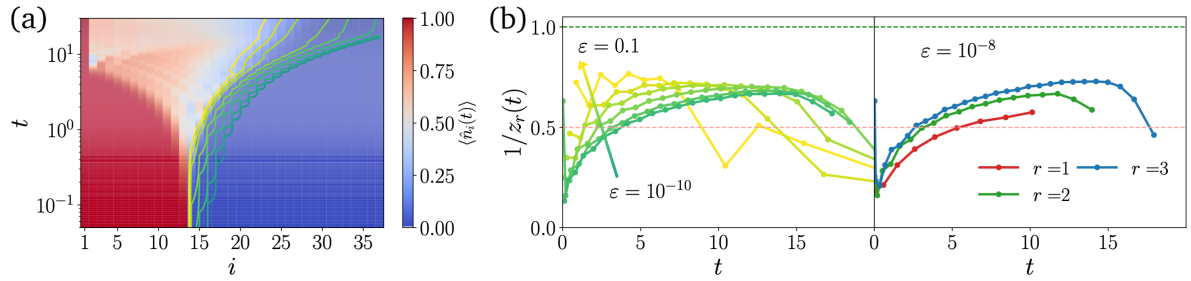

Figure A.6: (a) Spreading of the density in a system with $L = 37$ sites and $N_p = 13$ bosons. Lines of constant value ε highlight the very different behavior observed in the two regions $i \lesseqgtr 2N_p$. (b) The inverse dynamical exponent $1/z_r(t)$ is always super-diffusive. While for a large threshold it decays to 0 indicating the onset of logarithmic growth, for small values of ε the dynamical exponent seems to saturate approaching the asymptotic value (weakly dependent on the threshold value), before the onset of boundary effects. As shown in the right panel, the asymptotic $1/z_r$ is super-diffusive behavior is generic irrespective of the choice of the range of the constraint. The data shown in this panel correspond to $N_p = 11$ and $L = 21, 31, 41$ for $r = 1, 2, 3$ respectively.

at $r \to \infty$ the system should approach ballistic dynamics.

APPENDIX B

Benchmark of TEBD algorithm for Chapter 3

In this Appendix, we provide benchmarks of the TEBD algorithm and its accuracy for the model used in Chapter 3. While the instantaneous errors related to the truncation and finite time step are known, understanding the propagation of these errors with time and their possible interference is challenging.

First we tested the TEBD algorithm by evolving the ground state of the same model. Provided that the time evolution is numerically exact, the overlap between the TEBD-evolved ground state,

$$|\psi_0(t)\rangle = U^{\mathrm{TEBD}}(t)\,|GS\rangle \tag{B.1}$$

and the exact time evolution of the ground state, $|GS(t)\rangle = e^{-\imath E_0 t}\,|GS\rangle$, is supposed to give the identity $\langle\psi_0(t)|GS(t)\rangle = 1$ at all times. For the fourth-order Trotterization the behavior of the deviation from unity is known to be proportional to $(\delta t)^8$

$$F = 1 - |\,\langle\psi_0(t)|GS(t)\rangle\,| \propto (\delta t)^8 \tag{B.2}$$

The numerical results plotted in Fig. B.1(a), confirm these expectations.

Next, we performed a benchmarking of TEBD algorithm against ED time evolution for several disorder realizations and simulation parameters. An illustration of such benchmarking is shown in Fig. B.1(c) and (d). In particular, we observed that time step $\delta t = 0.05$ and cutoff $\varepsilon = 10^{-9}$ result in a good agreement between ED and TEBD dynamics. Smaller values of $\delta t, \varepsilon$ would improve the agreement but would result in a dramatic slowdown of the evolution time. Therefore, we decided to use these parameters in the simulations presented in the main text.

When larger system sizes are involved, as it is the case for the simulations actually used in the main text, comparison with exact results is not available. Therefore, other indicators for the accuracy must be studied. Among these, energy conservation through the time evolution is a straightforward probe. The energy deviation

$$\Delta E(t) = |E(0) - E(t)|/E(0), \quad E(t) = \langle\psi(t)|\,\hat{H}\,|\psi(t)\rangle\,, \tag{B.3}$$

allows to control the propagation of the error during the Trotter time evolution. In the left panel of Fig. B.2 we show the results for $\Delta E(t)$ in the two quenches presented in the

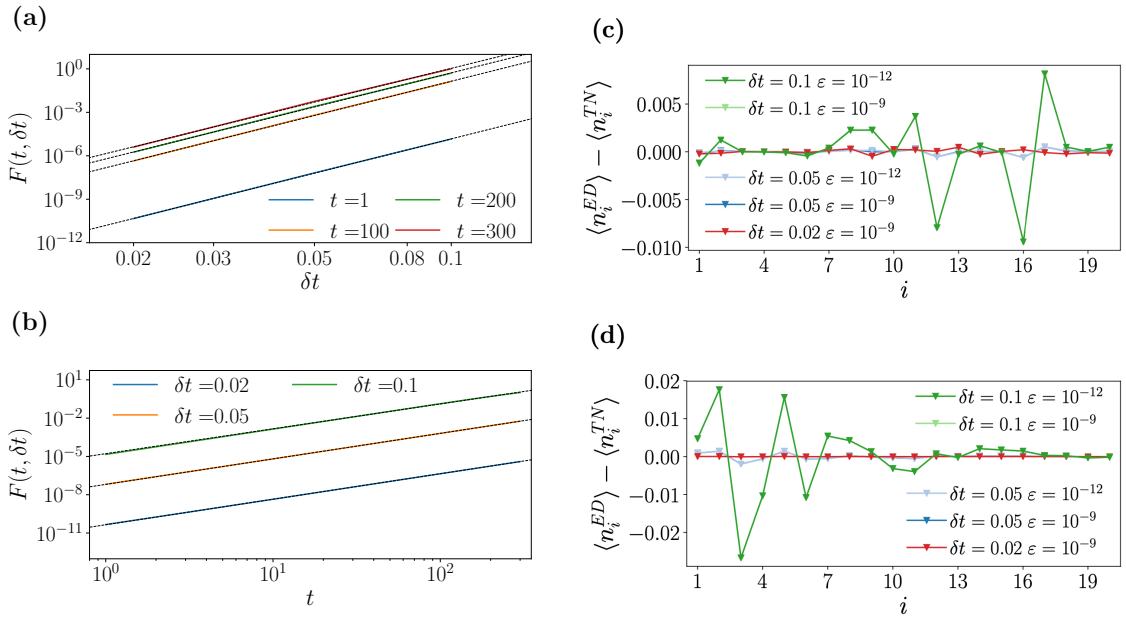

Figure B.1: (a-b) Deviation of ground state fidelity from 1 in Trotter time evolution, $F(t, \delta t)$, shows power-law behavior both in time and in time-step, as expected. The data is obtained at density $\nu = 1/5$, system size $L = 20$ and disorder $W = 6.5$ for a particular disorder realization. The plots for other disorder realizations are qualitatively similar. (c-d) The comparison between ED and TEBD time evolution reveals that the most effective way to increase accuracy of TEBD is to decrease the time-step δt. Indeed, the change in the truncation between $\varepsilon = 10^{-9}$ and $\varepsilon = 10^{-12}$ does not have much effect on the the difference between density profiles of exact diagonalization and TEBD. At the same time, the decrease of time step brings the local density profile closer to ED results. The density profiles are calculated by propagating uniform density wave (c) and uniform pair-density wave (d) initial states to time $t = 500$ for a particular disorder realization with $L = 20$, $\nu = 1/5$, $W = 6.5$.

main text, for $L = 30$. The two plots highlight that the average energy deviation is very small in both configurations. In spite of that, a clear difference can be observed among the two quenches, noticing that the non-uniform state has larger error. This is probably due to the enhanced entanglement caused by the presence of the bubble in the lattice. Nevertheless, $\Delta E(t)$ remains very small even at long times, thus confirming the reliability of our long-time numerical simulations.

Besides the inaccuracies due to Trotterization and studied in detail above, the truncation on the singular values can also affect the validity of the results. Although we chose a small truncation error $\varepsilon = 10^{-9}$, if the bond dimension saturates the approximation of the wave function becomes uncontrolled, and eventually as time increases relevant information will be discarded. To support the accuracy of our results, already benchmarked against exact diagonalization, we report the statistics of the maximal bond dimension reached by the various states. To obtain the results presented in the main text, we set the bond dimension to be $\chi_1 = 500$ and $\chi_2 = 3000$ for the density-wave and bubble state respectively. As the histograms in Fig. B.2 show, all the disorder realizations remained well below the maximum threshold. This fact ensures that we have a control on the error encountered in the evolution, in contrast to time evolution with TDVP with fixed bond dimension,

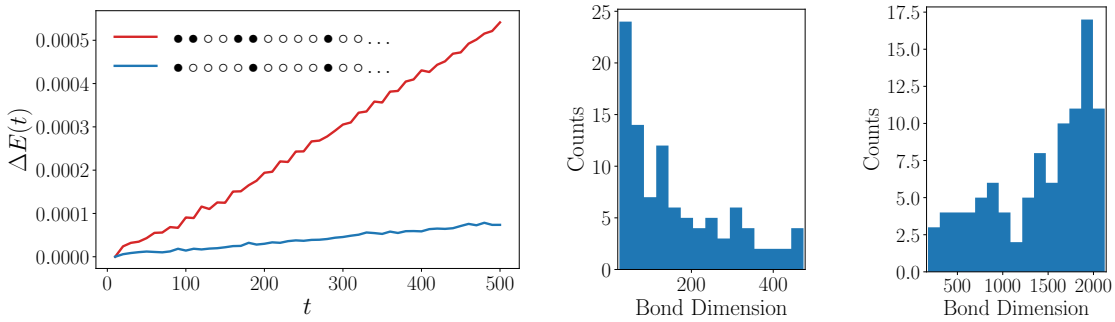

Figure B.2: Left: the normalized absolute value of the energy difference from the initial energy $\Delta E(t) = |\langle H(t)\rangle - E(0)|/|E(0)|$ remains very small for both the density wave, blue curve, and the non-uniform, red curve, configurations, confirming the good accuracy of our numerical simulations beyond the ED benchmark. The larger deviation displayed by the non-uniform configuration is understood as a result of the presence of the bubble in the lattice, that increases entanglement growth. The results here shown are obtained averaging over 100 disorder realizations, for the system sizes, $L = 30$, and initial states described in the main text. Center and right: the histogram representing the maximum bond dimension of different disorder realizations show that the threshold values of 500 and 3000 for the uniform density wave (center) and bubble states (right) were never saturated in our simulations.

where error estimation is more challenging [221].

Finally, we remark that in all the simulations performed using ITensor [176], we took advantage of the conserved $U(1)$ symmetry. Indeed, simulations that use quantum numbers have an advantage as the tensors can be written in block diagonal form, each block being labeled by a quantum number. Consequently, even at large bond dimensions, the operations are done on smaller matrices with a net increase in the efficiency of the algorithm.

APPENDIX C

Appendices to Chapter 4

C.1 Parallel implementation of TEBD

In Chapter 4 we use the TEBD algorithm [114] to perform the time evolution of the wave function of the large system represented as an MPS. The algorithm splits the unitary evolution into time steps (Trotterization), dt, and further divides them into even and odd gates, $\hat{G}_{i,i+1} = \exp\{(-\imath dt \hat{h}_{i,i+1})\}$, where $\hat{h}_{i,i+1}$ is the Hamiltonian density on sites i and $i+1$. Since even(odd) gates do not overlap with one another, all even (odd) gates commute and can be applied independently to the state. This allows a natural parallel implementation of the algorithm, where all even (odd) gates are applied simultaneously. The time-evolution can thus be performed in parallel, assigning to one thread a portion of the chain, as pictorially shown in Figure C.1. When multiple nodes are involved, one must carefully transfer information after each sweep, as the time-evolved states at the boundaries between different nodes need to be transferred in order for the evolution to be

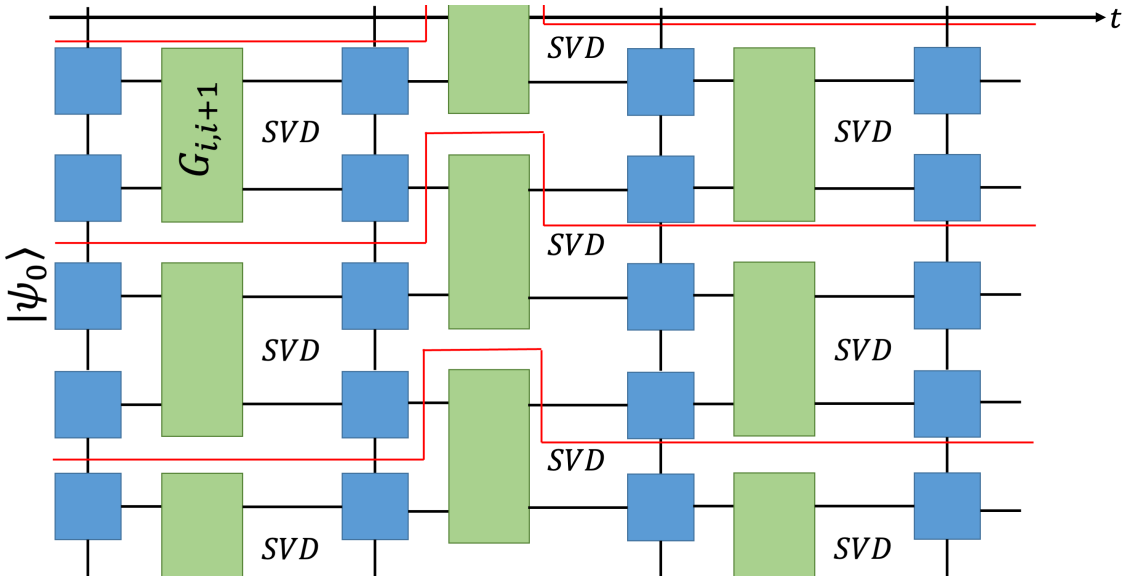

Figure C.1: Cartoon representation of the TEBD algorithm. The time evolution can be naturally parallelized, by sharing each of the operations contoured in red to a different core.

exact. Additionally, the dishomogeneity of the problem naturally introduces a workload imbalance, that can however be taken care of rebalancing the portion of the chain assigned to each node.

The TEBD algorithm has two main sources of error: the finite value of time-step used in Trotterization and the truncation error in the singular-value decomposition (SVD). The time step error naïvely scales as $O(dt^2)$, but it can be reduced to $O(dt^4)$ with an appropriate higher order Suzuki-Trotter decomposition. By choosing sufficiently small time steps, then, the accuracy of the simulation remains reliable for long timescales. The accuracy of the simulation can be controlled by the degree of energy conservation violation, i.e. by tracking $\Delta E(t) = |\langle\psi_0|\hat{H}|\psi_0\rangle - \langle\psi(t)|\hat{H}|\psi(t)\rangle$. In our simulations, we fixed $dt = 0.05$. In spite of a slower execution time, such a small time-step ensures very accurate results, as evidenced by $\Delta E(T) < 10^{-4}$ at the final simulation time $T = 200$.

The second source of error, i.e. the singular values truncation ε, arises from the singular-value decomposition performed after each gates application in order to restore the MPS form. In order to avoid the exponential growth of the MPS bond dimension χ, one needs to select the most relevant singular values by neglecting all those which are smaller than a certain threshold ε. The truncation then corresponds to neglecting some weight of the wave-function, and the error can be estimated by the sum of the discarded singular values $\sum_{\lambda_i<\varepsilon}\lambda_i^2$. A further limit on the number of singular values is imposed by the maximal bond dimension, χ. If during the time evolution the number of singular values smaller than ε becomes larger than χ, i.e. the bond dimension is saturated, then the control on the accuracy of the results is lost, as there is no guarantee that large singular values will be discarded in the future. In our simulations, we fix $\epsilon = 10^{-9}$ and $\chi = 3000$. This set of parameters guarantees the reliability of the results as the maximum bond dimension is saturated only in the last 10 time-steps (in hopping parameter units) of less than 1/10 of the central bonds. Furthermore, we can ensure accuracy by comparison to exact diagonalization results on smaller systems, which for the chosen simulation parameters show discrepancies in local observables and entanglement typically of the order $O(10^{-4})$.

The choice of these parameters, however, makes the simulations extremely demanding. However, the structure of the algorithm is naturally suited for parallelization, as shown in Figure C.1, and the use of a parallel implementation of the code allowed us to study the dynamics even in the high entanglement regime, where most of the tensors have a large bond dimension of order 1000.

C.2 Details and benchmark on DMRG-X

The DMRG-X algorithm [110, 111, 112] used to obtain the highly excited eigenstates of the Hamiltonian (4.4) relies on the shift-invert method applied to MPS states. The variant of the algorithm used in this work is described in detail in the supplementary material of [111]. In this section, we will give a brief overview of the algorithm and then explore the dependence of the quality of the results with respect to various tuning parameters such as bond dimension, system size, etc.

The DMRG-X algorithm used can be understood as a simple modification of the standard two-site DMRG [102] algorithm which is extensively used to target ground states of one-dimensional systems. We describe the two differences compared to the ground state algorithm.

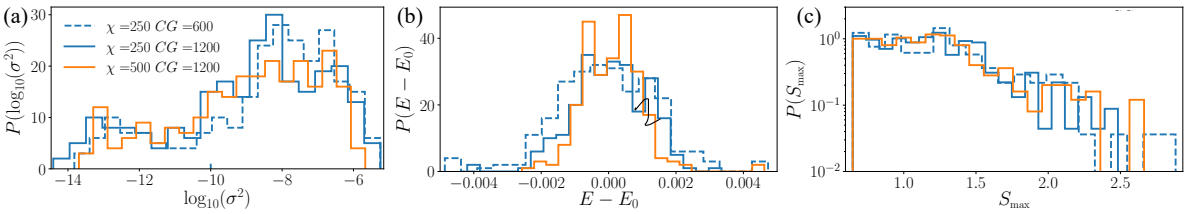

Figure C.2: (a) Increasing the bond dimension χ leads to a better distribution of the variance of the energy of the states σ^2, shifting it to lower values. Similarly, the increase of the number of conjugate gradient iterations at fixed χ improves the dataset quality. (b) The distribution of the distance of the final energy E from the target energy E_0. At fixed bond dimension $\chi = 250$ doubling the number of conjugate gradient iterations produces a dramatic improvement of the final energy distribution. Further increasing the bond dimension to $\chi = 500$ then gives an additional refinement of the distribution. (c) The entanglement distribution $P(S)$ for the bonds closest to $i_{\max}$ becomes narrower as the number of conjugate gradient iterations is increased. However, as the bond dimension is increased at fixed CG the MPS states can host larger entanglement, as is confirmed by the broader $P(S_{max})$ at $\chi = 500$.

First, the ground state DMRG uses the matrix product operator (MPO) form of the Hamiltonian, H, to perform the variational optimization. The DMRG-X algorithm, in contrary, employs $\mathcal{H} = (H - E_0)^2$, which is still efficiently represented by a MPO with a slightly larger bond dimension. The energy E_0 is the target energy, i.e. the energy of the eigenstates we are aiming to calculate. We square the operator in order to make it semi-positive definite. This is done in order to use iterative inversion algorithms (see below) which require such property and can be avoided if a different iterative algorithm is chosen. We have numerically observed that different iterative algorithms are less stable and converge slower for most cases.

Second, in the DMRG-X algorithm, we are not aiming to find the eigenstate of $\mathcal{H}$ with the largest magnitude eigenvalue. Instead, the goal is to find the eigenstate corresponding to the lowest magnitude eigenvalue, i.e. the one which corresponds to the eigenstate closest to energy E_0. This is taken into account in the local optimization step, present in DMRG-type algorithms, i.e. when two adjacent local tensors are optimized. In this step, one generates an effective operator by tracing the left and right environments, $\mathcal{H}_{\text{eff}}$ [102]. Calculating the lowest magnitude eigenvalue of $\mathcal{H}_{\text{eff}}$ is equivalent to calculating the largest eigenvalue of $\mathcal{H}_{\text{eff}}^{-1}$. We use a power-method to converge to the largest magnitude eigenvalue geometrically. Instead of applying $\mathcal{H}_{\text{eff}}^{-1}$ at each iteration, we solve the linear system $\mathcal{H}_{\text{eff}}\mathbf{x}_{i+1} = \mathbf{x}_i$ using a conjugate gradient algorithm. Due to the sweeping nature of the DMRG-type algorithms we have observed that a single iteration of the local power method leads to a faster convergence of the global wavefunction (for fixed runtime), indicating that increasing the number of sweeps is a more important factor. The iterative algorithm scales as $O(CG\chi^3)$, where CG is the number of conjugate gradient iterations, instead of the $O(\chi^6)$ scaling of the exact diagonalization of $\mathcal{H}_{\text{eff}}$. This scaling, together with the explicit conservation of both particle numbers, allow us to reach bond dimensions up to $\chi = 500$.

For the simulations presented in this work we used the following parameters: In the global level we restricted to 100 DMRG sweeps. However, we do not always keep the final state but the state with the least energy variance as measured at the end of every sweep for the

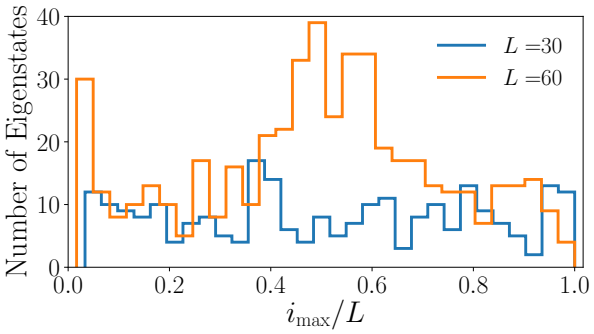

Figure C.3: The distribution of the peak of the c-boson is almost homogeneous through the whole system in the $L = 30$ case, but as the system size is doubled the typical position of $i_{\max}$ is more restrained to the center of the chain. The broad distribution of $i_{\max}$ is expected, as the local optimization performed in the algorithm can indeed update the position of the c-boson from its initial value and "move" it through the system.

last 50 sweeps. This is because the algorithm tends to switch between different eigenstates as it converges towards the target energy and during the switching period it is not always accurately converged. This behaviour is not present in the standard DMRG algorithm and is attributed to the exponentially large density of states around the target energy. For the solution of each local optimization problem, we use a single power method iteration which is performed using the conjugate gradient algorithm. For the singular value decomposition which is used to extract the updated local tensors we have used a very low probability truncation cutoff $\epsilon = 10^{-28}$, in order to avoid any statistical bias towards eigenstates of low entanglement. We found that the most important tuning parameters are the bond dimension χ and the number of conjugate gradient iterations CG. Below we show various benchmarks for different parameters and system sizes.

We compare the quality of the resulting eigenstates for $\chi = 250, 500$ and $CG = 600, 1200$. A first check is obtained by comparison of the energy variance

$$\sigma^2 = \langle \hat{H}^2 \rangle - \langle \hat{H} \rangle^2 \tag{C.1}$$

of the resulting states. As true eigenstates have exactly 0 energy variance, a small σ^2 is an indicator of good convergence. In Figure C.2(a), we compare the variance distribution for the different range of parameters, observing, as expected, that increasing both the number of iterations and the bond dimension leads to a better quality result.

The low-valued distribution of the variance suggests that the final states obtained with the DMRG-X algorithm are actually extremely close to exact eigenstates of $\hat{H}$. As a next step, one must check whether the obtained states are indeed highly excited. We thus study the distribution of the energy difference among the obtained state and the target energy E_0. As shown in Figure C.2(b), increasing χ and CG yields a narrower distribution close to 0.

Since the amount of entanglement entropy an MPS state can host is strictly related to its bond dimension, it is important to observe how the entanglement varies as we increase χ. We thus study the distribution of the entanglement entropy on the 10 bonds closer to the peak of the c-boson, $i_{\max}$, where entanglement is supposed to be largest. The results are shown in Figure C.2(c) and show that at fixed bond dimension, a larger number of iterations leads to a narrower distribution, in agreement with the small entanglement

of exact eigenvalues of MBL Hamiltonians. On the other hand, fixing $CG = 1200$ and increasing the bond dimension gives access to states with larger entanglement, as verified by the broader distribution of S at $\chi = 500$.

Finally, we study the distribution of the position of the peak of the c-boson. As initial state in the DMRG-X algorithm we always used a version of $|\psi_0\rangle$, Eq. (4.7), with the c-boson shifted of a few sites from the center, provided the site is not already occupied by a d-boson to avoid stable doublons. However, the local optimization performed by the algorithm can easily "move" the c-boson, as can be seen by the almost even distribution of $i_{\max}$ shown in Figure C.3, for $L = 30$. This behavior is consistent in all the datasets studied and does not seem to have a particular relation with the quality of the eigenstates. As the system size is doubled, the distribution of the peak of the c-boson becomes more centered around $L/2$, probably due to the larger density of state which increases the possibility of finding an eigenstate close to the target energy for smaller displacement of the c-boson.

C.3 Weak coupling regime for the intensive bath

In the main text, we showed numerical results suggesting the existence of a transition to a delocalized phase as the interaction strength between the bath and the disordered particles is decreased. In this Appendix, we provide some additional numerical results for the dynamics of the bath, of the d-bosons and of the system as a whole.

C.3.1 Evaluation of the accuracy of TEBD simulations

Due to the finite bond dimension χ and the finite truncation error ε, the wavefunction evolved using the TEBD algorithm $|\psi_\chi(t)\rangle$ deviates from the true state $|\psi(t)\rangle$. The error produced by the truncation of the singular values λ_a and corresponding Schmidt states, however, is well controlled and can be easily evaluated. At each singular value decomposition, the local weight of the wavefunction lost is given by

$$\epsilon_n = \sum_{\lambda_a < \varepsilon} \lambda_a^2 \quad \text{or} \quad \epsilon_n = \sum_{a > \chi} \lambda_a^2 \tag{C.2}$$

depending on whether the bond dimension at the evaluated link is saturated or not.

The global error at each timestep, then, corresponds to

$$\epsilon(t) = 1 - |\langle \psi(t) | \psi_\chi(t) \rangle|^2 = 1 - \prod_n (1 - \epsilon_n). \tag{C.3}$$

The total discarded weight at the end of the time evolution finally amounts to the integrated error $\epsilon(t)$.

In the work presented in the main text, we use extremely large bond dimension and low truncation error, thus ensuring the good accuracy of our simulations. In the Hamiltonian case we set $\chi = 5000$ and $\varepsilon = 10^{-9}$, resulting in a maximum error of $\epsilon = 2 \times 10^{-5}$ arising close to the putative transition, at $U = 1.25$. In the Floquet simulations we use a smaller $\chi = 2048$ and the same truncation as the Hamiltonian evolution. This gives rise to a maximum error of $\epsilon = 8 \times 10^{-3}$, again at an interaction strength $U = 1$ in the vicinity of the transition.

C.3.2 Additional evidence of bath delocalization

In Section 4.4.1, we studied the density profile of the clean boson, highlighting the stark difference at weak and strong U. We now use the ansatz for the density introduced in Eq. (4.27) to study the behavior of the decay length $\ell_c(t)$ as the interaction is changed.

In Figure C.4, the dynamics of the decay length is presented for both the Floquet (a) and the Hamiltonian (b) models. The data show a continuous increase of the value of $\ell_c(t)$ as U is decreased, in agreement with the transition predicted. In particular, the decay length shows signatures of saturation to a value much smaller than the system size for $U \geq 2$ and $U \geq 4$ in the Floquet and Hamiltonian dynamics respectively. At weaker interactions, instead, it keeps growing suggesting delocalization.

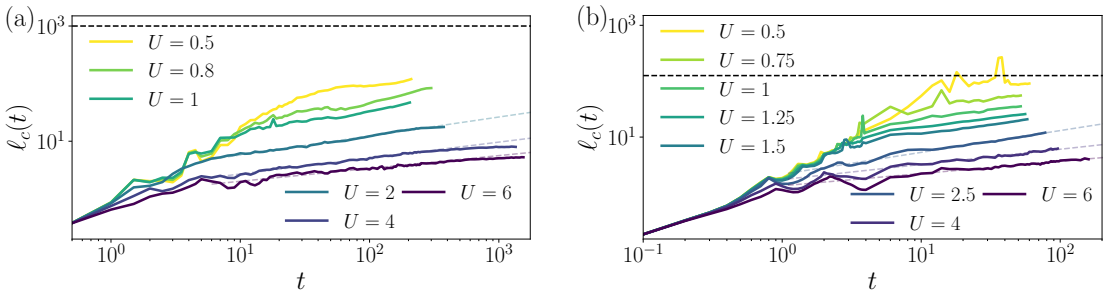

Figure C.4: c-boson decay length $\ell_c(t)$ shows different behavior at weak and strong interactions both in the Floquet (a) and Hamiltonian (b) time evolution. At small values of U, below the estimated transition, $\ell_c(t)$ grows persistently with no signs of saturation, reaching the value of half system size $L/2 = 126$ for the Hamiltonian dynamics (black dashed line). As the interaction is increased, the decay length first grows as a power-law in time (shaded dashed lines), but at eventually at long times accessible in Floquet evolution, starts saturating. This saturation suggests stability of localization at large U.

C.3.3 Disordered bosons imbalance and global entanglement

Due to the vanishing density of the bath particle in the extremely large systems we study, its effect on the d-bosons density is weak and hard to capture from the study of their density alone. In Section 4.4.1, however, we demonstrate that a study of the density-density connected correlations allows to observe a qualitative change in behavior at weak interaction strength U also for the disordered particles.

We now show numerical results concerning the density profiles and the relative imbalance, to highlight the necessity of studying more complicated operators, such as the connected correlations, and entanglement entropy, to distinguish weak and strong interactions behavior. In Figure C.5 (a)-(c) we show the d-boson density profile in Floquet (Hamiltonian) dynamics at late times $T = 205$ ($T = 54$), respectively. Close to the central site $i = L/2$ a monotonously enhanced relaxation is observed as the interaction increases. This observation that density of localized bosons is more affected by the clean particle at strong interactions (when the clean particle is localized) is readily explained by the fact that confinement of the clean boson to smaller regions helps to relax the density pattern of disordered particles within the localization volume. Far from the center of the chain, however, no significant variation is shown as U changes.

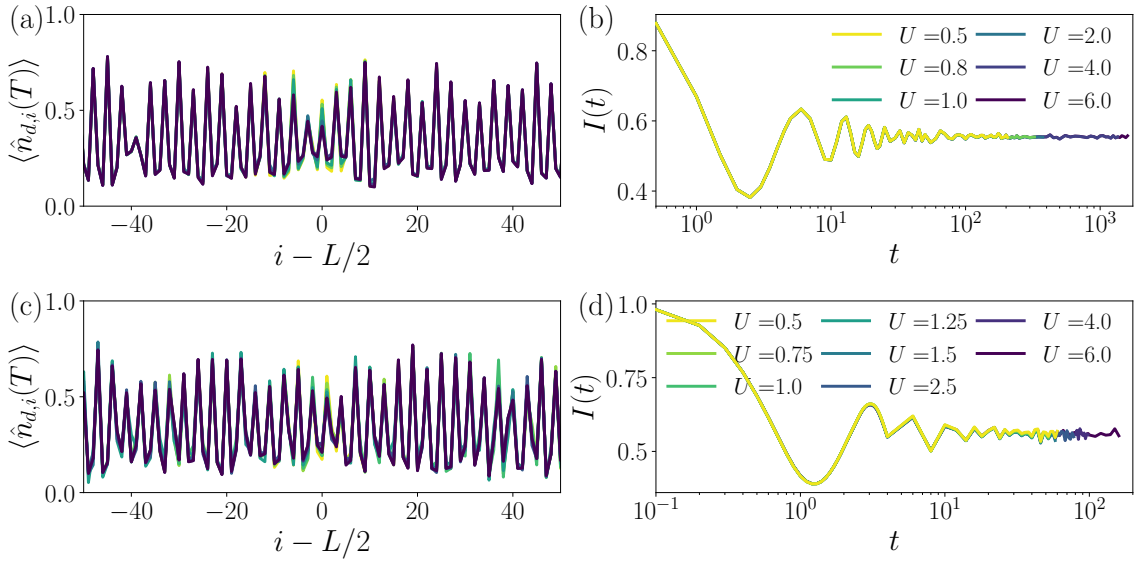

Figure C.5: Late time d-boson density profiles [shown for the latest common time among different values of U, $T = 205$ and $T = 54$ for Floquet (a) and Hamiltonian (c) dynamics] show very weak dependence on the interaction strength. The slight enhancement of relaxation at the center of the chain at large U is caused by the increased effect of localized c-bosons on disordered particles. The dynamics of imbalance $I(t)$ in panels (b) [Floquet] and (d) [Hamiltonian] also illustrates nearly complete absence of density pattern relaxation.

A more quantitative understanding can be obtained from the study of the imbalance

$$I(t) = \frac{N_o(t) - N_e(t)}{N_o(t) + N_e(t)}, \tag{C.4}$$

where $\hat{N}_{o/e}$ represent the density in the initially occupied/empty sites. For a period $1/\nu_d = 3$ density wave, they read

$$\hat{N}_o = \sum_{i=1}^{L/3} \hat{n}_{d,3i-2}, \quad \hat{N}_e = \frac{1}{2} \sum_{i=1}^{L/3} (\hat{n}_{d,3i} + \hat{n}_{d,3i-1}). \tag{C.5}$$

As imbalance measures the *memory* of the initial condition, its vanishing implies delocalization. However, as can be seen in panels (b)-(d) of Figure C.5, both in Floquet and Hamiltonian dynamics the imbalance does not show any sign of decay on the accessible timescales, irrespective of the interaction strength. This suggests that the relaxation of the d-bosons quantified by their density pattern is extremely slow.

The study of the entanglement entropy

$$S(i,t) = -\operatorname{tr} \rho_A(t) \log \rho_A(t), \tag{C.6}$$

where the chain is split into two subsystems $A = [1, i]$, $B = [i + 1, L]$, and we consider density matrix $\rho_A(t) = \operatorname{tr}_B |\psi(t)\rangle \langle\psi(t)|$, provides further evidence in favor of the existence of a transition. In many-body localized systems, entanglement entropy is expected to grow logarithmically [55, 80], hence a deviation from the logarithmic behavior can be interpreted as a breakdown of MBL. As we show in Figure C.6 (a)-(c) entanglement entropy at weak interactions shows faster than logarithmic behavior, suggesting thermalization. In

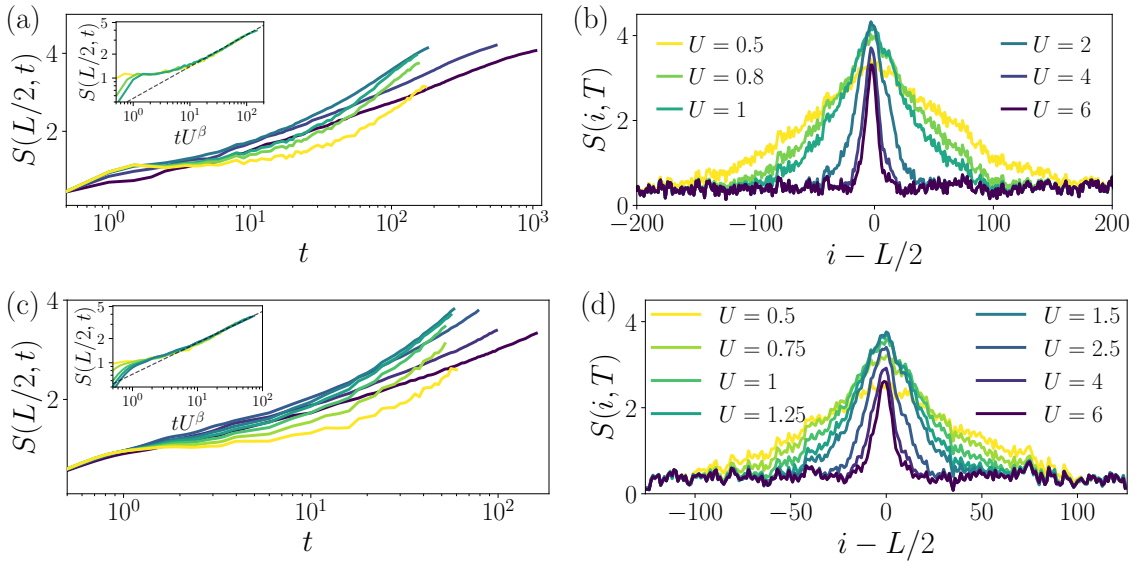

Figure C.6: Dynamics of entanglement entropy shows signatures of delocalization for weak coupling U both in Floquet (a)-(b) and Hamiltonian (c)-(d) dynamics. The power-law growth of entanglement across the central cut shown in panels (a)-(c) at weak coupling is clearly distinct from the logarithmic behavior observed for $U \geq 4$. The different behavior is also highlighted by the entanglement collapse shown in the inset, suggesting a universal power-law behavior in the ergodic phase. The behavior of real-space entanglement profile at fixed time ($T = 205$ for Floquet (b) and $T = 52$ for Hamiltonian dynamics (d)) in panels (b)-(d) also shows non-monotonic behavior, with a peak in the region $U \in [1, 2]$ separating two distinct regimes. At weaker interaction, entanglement spreads more uniformly through the chain, suggesting the presence of a large ergodic region close to the center. In contrast, at strong coupling, entanglement growth remains limited to the center of the chain, in agreement with the phenomenology of the MBL proximity effect.

particular, this leads to a universal power-law scaling of entanglement given by $S \approx (tU^\beta)^\gamma$ with the value of $\gamma \approx 0.39$ for both Floquet (a) and Hamiltonian (b) case. The value of β is similar between the two models $\beta \approx 1.1$, however only for $U \leq 1$. For larger values of U up to 1.5, β stays the same in the Floquet case and abruptly changes to $\beta \approx 0.6$ (not shown) in the Hamiltonian case. The universal behavior is captured by the collapse of the different entanglement curves shown in the inset of Fig. C.6 (a)-(c). As interaction strength increases logarithmic growth is eventually restored at $U = 4, 6$, in agreement with MBL.

The different behavior is also highlighted by the spatial profile of entanglement, i.e. the entanglement entropy shown as a function of the size of subsystem A at a fixed time T ($T = 205$ in panel (b) and $T = 52$ in panel (d)). Figure C.6 (b)-(d) shows that at strong interactions entanglement growth is limited to the center of the chain, in agreement with the phenomenology proposed in Section 4.3. At weaker interactions entanglement starts spreading more uniformly through the chain, indicating the creation of large ergodic regions in the chain. Interestingly, this phenomenon gives rise to a non-monotonicity of the peak of the entanglement profile as a function of interaction strength. At very weak interactions, entanglement spreads to far regions, and in turn its value in the center is lower than at intermediate U, where its spreading is reduced. We observe then a maximum of the peak around $U \approx 2$ in the Floquet case and $U \approx 1.5$ in the Hamiltonian dynamics,

which could correspond to the transition point, clearly separating the two entanglement regimes. The value U at which we observe the largest entanglement appears to be stable with respect to the fixed time T for all accessible times $T > 10$.

C.3.4 Hopping matrix element for effective mapping to Bethe lattice

In the main part of the text, we used the approach of Ref. [213] to estimate the critical interaction strength separating the localized and ergodic phases. In this appendix, we detail the evaluation of the typical matrix element, crucial in estimating the transition. As mentioned in the text, the functional form of the matrix element Eq. (4.39) depends on the relative position of the different particles involved in the process. In particular, they can be either *mixed*, i.e. *dcdc*, *dccd*, *cdcd*, *cddc*, or they can be *ordered*, corresponding to *ddcc*, *ccdd*.

Let us consider first the mixed case, and analyze in detail the case *cdcd*. We define the different positions of the particles as $x_{c,d}^{(1,2)}$ where the numerical indices represent the ordering from left to right. It will be useful to define the distance among same type particles $r_{c(d)} = x_{c(d)}^{(2)} - x_{c(d)}^{(1)}$ and the centre of mass $\overline{x}_{c(d)} = (x_{c(d)}^{(2)} + x_{c(d)}^{(1)})/2$. In this setup, we identify three different regions. Region (I): $j \leq x_d^{(1)}$. Region (II): $x_d^{(1)} < j < x_c^{(2)}$. Region (III): $j \geq x_c^{(2)}$. In region (I) the summand $f(j) \leq e^{-r_c/\xi_c} e^{-2(\overline{x}_d - j)/\xi_d}$, in region (II) $f(j)$ is constant and attains its maximal value $f(j) = e^{-rc/\xi_c - r_d/\xi_d}$, finally in region (III) $f(j) \leq e^{-r_d/\xi_d} e^{-2(j-\overline{x}_c)/\xi_c}$. Consequently, the sum in Eq. (4.39) can be split into three terms

$$V \leq \frac{U}{\xi_c \xi_d} \Big[e^{-r_c/\xi_c} \sum_{j \leq x_d^{(1)}} e^{-2(\overline{x}_d - j)/\xi_d} + e^{-rc/\xi_c - r_d/\xi_d}(d_{cd} - 2) + e^{-r_d/\xi_d} \sum_{j \geq x_c^{(2)}} e^{-2(j-\overline{x}_c)/\xi_c} \Big], \quad \text{(C.7)}$$

where we introduce $d_{cd} = x_c^{(2)} - x_d^{(1)}$ as the distance between the two middle particles.

The two sums now can be reshaped to reproduce the geometric series

$$\sum_{j \leq x_d^{(1)}} e^{-2(\overline{x}_d - j)/\xi_d} = \sum_{j \leq x_d^{(1)}} e^{-(r_d - 2(j - x_d^{(1)})/\xi_d} = e^{-r_d/\xi_d} \sum_{k \geq 0} e^{-2k/\xi_d} = \frac{e^{-r_d/\xi_d}}{1 - e^{-2/\xi_d}} \quad \text{(C.8)}$$

and similarly for the second sum in Eq. (C.7). The matrix element for the case of *cdcd* configuration can thus be estimated to be

$$V \approx \frac{U}{\xi_c \xi_d} e^{-r_d/\xi_d - r_c/\xi_c} \Big[\frac{1}{1 - e^{-2/\xi_d}} + (d_{cd} - 2) + \frac{1}{1 - e^{-2/\xi_c}} \Big]. \quad \text{(C.9)}$$

With a similar approach, we can also obtain the upper bound for the matrix element in the remaining cases of mixed bosons, leading to the same result for the *dcdc* case and to

$$V \approx \frac{U}{\xi_c \xi_d} e^{-r_d/\xi_d - r_c/\xi_c} \Big[\frac{2}{1 - e^{-2/\xi_{c(d)}}} + (d_{cc(dd)} - 2) \Big] \quad \text{(C.10)}$$

for the *dccd* (*cddc*) cases. We checked numerically that, in most cases, the bound is reasonably tight, yielding a very small percentage difference from the actual value.

Now, we consider the case of ordered particles. In this case, the summand $f(j)$ is peaked at the position of the middle boson with shorter localization length. Again, for the sake

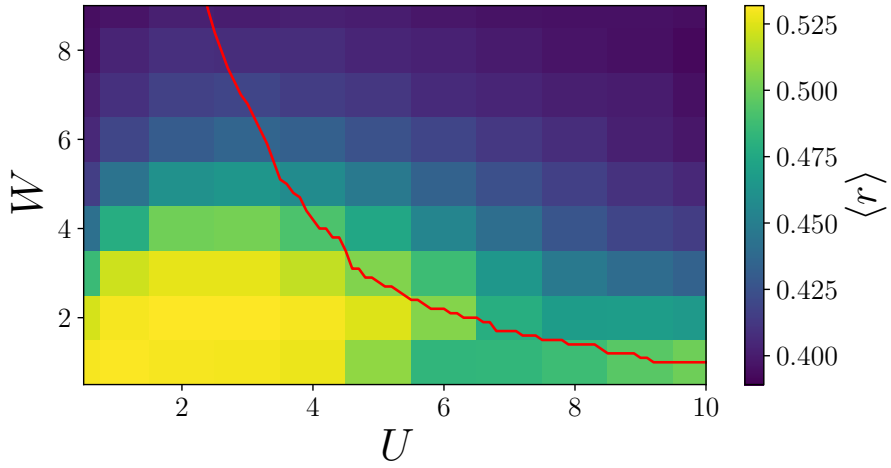

Figure C.7: The critical curve obtained from solving Eq. (C.13) numerically (red line) compared with the level spacing ratio for a small $L = 15$ system. Our analytical approach predicts a transition at a critical interaction strength $U_c \approx 3$ for the disorder $W = 6.5$ used in the numerical simulations. This estimate is compatible with the transition window that shows up in the results of our large scale numerical simulations.

of clarity, we illustrate a particular configuration, but an analogous approach can be used for the other configurations. We choose to show the results for the case *ddcc* where the localization length of d-bosons is shorter than the one of the c-boson (the most typical case). In this setup we can identify two different regions. Region (I), $j \leq x_d^{(2)}$, where $f(j) \leq e^{-r_d/\xi_d} e^{-2(\overline{x}_c - j)/\xi_c}$. Region (II), $j > x_d^{(2)}$, where $f(j) \leq e^{-2(j-\overline{x}_d)/\xi_d - 2(\overline{x}_c - j)/\xi_c}$. The matrix element in region (I) then is upper bounded by

$$\begin{aligned} V^{(I)} \leq \frac{U}{\xi_c \xi_d} e^{-r_d/\xi_d} \sum_{j \leq x_d^{(2)}} e^{\frac{2j - x_c^{(1)} - x_c^{(2)}}{\xi_c}} &= \frac{U}{\xi_c \xi_d} e^{-r_d/\xi_d - r_c/\xi_c - 2d_{dc}/\xi_c} \sum_{j \leq x_d^{(2)}} e^{\frac{2(j - x_d^{(2)})}{\xi_c}} \\ &= \frac{U}{\xi_c \xi_d} \frac{e^{-r_d/\xi_d - r_c/\xi_c - 2d_{dc}/\xi_c}}{1 - e^{-2/\xi_c}}. \end{aligned} \tag{C.11}$$

In region (II) instead we obtain

$$\begin{aligned} V^{(II)} \leq \frac{U}{\xi_c \xi_d} \sum_{j \geq x_d^{(1)} + 1} e^{\frac{-2j + x_d^{(1)} + x_d^{(2)}}{\xi_d}} e^{\frac{2j - x_c^{(1)} - x_c^{(2)}}{\xi_c}} &= \frac{U}{\xi_c \xi_d} e^{-\frac{r_d + 2}{\xi_d}} e^{-\frac{r_c + 2d_{dc} - 2}{\xi_c}} \sum_{k \geq 0} e^{-2\frac{\xi_c - \xi_d}{\xi_c \xi_d} k} \\ &= \frac{U}{\xi_c \xi_d} \frac{e^{-\frac{r_d + 2}{\xi_d}} e^{-\frac{r_c + 2d_{dc} - 2}{\xi_c}}}{1 - e^{-2\frac{\xi_c - \xi_d}{\xi_c \xi_d}}}. \end{aligned} \tag{C.12}$$

The case for $\xi_c < \xi_d$ can be obtained in the same way, bearing in mind that now $f(j)$ is peaked at $j = x_c^{(1)}$, and yields the same results as Eqs. (C.11)-(C.12), except with subscripts for c- and d-bosons exchanged. A similar statement is valid for the case of *ccdd* ordered bosons.

Now the estimate of the typical matrix element corresponds to evaluating the average distances $r_{c/d}$ and d_{cd}, which results in $\langle r_{c/d} \rangle \approx \xi_{c/d}/2$ and $d_{cd} \approx \min(\xi_c, \xi_d)$. Finally, using the localization length obtained numerically in the Hartree approximation [89] and

solving the equation for the critical point

$$\frac{2KeV_c}{\mathcal{W}} \log\left(\frac{\mathcal{W}}{2V_c}\right) = 1 \tag{C.13}$$

numerically, we draw the critical line shown in red in Figure C.7. In the heat map we additionally show results for the average level spacing ratio $\langle r \rangle$ obtained from exact diagonalization of the Hamiltonian (4.4) on $L = 15$ sites. From this approximate analysis, then, we extract a critical value of the coupling $U_c \approx 3$ for the disorder strength $W = 6.5$ used throughout this work. This result is somewhat counterintuitive, given that the hopping amplitude $V \propto U$. Nevertheless, as already obtained in our previous work [89], the effective disorder for the c-boson is proportional to the coupling strength, and hence its localization length $\xi_c \propto U^{-2}$. This results in the observed trend yielding delocalization at weak U and localization at strong interactions.

C.4 Extensive bath

When studying the behavior of the model with a finite density of c-bosons we employ two distinct approaches. At relatively low densities we use MPS simulations with the c-bosons initially equidistant to one another. However at higher densities this approach will lead to a prohibitively fast growth of entanglement entropy, which slows down numerical simulations and prohibits us from reaching long timescales. To avoid this issue, at large densities around half-filling we employ an MPO-based approach, where we simulate the dynamics of the system's density matrix. In particular we prepare an initial density matrix with a small step in the c and d boson densities, which can be written as a trivial MPO with bond dimension one. Provided, the local boson density remains near half-filling (such as 1/2 or 1/3) this initial density matrix leads to relatively slow growth of operator space entanglement entropy (as was also observed in earlier work [156]). This allows us to reach the timescales necessary to extract information on the transport properties of our model at a high density of c bosons.

C.4.1 Bond dimension comparison for density matrix TEBD

In order to estimate the accuracy of our simulations, we compare the value of observables throughout time-evolution for different bond dimensions. In Figure C.8 we present the different density profiles of the d-bosons and the bath for different values of the interaction and different size of the bath. In the top row we show $U = 6$ and $\nu_c = 1/2$, while panels (c)-(d) present $U = 2$ and $\nu_c = 1/3$. The density profiles at $T = 300$, shown in the main panels, are converged at the bond dimensions used in the simulations presented in the main text, thus confirming their accuracy. Additionally, in the insets we plot the time-evolution of the density at the central site for different bond dimensions, similarly showing converged dynamics at the largest bond dimensions.

C.4.2 Transport in the disordered Heisenberg chain

The clear diffusive behavior observed in the transport of d-bosons in Section 4.5.1 is not commonly observed in disordered systems. Previous studies [198, 199, 214] have reported slow, subdiffusive, transport in the ergodic phase of disordered Hamiltonians.

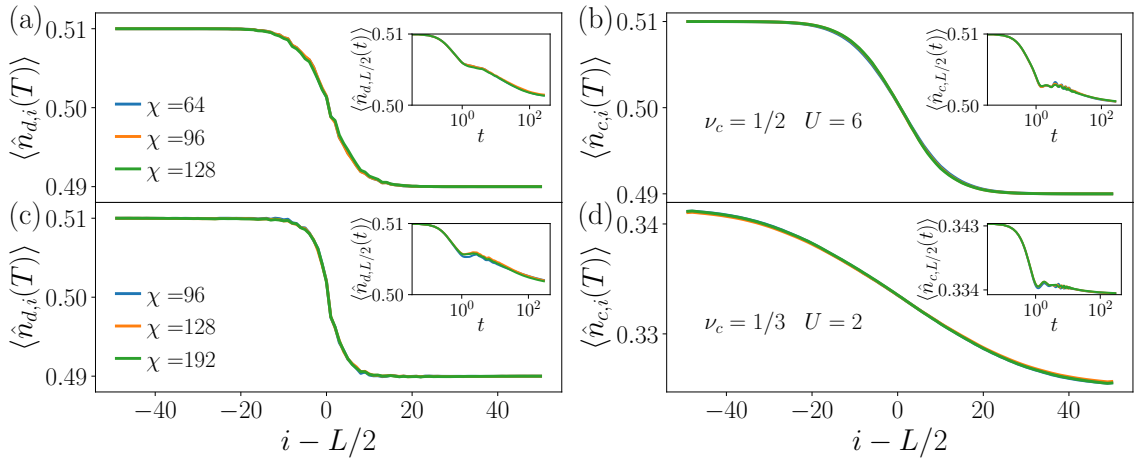

Figure C.8: Bond dimension comparison for the two exemplary values of interaction strength and density, $U = 6$, $\nu_c = 1/2$ in panels (a)-(b) and $U = 2$, $\nu_c = 1/3$ in panels (c)-(d). The main panels show the density profiles for d- and c-bosons at the latest time $T = 300$, confirming the convergence of our results for the bond dimensions used. Additionally, in the insets we compare the time-evolution of the density at the central site, which also shows good convergence with increasing bond dimension.

In this Appendix, we explore dynamics in the disordered Heisenberg chain in a parameter range where disorder and hopping comparable to the one investigated in our work. The aim of this study is to check whether there exists a coupling strength such that the nearest-neighbor interaction of the disordered Heisenberg chain can reproduce diffusive dynamics in a similar timescale as the one observed in the main text.

Although the two species Hubbard model and Heisenberg chain have different local Hilbert space, one can transform the Hubbard model to the spin language to identify the comparable range of parameters. Under this transformation the hopping t_d becomes equivalent to exchange terms that are proportional to J in Heisenberg model, and we set $J = 1$. The random chemical potential ϵ_i acting on bosons translates to a random magnetic field $h_i = \epsilon_i/2$. Thus we choose the Heisenberg model with the following parameters,

$$\hat{H} = \sum_i \left[s_i^x s_{i+1}^x + s_i^y s_{i+1}^y + \frac{J_z}{2} s_i^z s_{i+1}^z + \frac{\epsilon_i}{2} s_i^z \right]. \tag{C.14}$$

We set $W = 6.5$ that controls distribution of $\epsilon_i \in [-W, W]$, and sweep through different interaction strengths J_z since nearest neighbor interaction does not have a direct analog to on-site Hubbard interaction. The Heisenberg model (C.14) conserves total magnetization, allowing for the study of spin transport across a small step, in analogy with the mixed state used in Eq. (4.40) in the main text.

A similar analysis to the one carried out in the main text results in the inverse dynamical exponent $1/z(t)$ shown in Figure C.9. The data reveal much slower transport as compared to the results of Figure 4.27 in the whole parameter range explored, suggesting that the effect of the c-bosons cannot be accounted for by an emergent local interaction term among disordered bosons. A possible explanation, then, is that the c-bosons effectively act as a long-range interaction, justifying the faster transport observed for the two particle species Hubbard model.

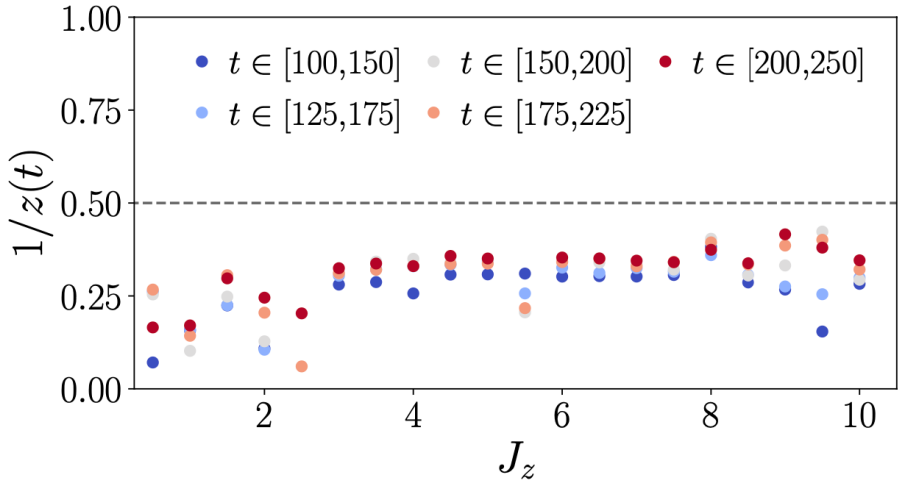

Figure C.9: The inverse dynamical exponent as a function of the interaction strength U. At small values of J_z, dynamics are extremely slow and oscillations complicate the estimation $1/z$ on available timescales. For larger $J_z \geq 3$, $1/z$ shows more regular behavior, highlighting much slower transport in the Heisenberg chain compared to the two species Hubbard model. The data are obtained averaging over 50 disorder realizations and using a bond dimension $\chi = 256$.

C.4.3 Dynamics at small density of clean bosons

In the main text, we reported the deviation from logarithmic entanglement growth as a probe of delocalization at small, albeit extensive, bath size. Here we present some additional data regarding the density profiles and the imbalance, as defined in Eq. (C.4).

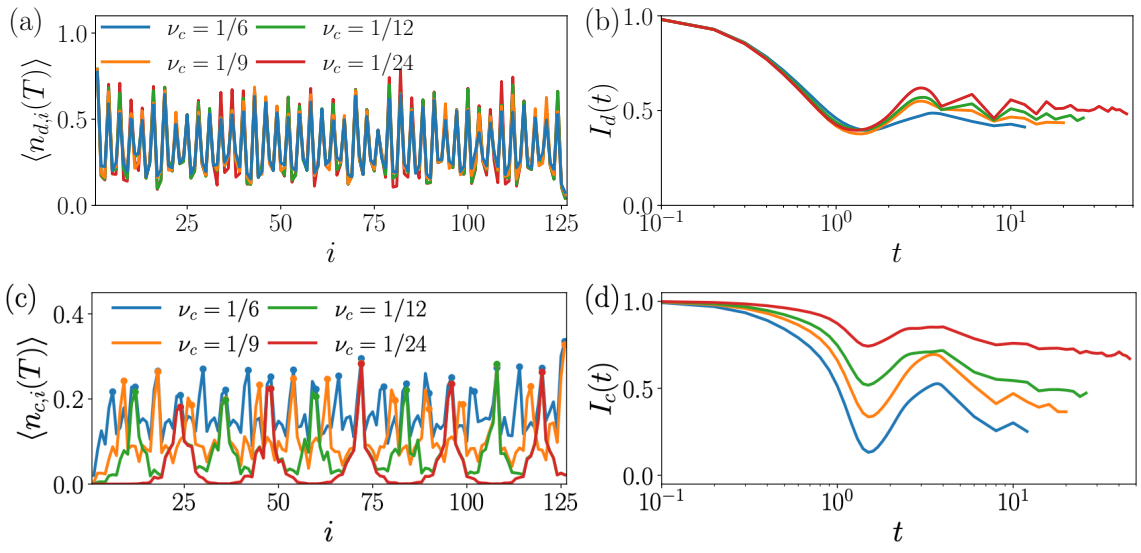

Figure C.10: The density profiles of both particle types show a clear trend suggesting thermalization at large bath density. However, at $\nu_c = 1/24$ $\langle \hat{n}_{c,i} \rangle$ keeps the characteristic density wave structure and the d-bosons density profile is significantly farther from relaxation than at larger densities. The imbalance confirms a monotonous slow down of the relaxation towards thermal equilibrium as the bath density is decreased. The density profiles are shown at the latest time reached by the $\nu_c = 1/6$ simulation, the most expensive, $T = 16$. The value of the coupling is fixed to $U = 6$.

Figure C.10 (a) and (b) show the behavior of d-bosons. In panel (a) we compare the density profile for different bath densities $\nu_c \in [1/24, 1/6]$ at fixed $U = 6$ and $W = 6.5$. The relaxation of the initial density wave towards equilibrium becomes monotonously more pronounced as the density ν_c is increased, in agreement with the results of the main text. A similar phenomenology can be observed in the dynamics of the imbalance, that shows much faster decay at $\nu_c = 1/6$ compared to $\nu_c = 1/24$.

The bottom panels in Fig. C.10 are dedicated to the c-bosons. Similarly to the disordered particles, the density wave is substantially smeared at large c-bosons density, while at $\nu_c = 1/24$ large regions with nearly zero density of clean bosons are visible. Panel (d) reveals that at every bath size explored in this work the imbalance of the c-bosons (I_c) decays in time, although in a slower fashion at smaller bath densities.

Finally, we analyze the connected correlation function of c-bosons. The data shown in the main text leads to hypothesis that the deviation from logarithmic growth of the entanglement entropy could be generated by a significant correlation among the different c-bosons. To check this hypothesis, we studied the behavior of density-density connected correlation function among different sites l_p and $l_p^{'}$, where distance between sites l_p and l_p' corresponds to the initial position of adjacent c-bosons. The results are shown in Figure C.11. The density-density correlations start growing at progressively earlier times as the density ν_c is increased and the correlation function crosses the threshold value $\varepsilon = 10^{-4}$ (dashed line) at a timescale τ_{cc} scaling in bath size with the power-law observed for the onset of the deviation of entanglement growth from logarithmic. This indeed suggests that correlations among clean bosons may be responsible for the onset of more rapid entanglement growth shown in Fig. 4.28 in the main text. Also, consistent with all other probes, the connected correlation function for the lowest density case, $\nu_c = 1/24$, does not cross the threshold value ε within the available simulation time.

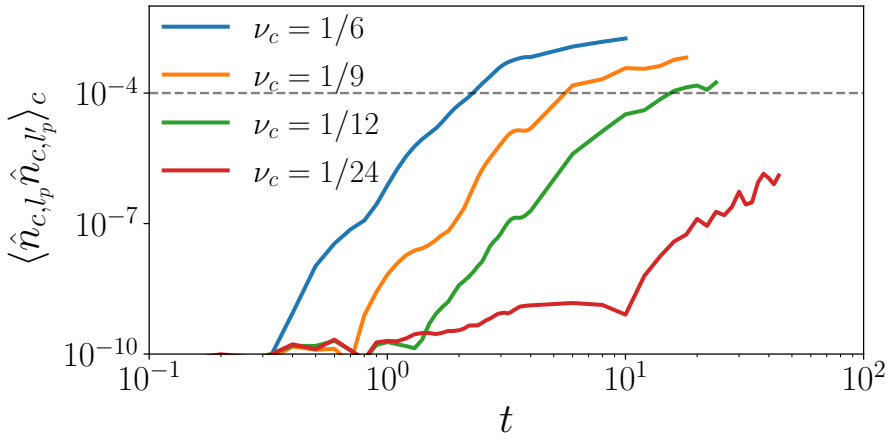

Figure C.11: Density-density connected correlations among different c-bosons at fixed $U = 6$. The characteristic time at which they become larger than $\varepsilon = 10^{-4}$ defines an additional timescale $\tau_{cc}(\nu_c)$ that shows approximate power-law dependence on ν_c, $\tau_{cc} \propto 1/\nu_c^k$ with $k \approx -2.53$ for larger values of ν_c. For the smallest density $\nu_c = 1/24$, correlations may be speculated to show signatures of saturation to a value much smaller than ε, but longer times are needed to support this conclusion.